MANIPULATING LIGHT AT SUBWAVELENGTH SCALES USING HIGH-Q NANOSTRUCTURES: APPLICATIONS IN OPTICAL TRAPPING, OPTOFLUIDICS, AND THERMAL EMISSION CONTROL

By

Sen Yang

Dissertation

Submitted to the Faculty of the

Graduate School of Vanderbilt University

in partial fulfillment of the requirements

for the degree of

DOCTOR OF PHILOSOPHY

in

Interdisciplinary Materials Science

August 11, 2023

Nashville, Tennessee

Approved:

Justus Ndukaife, PhD

Joshua Caldwell, PhD

Sharon Weiss, PhD

Jason Valentine, PhD

Richard Haglund, PhD

This dissertation is dedicated to my dearest parents, Shuai Yang (杨帅) and Jinzhi Zhang (张金枝), to my most adorable girlfriend, Wenyi Ren (任文懿), and to all the people who have supported me along this arduous journey.

ACKNOWLEDGMENTS

I've chosen to write this acknowledgement at the end of my doctoral dissertation, as it feels more like a summary of my five-year doctoral journey, which I would rather call an epilogue. People often say that every PhD is deserving of respect because they have braved many challenges along the way. Back to 2021, I thought the same way. But fortunately, I found direction in my perplexing and challenging research topic and successfully made it to graduation with my advisor's and my friends' help. As I pen down this acknowledgment, I can finally say, graduating as a PhD is not difficult. The real challenge lies in becoming a qualified doctorate holder, an independent researcher, and an idealist who retains a passion for scientific research.

During the journey of pursuing a doctorate degree, encountering difficulties, overcoming them, and eventually finding light at the end of the tunnel, is a recurring theme. Let me start with a story from my research. In the summer of 2021, after several months of hard work, I built a system from scratch for conducting BIC experiments. However, during the experiment, the expected phenomena were not observed no matter what I did. This was the stage I mentioned earlier, where I was lost and anxious about not being able to graduate. Fortunately, one afternoon, I invited my advisor to observe my experiment, hoping that he might have some good suggestions. It was during this experiment that my advisor astutely suggested a change of approach to consider thermal effects in the system, which instantly enlightened me. Following this line of thought and under his guidance, this work was eventually accepted by the reputable optics journal, *Light: Science & Applications*.

I had a similar experience when job hunting. In the summer of 2022, I started looking for jobs in the industry. I received positive feedback from interactions with well-known companies such as Huawei, GlobalFoundries, and KLA, some of which had already progressed to the final round of interviews. Just as I thought I had my job situation under control, the recruitment situation took a drastic turn in August and September, and the process was interrupted. It was from then that many high-tech companies in the United States began to freeze recruitment, which has not yet resumed to this day. With no other choice, I turned to seeking positions in academia. Although I am passionate about research, my initial goal in job hunting was not academia, because the competition there is fierce and I was not confident in my academic achievements. However, after interacting with some universities and research institutions, my resume received much more recognition compared to the industrial sector. In the end, I successfully applied for a fellowship from the Institute of Physics, Chinese Academy of Sciences, and secured a postdoc position.

These are just two of the more easily narratable experiences from the repeated experiences I had during my doctoral studies. Therefore, I believe, this journey of earning a doctorate has not only brought me this doctorate degree that can keep me fed, but more importantly, it has taught me how to be a person with a balanced mentality. No matter what difficulties you encounter, don't be discouraged. You can complain but you should never give up. For many things, you should have an open mind. It's okay to be envious, but it's unnecessary to demand that you should be the same. It is this mentality that has allowed me to make a "zero breakthrough" in my papers after 2021, continuously achieve new results, publish several high-level papers in a row, and win awards like the *2021 Vanderbilt IMS Best Student Paper Award* and the *International Young Scientist Fellowship*. I would like to use the famous poem "If You Were Deceived by Life" by Pushkin to summarize my insights. "If by life you were deceived, Don't be dismal, don't be wild! In the day of grief, be mild: Merry days will come, believe. Heart is living in tomorrow; Present is dejected here: In a moment, passes sorrow; That which passes will be dear."

So, apart from self-regulation, how have I managed to continuously overcome difficulties over these five years and maintain a relatively peaceful heart? Of course, this brings us back to the theme of this acknowledgment - I must express my gratitude for the support I received from those important people throughout this journey.

First and foremost, I would like to express my deepest gratitude to my advisor, Professor Ndukaife. Without his careful guidance and the platform he provided, I wouldn't have been able to achieve my current accomplishments, nor would I have more and better opportunities when seeking jobs in industry and academia. At the same time, it was he who taught me how to conduct research, as well as the capabilities and virtues a qualified researcher should possess. If I am fortunate enough to become a professor in the future, I will convey the words he said in group meetings, such as "We want to be the first in the world to achieve this result," to my students verbatim. This is the legacy I have inherited from LION LAB, and it is the most

important thing I have learned in my five years of research career.

Secondly, I want to thank Professor Weiss and Professor Caldwell. In collaborating with their research groups, I received many valuable suggestions from them. Without them, many of my projects could not have progressed. Beyond academic research, as a member of VINSE and a student in the IMS program, I have also received an abundance of assistance from them, such as arranging defenses, providing strong recommendation letters, the assistance provided when I applied for a short-term postdoc position, and the pleasant surprise when awarding me the *2021 Vanderbilt IMS Best Student Paper Award*. They are truly exceptional professors, and encountering them is one of the luckiest things that happened to me at Vanderbilt.

I would also like to thank Sarah, the Program Manager of our IMS program. She is a very dependable person. She has done an excellent job with all the VINSE activities. She is also a very enthusiastic person; I have lost count of how many times she has helped me. For example, during my recent application to stay as a postdoc, she kept up with my progress, helping me communicate with professors, departments, HR, etc., and smoothly resolving my problems. I am truly grateful to her. She is the best Program Manager I have ever met.

I also want to give special thanks to my two colleagues and friends, Chuchuan and Mingze. Every time I discuss academic problems with them, I gain invaluable insights. The thought of not having the chance to discuss problems with them and "steal ideas from them" after graduation saddens me. In daily life, they are also my best companions. I go to the gym with them, learn new food recipes from them, and I can always count on them for advice and inspiration when encountering distressing difficulties. I hope their paths after graduation will be smooth sailing because they are both such lovely people.

I also want to thank all the friends I've met during my five years at Vanderbilt. Every encounter with you, whether in dark or bright times, is a destined connection. To quote a film review from *Spirited Away*, "Life is a train heading towards the grave, and there will be many stops along the way. It's rare that someone can accompany you from beginning to end. When those accompanying you have to get off, even if you're reluctant to part, you should be grateful, and then wave goodbye." Even if there may not be a chance to meet again in the future, I still hope that everything will go well for you, and all your wishes come true.

Finally, I want to thank my parents, my father Shuai and my mother Jinzhi. I left home to pursue my degrees in colleges in 2011, and it's been nearly 12 years now. When I was in China, I always thought that I was good at taking care of myself and that my parents wouldn't worry about me. And during the winter and summer vacations, I would stay at home, so I wouldn't talk to my family much during the semester. When I went abroad in 2018, it was the same at first. I started the habit of calling home every week probably after breaking up with my ex and the start of the 2020 pandemic. The funny thing is that at first, my parents were quite interested and we could chat for an hour each time. But later on, especially in recent months, our conversations gradually began to revolve around national affairs and economics. Although they have just entered their fifties, I have clearly felt that their hair has become much grayer in the past two years, especially now that their son is about to buy a house and raise a family. Don't worry, mom and dad, I am coming home soon. It's just a couple of hours by high-speed train to Beijing. It's very quick, and we'll be able to see each other often in the future.

Hold on, is this the end? Did I miss someone? Of course not, I could never forget, because this acknowledgment is also the two-year anniversary gift I promised to my most adorable girlfriend, my "ceiling of adorability" Wenyi. I acknowledged her in the first paper of my PhD. Now, I acknowledge her again in my graduation thesis. Just like our love, I remain true to our original aspiration.

Though she never believes it, I felt she was my type the moment I first met her. At that time, she was walking with her ex. Our relationship was fraught with hurdles before we got together, and I often joke that it was my bad luck that cast a negative shadow. I am genuinely grateful for her willingness to let bygones be bygones, and that we could put aside our previous misunderstandings and conflicts, eventually coming together just as she was about to return China. Being in a long-distance relationship across countries is incredibly challenging, particularly for a girl. She was hesitant in the beginning, but I was confident that we could make it through because once she took that step, how could I not be responsible till the end? Even if it's mere pretense, I should at least be responsible for a hundred years, right? (laughs)

From an outsider's perspective, it's almost unfathomable how we managed to maintain a smooth relationship for two years without being able to meet each other, and that our feelings have only grown stronger to the point where we're considering marriage. But I know it's because we're both willing to adapt. In the early days of our relationship, arguments were a regular occurrence, sometimes even requiring a third party to

mediate. However, over time, we both learned to control our emotions. For instance, many times, no matter what she says, I simply say 'yes' and genuinely believe that 'yes' is the right response, thus avoiding many unnecessary conflicts.

In the blink of an eye, we've been together for two years. She used to criticize me for only buying her gifts, and not spending time preparing them. So, to commemorate our second anniversary, I've decided to once again answer the four questions she always enjoys asking before she goes to sleep. This time, the answers will be permanently preserved in Vanderbilt's library. (hehe)

1. Do you love me?

Answer: I love you very much, extremely much. You are the girl I love the most in this world. Meeting you used up all the luck I had.

2. When did you fall in love with me?

Answer: It started when you sewed a teddy bear charm for me. Although you grumbled a bit, you persisted despite burning and pricking your fingers. I deeply felt your genuine care for me.

3. Why do you love me?

Answer: There are so many reasons. At first, it was because you have fair skin, you were adorable in private, and you were polite, voluntarily washing dishes when visiting others' homes. As time went on, I discovered more of your qualities, like your talents in drawing, playing the piano, and singing. You love learning, achieving high scores in the PRC bar; you respect knowledge and never see studying as useless; you're diligent and proactive at work. You have great consumption habits, never wasting money, and your circle of friends is of high quality, which gives us more common ground. The longer we've been together, the more you've managed to curb your tendency to complain and be impatient, becoming better and better. And all this while we're not even living together. So I believe that after we start living together, with mutual tolerance and shared progress, we will only grow happier.

4. How much do you love me?

Answer: I am not the kind of person who is good at or interested in pleasing girls with various tricks, but I am a serious person. Thanks to habits formed during my PhD, I value the concept of "responsibility" very much. Just as a qualified researcher must be responsible for every word in his published articles, I constantly remind myself to be responsible for you. The reason is that it's what I should do as a boyfriend. In the future, as a husband, I will undertake the corresponding role and responsibility towards you and our family, which is something I learned from my father. So, I don't know how much I can love you, but I will definitely hold myself to the standards that a husband who treasures his wife should meet, remaining true to my original aspiration and being consistent.

Lastly, I hope my most adorable Wenyi, in each subsequent two-year period, will always be satisfied with my performance during that period!

TABLE OF CONTENTS

LIST OF TABLES

LIST OF FIGURES

CHAPTER 1

Introduction

Nanostructures that exhibit high quality factors, strongly enhanced and tightly confined electromagnetic fields down to subwavelength scales, and accessible hotspots are of paramount importance for photonic devices. Plasmonic nanostructures can generate highly enhanced and tightly confined electromagnetic hotspots but suffer from inherent metal losses that limit their quality factors. Dielectric Mie resonators using high-index dielectric materials have emerged as alternatives due to their negligible intrinsic losses; however, they typically exhibit lower quality factor values and larger mode volumes compared to plasmonic counterparts.

In this dissertation, two novel platforms are investigated that achieve high quality factors, strong field enhancement, and exposed hotspots simultaneously, demonstrating new physical concepts and mechanisms that were previously unattainable. Applications of these platforms in optical trapping, optofluidics, and thermal emission control are presented.

The following sections in this chapter briefly introduce the fundamental concepts and principles used in this dissertation, including photonic crystal nanobeams, bound states in the continuum, plasmonic nanotweezers, fluid dynamics, and thermal emitters.

1.1 Photonic crystals

Photonic crystal (PhC) microcavities are characterized by regions of diverse materials, each with distinct refractive indices and arranged periodically. These microcavities exhibit a multitude of optical properties such as confinement and slowing down of light. The photonic bandgap (PBG) emerges from the periodic organization of these contrasting dielectric materials [5]. By modulating the dielectric constant in one, two, or three orthogonal directions within a structure, PhCs can be created. One-dimensional (1D) PhCs can be generated either by periodically stacking alternating dielectric layers [5] or by carving a sequence of air holes into a dielectric waveguide, as depicted in Figure 1.1(a) [1]. Two-dimensional (2D) PhCs can be achieved by growing high aspect ratio dielectric columns [41] or by etching holes into a dielectric material in a two-dimensional periodic pattern. The latter method is usually called a PhC slab and has been widely investigated [42] due to its simpler fabrication process. Three-dimensional (3D) PhCs involve complete PBG formation and refractive index modulation in all three directions [43], but fabricating these structures is a complex task. Figure 1.1 [1] schematically illustrates the PhC cavities constructed using these three types of PhCs.

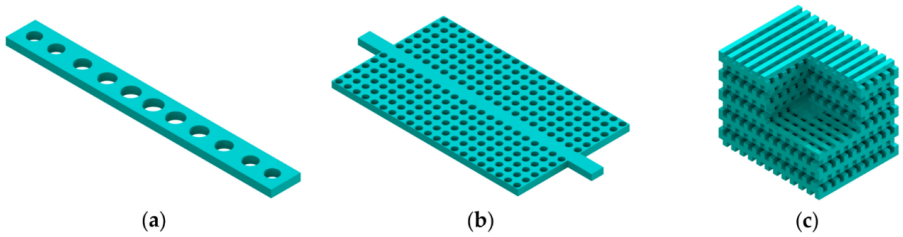

Figure 1.1: Schematic diagrams of (a) 1D, (b) 2D, and (c) 3D PhCs [1].

1.1.1 Photonic crystal nanobeam

In 1997, Foresi et al. [44] showcased the concept of the PhC nanobeam cavity for the first time by incorporating PBG structures directly into a silicon waveguide. This nanobeam cavity exhibited a mode volume (V) of 0.055 μm^3 and a Q factor of 265 at 1.56 μm. The high Q/V ratio and substantial bandgap of this proposed nanobeam cavity rendered it superior to traditional vertically integrated resonant-cavity devices and allowed a light-emitting cavity to be directly coupled into a waveguide. Generally, the Q factor and mode volume V serve as metrics for evaluating the performance of a PhC cavity, with a high Q/V ratio being favorable for various applications such as sensors, lasers, and high Purcell factors.

Subsequently, numerous experimental and numerical efforts have been made to enhance the Q/V ratio by delicately adjusting the geometry surrounding the cavity defect. Notably, Lalanne et al. introduced the concepts of engineering Bloch modes and identified two physical mechanisms for the fine-tuning of hole geometry in PhC cavities [45]. The first mechanism, known as recycling, could be interpreted as the interference between leaky modes and fundamental modes. Additionally, the authors adapted a conventional Fabry-Perot cavity model to account for energy recycling through leaky waves, thereby physically explaining the importance of a phase-matching condition for obtaining a high Q/V ratio. On the other hand, the second mechanism could be achieved by tapering the guided mode of the center defect into Bloch modes of the outside mirror region to minimize out-of-plane far-field radiation [46]. Both methods potentially lead to a Q/V ratio increase by several orders of magnitude. We note that the second approach has since emerged as the most widely adopted design principle and is utilized in this dissertation. These investigations offer valuable physical insights into nanobeam cavity optimization and serve as a foundation for future advancements in the nanobeam cavity design.

Drawing on the concepts of Bloch mode engineering [45, 46], Velha et al. [47] adjusted the cavity defect length based on the number of mirror holes, resulting in a mode volume of $0.6(\lambda/n)^3$ and a Q factor of 58,000 in 2007. Numerous studies have since focused on design concepts and methodologies for optimizing the Q and V of nanobeam cavities. For example, M. Notomi et al. [48] numerically introduced size-modulated PhC

cavities based on mode-gap waveguides, demonstrating an ultrahigh Q of 2.0×10^8. Typically, the design process involves modulation of three elements: the PhC mirror, cavity length, and taper (as depicted in Figure 1.2 [1]). Notably, a deterministic method was proposed by Q. Quan et al. for creating a nanobeam cavity with a high Q/V ratio [49, 50]. The authors employed photonic band calculations, e.g., mirror strength calculation and quadratic tapering, instead of a trial-based approach in the design process, reducing computation costs and enhancing design efficiency. This method enabled the attainment of a final cavity resonance with only a minor deviation from the predetermined wavelength. In particular, cavities are created by tapering the PhC unit cells between highly reflective regions and the cavity region, ensuring a smooth transition and minimizing sudden alterations between unit cells. This can be achieved by progressively changing the unit cell radius, lattice spacing, or nanobeam width. As a result, a Gaussian field profile with low scattering losses is enabled [51]. It is worth mentioning that this approach has become an established design technique for traditional PhC designs and is utilized in this dissertation. Subsequent developments have led to alternative tapering techniques, such as tapering the width of the waveguide [52], which are based on this approach.

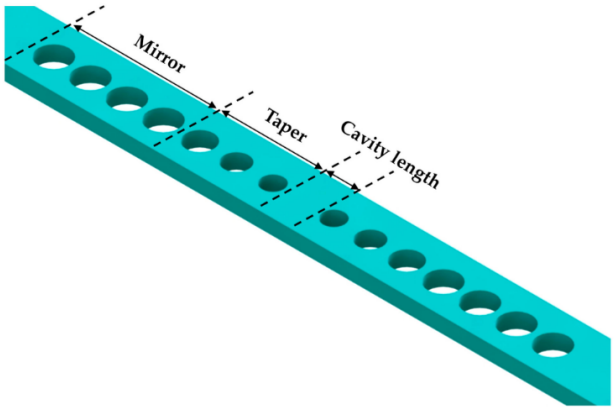

Figure 1.2: Mirror, taper and cavity regions involved in the optimization of PhC nanobeam cavities [1].

1.1.2 Bowtie photonic crystal nanobeam (BPCN)

Simultaneously achieving exceptional temporal confinement (high Q factors) and spatial confinement (low mode volume) is essential for realizing technological advancements in a broad array of photonic and optoelectronic applications. These include compact, low-power light sources, swift and low-power optical switches and modulators, highly sensitive biodetectors for detecting minuscule concentrations of chemical and biological molecules, enhanced and small-volume nonlinear processes, and more. Metal-based plasmonic nanostructures can concentrate light into deep-subwavelength volumes with a typical mode volume of $10^{-3}(\lambda/n)^3$, but their intrinsic ohmic losses restrict the Q factor to around 10. Low-loss photonic crystal cavities can attain extremely high Q factors ($Q \approx 10^5 - 10^6$), but their mode volume is generally three orders

larger ($\sim (\lambda/2n)^3$). To address this trade-off, S. Hu et al. introduced the BPCN for the first time [2, 3], enabling an extremely strong light-matter interaction regime that simultaneously incorporates both an ultra-low mode volume and an ultra-high quality factor.

The operational principle of BPCN stems from the boundary conditions of the electric field and the electric displacement field. As depicted in Figures 1.3(a)-(c), the antislot configuration concentrates the electric field energy in the central dielectric beam due to the continuity of the tangential component of the electric fields. Conversely, as shown in Figures 1.3(d)-(f), the slot configuration confines the electric field energy in the nanoscale low-permittivity region, or the air slot, due to the continuity of the normal component of the electric displacement field. In both cases, the electric field energy density, defined as $u_E = \frac{1}{2}DE$, has an enhancement factor of $\varepsilon_{\text{Si}}/\varepsilon_{\text{air}}$.

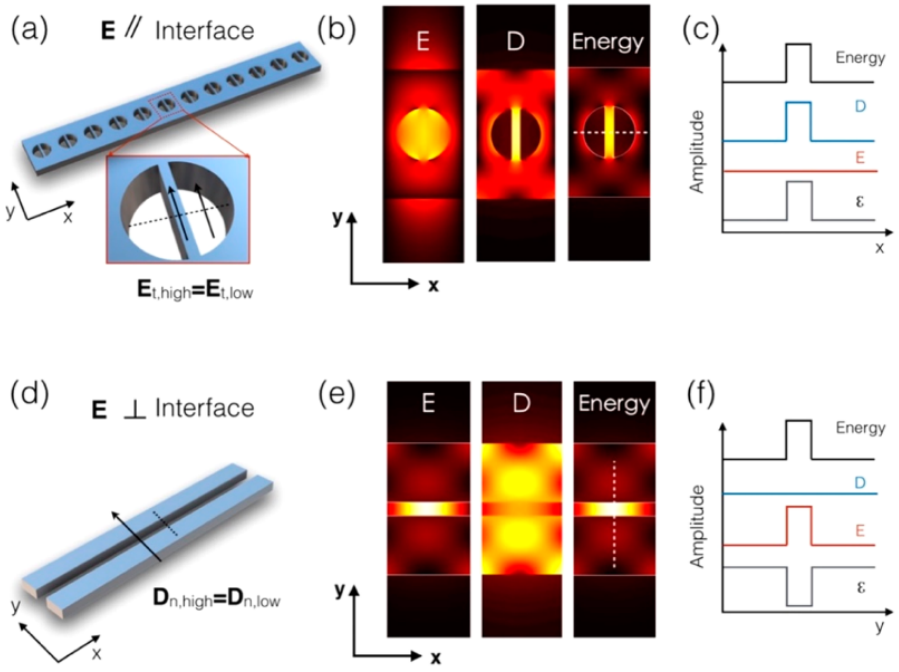

Figure 1.3: Schematic diagrams and field distributions for antislot ((a)-(c)) and slot ((d)-(f)) configurations, respectively [2].

Owing to the orthogonal nature of the electromagnetic boundary conditions, light can be progressively compressed in both the propagation direction and the perpendicular in-plane direction by incorporating a series of interlocked antislots and slots. As illustrated in Figure 1.4, light is continually compressed in the x-direction by adding an antislot and in the y-direction by adding a slot. Consequently, optical energy is gradually confined to increasingly smaller mode volumes. When an infinite number of antislots and slots are added to the unit cell, the geometry approximates that of a bowtie shape, where light is highly concentrated in the central region.

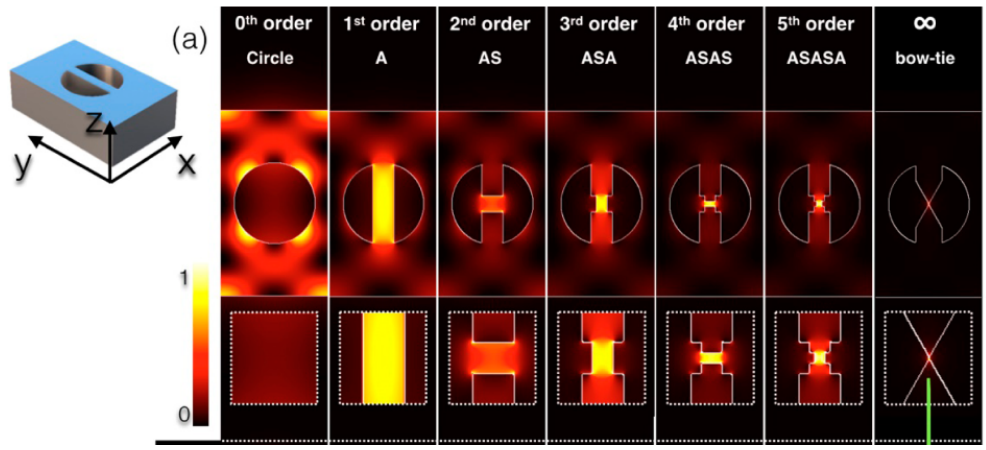

Figure 1.4: Distributions of electric field energy for increasing numbers of incorporated silicon antislots and air slots from left to right [2].

To create a cavity with deep subwavelength confinement at the level of plasmonic components and an ultra-high Q comparable to photonic crystal cavities, the authors developed the BPCN. A bowtie-shaped subwavelength dielectric inclusion added to the lattice holes allows for the optical mode to be redistributed to the bowtie tips. Based on the design methods outlined in the previous section, the BPCN comprises the mirror, tapering region, and the bowtie cavity, as demonstrated in Figure 1.5. The air band of the cavity is positioned in the middle of the mirror bands' bandgap. The v-groove cross-sectional profile results from the fabrication process. In this instance, the authors numerically exhibited a mode volume as tiny as $5 \times 10^{-4}(\lambda/n)^3$ with a quality factor as large as 1.75×10^6 [2], and experimentally demonstrated a loaded Q factor on the order of 10^5 and record deep-subwavelength mode confinement in silicon ($V_{\mathrm{m}} \sim 10^{-3}\,(\lambda/n_{\mathrm{Si}})^3$) [3].

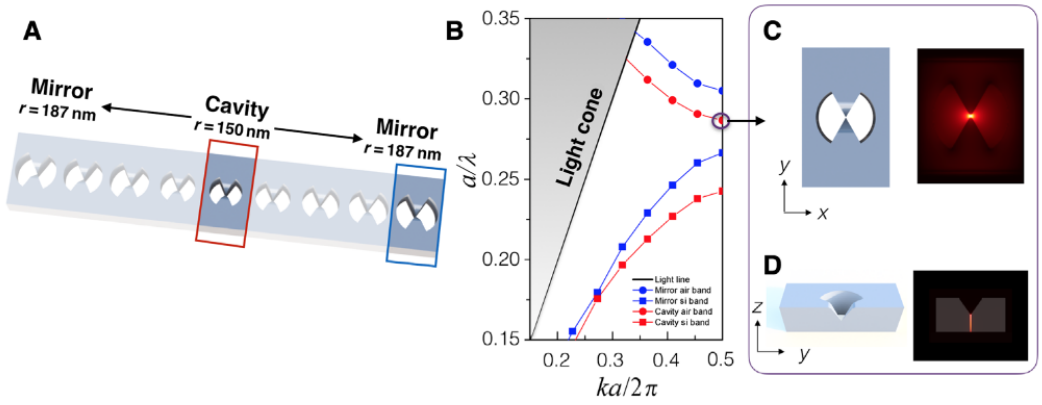

Figure 1.5: Configuration, band structure and field distribution of the experimentally demonstrated BPCN [3].

BPCNS simultaneously incorporate both an ultralow mode volume and an ultrahigh quality factor, thus bridge the long-standing gap that had remained elusive in optical resonators. Due to the strong electric

field enhancement and tight light confinement, it presents great potential in optical trapping applications. In Chapert 3, we demonstrate a nanotweezer system based on cascaded BPCNs. By cooperating with thermal effects in microfluidics such as the electrothermal effects and thermophoresis, we propose Multiplexed long-range electrohydrodynamic transport and nano-optical trapping of sub-20nm particles.

1.2 Bound states in the continuum (BICs)

Bound states in the continuum (BICs) represent localized states with energies embedded in the continuous spectrum of radiating waves. BICs were first predicted as a mathematical curiosity in quantum mechanics in 1929 [53]. In spite of the fact that the system proposed in that work has never been implemented experimentally, the physics of BIC was widely used in wave-relevant fields [4]. For last years, BICs have been attracting very broad attention in photonics, primarily because they provide a simple way to enhance substantially the quality factors (Q factors) for photonic crystals [54], waveguide arrays [55], metasurfaces [6, 9, 10], and even subwavelength isolated resonators [8, 11, 12].

Here, we provide a general background of the concept of BIC, as well as the underlying physics and manifestations of the very recent results in photonic BICs. The key idea underlying bound states in the continuum is vanishing coupling between the resonant mode and all radiation channels of the surrounding space. We follow the classification adopted from Ref. [4] and briefly summarize the two different BICs with respect to the physical origin of radiation suppression. Some applications of this novel photonic nonradiating states reported recently under each category are also introduced.

1.2.1 Bound state and extended state

The confinement of waves is ubiquitous in nature and in wave-based technology. Examples include electrons bound to atoms and molecules (i.e. electrons in potential wells), light confined in waveguides and so on. To determine whether a wave can be perfectly confined or not (that is, if a 'bound state' exists or not) in an open system, a simple criterion is to look at its frequency. If the frequency of the oscillation is outside the continuous spectral range spanned by the propagating waves, it can exist as a bound state because there is no pathway for it to radiate away. Conversely, if the frequency of the wave is inside the continuous spectrum, it can only be a 'resonance state' that leaks and radiates out to infinity. This is the conventional wisdom according to our previous experience. A bound state in the continuum (BIC) is an exception to this conventional wisdom: it lies inside the continuum and coexists with extended waves, but it remains perfectly confined without any radiation. BICs are found in a wide range of wave systems through confinement mechanisms that are fundamentally different from those of conventional bound states.

The general picture describing the spectrum and the spatial profile of the modes are shown in Figure 1.6.

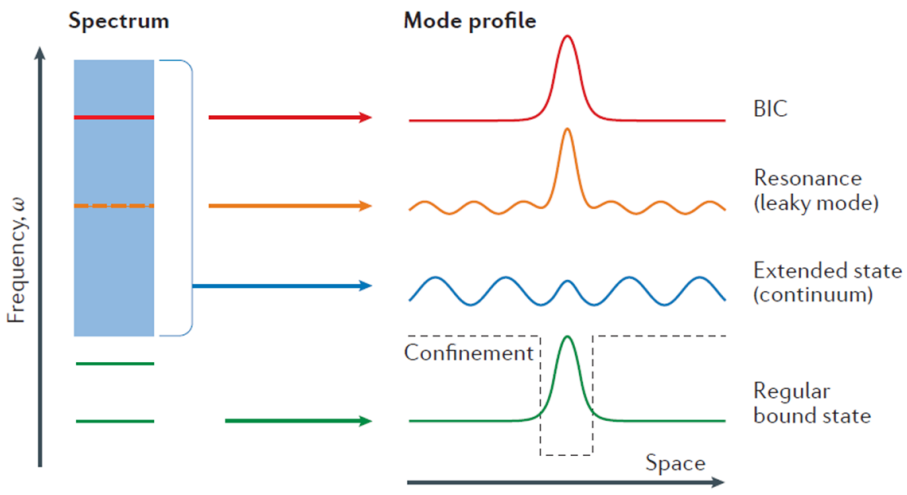

Figure 1.6: Illustration of the spectrum and the spatial profile of the modes. Blue solid line: continuum of spatially extended states. Green solid line: discrete levels of bound states that doesn't radiate energy. Black dashed line: a confining structure or potential well that leads to the spatial localization of the bound states. Orange solid line: leaky resonance modes that lie inside the continuous spectrum and couple to the extended waves and radiate. Red solid line: bound states in the continuum (BICs; red) that lie inside the continuum but remain localized with no radiation [4].

Here we consider a wave that oscillate in a sinusoidal way as $e^{-i\omega t}$ in time t and at angular frequency ω. Extended states (blue region) exist across a continuous range of frequencies. Discrete levels of conventional bound states (green) lie outside this continuum that have no access to radiation channels. A typical example in quantum physics is a bound electron in an infinite potential well. A corresponding example in optics is the discrete modes in a photonic crystal, shown in Figure 1.7(a).

Inside the continuum, the most normal state is the extended state or in other words the propagating waves (blue). The resonance modes (orange) can kind of confine the energy locally as a bound state but in fact the energy still couples to the extended waves and leak out. They can be associated with a complex frequency, $\omega = \omega_0 - i\gamma$, in which the real part ω_0 is the resonance frequency and the imaginary part γ represents the leakage rate. This complex frequency is defined rigorously as the eigenvalue of the wave equation with outgoing boundary conditions. A typical example is a one–dimensional photonic crystal cavity at resonance frequency, shown in Figure 1.7(b).

In addition to these familiar wave states, there is the less known possibility of bound states in the continuum (BICs, red) that lie inside the continuum but remain perfectly localized with no leakage, namely $\gamma = 0$. In a conventional scattering experiment, waves coming in from infinity can excite the resonance modes, causing a rapid variation in the phase and amplitude of the scattered waves with a spectral linewidth of 2γ. However, such waves cannot excite BICs, because BICs are completely decoupled from the radiating waves and are in-

visible in this sense. Therefore, a BIC can be considered as a resonance with zero leakage and zero linewidth ($\gamma = 0$; or an infinite quality factor $Q = \omega_0/2\gamma$). BICs are sometimes referred to as embedded eigenvalues or embedded trapped modes.

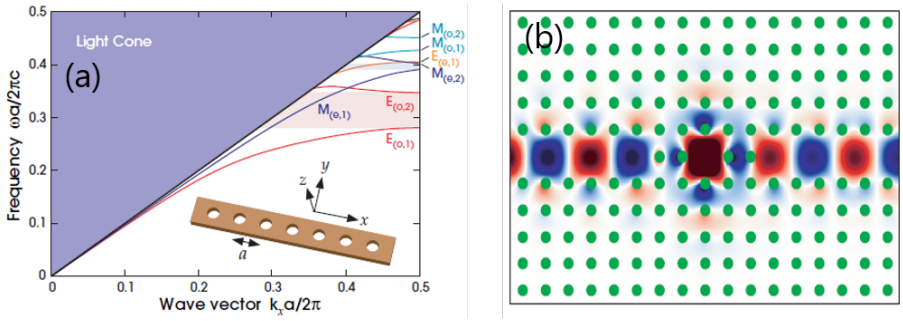

Figure 1.7: (a) Band diagram of a 1D photonic crystal. The discrete lines show the available bound states in the photonic crystal. (b) Field distribution of a 2D photonic crystal cavity [5]. The input frequency is at the resonance frequency of the cavity thus the cavity region shown as a hot spot [5].

Since the linewidth of true BICs is zero, it can't be observed directly in the experiment. To see a resonance peak in the transmission spectrum, researchers usually break the complete confinement and open some small leaky channels. As shown in Figure 1.8, a metasurface is composed of the silicon ellipse pair arrays. When the tilted angle of the ellipse pair becomes not zero, resonance peak start to appear in the transmission spectrum, providing an observable signal. By introducing leaky channels, true BICs are transformed into quasi-BICs and the most recent studies on BICs are actually focusing on quasi-BICs. It has to be noted that the bound state frequency may shift when transformed into a quasi-BIC.

Most of the current study on BICs are based on high-index dielectric meta-optics. According to my knowledge, the only work demonstrating a plasmonic induced BIC is a metal-dielectric system in Ref. [56] which consists of a plasmonic grating coupled to a dielectric optical waveguide. One important reason for that is the low magnetic resonance response of plasmonic nanostructures. However, to generate BICs in nanophotonics, the coupling between multiple modes is fundamentally required. High-index dielectric meta-atoms can support both electric and magnetic Mie resonances including electric and magnetic dipole modes and high-order modes in the visible and mid-IR spectral ranges, which can be tailored by the nanoparticle geometry. And to emphasize the importance of optically-induced magnetic response, the field of all-dielectric resonant nanophotonics is often termed as meta-optics [8]. Figure 1.9 shows the electric and magnetic field enhancement at the midpoint of a plasmonic (gold) and a dielectric (silicon) dimer, both composed of two spherical particles and illuminated with CP light propagating orthogonal to the dimer axis. It's apparent that although both the dielectric and plasmonic dimer have a high electric field enhancement and the gold dimer even has a higher enhancement, the magnetic field enhancement of the gold dimer is almost negligible

compared to the silicon dimer. Therefore, current studies on BICs are mostly focusing on dielectric meta-optics devices rather than plasmonic nanostructures.

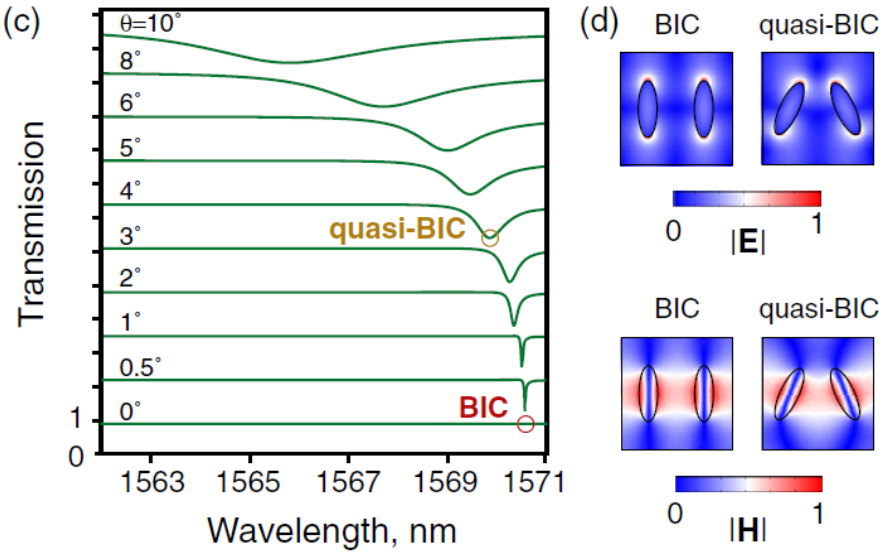

Figure 1.8: Evolution of the transmission spectrum from BICs to quasi-BICs by tuning the tilted angle of the ellipse pair [6].

1.2.2 Classification of BICs

The key idea underlying bound states in the continuum is vanishing coupling between the resonant mode and all radiation channels of the surrounding space. In other words, the light is confined in the structure at a resonance frequency while has no radiation paths to leak its energy into the surrounding environment. Different BICs can be categorized with respect to the physical origin of radiation suppression; here, we follow the classification adopted from Ref. [4] and Ref. [8].

The coupling coefficient could vanish due to the symmetry breaking when the spatial symmetry of the mode is incompatible with the symmetry of the of outgoing radiating waves. Such kind of BIC is called symmetry-protected. It appears in a variety of photonic structures such as grating and metasurfaces [6], photonic crystal slab [54] and waveguide arrays [55].

In contrast to the symmetry-protected BIC, there is also a so-called accidental BIC forming due to accidental vanishing of the coupling coefficients to the radiation waves via continuous tuning of one or several system parameters. The simplest example of accidental BIC is a Fabry-Perot-type BIC. Such a state is formed between two mirrors resonantly reflecting the waves placed at a proper distance providing the phase shift multiple times of 2 after the round-trip [57]. Some of accidental BICs could be explained in terms of destructive interference of two (or more) leaky waves, whose radiation is tuned to cancel each other completely. This mechanism is known as Friedrich-Wintgen scenario [11, 12].

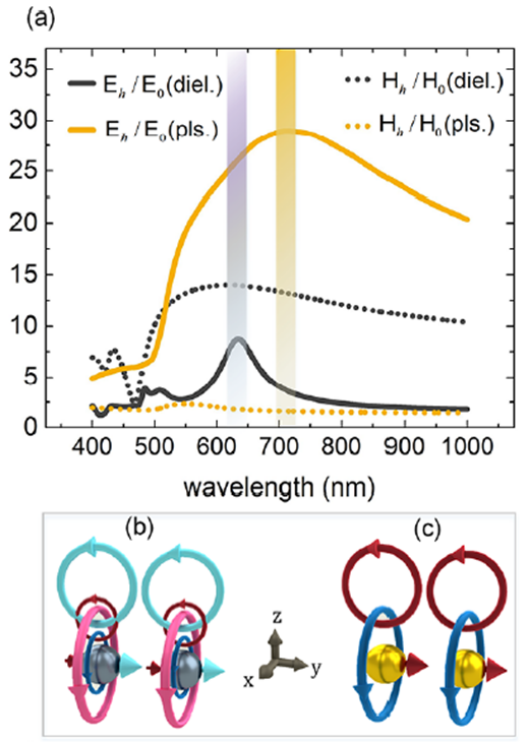

Figure 1.9: Comparison between local electric and magnetic field enhancement at the midpoint of a plasmonic (gold) and a dielectric (silicon) dimer, both composed of two spherical particles and illuminated with CP light propagating orthogonal to the dimer axis. The gray shaded area highlights the spectral range of overlapped electric and magnetic resonances in the dielectric dimer, whereas the yellow shaded area specifies the spectral range of the electric resonance in the plasmonic dimer [7].

1.2.2.1 Symmetry–protected BICs

As we just mentioned, the symmetry-protected BIC can be found in a variety of photonic structures. Here we discuss the most recent studies on generating quasi-BICs in dielectric metasurfaces. Sharp spectral resonances (i.e., high Q factors) for various types of metasurfaces originate from the distortion of the symmetry-protected BIC. A true BIC can transform into quasi-BICs (i.e., super cavity modes) when the in-plane inversion symmetry of a unit cell becomes broken. A typical example is the metasurface of which each unit cell is composed of a pair of ellipse nano-bars made of silicon, as shown in Figure 1.10. The polarization of the incident linear polarized light is along the x direction.

To understand the radiation suppression that generating the quasi-BIC, we need to analyze the electric field distribution in the near-field. As shown in Figure 1.11(a), the dominant polarization component within the Si region is E_y (i.e., the black arrows are almost along y direction with a very tiny inclination angle), while the main polarization component of the back-scattered field is E_x. This is due to the antisymmetric distribution of the dominant polarization components E_y of the meta-atoms within each unit cell, consistent with the collective modes described in Ref. [58, 59]. Two inverse electric dipoles are excited in the two

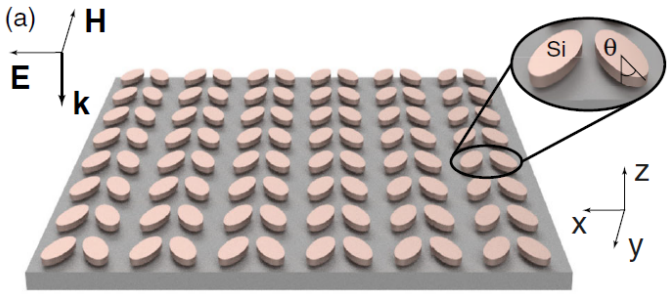

Figure 1.10: Illustration of the metasurface composed of square lattices of tilted silicon-bar pairs [6]. The corresponding evolution of the transmission spectrum is shown in Figure 1.9.

elliptical- cylinder resonators (i.e., p_x and p_y, seen in Figure 1.12. Although p_y is dominant in each meta-atom, the directions of the p_y components are inverse for the two meta-atoms in the unit cell (clearly shown by the black field vector arrows in two meta-atoms, and also seen in Figure 1.12), which cancel with each other and thus the out-coupling of E_y is forbidden. When the orientation angle θ is small, the overall radiative loss is then suppressed significantly. Thus, a fairly narrow reflectance peak as well as a high field enhancement are obtained. On the other hand, although the p_x components are relatively small, they are in the same direction. Therefore, only E_x contributes to the radiative loss and becomes the dominant polarization component of the back-scattered field.

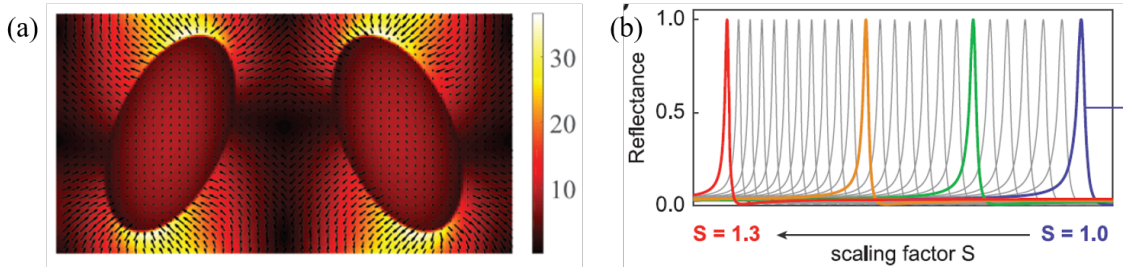

Figure 1.11: (a) Electric field distributions of *xy* plane at the middle height. The black arrows in the figures show the electric field vectors and the colorbar represents the field enhancement. (b) The reflection spectrum of the metasurface with different dimensions of the meta-atoms [8].

Since the materials of both the resonators and the substrate have almost no loss, the leaky channels are strongly suppressed and only very small part of the incident energy can radiate into the far field. Therefore, the field enhancement is high and can be even higher with small tilted angles. Furthermore, scaling the whole unit cell by ratio can further increase the field enhancement due to a smaller mode volume. It has to be noted that, due to the specially designed geometry, this metasurface allows for a straightforward and nearly linear resonance frequency tuning via scaling of the unit cell geometry by a factor S, as shown in 1.11(b).

Yuri Kivshar et al. developed an analytical approach [6] to describe light scattering by arrays of meta-

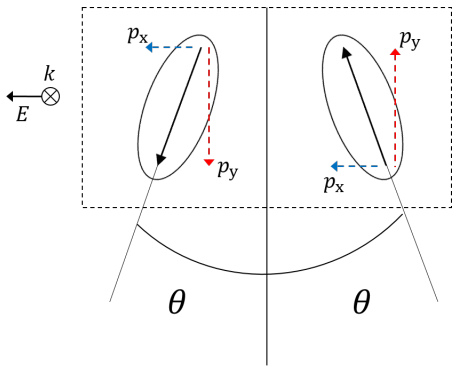

Figure 1.12: Diagram presenting the two inverse electric dipoles excited in the ellipse pair resonators. The blue and red dash arrows represent the two components p_x and p_y, respectively.

atoms based on the explicit expansion of the Green's function of open systems into eigenmode contributions, and demonstrate rigorously that the Q factor of such an asymmetric metasurface governed by BICs has a simple relationship which can be expressed as $Q = Q_0\alpha^{-2}$. Here Q_0 is a constant determined by the metasurface design and represents the asymmetric parameter as shown in Figure 1.13.

1.2.2.2 Applications of symmetry-protected BICs

Based on the symmetry-protected BIC metasurface we just discussed, several applications have been demonstrated recently. Here we introduce two prominent works that both are reported by Hatice Altug's group.

Since this metasurface allows for a straightforward and nearly linear resonance frequency tuning via scaling of the unit cell geometry, it can work as pixels. Researchers arrange these metasurfaces with different geometries into an array and feature a big two dimensional pixelated dielectric metasurface with a range of ultrasharp resonances, each tuned to a discrete frequency; this enables molecular absorption signatures to be read out at multiple spectral points, and the resulting information is then translated into a barcode-like spatial absorption map for imaging. As shown in Figure 1.14, the one-dimensional discrete reflection spectrum of a protein molecular monolayer can be transformed into a readable two-dimensional barcode-like map, which is specific for the chosen protein molecular.

Researchers demonstrate the detection on signatures of protein, polymer, and pesticide molecules with high sensitivity which corresponds to a detection limit of 2130 molecules per μm^2, covering potential applications such as biosensing and environmental monitoring. This technique can resolve absorption fingerprints without the need for spectrometry, frequency scanning, or moving mechanical parts, thereby paving the way toward sensitive and versatile miniaturized mid-infrared spectroscopy devices.

Besides the imaging-based chemical identification in mid-IR, they also show the application of hyperspectral imaging in near-IR. As shown in Figure 1.15, their device comprises an array of all-dielectric sensors,

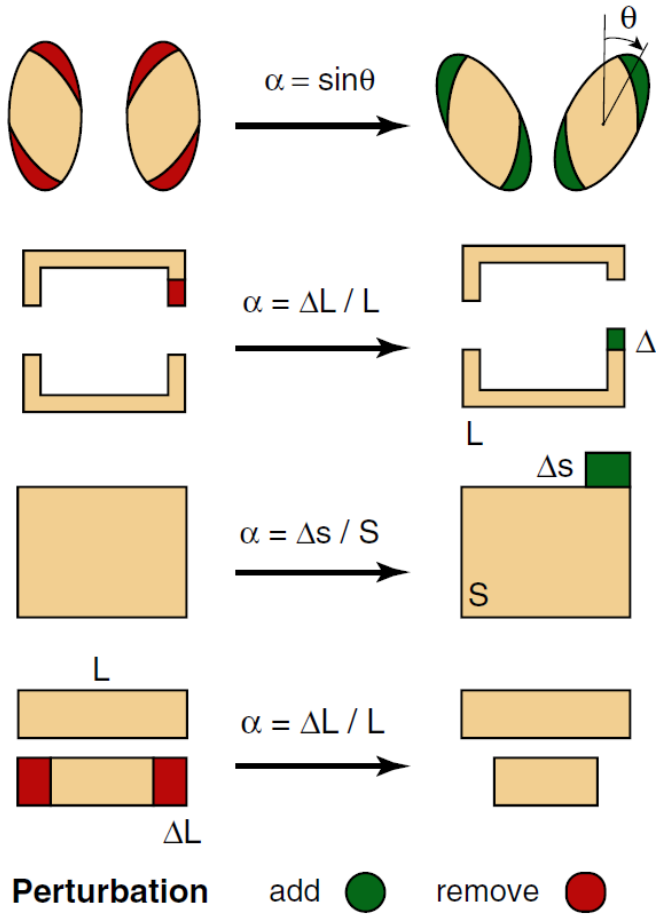

Figure 1.13: Definitions of the asymmetry parameter α for different metasurfaces. Green and red region represent "add" and "remove" part of the original geometry to introduce asymmetry [6].

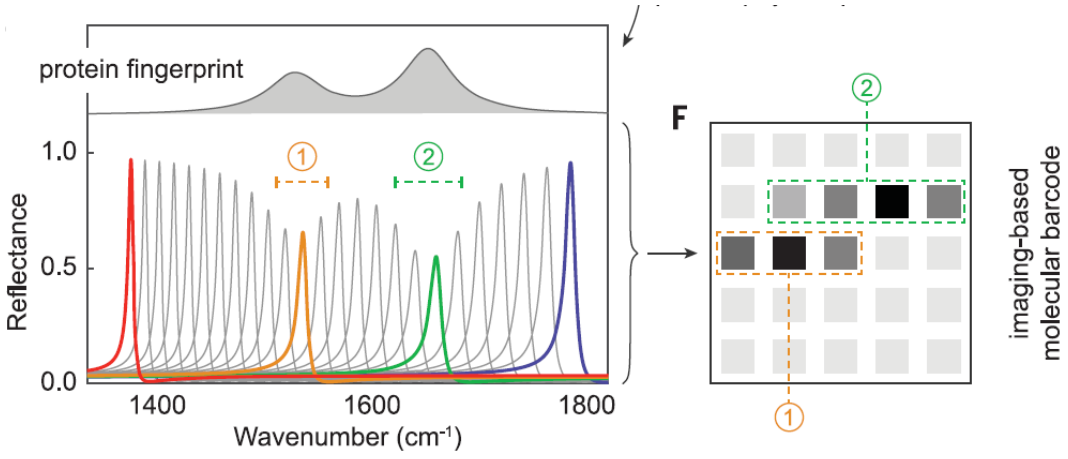

Figure 1.14: The envelope of metapixel reflectance amplitudes of a model protein layer (top inset) and how to obtain the molecule-specific barcode by the metasurface's reflectance response [9].

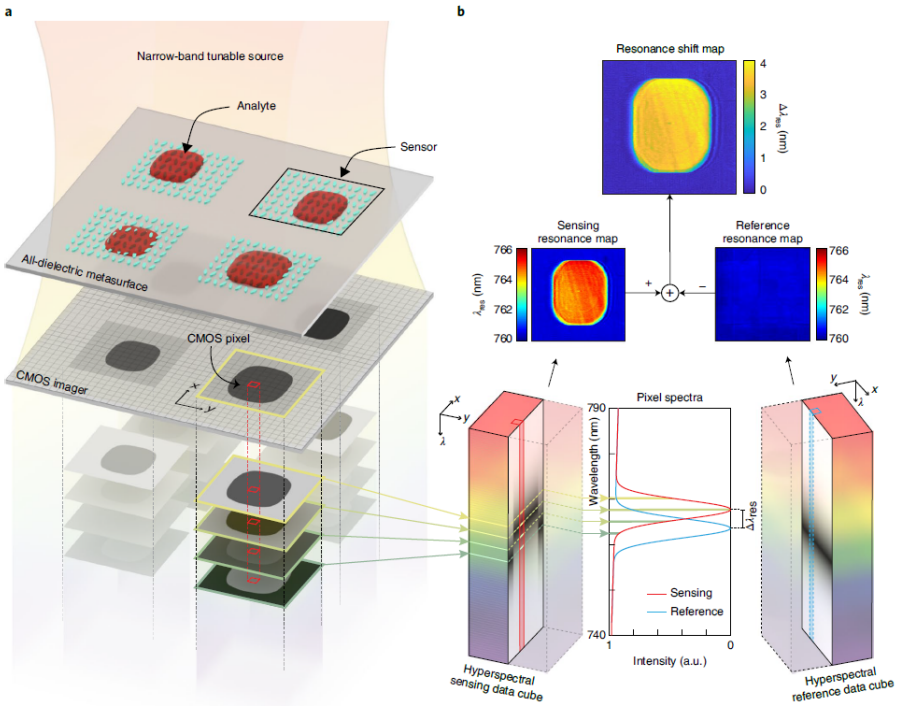

Figure 1.15: Sketch of the hyperspectral imaging principle and processing of the hyperspectral data cube [10].

allowing for multiplexed analyte detection in a single measurement. In the optical set-up, they use a continuously tunable narrow bandpass filter coupled to a supercontinuum laser source for continuously tunable excitation and record transmission images at each illumination wavelength using a CMOS camera. This optical configuration can spatially probe the metasurface spectral response over large areas, in contrast to traditional spectrometers. Each metasurface pixel has a specific resonance wavelength and generates a resonance shift when covered by the analyte. Specifically, they use an extremely narrow bandwidth (~ 2 nm) and tunable excitation with high spectral resolution ($\Delta\lambda = 0.1$ nm) to build a hyperspectral data cube of the field of view that contains full spectral information from the entire sensor array, where each sensor is mapped by tens of thousands of CMOS pixels. This technique reveals biomolecular detection information at molecular counts as low as around 3 IgG molecules per μm^2).

1.2.2.3 Accidental BICs

In nanophotonics, conventional ways to enlarge the Q factor are to increase the size of a resonator, for example, by exploiting whispering gallery modes and cavities in photonic crystals, as shown in Figure 1.16(b) and Figure 1.16. Although such techniques allow for light confinement with reduced energy losses, the size of the resonating system is still large compared to the operating wavelength. Here we introduce a completely

different approach based on the concepts of BICs and supercavity modes in isolated nanoparticles.

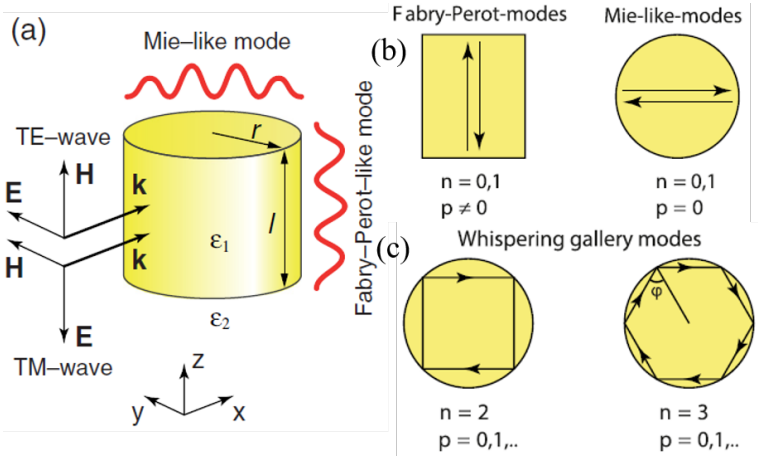

Figure 1.16: Classification of eigenmodes of an isolated dielectric cylindrical resonator [11].

As shown in Figure 1.16(a), the electric field of the incident wave is assumed to be perpendicular to the axis of the cylinder. The eigenmodes of such a finite-length nanocylinder can be roughly divided into two families, namely, radially oscillating and axially oscillating modes. The radial resonances are formed mainly due to reflection from a side wall of the cylinder, and they could be associated with the Mie resonances of an infinite cylinder. The axial resonances are formed mainly due to reflection from the faces of the cylinder, and they could be associated with the Fabry–Perot modes (FP modes). A pair of low-frequency FP-like and Mie-like modes can undergo strong coupling via continuous tuning of the disk aspect ratio r/h, producing the characteristic avoided resonance crossing feature, as labeled by red circles in Figure 1.17(a). The avoided resonance crossing is a key feature for generating a quasi-BIC near the crossing region, which can be understood in Figure 1.17(b).

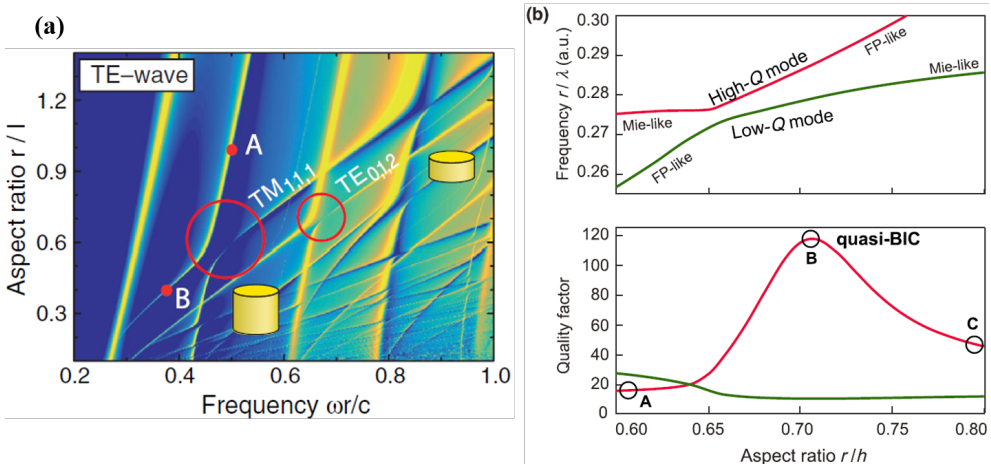

Figure 1.17: . Strong coupling of two resonator modes resulting in the emergence of a quasi-BIC. Colorbar in (a) represents the scattering cross section effiency [11].

This avoided crossing reflects a strong coupling between the FP-like and Mie-like modes, corresponding to a supercavity mode. The near-field electric field profiles and far-field radiation pattern of the high-Q mode for the aspect ratio in- and out of this supercavity regime are shown in Figure 1.18. It is clearly seen from the near-field distributions that a Mie-like mode smoothly transforms to a FP-like mode through a quasi-BIC with a hybrid field distribution. Away from the quasi-BIC condition, the far-field distribution of the high-Q mode is dominated by the magnetic dipole contribution for both Mie-like and FP-like modes. Since both FP-like and Mie-like modes are characterized by the magnetic dipole radiation pattern, their coupling leads to sufficient suppression of the magnetic dipole component enabling a highly symmetric magnetic octupole term [11].

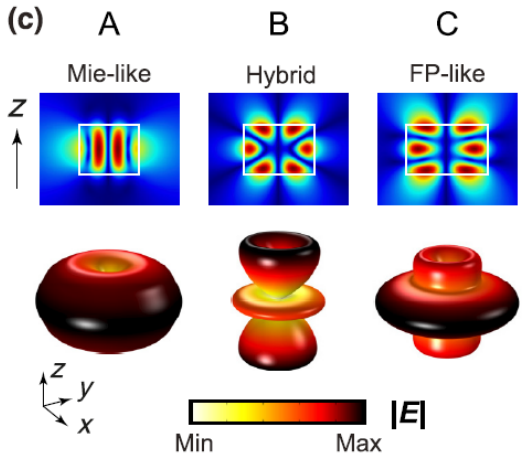

Figure 1.18: Upper panel: Near-field distributions of the electric field at the points A, B, and C in Figure 1.17(b). Lower panel: Transformation of the radiation pattern for the high-Q mode while passing the avoided resonance crossing regime [8].

1.2.2.4 Applications of accidental BICs

The theoretical analysis discussed in the previous part is based on an illumination from the side of the resonator. It's really difficult to realize such an optical set-up or fabrication in nanophotonic experiments. Recently, a work reported by Yuri Kivshar's group demonstrate a second-harmonic generation (SHG) enhancement which is based on the accidental BIC while the individual nanodisk is illuminated from top.

As shown in Figure 1.19, the quasi-BIC mode is generated in a nano-cylinder made of AlGaAs (aluminum gallium arsenide, a kind of nonlinear material with superior second order nonlinear properties) placed on a three-layer substrate ($SiO_2/ITO/SiO_2$). Similarly, the physics of quasi-BIC relies on destructive interferences of two leaky modes with similar far-field patterns. The cylindrical resonator supports two families of leaky modes, which we have discussed previously as radially and axially polarized modes, as depicted in Figure 1.20(a). Away from the hybrid regime, both of them demonstrate dipolar magnetic response in the

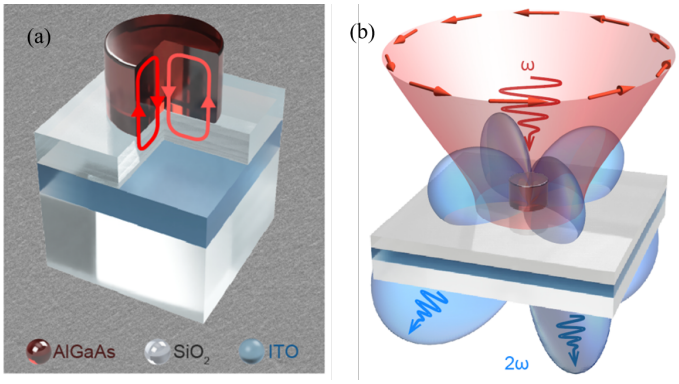

Figure 1.19: Schematic diagram of the isolated subwavelength nanodisk and the generation of SHG [12].

far-field. To couple incident light illuminated from top efficiently to the quasi-BIC resonant mode from the far-field, they employ an azimuthally polarized vector beam which has a similar electric field profile with the hybrid mode. Decreasing the difference between their frequencies via tuning of the disk diameter they achieve the strong coupling regime which produces the characteristic avoided resonance crossing of frequency curves and enhancement of mode radiative Q factors (see Figure 1.20(b) and 1.20(c)).

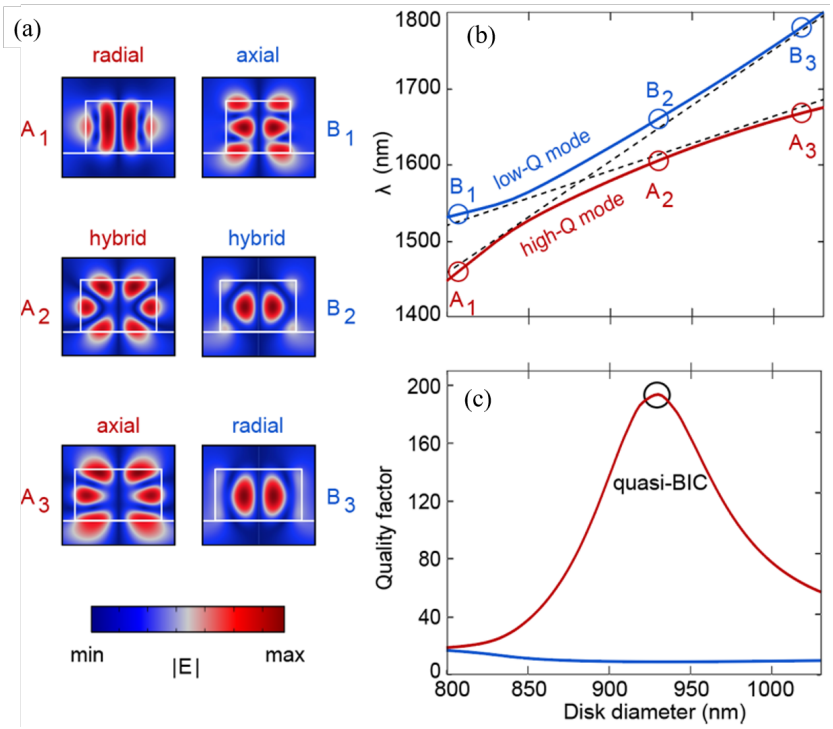

Figure 1.20: (a) Near-field patterns transition between the radial mode and the axial mode. (b) Avoided resonance crossing between the high-Q and low-Q modes. (c) Q factor for the high-Q and low-Q modes vs. resonator diameter.

To compensate the decrease of the Q factor induced by energy leakage into the substrate, they engineer

the substrate with an additional layer of ITO (indium tin oxide) exhibiting epsilon-near-zero transition acting as a conductor above 1200 nm wavelength (i.e. at the quasi-BIC wavelength and thus reflect the leaky light), and as an insulator below this wavelength (i.e. at the SHG wavelength and thus not affect the transmission of 2ω wave). The ITO layer is separated from the resonator by a SiO_2 spacer. Thickness of the SiO_2 spacer layer allows to control the phase of reflection, also enhancing the destructive interference of the two leaky modes in the far-field and thus increasing the Q factor.

To maximize the SHG efficiency, firstly the spatial profile of the pump must be structured to match the distribution of the excited mode. To provide the perfect spatial matching, they use the cylindrical vector beam with azimuthal polarization resembling the far-field pattern of the quasi-BIC mode. Next, the optimal structure must be resonant simultaneously at pump and second-harmonic wavelengths (magnetic octupole and quadrupole modes respectively) and both resonances must be of a high Q factor. The ITO film of the structured substrate, while acting as a mirror at the pump wavelength, is transparent at the SHG wavelength with material properties similar to glass, allowing second-harmonic radiation to propagate in both forward and backward directions.

1.2.2.5 Summary

In this section, we briefly introduce the concepts of bound states in the continuum in general wave physics and photonics and discuss the two different types of BICs. We use specially designed dielectric metasurface as an example for the symmetry-protected BIC and individual dielectric nano-cylinder antenna as an example for the accidental BIC. Relevant applications are reviewed for each type respectively.

Strong field enhancement and high quality factor are crucial for many applications in nanophotonics. BICs based on dielectric meta-optics have attracted great attention recently and provide different ways to achieve large enhancement of electromagnetic fields and confinement of light in high-index dielectric resonators with significant advantages for integrated photonics applications under mature semiconductor fabrication technologies. Since the basic physical principles of photonic BICs have now been understood and demonstrated, further exploitation of the physics of BICs and the study of their properties would involve a design of different types of resonant structures with a higher field enhancement and stronger magnetic field confinement in specific "hot spots", which is important for broad applications such as optical trapping and Raman signal enhancement. Due to the narrow spectrum linewidth and nearly loss-free material properties, dielectric BICs have an enormous potential in taking place of conventional plasmonic nanostructures in many domains of nanophotonics, including but not limited to biological sensing, Raman scattering, multifunctional on-chip lasers and particle trapping.

As an investigation, this dissertation explores several interesting applications based on the quasi-BIC

metasurface composed of elliptical resonators, including optical trapping (Chapter 2), optofluidics (Chapter 4) and thermal emission control (Chapter 5) at mid-infrared. These studies demonstrate the enormous potential of BIC metasurfaces in optoelectronic devices, and have attracted a lot of attention in the BIC community.

1.3 Plasmonic nanotweezers

Optical trapping technology has been widely used in biology, medicine, and colloidal assembly [60–63] due to its precise control and non-invasive manipulation of microscale particles. Traditional optical tweezers have been employed to manipulate objects such as bacteria, colloidal particles, and cells [64–66], and Arthur Ashkin received the 2018 Nobel Prize in physics for his groundbreaking work on optical tweezers [67]. Single-beam optical tweezers, first demonstrated in 1986, use a tightly focused laser beam to trap particles near the laser's focal spot. However, the diffraction limit of light makes it challenging to focus light on nanoscale subwavelength volumes and, thus, to trap nanoscale objects using low-power optical tweezers. Plasmonic nanotweezers [68] have garnered considerable interest due to their ability to confine light in nanoscale volumes with high field enhancement, creating tight trapping potential wells required for trapping nanoscale objects. Despite overcoming the diffraction limit, plasmonic materials inherently suffer from Ohmic loss and generate photo-induced heating, which can harm trapped particles and destabilize trapping if heat management is not properly addressed.

1.3.1 Plasmonic nanotweezers

The strong enhancement and tight confinement of the light field in plasmonic resonances enable plasmonic nanotweezers to exert strong optical gradient forces given by

$$F_{\text{grad}} = \pi\varepsilon_e a^3 \frac{\varepsilon_p - \varepsilon_e}{\varepsilon_p + 2\varepsilon_e} \nabla |\vec{E}(r)|^2 \tag{1.1}$$

,allowing for low-power optical trapping compared to traditional optical tweezers. Various designs of plasmonic resonators have been explored in the rapidly growing field of plasmonic nanotweezers.

One design involves extruded metal resonators sitting on a flat surface, which are commonly used structures for creating localized plasmonic resonances. Examples include nanopillars, plasmonic bowties, and nano-dimers, as shown in Figure 1.21(a) to (c). This design is fabricated using standard metal-based lithography and lift-off technology. Another resonator design involves apertures in a continuous metal film, such as bowtie apertures, double nanoholes, and coaxial apertures shown in Figure 1.21(d) to (f). These are fabricated by directly removing portions of the metal from the film to create discontinuity, using a focused-ion beam, for instance. Targets as small as sub-10nm nanoparticles, such as single protein molecules [17] and

silica beads [69], have been demonstrated.

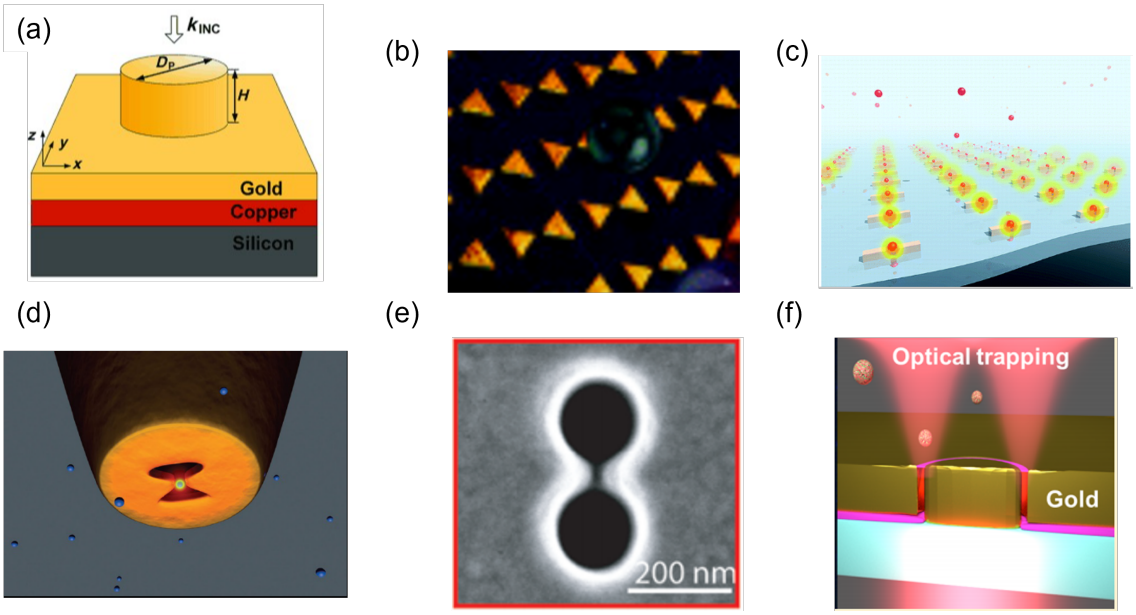

Figure 1.21: Examples of plasmonic nanotweezers utilizing (a) nanopillar [13], (b) plasmonic bowtie [14], (c) nano-dimers [15], (d) bowtie aperture [16], (e) double nanohole [17] and (e) coaxial aperture [18].

However, one drawback of plasmonic nanotweezers is the photoinduced heating effect resulting from the intrinsic loss of metallic materials, which can generate undesired thermal effects that interfere with trapping and reduce trapping stability. Furthermore, excessive temperature increases can damage trapped particles, especially biological objects like cells. Regrettably, all previously reported plasmonic nanotweezers trap particles at the location of maximum temperature rise. It is important to note that extruded resonators generally suffer more from these effects, as they are situated on low thermal conductivity substrates and surrounded by a low thermal conductivity dielectric environment. Such weaker heat dissipation leads to a higher temperature rise. In contrast, nanoaperture-based plasmonic nanotweezers experience less heat dissipation due to their embedded position in a continuous metal film, which allows for direct heat dissipation by the metal film and a more moderate local temperature rise [70].

Another challenge for plasmonic nanotweezers is the lack of dynamic manipulation capability. Typically, a plasmonic resonator is fabricated on a substrate and fixed at a specific location. Loading the plasmonic cavity relies on non-deterministic Brownian diffusion, rendering the particle loading process random and slow [71].

1.3.2 Photothermal effects in plasmonics

As previously mentioned, plasmonic structures inherently exhibit loss, leading to light absorption and heat generation. The absorption of an object increases with the intensity of the electromagnetic wave.

Excessive heating can cause several disadvantages. First, it can damage trapped targets, such as denaturing DNA molecules [72] or deactivating and restructuring proteins. Second, positive thermophoresis moves particles away from hotspots to colder regions, compromising trapping stability. This phenomenon can be explained by the fact that, when a particle is within a temperature gradient, the side exposed to higher temperatures experiences more active Brownian motion of water molecules. The momentum transferred to the particle from collisions with water molecules is greater on the hotter side than on the colder side, causing the particle to move toward the colder region. Third, buoyancy-driven convection can destabilize the particle trapping. This effect arises from the heat expansion of water within a temperature field gradient, leading to the change of water density and creating bulk water motion [73]. One way to mitigate convection's impact is to reduce the microfluidic chamber's height.

Several methods have been proposed to lessen the effects of photothermal phenomena on trapping stability. For example, Wang et al. [13] suggested placing a heat sink made of metals (i.e., gold and copper) beneath the plasmonic resonator to dissipate heat. Another approach is to detune the resonant wavelength from the plasmonic resonance, though this sacrifices the field enhancement that could have been utilized [74]. It is important to note that photothermal effects in plasmonics are not always detrimental. Recently, researchers have discovered that the enhanced light absorption can efficiently transform metal nanostructures into nanoscale heat sources, giving rise to the study of thermoplasmonics [75, 75, 76]. This finding has led to numerous applications in nanotechnology, such as photothermal cancer therapy [77], targeted drug delivery [78], solar-powered steam generation [79], and nanoscale temperature distribution control for optofluidics. Both single [80] and arrays [73, 81, 82] of metal nanostructures have been investigated to regulate convection-driven dynamics. With careful management, these effects can contribute to trapping and endow nanotweezers with unique functionalities, including dynamic manipulation and rapid particle transport.

According to these discussions, we realize that the photoinduced heating is an important topic in plasmonic nanotweezers. This dissertation has tried to play with this from two sides. In Chapter 2, we propose a lower-power optical trapping system based on an all-dielectric quasi-BIC metasurface, in which the heating effect is supressed. In Chapter 4, we propose a new method to manipulate temperature field distribution and fluid motion at the micro-nano scale levearaging the narrow lindwidth of the quasi-BIC resonance.

1.4 Fluid dynamics

Non-uniform AC electric fields have been used to analyze and process particles for over 50 years. The movement of polarizable particles in non-uniform electric fields is called dielectrophoresis (DEP) and was first demonstrated by Pohl in 1951 [83]. In the later particle trapping and separation experiments, people gradually observed that fluid flow driven by electrohydrodynamic (EHD) forces also played an important

role in governing the behavior of particles. In 1998, A Ramos et al summarized these AC electrokinetic forces in a publication that described the frequency and voltage dependence of both the DEP and EHD forces for a simple co-planar electrode system[84] (see Figure 1.28). It was shown that fluid flow could be driven by both electrothermal (ET) forces caused by Joule heating (from the electric field) and by AC electro-osmosis (EO) caused by the reaction of the induced charge at the electrode surface to the applied electric field. Later in 2003, A Castellanos et al presented a comprehensive discussion laying out a whole set of equations for these forces, providing a tool to predict the behavior of particles and fluids subjected to non-uniform AC electric fields [85].

Over the last 25 years the field of AC electrokinetics has grown exponentially and many interesting innovations have appeared. One area of interest is the Lab-on-a-Chip: technologies that offer new approaches for processing and analyzing cells and particles. Exploiting the effects of both the EHD and DEP is an area of growing interest. DEP is a short-range force, whereas EHD drives the fluid (and the suspended particles) over large distance. Combining the two provides new routes to processing and analyzing cells and other particles, particularly in the high conductivity media that cells require for growth [86]. In other areas, AC electrokinetics is also being used for the directed assembly and separation and alignment and trapping of protein molecules [87].

Recently, by leveraging the development of plasmonic nanostructures which are made of metal materials (gold for example) and show highly confined and enhanced electric field in the subwavelength scale when reaching resonance peak under laser illumination. Due to the good thermal and electric properties, a new way to reconsider EHD by a hybrid combination of optical effects with AC electrokinetics has attracted a lot of attention [33, 80].

In this section, we will briefly discuss the three main forces, i.e. DEP, EO, ET. The structure of each section is as following. Firstly, we will summarize the relevant equations and properties of the force. We will then take several examples showing the applications of this force in pure microelectrode-structure based systems and finally in hybrid optoelectronic-structure based systems. Comparisons between these forces will also be given in the passage.

1.4.1 Dielectrophoresis (DEP)

1.4.1.1 Formula and properties of DEP

The movement of polarizable particles in non-uniform electric fields is called dielectrophoresis (DEP) and was first demonstrated by H. Pohl in 1951 [83] in a paper describing the polarization of matter and its subsequent movement in divergent electric fields. The principle is as follows. When a particle is immersed in a dielectric medium, and an electric field is imposed on the system, a dipole is induced in the particle

whenever there is a mismatch between the dielectric properties of the particle and the medium [88]. If the field is uniform, the electric forces are balanced and thus the net force on the particle is zero. However, if the field is gradient, i.e., the field is non-uniform, there will be a force on the particle. For a particle whose dielectric permittivity is greater than the medium, a dipole will be induced that aligns with the field, and the particle will be attracted towards regions of higher field, i.e. a positive DEP. Whereas for a particle with dielectric permittivity less than the medium, it will be polarized in the opposite sense, and migrate down the field gradient, exhibiting negative DEP, as shown in 1.22.

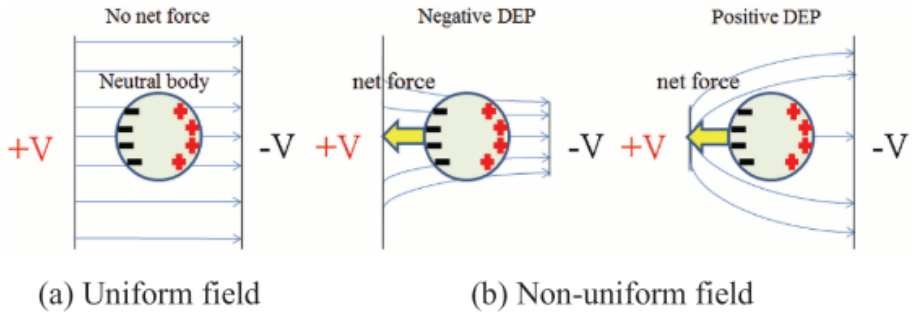

Figure 1.22: Effect of dielectrophoresis [19].

The basic equation on the effective of positive and negative DEP is described in Eq. 1.2

$$F_{DEP} = 2\pi\varepsilon_m R^3 \,\mathrm{Re}(K(\omega))\nabla E^2 \tag{1.2}$$

where R is the radius of the particle (normally regarded as a sphere), E is the external electric field strength which is related to the geometry of the electrodes polarizing the particle, ε_m is the permittivity of the medium, $\mathrm{Re}(K(\omega))$ is the real part of the very important Clausius-Mossotti factor $K(\omega)$ defined as

$$K(\omega) = \frac{\varepsilon_p^* - \varepsilon_m^*}{\varepsilon_p^* + 2\varepsilon_m^*} \tag{1.3}$$

where ε_m^* is the complex permittivity of the medium and ε_p^* is the complex permittivity of the particle. The complex permittivity here is defined by

$$\varepsilon^* = \varepsilon + \frac{\sigma}{j\omega} \tag{1.4}$$

and depends on the permittivity (ε) and conductivity (σ) of the particle or the medium and the angular frequency ω of the applied electric field. The permittivity (ε) can be a complex number when the dissipation of the material associated with the passage of current through is considered. j represents the imaginary unit. $\mathrm{Re}(K(\omega))$ can vary from -0.5 to 1.

Eq. 1.2 to 1.4 are concise but can give us a lot of intuition. DEP force is proportional to particle volume

and to the permittivity of the dielectric medium. DEP force is directed along the gradient of the electric field intensity, which in general is not parallel to the electric field vector.

Since the DEP force is sensitive only to the field intensity gradient rather than to the field direction, particles experience DEP only when the field is non-uniform and are unaffected by reversing the field. Thus the DEP will occur in the same way in an AC field as in a DC field, and AC has the advantage of eliminating the effect of any electrophoretic force due to the presence of an electric double layer. What's more, DEP force highly depends on the sign and magnitude of the Clausius-Mossoti factor $K(\omega)$, which is frequency dependent. Therefore, by judicious choice of suspending medium conductivity and applied frequency, even particles with very similar dielectric properties can be efficiently separated.

1.4.1.2 DEP in microelectrode structures

To generate DEP, an electric field gradient is required. The most common way is to use specific electrode geometries, for example a point together with a plane. This rule is still working even when going down to micro and nano-scales. Early work used large electrodes (cm to mm scale) and thus required high voltages to induce strong enough field gradient (then useful particle motion). For example, H. Pohl himself showed how to separate live and dead yeast cells in an electric field in 1966, in which the system applied a voltage of 30 to 200 volts [89].

A breakthrough occurred when it was realized that simple planar micro (rather than mm) electrodes with precise dimensions could generate much stronger gradients and field magnitudes with only moderate applied voltages since the electric field E is approximately expressed as U/d (where d is the distance between electrodes), as shown in Figure 1.23 [20].

Due to the mature fabrication techniques from semiconductor industry, new avenues of research were opened. With electrode structures become smaller and more precise, it becomes possible to study the behavior of smaller and smaller objects. Electrode arrays with dimensions in the micrometer size have been used to trap, separate and analyze nano-particles including DNA [90] and virus [91]. For example, H Morgan et al. firstly reported a separation of latex beads with diameters of only 94 nm in 1997 [92]. In their work, the electrode structure is similar to that in Figure 1.23 but the distance between electrodes is less than 10 μm. Typical micro-electrodes include metal electrodes which can be fabricated on metal films (particularly gold films, as shown in Figure 1.24(a)) by photolithography, and insulator electrodes by non-conductive materials such as glass and polymer, as shown in Figure 1.24(b)). With well-designed geometries (such as pillars), metal electrodes only need a few volts to polarize the particles compared with several hundred volts previously. However, under experimental conditions, metal electrodes can interact with the sample which leads to sample electrolysis, bubbling, and electrode arcing which reduces the lifetime of the device.

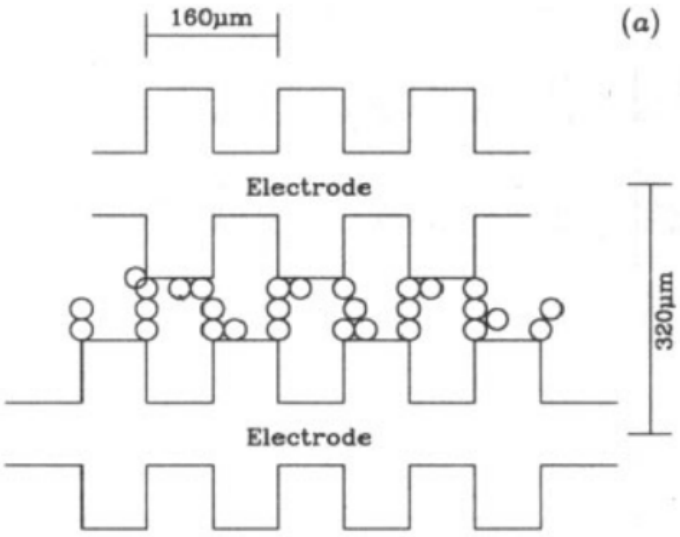

Figure 1.23: One example of precisely designed micro-electrodes, in which the voltage applied was 15 volts [20].

Insulator electrodes, on the other hand, can avoid the contact with samples and create desired electric field gradient by specific geometries or even by pores in polymer membranes to distorts the field. Unfortunately, A voltage as high as hundreds of volts, sometimes even a few thousands, is commonly required since the micro-scaled electrode are now separated by millimeters to a few centimeters.

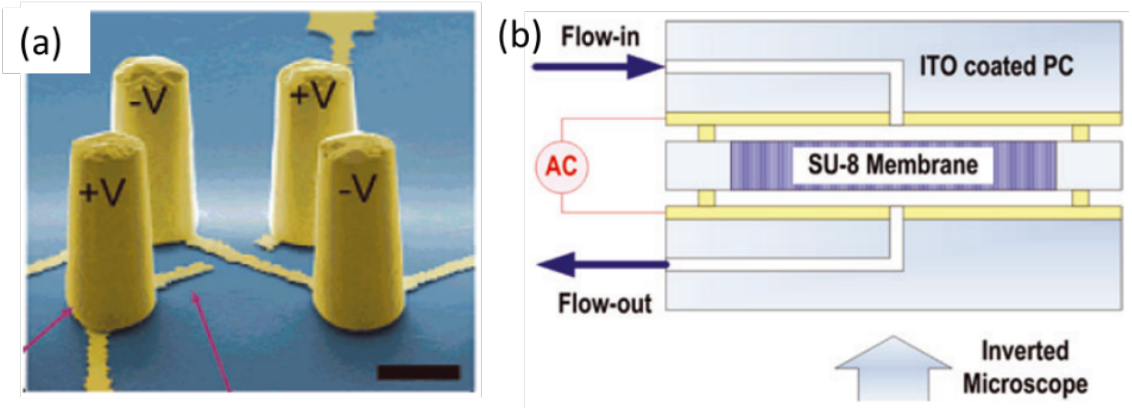

Figure 1.24: (a) A single quadrapole trap consisting of four electroplated gold electrodes [21]. (b) SU-8 membrane is positioned in between a couple of planar electrodes (ITO-coated polycarbonate). Upon polarization of the planar electrodes, bacteria cells are trapped in the electric field gradients formed at the edge of the pores in the membrane [22].

A more up-to date example demonstrated dielectrophoresis-based separation of intact cells from damaged cells based on 3D carbon-electrode arrays, which could be used for rapid label-free enrichment of intact persister cells from antibiotic-treated cultures while preserving the metastable persister phenotype [23], as shown in Figure 1.25. This work shows the importance of developing electrode techniques.

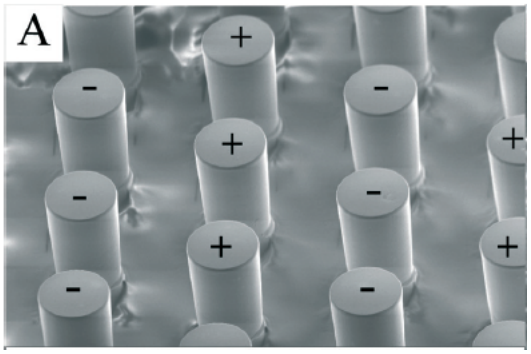

Figure 1.25: Glass-like 3D carbon-electrodes on a transparent fused silica substrate. The electrical configuration is indicated as '+' and '−'. Electrode dimensions are 50 μm diameter by 100 μm height [23].

The 3D carbon-electrode array used in this work combines some of the advantages of metal-based and insulator-based electrodes. For example, the possibility of sample electrolysis and bubbling is reduced with the use of carbon electrodes, an advantage shared with insulator-based electrodes, whereas low voltages are enough to polarize the carbon electrodes and create an electrical field suitable for DEP, an advantage shared with metal-electrode electrodes [93].

1.4.1.3 DEP in optoelectronic structures

In the field of optical manipulation, one direct way is using tightly focused laser beam, which is called optical tweezers and was invented by Ashkin et al in 1970 [94]. Particles are trapped at the focal spot by the optical gradient force which is created by the interaction between particles and the gradient optical field, and thus can be dynamically moved by moving the laser spot. The biggest limitation of optical tweezers is that to create a stable trap, optical tweezers require very high optical power intensities which limit their effectiveness in performing high-throughput and large-scale optical manipulation functions. One the other hand, DEP only need an AC field of several volts but the micro-electrode structures have to be made before hand and hence not amenable for dynamic translation of particles.

The technique, called optoelectronic tweezers (OET), combines the advantages of the two particle manipulation methods mentioned above. This technique uses light to excite a photoconductive layer and create an electric field gradient in the sample. In other words, it is not the optical field that is performing the manipulation directly; it is the electric field gradient created by the interaction of the optical field with the photoconductive material (usually using a-Si) that is trapping the objects. Therefore, OET is capable of manipulating objects with optical power intensities that are approximately 5 orders of magnitude smaller than optical tweezers [24]. In practice, an OET can work under an simple incoherent light source such as a light-emitting diode or a halogen lamp without any necessity for a laser beam.

A typical configuration of an OET is shown in Figure 1.26(a). The sample is contained in between a conductive layer and a photoconductive layer; the photoconductive layer is on top of another conductive layer. An AC field is applied between the two conductive layers. It is important to note that in principle these layers are featureless (which is different from a well-designed micro-electrode structure) and are deposited on a substrate transparent to the wavelength of the light used.

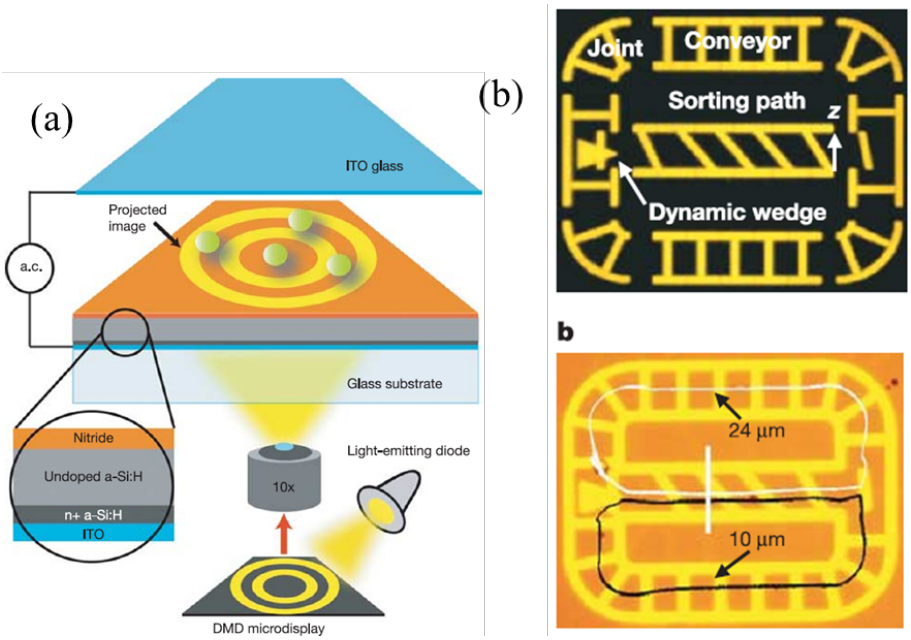

Figure 1.26: (a) Typical configuration of an OET. Indium tin oxide (ITO) is a good conductor and transparent at visible region. (b) Two polystyrene particles with sizes of 10 mm and 24 mm pass through the sorter path [24].

When a projected light illuminates the photoconductive layer, the impedance of the illuminated area has a lower impedance than the area in the absence of light. The photoconductive layer is commonly implemented using hydrogenated amorphous silicon, or a-Si:H. Since light is shined in patterns by a digital micromirror spatial light modulator, and not on the whole layer, the electric field in the sample becomes nonuniform. Hence virtual electrodes are turned on and gradients of electric field are formed. By dynamically controlling the patterns of the light, the particles can be transported along designed paths. What's more, by constructing an asymmetric optical pattern, particle separation can be achieved. As shown in Figure 1.26(b), two particles of different sizes can be moved in the upper and lower region respectively, shown as the white and black trajectory.

Even though the main operational principle of OET has been DEP, it has to be noted that the particle transporting and trapping can be a hybrid process which may contain DEP, electro-thermal flow, and light-actuated AC electro-osmosis. The different operational methods can be achieved in OET by tuning the

parameters such as optical power and frequency. Also, although cells with a size of 20 μm were reported to be able to move with speeds higher than 30 μm/s, the nano-scale particles that can be manipulated by DEP are usually several to tens of micrometers in diameter21 since DEP is proportional to the volume (R^3) of the particle.

1.4.2 Electro-osmotic flow (EOF)

1.4.2.1 Formula and properties of EOF

If an electric field is applied tangentially to a surface bathed in electrolyte, the charges in the double layer between the surface and the electrolyte experience a force. The consequence of this is that these double layer charges move, pulling the fluid along and generating a flow. This flow is zero immediately at the surface and rises to a maximum (and constant thereafter) at the slip plane. This flow is called electroosmosis. As shown in Figure 1.27(a), a DC field is linearly applied along x direction, then the slip velocity of the electro-osmotic flow at lower zeta potential (Debye–Huckel limit [95]) is given by:

$$u_s = -\frac{\varepsilon_w \zeta}{\eta} \mathbf{E}_{\|} \tag{1.5}$$

where ε_w is the dielectric permittivity of the solvent, ζ is the is the zeta potential, η is the fluid viscosity and $\mathbf{E}_{\|}$is the tangential component of the of the bulk electric field. For a freely suspended particle with fixed surface charge, the electro-osmotic slip velocity gives rise to motion of the particle itself (Figure 1.27(b)), also termed electrophoresis. In the thin-double-layer limit, the electrophoretic velocity is given by Smoluchowski's formula [26]:

$$u = \frac{\varepsilon_w \zeta}{\eta} \mathbf{E}_{ext} \tag{1.6}$$

where $\mathbf{E}_{\text{ext}}$ is the externally applied field. For an AC field and with this geometry, the fluid would move in anoscillatory manner with zero time-averaged displacement. For an AC field and with the geometry in Figure 1.27(a), the fluid would move in an oscillatory manner with zero time-averaged displacement [25].

When the AC field is non-uniform, however, a non-zero time-averaged flow can be created. This is similar as that a non-uniform field results in DEP but a uniform field does not. The typical configuration of the microelectrodes is shown in Figure 1.28(a). As in Fig 7(a), voltages $\pm$V are applied to either electrode, which give rise to the electric field E with tangential components E_t outside the double layer and induced charges with an opposite sign on each electrode. The induced charge experiences a force F_q due to the tangential field, resulting in fluid flow shown in Figure 1.28(b). It has to be noted that the direction of the force vector remains the same when reversing voltages on the electrodes, giving a non-zero time-averaged force and a steady-state fluid flow in the AC field.

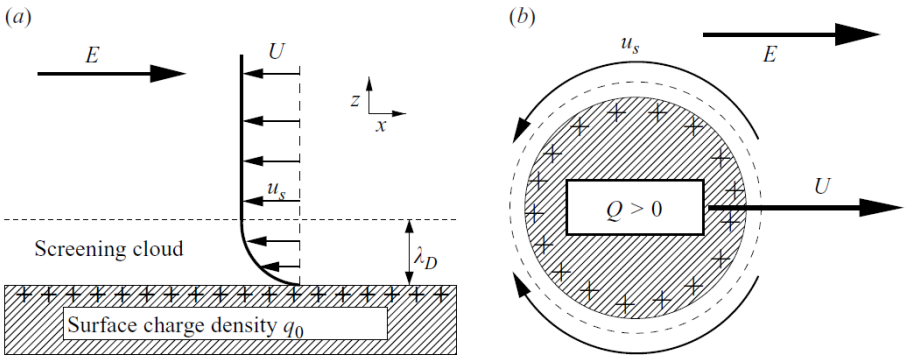

Figure 1.27: (a) Typical configuration of an electro-osmosis in a DC field. (b) Electrophoresis of a freely suspended particle with fixed surface charge.

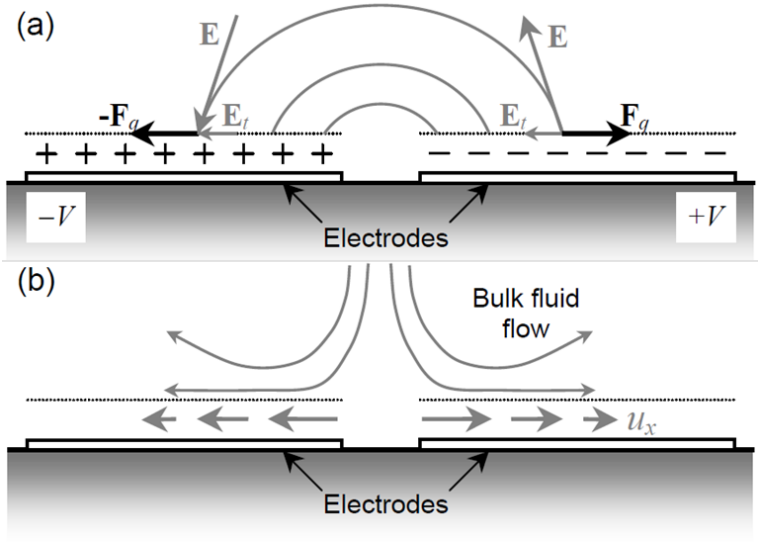

Figure 1.28: (a) Description of electric field distribution and forces on induced charges in AC electro-osmosis. (b) Description of bulk fluid flow lines in AC electro-osmosis [25].

AC electroosmotic fluid flow is governed by the charge induced by the electric field at the electrode/electrolyte interface. Since the amount of charge is frequency dependent, the magnitude of AC electroosmosis is also frequency dependent. As shown in Figure 1.29, the flow occurs mainly at low frequencies (of the order of Hz to tens of kHz, less than 100 kHz). In the low frequency limit, the magnitude of the AC electroosmotic flow tends to zero since there is no field in the bulk electrolyte and large fraction of the applied potential is dropped across the electric double layer. At high frequencies the AC electroosmotic flow again tends to zero, because there is insufficient time for the induced charge to form in the double layer. The time-averaged fluid velocity can be approximately expressed by a simple model as [25]

$$\langle u_x \rangle = \frac{1}{8} \frac{\varepsilon_w \phi_0^2 \Omega^2}{\eta x (1+\Omega^2)^2} \tag{1.7}$$

where Ω is the non-dimensional frequency $\Omega = (1/2)\pi\kappa x\,(\varepsilon_w/\sigma)\,\omega$.

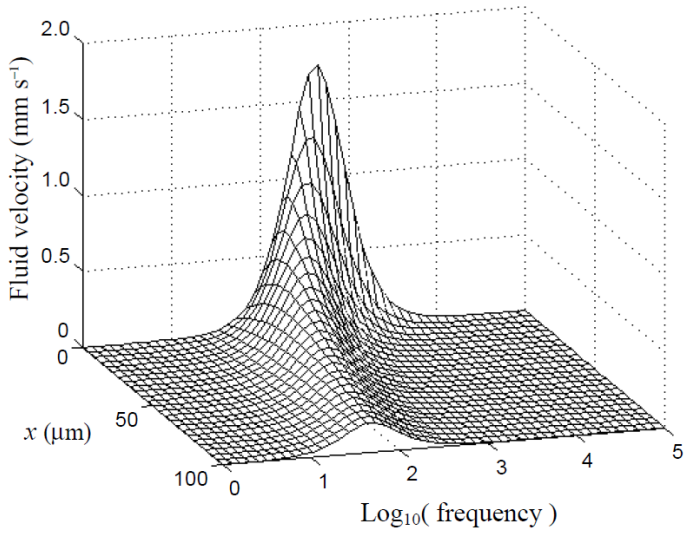

Figure 1.29: AC electro-osmotic fluid flow at the surface of an electrode calculated from Eq. 1.7 for the geometry configuration in Figure 1.28(a) [25].

Compared to the hundreds to thousands of volts often required in DC electro-osmosis, the AC electro-osmosis occurs at frequencies below the charge relaxation frequency of the electrolyte solution (less than 100 kHz as described above), and can drive fluids with voltages of 5 volts or less. In fact, frequencies can be used that are sufficiently high to avoid irreversible electrochemical reactions at the electrode interface, which minimizes electrolysis. This allows the electrodes to be positioned inside the microfluidic device, and therefore, high electric fields can be generated with relatively small voltages.

Another important non-linear scenario (named induced-charge electro-osmotic flow (ICEF)) appears when a sphere (as well as a cylinder) in the AC field (similar geometry configuration with Figure 1.27(b)) is now polarizable, which means the charge distribution on the surface is not fixed. The charge distribution after the relaxation time is shown in Figure 1.30(b). The applied DC electric field drives the positive ions in the electrolyte into a charge cloud on one side of the conductor and negative ions to the other. Then charges are induced on the cylinder surface which creates a dipole moment with the same direction of the applied electric field. A dipolar charge cloud grows as long as a normal field injects ions into the induced double layer, and a steady state is achieved when no field lines penetrate the double layer (shown as Figure 1.30(b)).

The tangential field drives an electro-osmotic slip velocity (Eq. 1.5 and 1.6) proportional to the local double-layer charge density, driving fluid from the 'poles' of the circular cross-section towards the 'equator' (Figure 1.31(a)). An AC field still drives an identical flow, since an oppositely directed field induces an oppositely charged screening cloud, giving the same net flow. For an isolated, uncharged polarizable cylinder of radius a submerged in an electrolyte solution with very small Debye length $\lambda_D \ll a$ (shown in Figure

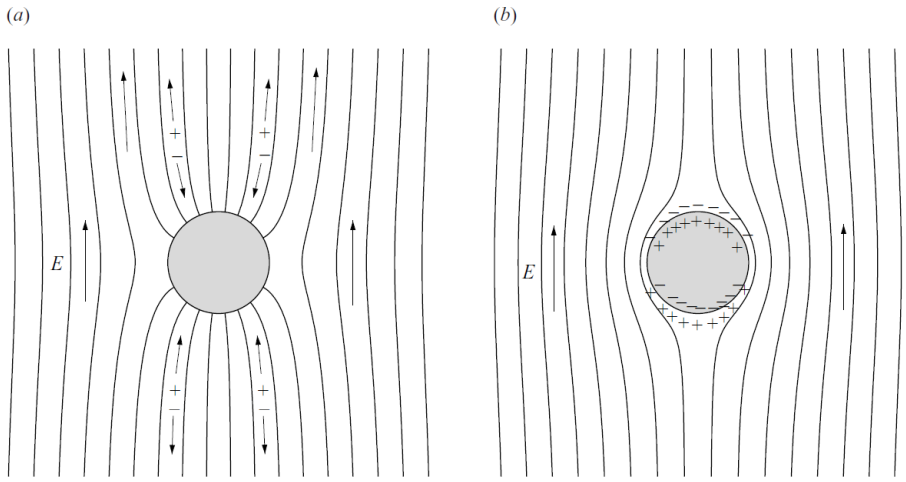

Figure 1.30: The evolution of the electric field lines around a solid, ideally polarizable cylinder immersed in a liquid electrolyte. (a) Electric field lines at $t = 0$ in which the lines intersect the surface. (b) A dipole cloud forms over a charging time [26].

1.31(a)), the tangential field drives the two sides of the charge cloud in opposite directions – each side away from the poles – resulting in a quadrupolar electro-osmotic slip velocity expressed by [26]

$$u_s = 2U_0 \sin 2\theta \hat{\theta} \tag{1.8}$$

where U_0 is the natural velocity scale described by

$$U_0 = \frac{\varepsilon_w E_0^2 a}{\eta} \tag{1.9}$$

The electro-osmotic flow around a polarizable cylinder with non-zero total charge, shown in Figure 1.31(b), simply superimposes on the non-linear flow described above the standard linear electro-osmotic flow discussed in Figure 1.27(b).

1.4.2.2 EOF in microelectrode structures

From Figure 1.28, we can find that EOF is a kind of body force which depends on the motion of the bulk fluid and has no relation with the size of the particles suspended in the solution. Therefore, it is a powerful tool for transporting small particles, even DNAs. And the induced particle surface velocity can exceed 100 μm/s [28]. However, to trap the particles after transporting, we also require other mechanisms such as DEP and electrophoresis. It has to be noted that when manipulating short, single strands of DNA, the DEP force is insufficient (due to the small volume) to hold the molecules down over the electrode and an electrophoretic force must be introduced.

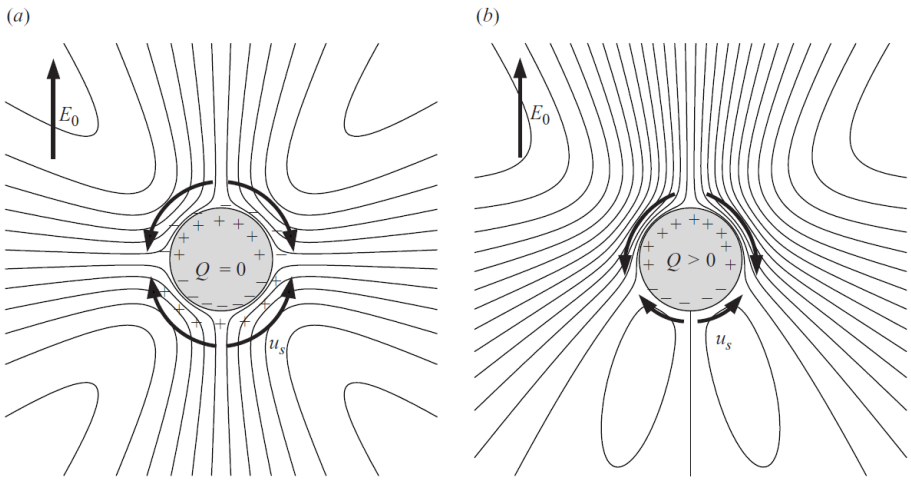

Figure 1.31: The steady-state ICEF around (a) a polarizable cylinder with zero net charge and (b) a positively charged polarizable cylinder [26].

As shown in Figure 1.33, a modified electrode configuration from Figure 1.28(a) is applied to trap DNA molecules. Similarly, since the sign of the electric field and the charge density change are in phase with each other, the fluid motion is always in the same direction under AC field. The bulk fluid flow (shown as light blue arrows) is driven by the movement of the double layer (shown as dark blue arrows near the surface) towards the center of the electrode. DNA molecules are then carried to the center of the electrode by the fluid where they are trapped by the vertical component of the DEP force (shown as red arrow arrows).

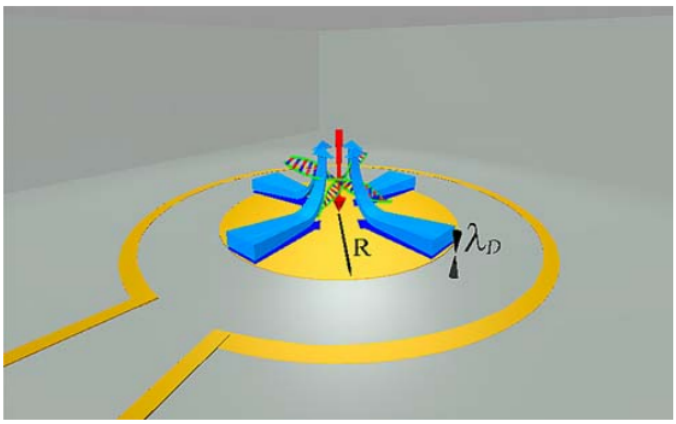

Figure 1.32: Electrokinetic DNA concentrator [27].

As shown in Figure 1.33(b), the inner disk and the outer ring are two electrodes. To give a general idea, the center electrode is 300 μm in diameter and the gap between the electrodes is 250 μm. The outer electrode is 25 μm wide and is open on one side to allow electrical connections to be made to the center electrode. A voltage of 4 volts and frequency $f = 1$kHz, with no DC offset, was applied for DNA concentration. The

DNA molecules used in the experiment are λ-phage DNA which contains a DNA molecule 15000 nm long inside a head 50 nm in diameter [96] and is labelled by fluorescent dye.

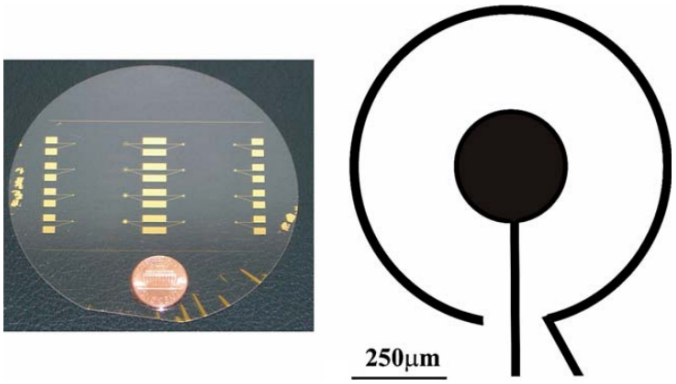

Figure 1.33: Picture of the wafer contains several DNA concentrators (a), and a schematic diagram of the electrode configuration (b) [27].

AC electro-osmotic flow is a surface flow that is highest at about 10 nm to 100 nm (i.e. the thickness of the electrode double layer) from the electrode surface. Hence, micron scaled particles are conveyed at the surface by the maximum fluid velocity in the microfludic channels. As a result, AC electro-osmotic flow is most effective at the surfaces of substrates, independent of particles or pattern dimensions down to nanometer, and capable of parallel processing over a large area [28]. One application for this property is the particle line assembly/patterning. As shown in Figure 1.34, with similar electrode configuration in Figure 1.28(a), two particle lines are generated on the electrodes where the light areas are the electrodes. From Fig 7(b), we know that the movement of the flow will particles toward the outer edge of each electrode. However, the particles are actually held at the edge. To explain this particle line assembly mechanism, researchers showed that another two minor vortices besides the two main vortexes (shown in Figure 1.28(b)) are generated to focus and hold particles into lines, as the simulated fluid velocity distribution described in Figure 1.34.

1.4.2.3 EOF in optoelectronic structures

Similar to DEP in optoelectronic structures, by introducing photoconductive electrodes and transparent substrates, dynamic particle manipulation can be achieved. This mechanism is called light-actuated AC electroosmosis (LACE). As shown in Figure 1.35(a), An aqueous medium containing nanoparticles and molecules of interest is sandwiched between a transparent ITO electrode and a photoconductive electrode coated with ITO and an undoped a-Si:H layer of which the photoconductivity increases by several orders of magnitude when illuminated by light. The equivalent circuit model in which the liquid and the undoped a-Si layer are regarded as resistors while the electrical double at the interface is regarded as a capacitor, is shown in Figure 1.35(b).

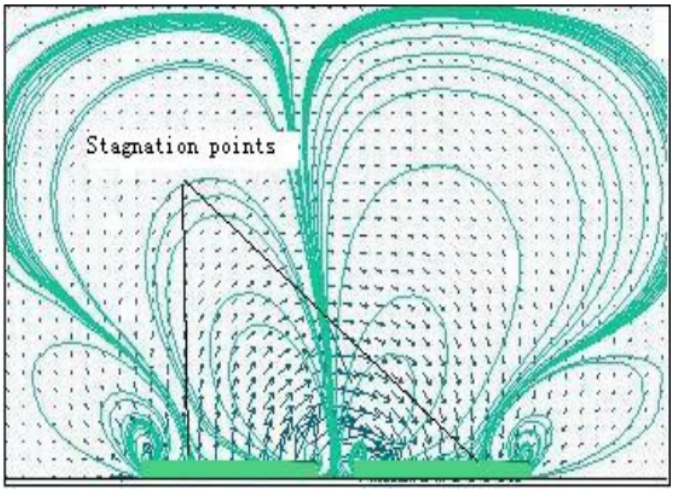

Figure 1.34: Simulation of the side view of the fluid velocity distribution inside the chamber [28].

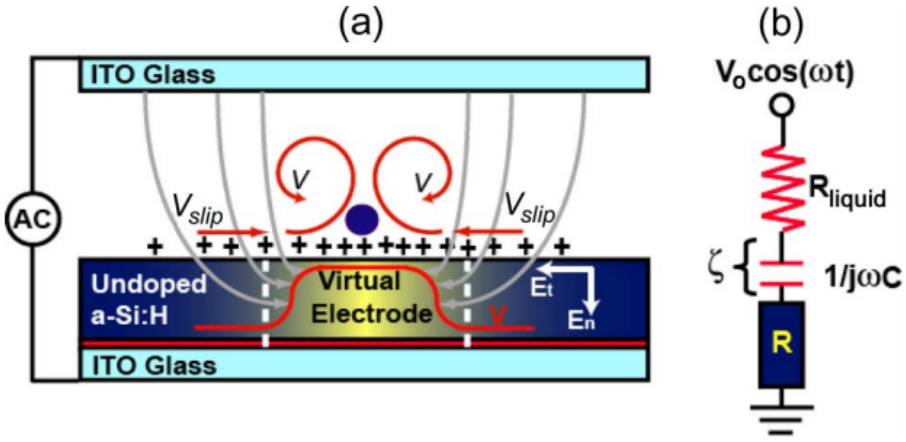

Figure 1.35: (a) The device structure and the working principle of the LACE. (b) The equivalent circuit model along an electric-field line [29].

For the left half cycle, the charged ions accumulated at the interface are driven toward the center of a virtual electrode by the tangential field on the surface, pumping the surrounding fluids to circulate around the virtual electrode. For the right half cycle, the polarities of the ions and also the direction of the tangential electric field are both inverse, resulting a fluid flow in the same direction as in the left half cycle. From the simulation of the liquid flow velocity shown in Figure 1.36, the highest flow velocity exists on the surface at the edge of a virtual electrode. Meanwhile, owing to the symmetrical flow pattern, there exists a stagnant flow zone near the middle surface of a virtual electrode. The nanoparticles than can be trapped there. By using light patterning to create virtual electrodes (i.e. light illuminated areas), electrode patterns can be changed quickly and efficiently and thus dynamic particle manipulation can be realized.

As shown in Figure 1.37(a) and (b), parallel trapping and transport of single 2 μm polystyrene beads are

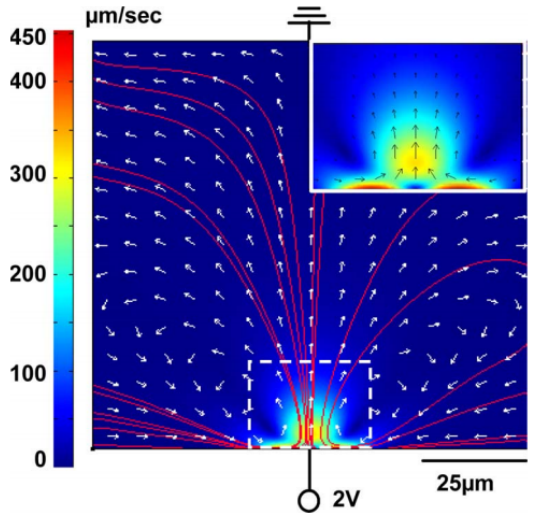

Figure 1.36: Velocity distribution of LACE flow near a virtual electrode [29].

demonstrated. Figure 1.37(c) shows the concentration of these polystyrene beads on a 20 μm diameter virtual electrode. These beads not only concentrate in the center of the virtual electrode but also form crystalline colloidal structures. This is because when particles are circulated to the surface of a virtual electrode, they perturb the electric double layer on the electrodes and create particle-induced AC electroosmotic flows around themselves, as shown in Figure 1.37(d). These particle-induced ac electroosmotic flows help these particles form compact crystalline structures. This mechanism is quite useful for self-assembly processes of micro- and nano-scale colloidal particles.

By benefiting from the combination of these electrokinetic forces generated in the platform shown in Figure 1.35(a), various arbitrary nanoparticles can be dynamically manipulated and patterned (shown in Figure 1.38). Surface enhanced Raman spectroscopy hot-spots can even be obtained by patterning gold nanoparticles of 90 nm diameter with enhancement factors exceeding 10^7. In this system, collection forces collect the particles from long-range (over 100 μm) distances and concentrate them in the light spot and immobilization forces strongly attract the particles and immobilize them on the electrode surface. The collection force benefits from DEP attracting particles over the short range and LACE and electrothermal flow-based (ET flow, which will be discussed later) collection of the particles over the longer range. The immobilization force on the other hand is mainly dominated by the DEP force but can also be affected by electrophoretic forces due to the particles surface charges [30].

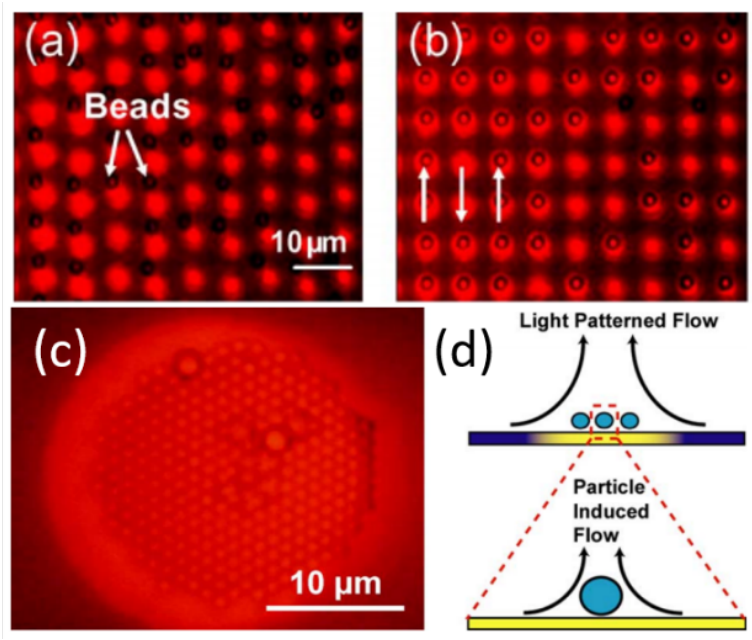

Figure 1.37: (a)-(b) Parallel trapping and transport of single 2µm polystyrene beads. (c)-(d) 2µm polystyrene beads form crystalline colloidal structures in the center of a virtual electrode [29].

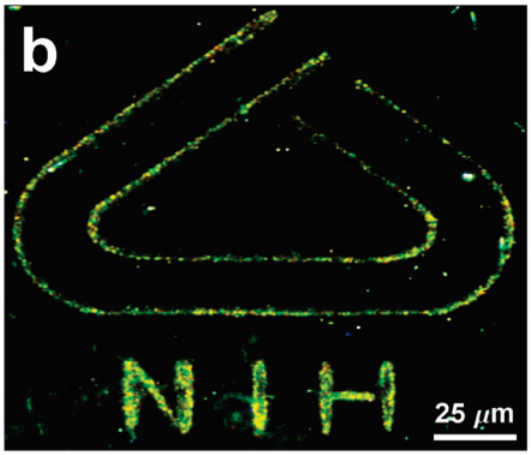

Figure 1.38: "NIH" logo patterning of nanoparticles [30] over $160 \times 140 \mu m^2$.

1.4.3 Electrothermal flow (ETF)

1.4.3.1 Formula and properties of ETF

In general, the application of electric fields to a fluid produces body forces and therefore fluid flow. We have discussed the electro-osmosis flow which is significant under lower frequencies (less than 100 kHz). With the increase of frequencies, the Joule heat due to current in the electrolyte become non-negligible and a new kind of body force needs to be considered. Besides the EOF induced by the motion of ions in the electric double layer at the electrode/electrolyte interface, a system with non-uniform permittivity and conductivity

can also induce another kind of body force. In such a system, a local free charge distribution must be present if Gauss's Law and charge conservation are to be satisfied simultaneously. The local charges, both free and bound, responds to the applied electric field, resulting in a non-zero body force on the fluid, i.e. the electrothermal effect.

The electric body force is given by [84]

$$f_e = \rho E - \frac{1}{2}|E|^2 \nabla \varepsilon + \frac{1}{2}\nabla\left(\rho_m \left(\frac{\partial \varepsilon}{\partial \rho_m}\right)|E|^2\right) \tag{1.10}$$

where ρ and ρ_m are the charge and mass densities respectively. On the right-hand side of this expression, the first term is the Coulomb force, the second is the dielectric force and the last term is the electrostriction pressure. For an incompressible fluid, the electrostriction pressure can be ignored since it is caused by displacement of ions in the crystal lattice upon being exposed to an external electric field [97] and has no effect on the dynamics of the system. For water, the relative changes in permittivity and conductivity are small which means that the changes in the charge density and the electric field are small and a perturbative expansion of the electric field can be performed. After the perturbative expansion and rewriting the equation in terms of the temperature gradient, the final expression of the electrothermal body force can be described as [84]

$$\langle f_e \rangle = \frac{1}{2}\mathrm{Re}\left[\frac{\sigma\varepsilon(\alpha-\beta)}{\sigma + i\omega\varepsilon}(\nabla T \cdot E_0)E_0^* - \frac{1}{2}\varepsilon\alpha|E_0|^2\nabla T\right] \tag{1.11}$$

where $\alpha = (1/\varepsilon)(\partial\varepsilon/\partial T)$ and $\beta = (1/\sigma)(\partial\sigma/\partial T)$. This electric body force is comprised of two parts: the first term is the Coulombic force and the second term is the dielectric force. At low frequencies the Coulomb force dominates, and at high frequencies, the dielectric force dominates. Typically, these two forces act in different directions and over a certain range of frequencies they compete, resulting in a changing flow pattern [84].

Let's consider the same electrodes configuration with Figure 1.28(a). In this system, if no external heat source is introduced, the temperature gradient is generated by the Joule heating and can be calculated from the electric field distribution in the electrolyte. In other words, the applied electric field heats the electrolyte of conductivity σ, giving the time-averaged power density dissipated in the system. Then the ETF body force is expressed by [98]

$$\langle f_e \rangle = \frac{2}{\pi^3 k}\frac{\varepsilon\sigma V_0^4}{r^3}\Pi\left(1 - \frac{2\theta}{\pi}\right)\hat{\theta} \tag{1.12}$$

where Π is a frequency dependent term expressed as [98]

$$\Pi = \left[\frac{\alpha-\beta}{1+(\omega\tau_p)^2} - \frac{\alpha}{2}\right] \tag{1.13}$$

and here τ_p is the charge relaxation time ε/σ.

On the other hand, if the heat is external to the system and for example a heated substrate, a temperature gradient will be established, as shown in Figure 1.39. Here the heat radiates upwards into the electrolyte to produce gradients in temperature, conductivity and permittivity as shown in the figure. In this case, the ETF body force is expressed by

$$\langle f_e \rangle = \frac{2}{\pi^2}\frac{\varepsilon V_0^2}{r^2}\left(\frac{1}{\sigma}\frac{d\sigma}{dT}\right)|\nabla T|\cos\theta\,\hat{\theta} \tag{1.14}$$

where the temperature gradient ∇T directly comes from the heat diffusion from the substrate.

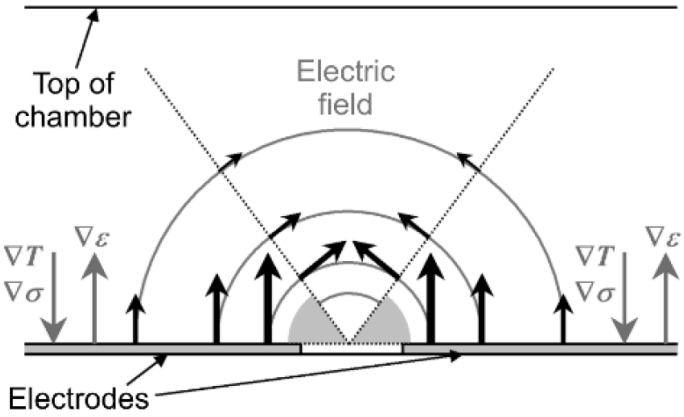

Figure 1.39: Schematic diagram of the temperature gradient generated by a heated substrate beneath the electrodes and the resulting gradients in conductivity and permittivity [25].

By substituting the electric body force into Navier-Stokes equation [25]

$$\rho_m\frac{\partial u}{\partial t} + \rho_m(u\cdot\nabla u) = -\nabla p + \eta\nabla^2 u + f_e \tag{1.15}$$

the ETF distribution can be solved. The two different ETF velocity field distributions are shown in Figure 1.40. Two things have to be noted. First, the directions of the fluid flow are inverse and second, the magnitude of the flow from Joule heating (Figure 1.40(b)) is approximately 40 times smaller, showing that even a moderate external temperature gradient can produce significant fluid flow. The differences appeared here will be very helpful when introducing external heat sources by well-designed micro-electrode structures.

1.4.3.2 ETF in microelectrode structures

As we have discussed, the AC electro-osmosis flow is typically limited to fluids with low ionic strength, for example de-ionized water since high conductivity will compress the thickness of the double layer, rendering electro-osmosis ineffective. For the same applied voltage, more conductive fluids have a lower peak velocity. It has been reported that the AC electro-osmosis flow is not observable for fluids with conductivity above

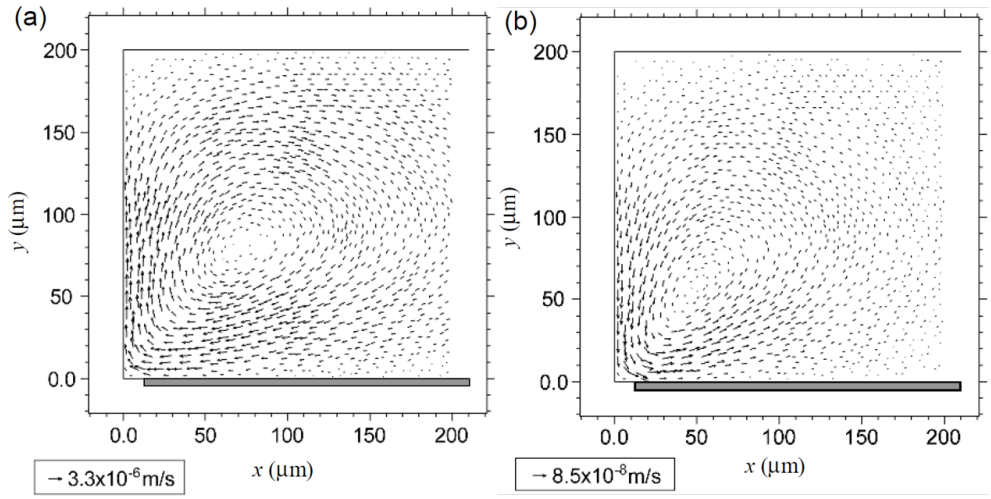

Figure 1.40: Numerical simulations of the ETF for one half of the two-electrodes system and two different heat sources: (a) a heated substrate and (b) Joule heating. Both solutions are for low frequencies2 [25].

140 mS/m [99]. However, labs-on-a-chip devices frequently involve samples with conductivity higher than 0.1 S/m and even higher for biological application (1 – 2 S/m). On the other hand, the AC electrothermal effect can utilize a higher electrolyte conductivity to generate more Joule heat, thus has shown promise in this aspect.

In this section, we will briefly introduce two works which either has a different electrode configuration or introduces a different external heat source. As shown in Figure 1.41, the electrodes in this system consist of a pair of parallel plate electrodes at a spacing of 500 μm, which is different from the side-by-side electrode configuration shown in Figure 1.28(a) which limits their application to low ionic strength solutions and the trapping range into the fluid in the order of the system characteristic length [31]. It has to be noted that the bottom electrode is shorter than the top one in order to create a non-uniform electric field, which in turn induces non-uniform temperature field and then the ETF field.

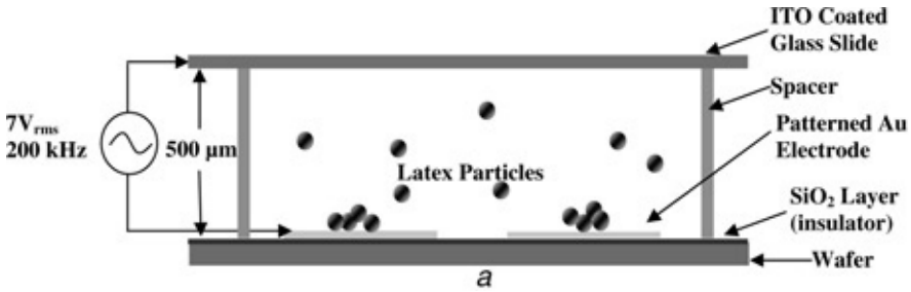

Figure 1.41: Schematic of the parallel-plate particle trap chamber [31].

The numerically simulated flow velocity field is shown in Figure 1.42, where the arrow length scales with the fluid velocity. Two counterrotating vortices are produced above the bottom electrodes. The flow direction

is upwards in the middle and downwards at the sides. Global velocity maxima are seen at the edge of bottom electrode, where the electrical field strength is also at the highest. Flow velocity decreases along the electrode inwards until it becomes zero at the middle. It's clear that the fluid motions in the middle of bottom electrode are cancelled out by flows in opposite directions and consequently producing stagnation. It is expected that micro/nano particles are deposited (i.e. trapped) in that area. It's different from the particle trapping by DEP which greatly depends on the size of the particle as previously discussed. Moreover, DEP decreases much faster than ETF/EOF with respect to the distance from the electrode (approximately $1/r^3$ for DEP and $1/r$ for ETF).

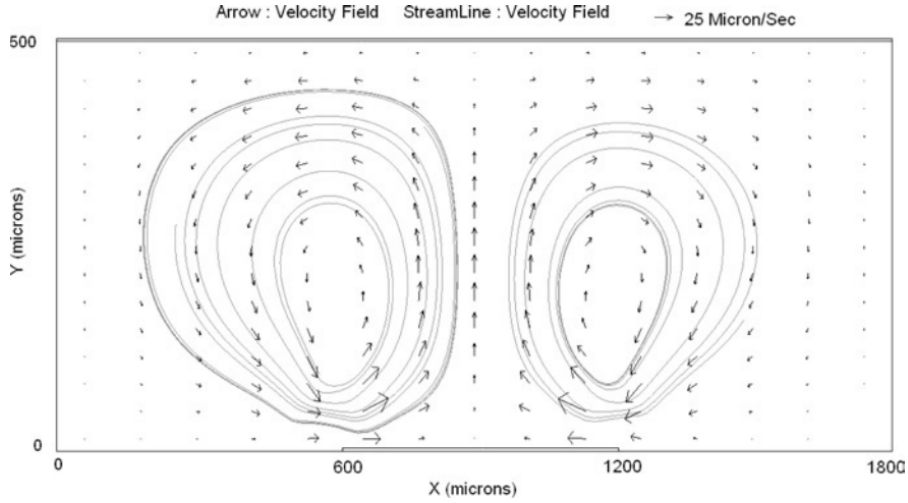

Figure 1.42: Simulated flow field profile in the parallel-plate particle trap chamber [31].

As shown in Figure 1.43, the other work we are going to discuss reported a four-coplanar-electrodes design subjected to a four-phase AC signal, generating a rotating field. In their experiment, electrothermal liquid flows are generated by alternating and rotating electric fields under strong illumination coming from the fluorescence microscope which is enough to heat the electrodes. A clear indication of this was the observation of natural convection (driven by buoyance) for a chamber with a height of 1 mm. In this chamber, the fluid was observed to move when the spot of incoming light was on the bottom electrodes with no applied electric field. At the level of the electrodes, the fluid flowed towards the light spot as expected by natural convection. However, when the spot of light was on the top glass, no observable fluid flow occurred. The conclusion is, therefore, that the light is heating the electrodes much more than the glass or the aqueous solution.

Then for chambers with smaller heights, gravity can't overcome the viscous friction and no observable natural convection could be detected without electric fields. However, with the application of electric fields under illumination, fluid flow was observed in chambers with heights even smaller than 200 μm when the buoyancy force was less important as the typical system length decreased [32]. This result confirms that

the flow is mainly driven by ETF rather than a natural convection due to non-uniform mass densities. The rotating flow on top of the four coplanar electrodes is shown in As shown in Figure 1.43.

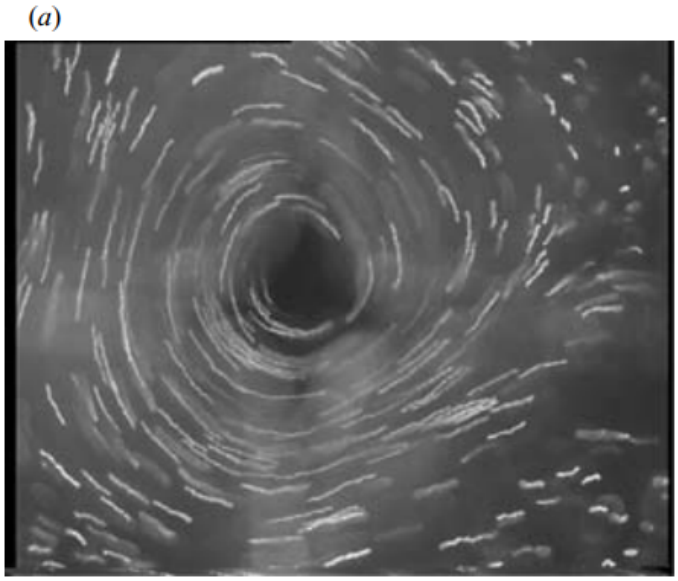

Figure 1.43: Rotating flow on top of the four coplanar electrodes by superimposing successive video frames [32].

1.4.3.3 ETF in optoelectronic structures

Plasmonic nanoantennas which are made by metal materials (typically gold) can create highly localized and intensified electromagnetic fields under the illumination of laser at resonance frequency. The highly confined field can provide hot spots at the subwavelength scale, overcoming the diffraction limit in traditional optical tweezers. Therefore, plasmonic nanoantennas are great candidates for particle trapping through a high optical gradient force (similar to DEP) generated by localized hot spots. However, the optical gradient force is a short-range force due to the rapidly decrease of the electromagnetic field. Hence, although the plasmonic nanoantennas can stably trap particles with subwavelength sizes (which can be as small as tens of nanometers), the process to wait for the target particle moving to the vicinity of the nanoantenna is time consuming. This process is usually based on Brownian motion. On the other hand, due to the high energy dissipation of gold (great imaginary part of the complex dielectric permittivity) and the low thermal conductivity of the glass substrate where the plasmonic nanoantennas are deposited on, the local temperature can also be very high under laser illumination, particularly the wavelength of the laser is close to the resonance position of the nanoantenna. It has to be noted that this heating can also produce strong fluid convection and thermophoresis to manipulate particles which we will not discuss here.

Recently, a novel optofluidic mechanism was proposed which generates fluidic transport and particle

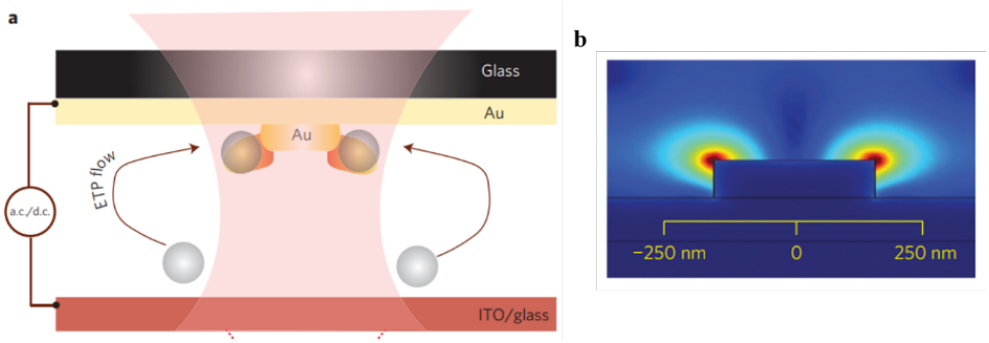

Figure 1.44: (a) Schematic of an ETP nanotweezer system. The illuminated plasmonic nanoantenna locally heats the fluid medium and induces local gradients in the fluid electrical permittivity and conductivity. With an applied AC electric field, an ETP flow is induced. (b) Side view: Electromagnetic field enhancement in the vicinity of the plasmonic nanoantenna. The system features two plasmonic hotspots [33].

delivery by combining the photo-induced heating of plasmonic nanoantennas with an AC electric field bias inside a suspension of particles [33, 98]. In this system, the target particles are transported towards the center of the nanoantenna array by ETF where the external heat source is provided by these gold nanoantennas under plasmonic resonances. Then particles can be stably trapped at the localized hot spots. By temporarily switching the AC field to a DC. field, the particles held in the plasmonic hotspots are immobilized. The researchers thus name it as an electrothermalplasmonic (ETP) flow. A typical configuration of such a system is shown in Figure 1.44(a) in which each nanoantenna is a gold nanopillar. The electric field distribution on the lateral cross-section is shown in Figure 1.44(b), clearly showing two hot spots aligned with the direction of the polarization of the incident beam. It has to be noted that the researchers compared the flow radial velocity with and without the applied electric field while keeping laser illumination and found that the velocities were 11.8 μm⁄s and 75 nm⁄s. This indicates that the thermal convection flow due to buoyance is much weaker than the ETP flow and thus can be ignored.

The ETF microfluidic device above can also be applied for facilitating biosensing applications35, as shown in Figure 1.45(a). The difference part here is that instead of using gold nanopillars with a circular cross-section, the authors used gold nanorods which have different resonance responses to incident polarizations along the long and short axis respectively (see Figure 1.45(b)). By leveraging on this property and properly designing the geometry parameters (i.e., length and width of the nanorod and the pitch), a transversal extinction peak is excited at 785 nm that can be used to induce heating whereas a longitudinal peak at 850 nm, used for sensing, as shown in Figure 1.45(c). In the experiment, local temperature gradients are created by shining a weakly focused 785 nm laser beam on the gold nanorod array (linearly polarized along the transverse resonance). While along the same optical path, a white light source linearly and cross-polarized to the heating beam excites the longitudinal resonance of the nanorods at 850 nm. When target particles are trapped

at the localized hotspots, the resonance peak will present a red shift due to the refractive index change in the vicinity which then can be regarded as the sensing signal.

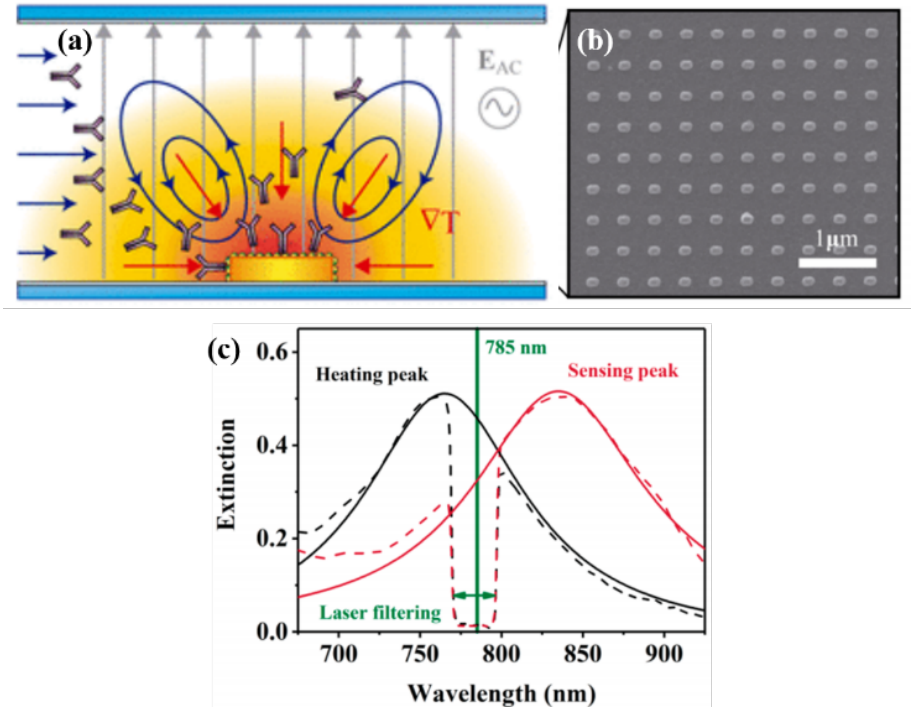

Figure 1.45: (a) Schematic of ETP flow facilitating biosensing. (b) SEM image of gold nanorod array. (c) Extinction spectra for each of the linear polarization, longitudinal and transversal with respect to the axes of the nanorods [34].

1.4.4 Summary

In this section, we briefly discuss the three main forces that may appear in an AC electrokinetic process in a microfluidic channel with an applied AC electric field. From the aspect of particle transport and capture, DEP is usually short-range and highly dependent on the size but can be a good candidate for particle separation due to the frequency-dependent Clausius-Mossoti factor. EOF and ETF, on the other hand, are both electric body forces which means they are independent on particle size (thus usually no separation ability) and the flow velocity can reach tens to hundreds of micrometers per second. EOF requires a lower frequency and lower solution conductivity since it relies on the ions motion in the electric double layer at the electrode/electrolyte interface. Nevertheless ETF dominates under a higher frequency and the solution conductivity be high which is a normal case particularly for biological samples. In a microfluidic system with an applied AC electric field, all of these forces can appear and play a part in the particle manipulation process. Recently, plasmon-enhanced particle manipulation has attracted a lot of attention. By leveraging on the great thermal and electric properties and specific resonance responses to laser illumination of plasmonic nanostructures, many forces

in colloid systems have been redemonstrated, paving ways for the development of new particle manipulation techniques, i.e. the hybrid optoelectroplasmonic nanotweezers.

In this dissertation, mechanisms discussed in this section are widely utilized through Chapter 3 and Chapter 4 where phenomena in microfludic channels are discussed. The synergistic effects of optofluidics and high-Q all-dielectric nanostructures greatly enrich the freedom of particle manipulation and hold enormous potential in applications including self-assembly of nanoparticles, high-sensitivity biosensing, drug delivery etc.

1.5 Thermal emitters

Thermal emitters generally exhibit a broadband spectrum determined by Planck's law. However, there is a strong motivation to realize narrowband thermal emission with high emissivity at a target wavelength range while suppressing it as much as possible at all other wavelengths [100]. We emphasize that the "narrow" means a peak with a Q factor of at least $\sim$ 10. In other words, we want to design a narrowband perfect absorber, not a "black" super absorber [101] with subwavelength thickness. Let's take some examples.

The first example is nondispersive infrared (NDIR) sensing. Basically, it leverages that the absorption spectra of most gases and liquids based on their molecular vibrations are located in this range. And their absorption linewidths typically correspond to a Q factor of more than 50 [100]. The majority of traditional NDIR sensors use a broadband lamp source and an optical filter to select a narrow band spectral region that overlaps with the absorption region of the gas of interest, together with an infrared detector to measure the power change. In this context, the "narrow" may be 50 - 300 nm bandwidth.

The second example is thermophotovoltaic (TPV) power generation. A spectrally selective emitter should have high emittance for energies above the photovoltaic bandgap (E_g) and low emittance for energies below the bandgap. To excite enough thermal modes for substantial emission above the bandgap, the emitter temperature should ideally be high enough that Planck's blackbody peak coincides with the bandgap. In other words, $T_{\mathrm{e}}^{\mathrm{opt}} \approx 2336 \left[\mathrm{KeV}^{-1} \right]$. For example, Figure 1.46 shows a classical work [102]. The absorber is made of an array of multiwalled carbon nanotubes, spaced by a silicon layer to spread the heat. The underneath emitter is made of five layers of Si/SiO_2 to form a 1D photonic crystal. As shown in Figure 1.46(c), the measured spectral emittance of the emitter at 1,285 K overlaps well with the internal quantum efficiency (IQE) of the InGaAsSb photovoltaic cell (E_g = 0.55 eV) at 1 – 2 μm. The experimental efficiency reaches 3.2%. For this area, i.e., thermophotovoltaic power generation, most works reported an actual system efficiency (ratio of output power to ingoing heat flux) less than 10% [102–104]. Given that a reasonably optimized theoretical TPV design yields system efficiencies of 40%, it is not clear if the complexity of the TPV arrangement provides a sufficient benefit over conventional multi-junction PV, which can achieve similar or greater effi-

ciencies. Therefore, Baranov et al [101]. suggested that applications of TPVs in which the heat source is not the Sun may be more promising, since existing technologies to convert, for example, waste heat, are far less efficient than state-of-the-art PVs for solar-energy conversion.

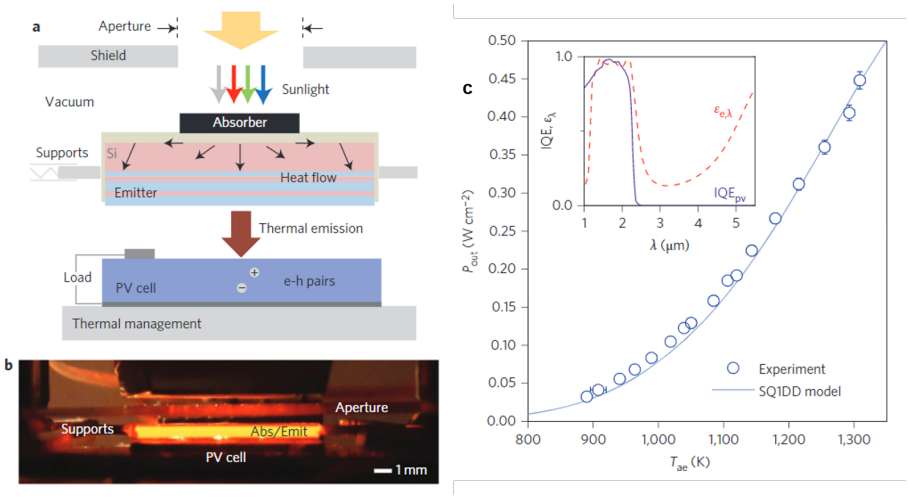

Figure 1.46: Ref. A nanophotonic solar thermophotovoltaic device.

Let's consider these concepts. The emissivity is defined as the ratio of spectral radiance of thermal emission from an object to that of a black body:

$$\varepsilon^l(\nu,\theta,\phi,T) = \frac{L^l(\nu,\theta,\phi,T)}{L_{\mathrm{BB}}(\nu,T)} \tag{1.16}$$

Therefore, the emissivity of any thermal emitter cannot exceed the black body radiation. For a black body, $\varepsilon^l(\nu,\theta,\phi,T) = A^l(\nu,\theta,\phi,T) = 1$ where A^l is the absorptivity. For emission from an arbitrary object, the emitted power is expressed as $L(\nu,T) = \varepsilon_\nu L_{BB}(\nu,T)$, where ε_ν is the wavelength-dependent emissivity and equivalent to absorption. $L_{BB}(\nu,T)$ describes the thermal emission from blackbodies. Figure 1.47 depicts such a concept to control thermal emission.

The principle of thermal emission control is based on Kirchhoff's law of thermal radiation, which states that the emissivity of an object equals its absorptivity for a given frequency, direction, and polarization. Therefore, by creating an optical resonance and maximizing the absorptivity at a specific frequency while minimizing it at all other wavelengths, a well-performing thermal emitter can be achieved. Based on this concept, various types of wave-length-scale optical nanostructures have been utilized for thermal emission control.

Metallic nanostructures have been extensively studied in this regard where optical resonances confined in the microcavities or surface plasmon polaritons excited on the metal surface enhance the absorptivity. Two typical works [105, 106] are shown in Figure 1.48. They both aim for potential applications in thermopho-

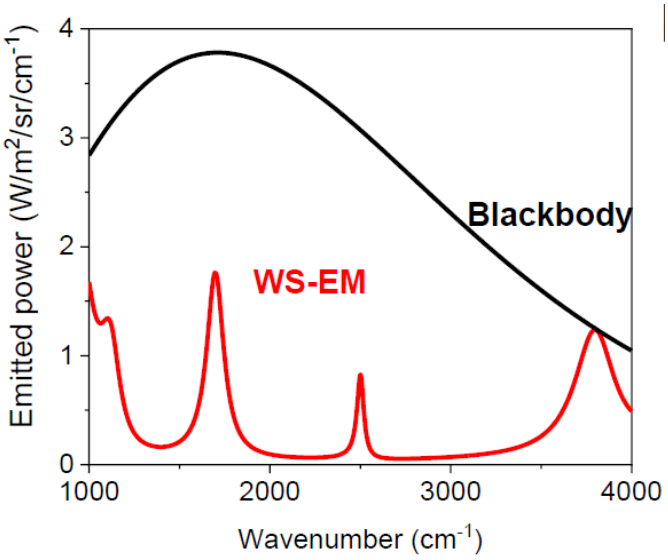

Figure 1.47: WS-EM represents wavelength-selective thermal emitter.

tovoltaic generation. Therefore, the chosen metals are tungsten and tantalum which are stable at the targeted high operating temperatures (> 1000 K) and long operational time span due to their high melting points (> 3000 K) and low vapor pressure.

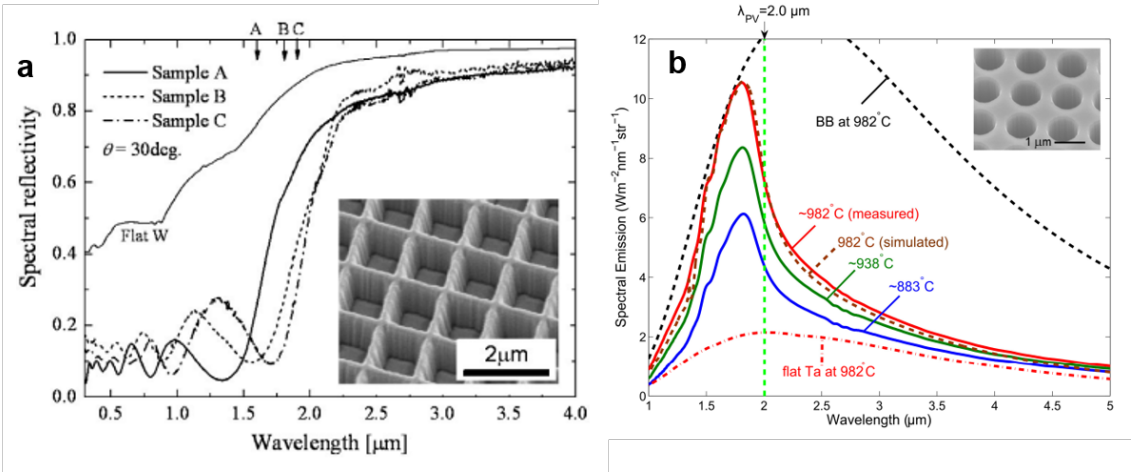

Figure 1.48: (a) Ref. High-temperature stability and selective thermal emission of polycrystalline tantalum photonic crystals. (b) Ref. Thermophotovoltaic generation with selective radiators based on tungsten surface gratings.

As a different approach, subwavelength metallic elements combined with thin dielectric layers (i.e., MIM structures) have realized narrowband thermal emission. Perfect absorption (i.e., maximum emission) at the resonant wavelength was demonstrated as well. Below are two typical works. The one [107] in Figure 1.49(a) is from Willie Padilla's group, who first proposed a series of works related to thermal emitters based

on metamaterial perfect absorbers [107–109]. Both works demonstrated a dual-band design (the standard specifications of dual-band detectors for CO_2 sensors in the market), i.e., one of the two peaks is used as a reference signal to cancel the sensitivity drift of the system. Both were based on the MIM structure with the metal as gold and the Q factors were ~ 10.

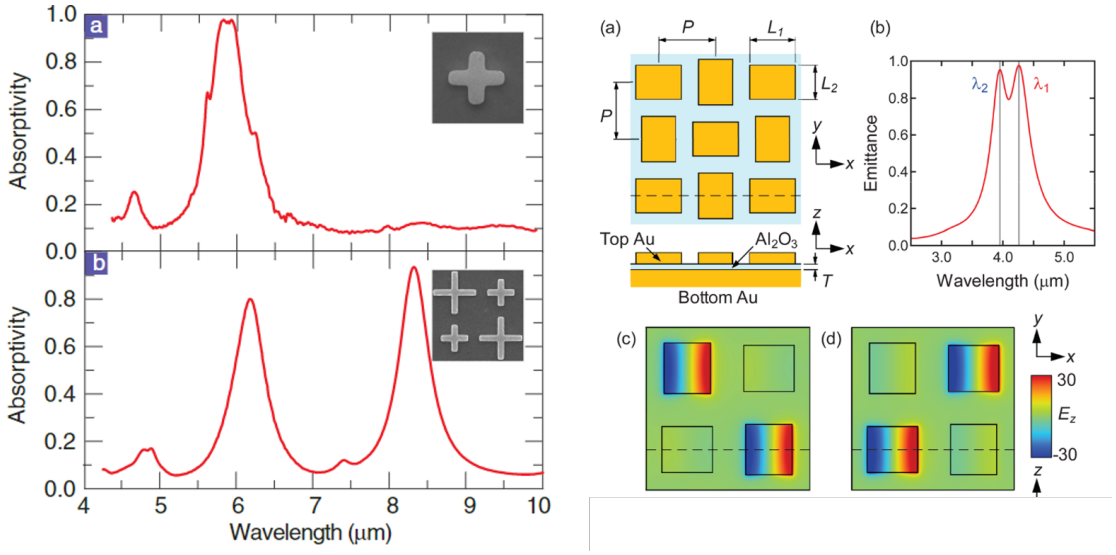

Figure 1.49: (a) Ref. Taming the blackbody with infrared metamaterials as selective thermal emitters. (b) Ref. Dual-band infrared metasurface thermal emitter for CO_2 [35].

It should be noted, although the aforementioned two types of metal-based thermal emitters have shown reasonable stability at high temperatures and trivial shifts of resonances, their strong free carrier absorption results in undesired emissions over a wide wavelength range, and the emission peaks are broadened ($Q < 10$). For our plasmonic quasi-BIC design, although we also adopt the MIM design, we achieved a much higher Q ($\sim$ 60 - 120) while maintaining a high absorptance by leveraging the BIC mode. It's noted that, to design such a perfect absorber system containing the intrinsic and radiation losses, a phase diagram method (under-damping/overdamping) was proposed by Qu et al [110], and used by Ref. [111] Mirror-coupled plasmonic bound states in the continuum for tunable perfect absorption (although the authors did not cite the former paper).

On the other hand, all-dielectric thermal emitters are promising for obtaining a narrower thermal emission peak due to their lower loss. One example is the use of surface-phonon polariton resonances in polar materials. Several examples are shown in Figure 1.50 [112–115]. Figure 1.50(a) and 1.50(c) are 1D grating structures while 1.50(b) and 1.50(d) are 2D metasurface designs (based on Kerker effect) from Joshua Caldwell's and Jason Valentine's group. Figure 1.50(a), 1.50(b) and 1.50(d) are SiC which has high-energy phonon resonances in the 10.6 – 13 μm wavelength range while Figure 1.50(c) is GaP exhibits strong phonon resonances Reststrahlen band (25–30 μm). Therefore, the emission wavelength cannot be tuned over a wide

range because such resonances require strong lattice absorption, which is limited by the property of the material. For our plasmonic quasi-BIC design, since our resonators are made of gold, the resonance position can be freely tuned within mid-IR range.

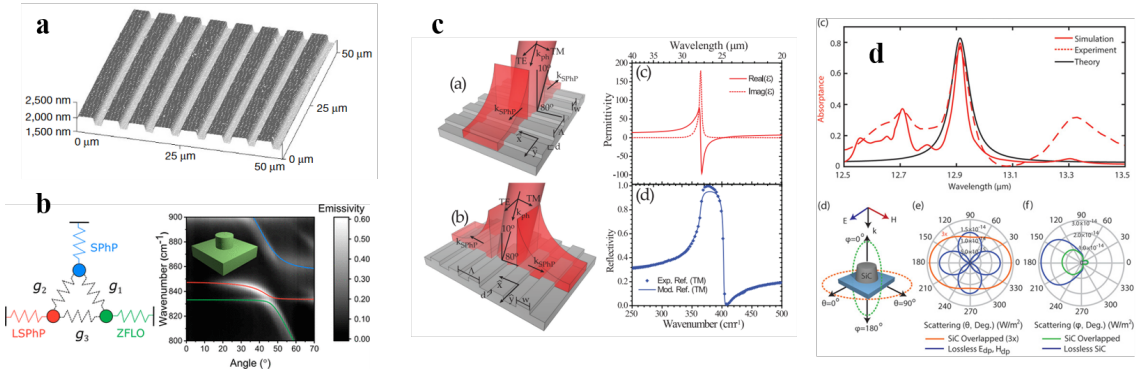

Figure 1.50: (a) Ref. Coherent emission of light by thermal sources. (b) Ref. Engineering the spectral and spatial dispersion of thermal emission via polariton–phonon strong coupling. (c) Ref. Engineering absorption and blackbody radiation in the far-infrared with surface phonon polaritons on gallium phosphide (d) Ref. Near-Unity and narrowband thermal emissivity in balanced dielectric metasurfaces.

To achieve full control of a thermal emission spectrum in an arbitrary frequency range, it is necessary to use more tunable absorbing materials and combine them with elaborated optical resonant structures. One approach is to use the intersubband transitions (ISB-Ts) in doped multiple quantum wells (MQWs). By modifying the structure and materials of the quantum wells, not only the magnitude of absorption (by changing the doping density), but also the absorption bandwidth can be controlled. A series of works leveraging this type of material for photonic crystal designs were developed by Susumu Noda's group. One example [116] is shown in Figure 1.51. A triangular lattice of air holes was introduced into the MQW layer to form a 2D photonic-crystal resonance (Figure 1.51(a)). As can be seen in Figure 1.51(b), the thermal emission control device reached much higher temperatures than the reference sample at the same input power. This is common for these narrowband thermal emitters and can be understood as a consequence of the narrowing of the wavelength and angular spread of the emission, which leads to an accumulation of energy inside the device. This then induces an increase in temperature until the total thermal emission power output via the controlled emission band and angle are equal to the input power.

To achieve a good performance, the important point is to attain a Q-matching condition (i.e., critical coupling) between the losses of an isolated photonic-crystal resonant mode determined by the optical confinement and the absorption of the material. However, the presence of a number of resonant modes in a typical photonic crystal makes it difficult to precisely Q-match just the desired ones to the absorption spectrum. Therefore, their strategy is to limit the absorption bandwidth and wavelength of the material in order to position a single isolated mode of the PC within the absorption range of the ISB-T. Figure 1.51(c) shows the

spectrum of a 2D photonic crystal where many peaks appear. So, one needs to carefully design the MQWs to overlap the ISB-T with one of these peaks. As a comparison, for our plasmonic quasi-BIC design, we can obtain a clean resonant response thanks to the mode property of BICs, i.e., a single peak within 3- 13 μm.

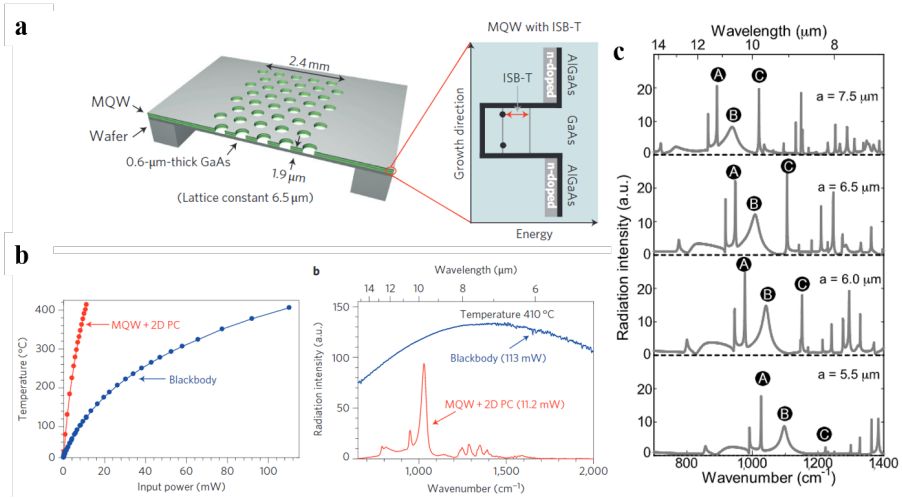

Figure 1.51: Ref. Conversion of broadband to narrowband thermal emission through energy recycling.

There are several concerns about this approach. First, the fabrication needs complex MBE (molecular beam epitaxy). For example, the MQW below contains 63 layers. Second, many ISB-T designs are sensitive to temperature. According to Mingze He's experiences, generally, the longer the working wavelength is, the more sensitive they are. While when the temperature is higher, such as 400 °C, the fluctuation declines. However, this paper does not show the emission spectra versus temperature, neither in the main text nor the supporting information. Moreover, although Noda's group made a series of demonstrations on thermal emission based on such an MQW design [116–119], they didn't show works on lasing, which is an intuitive idea. Noda's group is famous for PCSEL [120] (photonic-crystal surface-emitting lasers) and they demonstrated a 1.3 μm PCSEL by MQW. Several works from other groups have demonstrated PCSEL [121–124] or VCSEL (vertical-cavity surface-emitting laser)-based mid-IR lasing, two are shown in Figure 1.52. But these works are not cited often. Based on these works, it is possible to achieve mid-IR lasing by cavity design, such as BICs, and not only by laser pumping, but may also by electrical pumping. But why these have not been done, what are the difficulties, and why this field does not seem to be popular are unclear.

Another approach is to leverage the dielectric/spacer/absorber structure, where the absorber material can be metal. This is one promising way to achieve high Q factors and high absorptance (i.e., high emittance) at the same time. The reason can be understood as follows [125]. For an absorber, the total Q-factor Q_{tot} is determined by the radiative Q-factor Q_r and non-radiative Q-factor Q_n with the relationship $Q_{\text{tot}} = \left(Q_r^{-1} + Q_n^{-1}\right)^{-1}$. High-Q efficient absorption requires (1) simultaneously high Q_r and Q_n and (2) critical

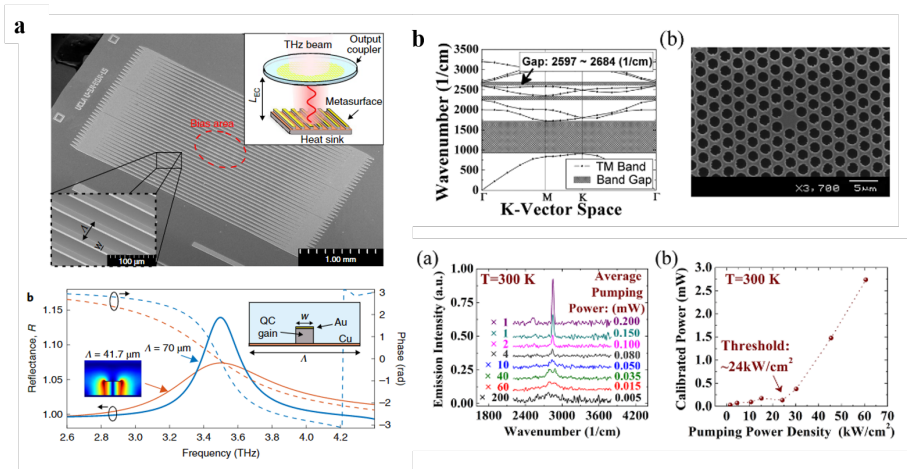

Figure 1.52: (a) Ref. Broadband continuous single-mode tuning of a short-cavity quantum-cascade VECSEL. (b) Ref. Room temperature mid-infrared surface-emitting photonic crystal laser on silicon.

coupling for the resonance, that is, $Q_r = Q_n$. In the design paradigm, efforts should be exerted not only to increase Q_r and minimize its degradation in the fabrication process but also to achieve a high Q_n and precisely engineer Q_n to reach the critical coupling condition since either overdamping $(Q_n < Q_r)$ or underdamping $(Q_n > Q_r)$ can decrease the absorptance dramatically. The low loss in dielectrics can thus make a high-Q design possible.

One recent example is the work [126] (Arbitrarily polarized and unidirectional emission from thermal metasurfaces) from Andrea Alu's group. Although it's not the main target of this paper (arbitrary polarization including circular polarization emission is the key highlight), the authors demonstrated a measured Q of $\sim$ 100 with 55% emissivity at $\sim 4\ \mu$m. The meaning of this work is that it represents a major step towards a generalized solution to flexibly custom wavefront thermal generation in which the metasurface does not need to be externally excited by a coherent source, but instead leveraging incoherent thermal oscillations, i.e., thermal metasurfaces. Some immediate applications can be light sources for chiral sensing in mid-IR, free-space communication by polarization multiplexing, etc. More importantly, this solution may also be used in other incoherent mechanisms such as luminescence [127] and fluorescence emission, and without a doubt in coherent mechanisms such as lasing, nonlinear, and quantum information.

It's noted that the refractive index of dielectric may vary with different temperatures, leading to a resonance shift. This might be a disadvantage of dielectrics-based thermal emitters compared with metal-based designs. Metallic nanostructures are less susceptible to temperature-dependent resonance variation as their permittivity is dominated by the imaginary part at mid-IR. Two examples of the temperature-dependent optical properties of amorphous silicon at elevated temperatures are shown in these references [128, 129].

On the other hand, in visible to near-IR, dielectric-based high absorption is much simpler. For example,

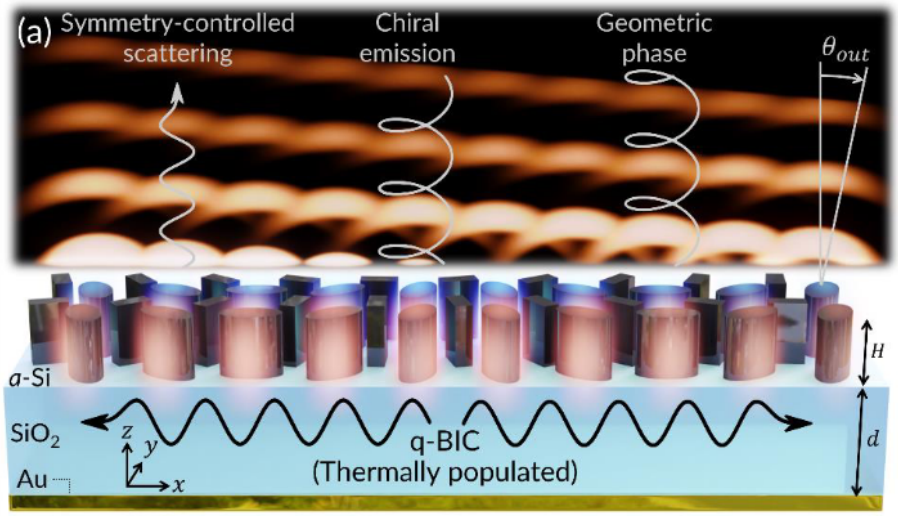

Figure 1.53: Ref. Arbitrarily polarized and unidirectional emission from thermal metasurfaces. Non-local quasi-BIC resonance and local geometry phase are combined.

absorption from silicon in visible by Yang et al [130]. (Kerker effect); absorption from silicon in near-IR by Yu et al [131]. (doped silicon), Pye et al [132]. (silicon with FP cavity, coherent perfect absorption); and absorption from germanium in near-IR by Tian et al [133]. (Kerker effect), Yu et al [134]. (PT symmetry breaking), Yu et al [125]. (dielectric/spacer/Ge film).

The last common method is to use the Tamm plasmon polaritons [135] (TPPs). Surface plasmon polaritons (SPPs) need complex nanostructures to excite the resonance which is a result of the large in-plane wave vector of surface plasmon modes. Typical TPP structures consist of a distributed Bragg reflector (DBR) on a conductor. The mode exists at their interface and can have a zero in-plane wave vector. The DBR provides optical phase matching to the metal surface, resulting in an absorptive resonance with a high Q factor at near-normal incident angles. As only thin-film deposition is required for fabrication, TPP thermal emitters [136–138] can be grown at the wafer scale with relatively low-cost and minimal fabrication steps without any lithography process, offering a promising candidate for wavelength-selective thermal emitters (WS-EMs).

Although TPP-EMs have so many benefits, there are several key concerns. First, despite the broad potential of TPP-EMs, the design of such structures is challenging, as most applications require simultaneous control over both emission frequencies and corresponding Q-factors, and suppression of emission at other frequencies. Due to the large parameter space associated with the design of aperiodic DBRs, forward-design methodologies are not efficient and thus, inverse design protocols must be used. Earlier works exhibited poor optimization efficiencies, requiring upwards of 24-day-long simulations per optimized structure [136]. Joshua Caldwell's work [139] well solved this problem by implementing a machine-learning algorithm. Second, the

physical properties of TPP-EMs fundamentally limit their ability to produce a "clean" emission spectrum over a large wavelength range, as shown in Figure 1.54(a) [139]. Again, as a comparison, for our plasmonic quasi-BIC design, we can obtain a clean resonant response, i.e., a single peak within $\sim$ 3 - 13 μm. Third, the temperature-dependent optical properties of the dielectrics in the DBR layer may shift the resonance. As an example, Figure 1.54(b) [137] shows a so-called wavelength-tunable TPP-EM which shows a 23-nm-redshift as the temperature changes from 100 to 150°C. Moreover, by combining a cavity, the performance can be improved as well [138] (Figure 1.54(c)).

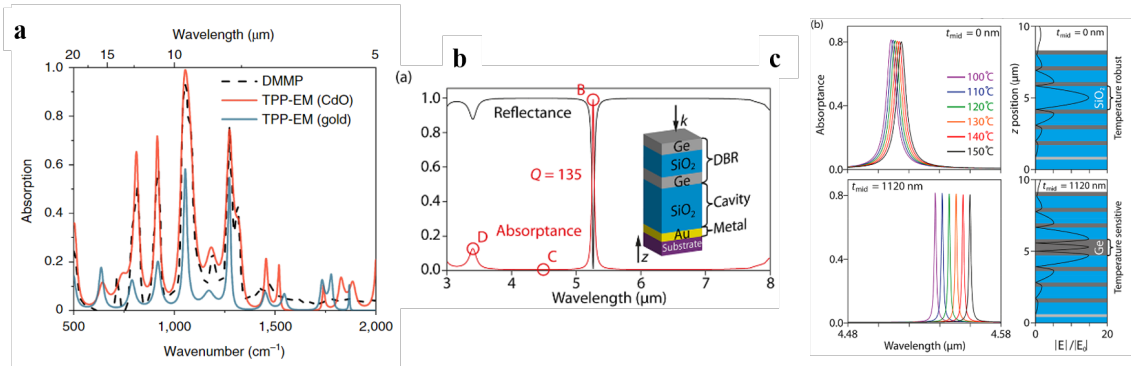

Figure 1.54: (a) Ref. Deterministic inverse design of Tamm plasmon thermal emitters with multi-resonant control. (b) Ref. Narrowband thermal emission realized through the coupling of cavity and Tamm plasmon resonances. (c) Ref. Ultranarrow and wavelength-tunable thermal emission in a hybrid metal–optical Tamm state structure.

Finally, for polarization and angle, both dependent or independent cases can have specific applications. For example, for our design, due to the different resonance peak positions for x and y polarization, the y-polarized emission can be stated to serve as a reference signal to calibrate the sensitivity drift of the system during elevating the temperature, similar to the dual-band detectors for CO_2 sensors [35]. As a comparison, Table 1.1 summarizes some of the recently experimentally reported thermal emitters in mid-IR in the past decades.

The high-Q property of quasi-BIC metasurfaces suggests a solution to the narrow band and high-efficiency thermal emitters. In Chapter 5, inspired by the slotting engineering of a quasi-BIC metasurface working at mid-infrared, we further propose and experimentally demonstrate the single-peak narrowband thermal emission of light based on plasmonic metasurfaces driven by quasi-BICs.

Table 1.1: Summary of some experimentally reported thermal emitters in mid-IR.

Structures & materials	Central wavelength (μm)	Peak emittance	Q	Temperature (K)	References
Al MIM	4.2	0.95	14	373	ACS Photonics 201543
Au MIM	4.25	0.85	~ 6.2	873	Physical Review Applied 2015 [140]
Au MIM	5.8	0.97	< 10	573	Physical Review Letters 2011 [107]
Au MIM	~ 4.0	0.97	11	573	Applied Physics Letters 2014 [35]
Au MIM	5.83	0.997	33		Advanced Optical Materials 2019 [141]
Au MIM (BIC)	4.5	0.97/0.67	65/111	673	Our work, simulation data
quantum well	10	0.74	72	473	Nature Materials 2014 [142]
MQW	8.936	0.4	109	453	Applied Physics Express 2014 [118]
MQW	9.1	0.4	107	473	Applied Physics Letters 2013 [119]
MQW	9.7	0.8	27	423	Nature Photonics 2012 [116]
MQW	9.5	~ 0.7	99	473	Optics Express 2016 [143]
TPP + cavity	4.731	0.90	88	323 - 423	ACS Photonics 2018 [138]
optimized TPP	6.534	0.82	188		ACS Central Science 2019 [136]
TPP with double DBR	4.565	0.35	780	tunable	ACS Photonics 2020 [137]
TPP with GD algorithm	2.5 – 10	0 – 1.0	26 – 10,117	423 - 523	Nature Materials 2021 [139]

Continued on next page

Table 1.1 Continued from previous page

Structures & materials	Central wavelength (μm)	Peak emittance	Q	Temperature (K)	References
SiC grating	11.36	0.94	~ 100	773	Nature 2002 [112]
SiC grating	11.5	0.46	200	770	ASME Journal of Heat Transfer 2008 [144]
SiC metasurface	12.9	0.78	170	523	Advanced Optical Materials 2019 [115]
SiC bowtie	~ 11.1	~ 0.45	~ 90	623	ACS Photonics 2017 [145]
SiC + Au grating	11.2	0.94	19	< 873	Applied Physics Letters 2019 [146]
SiC pillar array	~ 11.7	> 0.6	> 200	539	Nano Letters 2021 [113]
Si microsphere	~ 1.4		400	1073	ACS Photonics [147]
Si + spacer + Au	4	< 0.8	100 -200	573	arXiv [126]
Au MIM + GST	3	0.66-0.94	5.4	tunable	Advanced Optical Materials 2018 [148]
VO2 + sapphire 1D structure	11	0.3-1.0	4.1	tunable	Physical Review X 2013 [149]
GST-Au 1D structure	10	0.2-1.0	-3.6	tunable	Light: Science & Applications 2017 [150]

CHAPTER 2

Optical trapping of nanoparticles using an all-dielectric quasi-BIC metasurface

The following four chapters (including this chapter) contain material from author's published journal articles reporting relevant work. The text of each has been abridged and edited to better integrate into this document.

As we have discussed in Chaper 1, although plasmonic nanotweezers employing metallic nanoantennas provide a powerful tool for trapping nanoscale particles, the strong heating effect resulting from light absorption limits widespread applications. In this chapter, I numerically propose an all-dielectric nanotweezer harnessing quasi-BICs to enable the trapping of nanoscale objects with low laser power and negligible heating effect. The quasi-BIC system provides very high electromagnetic field intensity enhancement that is an order of magnitude higher than plasmonic systems as well as high Q factor resonances comparable to PhC cavities. Furthermore, the quasi-BIC metasurface tweezer array provides multiple optical hotspots with high field confinement and enhancement, thereby generating multiple trapping sites for the high throughput trapping of nanometer-scale objects. By purposefully truncating the tips of the constituent elliptical nanoantennas in the quasi-BIC system to leverage the asymmetric field distribution, the optical gradient forces are further enhanced by a factor of 1.32 in comparison to the intact elliptical nanoantenna, which has attractive potential in sub-wavelength particle trapping applications. In addition, this chapter shows that trapped particles can improve the resonance mode of the cavity rather than suppress it in a symmetry-broken system which in turn enhances the trapping process. Studies in this chapter paves the way for applying quasi-BIC systems to low-power particle trapping and sensing applications and provides a new mechanism to harness the self-induced back-action.

2.1 Introduction

Yang, Sen, et al. "Nanoparticle trapping in a quasi-BIC system." ACS Photonics 8, no. 7 (2021): 1961-1971.

Optical trapping technology has found many applications in biology and medicine [60, 61, 151–153] and colloidal assembly [62, 63] because it provides precise control and non-invasive manipulation of microscale particles. For example, the traditional optical tweezer has been utilized to manipulate microscale objects such as bacteria, colloidal particles and cells [64–66], and was recently recognized with a 2018 Nobel Prize in physics awarded to Arthur Ashkin for his pioneering work on optical tweezers [67]. The single beam optical tweezers demonstrated in 1986 [64] utilizes a tightly focused laser beam to trap particles near the focal spot of the laser. Due to the diffraction limit of light that precludes the focusing of light to nanoscale subwavelength volumes, the low power trapping of nanoscale objects by optical tweezers is challenging.

Plasmonic nanotweezers [68] have generated significant interest because plasmonic nanoantennas can confine light to nanoscale volumes with high field enhancement. Such subwavelength hotspots generate the tight trapping potential wells required to trap nanoscale objects. Different kinds of plasmonic nanoantenna geometries have been explored including nanoholes [33, 154–156], coaxial apertures [18, 157], double-nanoholes [17, 158, 159], nanopillar [160], dimers [15], bowtie [14, 161], and bowtie aperture [16]. Although plasmonic nanotweezers have been proven to be effective for trapping sub-wavelength nanoparticles by overcoming the diffraction limit, the photo-induced heating effect resulting from the intrinsic loss of the metallic materials generates undesired thermal effects such as thermophoresis and convection [68, 162], and the excessive temperature rise can damage trapped particles especially biological objects like cells. In addition, it is imperative to note that many of the previously reported near-field optical nanotweezers typically possess one or a few hots-spots that define the trapping potential where the target objects in the solution can be trapped. A platform that possesses multiple hotspots is crucial for achieving the multiplexed manipulation of multiple nanoscale objects. Although some works have demonstrated multiple nanoparticles trapping [163–166], this field presents many possibilities. Here we propose to realize these new features by harnessing an all-dielectric metasurface supporting super-cavity resonances enabled by bound-states-in-the-continuum. A metasurface [167–169] is an artificial nanostructured interface with a subwavelength thickness that manipulates light by spatially arranged nanoantennas. It has found many applications in wavefront shaping [170–172], waveguide [163], fiber [173, 174], and flat lens [175, 176]. Recently, bound states in the continuum (BICs), which were first proposed in quantum mechanics [53] and refers to a kind of non-radiating states of light in photonics, has attracted extensive attention in photonics due to the ability to achieve high quality-factor (Q factor) resonances as well as high field enhancement. An ideal BIC has no out-coupling. As a result, the Q factor of the mode is infinite, and it cannot be observed in the spectrum. True BICs cannot be realized in practice due to fabrication imperfections and material loss [177, 178]. If the outgoing radiation is not totally vanishing, a sharp peak can then be observed in the spectrum, and the Q factor does not go to infinity. Such a case is called a quasi-BIC. Many applications of quasi-BICs have been reported to date, including biosensing [9, 10, 179], nonlinear optics [180–182], chiral sensing [183], unidirectional radiation [184], and laser [185]. In this paper, we specifically focus on the symmetry-protected BIC [4, 6, 8], which is one class of BICs and appears when the spatial symmetry of the mode is incompatible with the symmetry of the outgoing radiating channels. Symmetry-protected quasi-BICs have been demonstrated in a variety of photonic structures such as metasurfaces [6, 9], photonic crystal slabs [186], and waveguide arrays [55].

The quasi-BIC system can provide very high field enhancement comparable to or even higher than in plasmonic systems. Additionally, the quasi-BIC system also provides much higher field enhancements than the levels achievable in Mie resonant dielectric nanoantenna systems [187] with no need for a critical geom-

etry [16, 161]. Moreover, in contrast to plasmonic nanostructures, the quasi-BIC system also has a very high Q factor ($10^2 \sim 10^6$) comparable to photonic crystals (PhC), making it a good candidate for trapping-assisted sensing applications. Additionally, the dielectric quasi-BIC system has almost no material absorption and thus negligible heating effects. This feature is especially critical for nano-optical trapping of biological specimens without detrimental photo-induced heating effects present in plasmonic systems. On the other hand, in comparison with a typical PhC cavity system [5], the quasi-BIC system has much higher field confinement, although some recent works have reported the realization of deep-subwavelength confinement by unique designs of PhC cavity geometries [2, 3].

We also present a new mechanism for harnessing the self-induced back-action (SIBA) effect based on the proposed quasi-BIC system. The SIBA effect first proposed using a plasmonic gold nanohole structure [156, 188] is a powerful technique for enhancing optical trapping under low optical intensities, reducing the power required for stable trapping by one order of magnitude. In the particle-cavity system, the trapped particle itself perturbs the local electric field and thus plays an active role in the dynamics of the trapping process. To be specific, when a particle moves away from its equilibrium position, by virtue of Newton's law, the momentum exchange between the photons and the particle induces a back-action force that pulls the particle back towards the cavity. SIBA effect has been shown to exist in some nanophotonic systems such as plasmonic nanoantennas [16, 17, 69, 189, 190] and photonic crystals [191, 192]. However, the previous works [190, 192, 193] have only analyzed the resonance frequency shift induced by the perturbation of particles to the cavity. How the trapped particles alter the resonance mode (the quality factor of the mode, for example) remains unclear. To reveal this mechanism, we need a system that meets three fundamental conditions: high quality-factor (Q factor), high field enhancement, and high sensitivity to perturbations. Traditional plasmonic nanostructures can fulfill the latter two requirements but usually have a low Q factor. The proposed quasi-BIC system supports these features, which provides a novel platform to investigate the SIBA effect from a new perspective.

In this work, we systematically discuss the optical trapping process in a dielectric quasi-BIC system for the first time (as shown in Figure 2.1). The organization of this paper is as follows. First, we study the optical trapping in a symmetry-protected quasi-BIC system comprised of pairs of complete elliptical dielectric nanoantenna elements and present its features, including high field enhancement, high quality factor, negligible heating effect, and multiple hotspots, which make it suitable for particle trapping applications. By purposefully breaking the symmetry of the trapping gaps where the two tips on one end of the nanoantenna elements in each unit cell are truncated, we demonstrate that the trapping force and stability can be further improved via the doubly truncated quasi-BIC system. The robustness of the system to fabrication uncertainties and the characterization of its trapping performances are then investigated. Owing to the high Q factor,

high field enhancement, and high sensitivity to perturbations of this quasi-BIC system, we also investigate the relationship between the trapped particles and the cavity resonance mode. Our analysis reveals that particles trapped in the original intact elliptical dielectric nanoantenna array will break the system's symmetry and slightly suppress the resonance mode of the cavity. We consider truncating only one tip of the nanoantenna elements in each unit cell to address this effect. Then, we present an idealized scenario, where we show the positive influence of the trapped particles on the resonant modes of the quasi-BIC system. The trapped particles partially compensate for the truncated part and improve the resonance performance of the symmetry-breaking quasi-BIC system. This in turn results in an increased Q factor and peak reflectance as well as stronger optical trapping forces. Both numerical and analytical investigations are presented to elaborate on this concept.

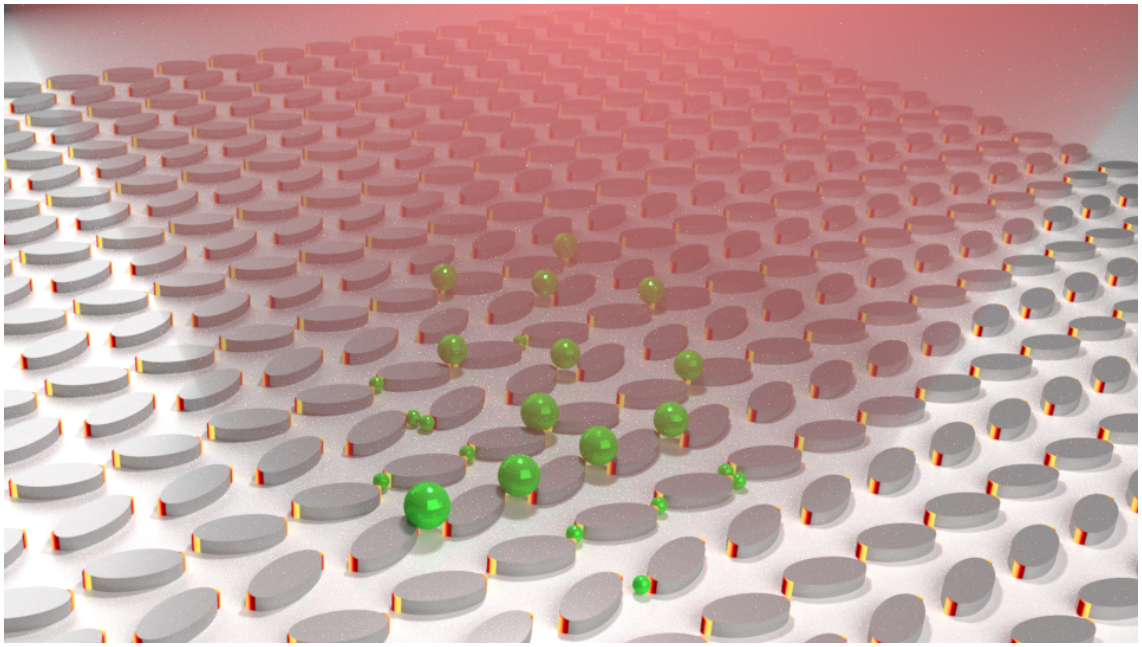

Figure 2.1: Schematic diagram for the quasi-BIC metasurface. Gradient colors at the tips show the field enhancement distribution.

2.2 Optical trapping in a quasi-BIC system

We start from the symmetry-protected quasi-BIC metasurface based on complete elliptical nanoantennas [6, 9]. As shown in Figure 2.2(a), a unit cell is composed of two silicon elliptical resonators with a tilt angle of The detailed geometrical parameters are given in the caption of Figure 2.2. Our design is tuned to work in the C band of the optical communication wavelength bands, and the resonator side is immersed in water for particle trapping purposes.

To understand the generation of the quasi-BIC mode, we consider the two inverse electric dipoles (black

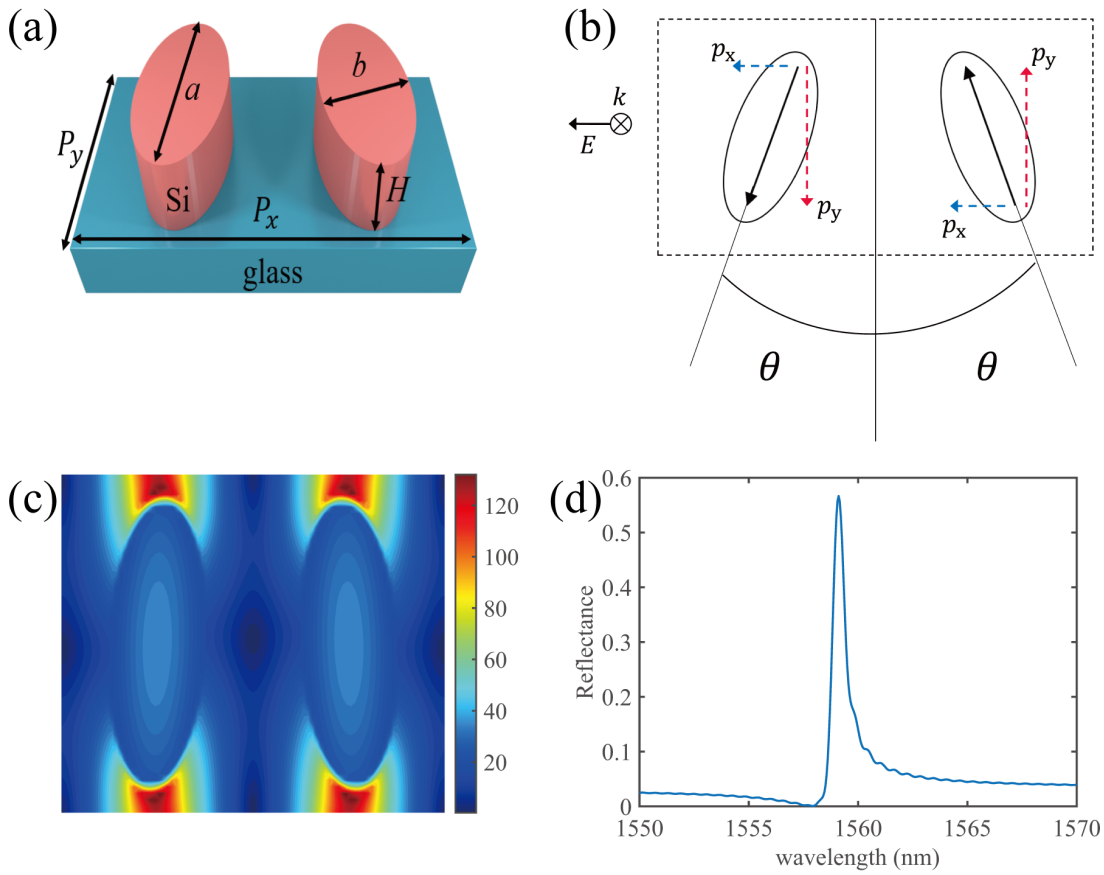

Figure 2.2: (a) Schematic diagram of a unit cell of the symmetry-protected quasi-BIC metasurface. Geometrical parameters are $P_x = 894$ nm, $P_y = 515$ nm, $a = 445$ nm, $b = 216$ nm, $H = 175$ nm, $\theta = 5°$. The resonator side is surrounded by water. The refractive indexes are extracted from the Palik database in Lumerical (see Methods for details). (b) Diagram depicting the electric dipoles induced in the two resonators. The incident light is linearly polarized light with polarization perpendicular to the mirror plane (yz plane in this figure). The blue and red dash arrows represent the two dipole components and respectively. (c) Electric field enhancement distribution of the xy plane ($z = H/2$) for one unit cell. The maximum field enhancement is 141, which is defined as the maximum electric field enhancement factor on the xy plane when $z = H/2$. The electric field is confined in the gaps, reflecting a collective effect. (d) Reflection spectrum for an infinite array. The reflectance peak is 56.6% due to water absorption in this wavelength band.

arrows in Figure 2.2(b)) excited in the two resonators by an incident x-polarized light. Each electric dipole is decomposed into two directions, i.e., P_x and P_y in Figure 2.2(b). Although P_y is dominant in each resonator, the directions of the P_y components are inverse for the two resonators, which cancel with each other and thus the out-coupling of is forbidden. When the tilt angle θ is small, the overall radiative loss is suppressed significantly. Hence, a fairly narrow reflection peak, as well as a high field enhancement, can be obtained. Since the Q factor of this system satisfies $Q \propto \sin^{-2}\theta$ [6, 9] and we have selected a small tilt angle of $\theta = 5°$, the electric field enhancement is extremely high (141) at the tips of each resonator, as shown in Figure 2.2(c). Therefore, water absorption cannot be neglected even though it is relatively small ($n = 1.31 + 0.00013$i at

$\lambda = 1550$ nm). This additional lossy channel perturbs the quasi-BIC mode, and the reflectance is reduced to 56.6% instead of approximately 100% reported in the previous work [9]. The reflection spectrum is shown in Figure 2.2(d), where the linewidth is 0.65 nm, and the corresponding Q factor is 1940.

The high field enhancement in our design, which is also spatially confined, provides a key advantage for optical trapping applications. Figure 2.3(a) shows the electric field distribution of two unit cells when a silicon sphere is trapped in one gap. Here we define a parameter "trapping density" $\sigma = 1/2$ which means every two unit cells share one trapped particle in the infinite array. Due to the high index contrast between the sphere and the medium, a much higher field enhancement is observed near the sphere's surface. Figure 2.3(b) shows the force spectra of the silicon sphere depicted in Figure 2.3(a). Figure 2.3(c) and 2.3(d) show the temperature fields when a 30 μm by 30 μm nanoantenna array on the glass substrate is excited at resonance. The negligible temperature rise (less than 0.01K) confirms the low heating effect from our design. This is because most heat dissipation comes from water absorption instead of the resonators.

Since the optical gradient force is proportional to the gradient of the square of the local electric field $F_{\text{grad}} \sim \nabla|\vec{E}(r)|^2$, we next investigate a truncated quasi-BIC system, wherein the trapping stability can be further improved by leveraging the asymmetry introduced in the gap. To demonstrate this, we purposefully truncate out a small part of both tips of the resonators in each unit cell to break the symmetry of the original system (see Figure 2.4(a)). We refer to this as the "2 cuts" system, and for the original system in Figure 2.2(a) we refer to it as the "0 cuts" system. For comparison with the "0 cuts" system, we have adjusted the gap size of the "2 cuts" system to have the same gap size as the "0 cuts" system. The tip-to-tip gap size for both the "0 cuts" and "2 cuts" system is approximately 70 nm. Figure 2.4(a) shows the electric field distribution of two unit cells of the "2 cuts" system that presents approximately the same maximum field enhancement compared with the original "0 cuts" system. The inset shows a higher field enhancement at the intact tip (the black dash ellipse) compared with the truncated tip (the white dash ellipse) due to the larger curvature of the intact tip, which can induce a larger gradient force on the particle trapped in the gap. As shown in Figure 2.4(b), the "2 cuts" system shows approximately the same peak reflectance value compared with the original "0 cuts" system. The force spectra of silicon spheres with the same size and relative position in the "2 cuts" and "0 cuts" systems are shown in Figure 2.4(c). It can be found that the peak value of F_y on the sphere (66.10 pN/mW) trapped in the gap of the "2 cuts" system is larger (by 1.32 times) than that of the same sphere trapped in the original "0 cuts" system (50.12 pN/mW), validating the improvement on trapping stiffness in the xy plane. This enhancement in the trapping forces for the "2 cuts" system relative to the "0 cuts" system is because truncating the tip of the antenna on one end results in an increased gradient of the electric field in the gap in comparison to the untruncated ("0 cuts") system. Since the optical gradient force in the quasistatic limit is proportional to the gradient in the electric field, the "2 cuts" system with the enhanced electric field

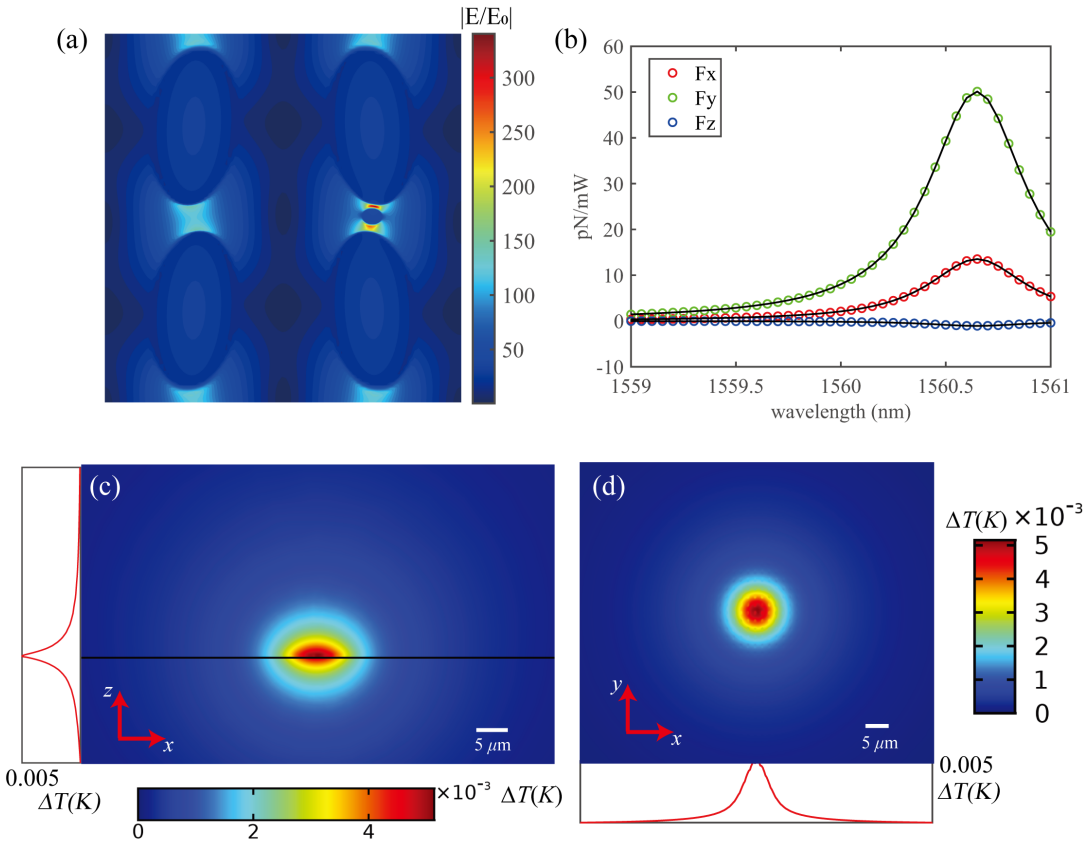

Figure 2.3: (a) Electric field enhancement distribution for $\sigma = 1/2$. The diameter of the trapped silicon sphere is D = 50 nm. The maximum field enhancement is 347. To describe the position of the sphere, we define $x_0 = P_x/4, y_0 = P_y/2, z_0 = H/2$. The center position of the left bottom resonator can be expressed as $x = -x_0, y = -y_0, z = z_0$. Therefore the center position of the sphere in (a) is described as $x = x_0, y =$ 5 nm, $z = z_0$. We will follow the coordinate notations here in this paper. This set of geometrical parameters are applied to all systems (except for the second section) for comparisons between different systems. (b) Force spectrums for the silicon sphere depicted in (a). Temperature fields of the (c) xz plane and (d) xy plane for a 30 μm by 30 μm quasi-BIC array on the glass substrate. The maximum temperature rise is 0.005K.

gradient generates an increased optical gradient trapping force. We have also investigated the impact of fabrication imperfections on the quality factor of the quasi-BIC antenna system. We have fabricated the "2 cuts" system and compared it with the designed system from numerical simulations. Figure 2.4(d) shows the SEM image of a fabricated antenna array. The tilt angle has been set to $\theta = 15^\circ$ because this is easier to be fabricated using the readily available nanofabrication facility. As shown in Figure 2.4(e), by inputting two unit cells of the SEM images into the numerical simulation model, the fabricated array presents a similar reflection spectrum compared to the designed array with only a slight redshift.

Subsequently, we have simulated the performances of the "2 cuts" system for practical optical trapping applications of relevant nanoscale particles, as depicted in Figure 2.5. Figure 2.5(a) shows the force spec-

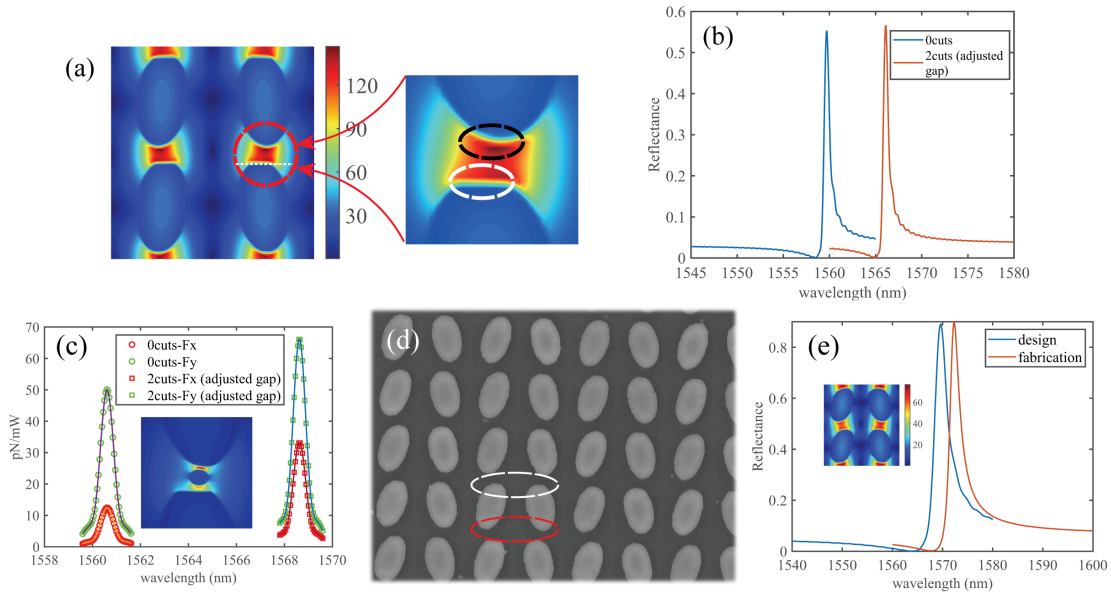

Figure 2.4: (a)Electric field enhancement distribution for the "2 cuts" system with adjusted gap size. The tip-to-tip gap size is approximately 70 nm in both "0 cuts" and "2 cuts" systems. Here we set $P_y = P_{y0} - 20$ nm $=$ 495 nm for the "2 cuts" system to keep symmetry while adjusting the gap size. Following the coordinates notation described above, the tip is vertically truncated along the z direction, and the line equation of the edge (labeled by the white dash line) is $y = -45.5$ nm. All other geometrical parameters of the resonators are the same. The maximum field enhancement is 147. Inset: Zoom-in figure showing the field enhancement difference between the two tips. (b) Reflection spectrum for the original "0 cuts" and the "2 cuts" system. (c) Force spectrums of the same silicon sphere trapped in the "0 cuts" system and the "2 cuts" system with $\sigma = 1/2$. The relative position of the sphere in the gap is approximately the same in the "0 cuts" and the "2 cuts" system for comparison. Inset: Zoom-in figure shows the field enhancement difference for the "2 cuts" system with $\sigma = 1/2$ which induces a larger gradient force. (d) SEM image of the fabricated "2 cuts" array. The tilt angle is designed as $\theta = 15°$. The white dash ellipse labels two truncated tips while the red dash ellipse labels two intact tips. (e) Reflection spectrums for the designed and fabricated "2 cuts" array calculated by FDTD Solutions. The tilt angle is $\theta = 15°$. Inset: Electric field enhancement distribution for the fabricated "2 cuts" array. Notice that the field enhancement is lower for $\theta = 15°$ in comparison to $\theta = 5°$. The model for the fabricated array in FDTD Solutions is built from the SEM image in (d).

trums for some small particles comprising exosomes, quantum dots, and BSA protein molecules. Their hydrodynamic diameters are taken as 30 nm, 20 nm, and 5 nm, respectively. Although the quantum dots are smaller than exosomes, they show larger forces due to their larger refractive index of 2.49 relative to that of the exosomes ($n = 1.38$) and the water medium ($n = 1.31$). Since the forces are normalized, the results show that stable trapping for these particles is expected even under lower laser power of a milliwatt. Figure 2.5(c) shows the trapping potential of a 30 nm polystyrene (PS) sphere located above the top surface of the resonators and moving along the path depicted by the red arrow in the inset. A broad and deep potential well is observed within the gap of the "2 cuts" system. The depth of the potential well is larger than 10 $k_B T/mW$, which is sufficient to trap the PS sphere stably in the xy plane. The corresponding optical forces with respect

to the sphere's positions along the y direction are shown in Figure 2.5(b). Figure 2.5(d) shows the optical trapping potentials for the same PS sphere trapped in the original "0 cuts" system and the "2 cuts" system along the z direction obtained by evaluating the integral $U(\mathbf{r}_0) = \int_{\infty}^{r_0} \mathbf{F}(\mathbf{r}) \cdot d\mathbf{r}$ [157]. It can be noticed that the middle height z_0 (the left black dash line) is the equilibrium position with $F_z = 0$, which corresponds to the bottom of the trapping potential well. Near the top surface level $z = H$ (the right black dash line), the steep slope of the potential curve indicates a strong force pulling the particle back towards the gap. The broad potential well indicates that the confinement in the z direction experienced by a trapped particle is not strong, while the large depth of the potential well ($59\ k_B T/mW$) guarantees a strong back force pulling the particle back when it reaches the top surface. Moreover, the "2 cuts" system presents a deeper trapping potential well along the z direction than the original "0 cuts" system, indicating improved trapping stability along the longitudinal direction. These properties make the "2 cuts" system an ideal platform for nanoscale particle trapping applications.

2.3 SIBA effect with truncated quasi-BIC antenna system

As we have mentioned previously, to the best of our knowledge, discussions on how trapped particles alter the resonance performance of the cavity rather than the resonance frequency have not been reported so far. This section investigates the relationship between the cavity resonance and trapped particles, and presents a new mechanism to generate the SIBA effect based on this quasi-BIC antenna system. Our discussions are based on an idealized scenario assuming an infinite array where trapped particles are periodically placed in the gaps.

To begin the discussion, we refer to the "0 cuts" system where the tips are intact and investigate the influence of the trapping density on the resonance performance. For demonstrating this concept, we make the assumption for the following section that trapped spheres are always placed in the right-side gap in each unit cell for all the trapping density values. The placement of particles for $\sigma = 2/3$ in the "0 cuts" system is intuitively depicted via the electric field enhancement distribution shown in Figure 6a. Due to the high Q factor, perturbation to the "0 cuts" system by trapped silicon spheres cannot be neglected, and a redshift when increasing the trapping density is observed (seen in Figure 6b). It should be noted that the reflectance of the system is also decreasing with increasing trapping density. This means that the quasi-BIC mode is slightly suppressed, and the scattering loss increases when a particle gets trapped in the gap. To verify that the quasi-BIC mode is suppressed in the "0 cuts" system, we have fitted the reflection spectrum to a Fano line shape to extract the Q factor for different (see Methods for details), as shown in Figure 6c. Both the Q factor and the field enhancement show a drop with a higher trapping density. A qualitative explanation is that the extra dipole moment excited in the silicon sphere breaks the original symmetry of the system. In other

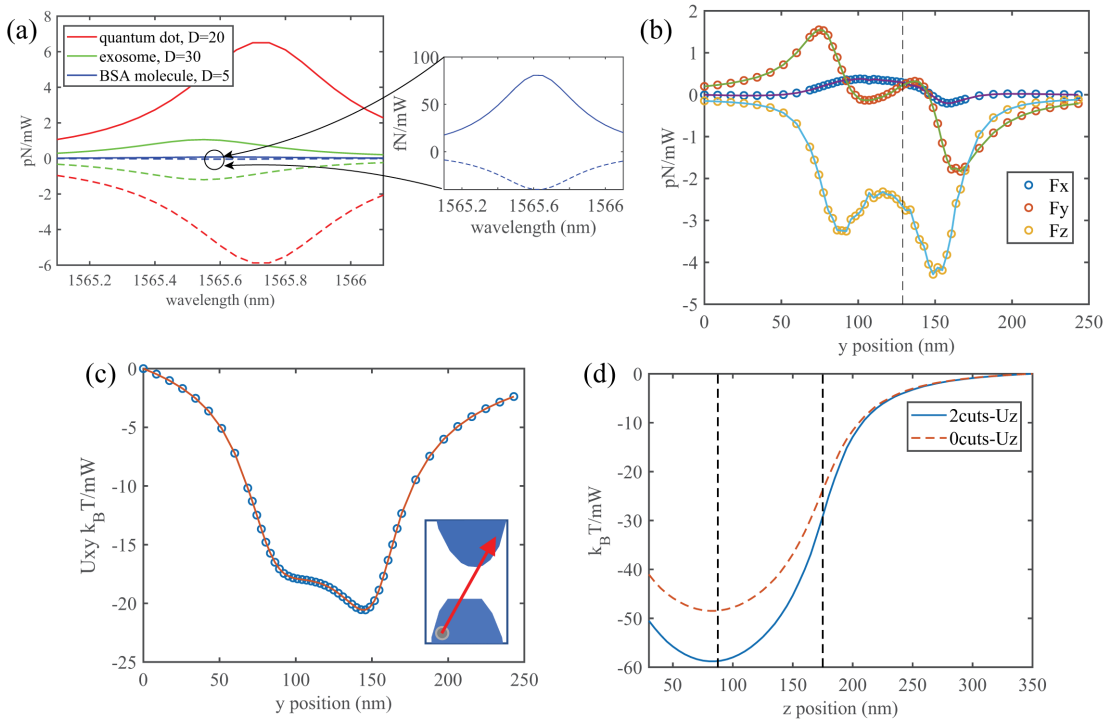

Figure 2.5: (a) Force spectrums for small particles, including exosomes, quantum dots, and BSA molecules. The geometrical parameters are $\sigma = 1/2, x = x_0, z = H, y = 8$ nm, $y = 12$ nm, $y = 23$ nm for exosomes, quantum dots, and BSA molecules, respectively. The refractive index for each particle, namely exosomes, quantum dots, BSA, is 1.38, 2.49 [36], and 1.45 [37], respectively. D in the legend denotes the diameter of each particle. Solid lines correspond to F_y while dash lines correspond to F_z. Inset shows a zoom-in view of the force spectrums for BSA molecules. (b) Trapping forces corresponding to the trapping potential in (c). The vertical black dash line indicates the center of the gap (i.e., close to the equilibrium position in the xy plane). The "y position" in both (b) and (c) is the y coordinates relative to the starting position. (c) Trapping potential of a PS sphere ($n_{\mathrm{PS}} = 1.59, D = 30$ nm) moving along the red arrow 5 nm above the top surface of the resonators. A broad and deep potential well is observed, corresponding to the gap region. Inset depicts the trajectory of the sphere. (d) Optical trapping potential wells for the "0 cuts" and "2 cuts" systems when moving a PS sphere along the z direction in the gap. The two vertical black dash lines correspond to $z = z_0$ and $z = H$ respectively. The trajectory of the sphere center is z = 30 nm to $z = 2H$ The geometrical parameters are $D = 30$ nm, $\sigma = 1/2, x = x_0, y = 0$ (center of the gap for comparison). The laser wavelength is set as the resonance wavelength when the sphere center is at $z = z_0$ in each case.

words, the components of the left and right resonators are not able to equally cancel with each other due to the extra dipole moments provided by the trapped particles.

We next consider a "1 cut" system where particles are trapped in the truncated region (see the inset of Figure 2.7(a)). In contrast to a negative impact on the quasi-BIC mode, particles trapped in the asymmetric gap of the "1 cut" system instead play a positive role in enhancing the performance of the mode. Direct evidence can be found from the reflectance spectrum shown in Figure 2.7(a), where the peak reflectance increases with increasing the trapping density σ. When no particles are trapped (i.e. $\sigma = 0$), the reflectance decreases dramatically from 56.6% in the "0 cuts" system to 46.0% attributed to breaking the symmetry, while

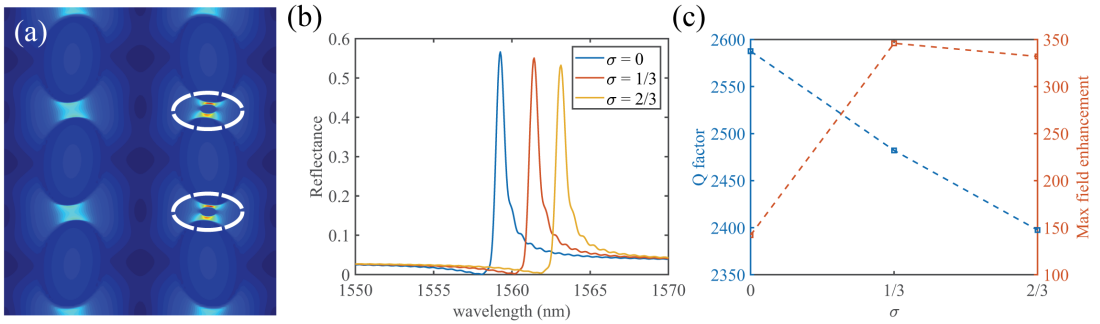

Figure 2.6: (a) Electric field enhancement distribution for $\sigma = 2/3$ depicting the placement of particles. White dash ellipses show the placement of the spheres. The positions of the silicon spheres are $x = x_0, y = 5$ nm and $y = 5$ nm $+ P_y$, respectively. (b) Reflection spectra for different trapping densities $\sigma = 0, 1/3$, and $2/3$ With a higher trapping density, the resonance wavelength shows a redshift, and the peak reflectance decreases. (c) Q factor and maximum field enhancement with respect to the trapping density. The Q factor is decreasing, denoting a suppression to the quasi-BIC mode by trapped particles. The maximum field enhancement jumps up when trapping density is not zero, originating from the high index contrast between silicon and water. It then gradually decreases due to the perturbation of trapped particles.

the reflectance increases again with increasing σ, in contrast to the trend of the "0 cuts" system where the reflectance decreases with increasing σ (see Figure 2.6(b)). The new dipole moment induced in the trapped silicon sphere partially compensates for the lost part of the truncated resonator and hence enhances the quasi-BIC mode. In other words, the effective index in the gap gets increased and becomes closer to that in the original system. By multipole decomposition analysis [194] shown in Figure 2.7(b), we can find that the electric dipole around the right antenna is increased after trapping a particle, consistent with our expectation. To further prove this positive effect, the Q factors and the maximum field enhancements with respect to the trapping density are shown in Figure 2.7(c). It is evident that the Q factors and maximum field enhancement both increase with increasing σ, which is opposite to the trend of the "0 cuts" system (see Figure 2.6(c)). Since both a higher Q factor and a higher field enhancement denote a higher local density of photon states, the improvement of the quasi-BIC mode is verified. This effect still occurs for low-index particles such as PS spheres (n = 1.59).

To qualitatively demonstrate how this particle-enhanced effect assists with the trapping process, we have derived the expression for the force F_y where the x and z components are not considered since they are much smaller in the gap. The equations of one-dimensional particle motion while only considering optical forces can be expressed as [193]

$$\frac{\mathrm{d}y}{\mathrm{d}t} = \frac{p}{m} \tag{2.1}$$

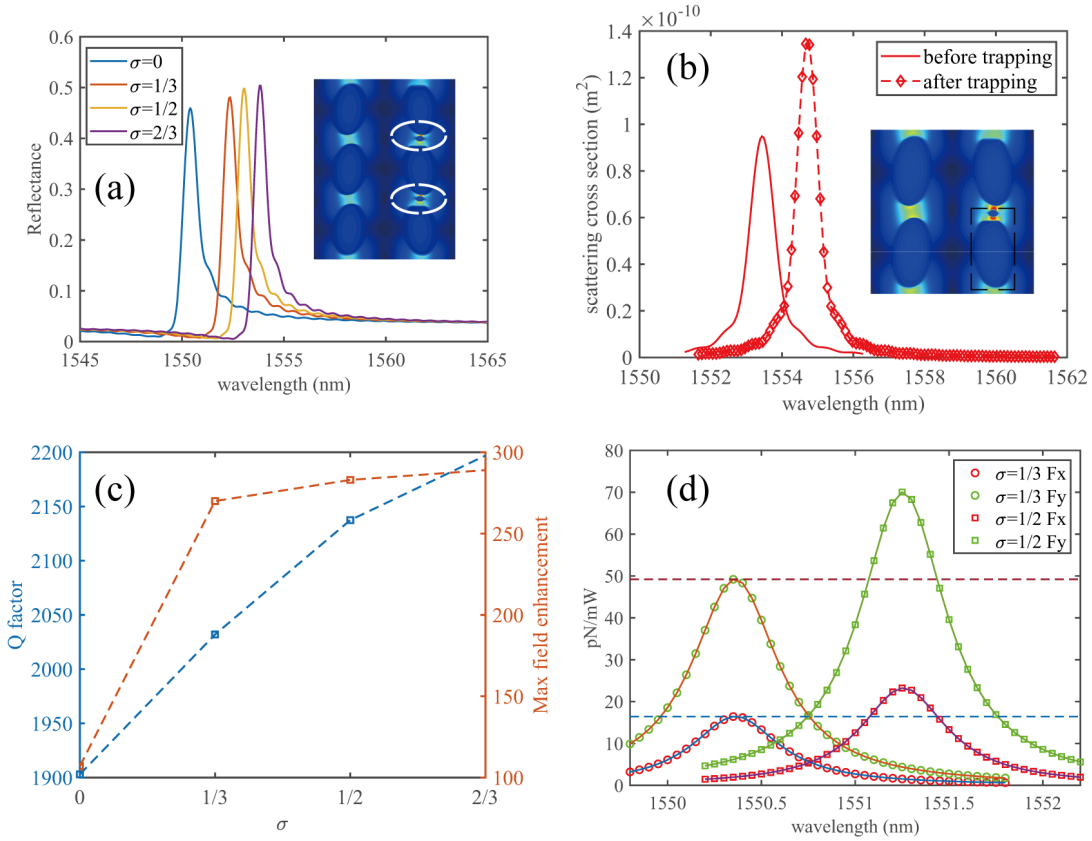

Figure 2.7: (a) Reflection spectrums for different trapping densities in the "1 cut" system: $\sigma = 0, 1/3$, and $2/3$. Similar to the "2 cuts" system, the line equation of the truncated edge is expressed as y = -55.5 nm. All other geometrical parameters are the same as the original "0 cuts" system (i.e., the gap size is not adjusted). With a higher σ the resonance wavelength shows a redshift and the peak reflectance is increased. Inset: Electric field enhancement distribution for $\sigma = 2/3$ depicting the placement of particles. White dash ellipses show the placement of the spheres. (b) Multipole decomposition analysis showing the electric dipole components before (solid line) and after (dash line with diamonds labeling data points) a silicon sphere is trapped with $\sigma = 1/2$. An increase can be seen after a particle is in the gap, indicating the compensation for the lost part of the resonator. Inset shows the region (the black dash rectangle) where the multipole decomposition analysis is applied. (c) Q factor and maximum field enhancement both increase with increasing σ, denoting a positive perturbation in contrast to particles trapped in the original system (seen in Figure 6c). (d) Force spectrums of silicon sphere trapped in the "1 cut" system with $\sigma = 1/3$ and $\sigma = 1/2$ respectively. The peak values of forces are: $F_x = 16.43\text{pN/mW}, F_y = 49.21\text{pN/mW}$ for $\sigma = 1/3$ and $F_x = 23.23\text{pN/mW}, F_y = 70.05\text{pN/mW}$ for $\sigma = 1/2$, respectively. The two horizontal dash lines denote the peak values of forces when $\sigma = 1/3$.

$$\frac{\mathrm{d}p}{\mathrm{d}t} = -n(y)\frac{h}{2\pi}\frac{\mathrm{d}\omega_c(y)}{\mathrm{d}y} \tag{2.2}$$

$$\frac{\mathrm{d}\beta}{\mathrm{d}t} = \mathrm{i}\left(\omega_L - \omega_c(y)\right)\beta - \frac{\kappa}{2}\beta + \mathrm{i}\sqrt{\kappa_{\mathrm{ex}}}E_0 \tag{2.3}$$

where p is the momentum of the particle, β is the expectation value of the photon amplitude while $n = |\beta|^2$ is the expectation value of the photon number in the cavity. $\omega_c(y) = \omega_0 + \delta\omega_c(y)$ denotes the resonance frequency of the system as a function of particle position y while ω_0 and $\delta\omega_c(y)$ describes the resonance

frequency of the empty cavity and the resonance shift due to the particle perturbation, respectively. $\kappa = \kappa_{ex} + \kappa_{int} + \kappa_{scat}(y)$ is the total cavity decay rate [195] (also the total linewidth), and the Q factor of the empty cavity is defined as $Q = \omega_0/(\kappa_{ex} + \kappa_{int})$. Here κ_{ex} denotes the decay rate of the empty cavity into particular external channels (such as backward scattering) which also serves as the source of injection of photons into the cavity with number flux E_0^2 and frequency ω_L. κ_{int} denotes the intrinsic loss rate resulting from water and material absorption. $\kappa_{scat}(y)$ describes the scattering rate of trapped particles and is a *negative* value here in contrast to that in the previous work [193] because the presence of particles increases the Q factor (i.e., decreases the total linewidth). By solving equations (2.1) to (2.3), we show that the y component of the optical forces satisfies $F_y \propto \kappa_{ex}/\kappa$ at the resonance wavelength. Here we assume that the laser wavelength can be freely tuned to reach a resonance for the particle at a specific position, which is different from the previous work [193] where the laser wavelength ω_L is considered to be fixed. With particles trapped in the gap, the Q factor increases, namely, the total decay rate κ decreases, giving rise to an increase of F_y. The numerical evidence from the aspect of trapping density is shown in Figure 2.7(d). When increasing the trapping density from $\sigma = 1/3$ to $\sigma = 1/2$ in the "1 cut" system, the peak values of F_x and F_y on the same sphere are increased, directly confirming the positive response of our "1 cut" system when particles are trapped.

Since we have assumed collective placement of multiple particles, it is instructive to investigate a scenario in the limit of low particle density. For this case, we have simulated a 20μm by 20μm "1 cut" array and placed only five silicon spheres in the truncated regions. We find that for such low particle density, trapping of particles in the truncated region does not improve the resonance quality of the quasi-BIC mode. Figure 8 shows the simulation results before and after five silicon spheres (i.e., $\sigma = 5/858$) are trapped at the center region of a 20μm by 20μm "1 cut" array illuminated by a Gaussian beam. The reflection spectrums present a slight redshift, while the differences between the reflectance peak values are small enough to be considered as numerical calculation tolerance. Based on our findings, we predict that the trapping stability would increase when more particles are trapped in the asymmetric gap, while no enhancement in the trapping stability is expected for low particle trapping densities such as the case of single-particle trapping. Such a trapping feature whereby increased trapping stability occurs as a result of increasing particle density represents a novel form of self-induced back action.

2.4 Conclusion

We have systematically studied the optical trapping process in a dielectric quasi-BIC system for the first time. We first investigate the optical trapping of dielectric sub-wavelength particles in a symmetry-protected quasi-BIC system which contains a pair of complete silicon elliptical cylinder resonators in each unit cell. Compared with traditional plasmonic nanotweezers, the high Q factor (~ 2000), strong field enhancement

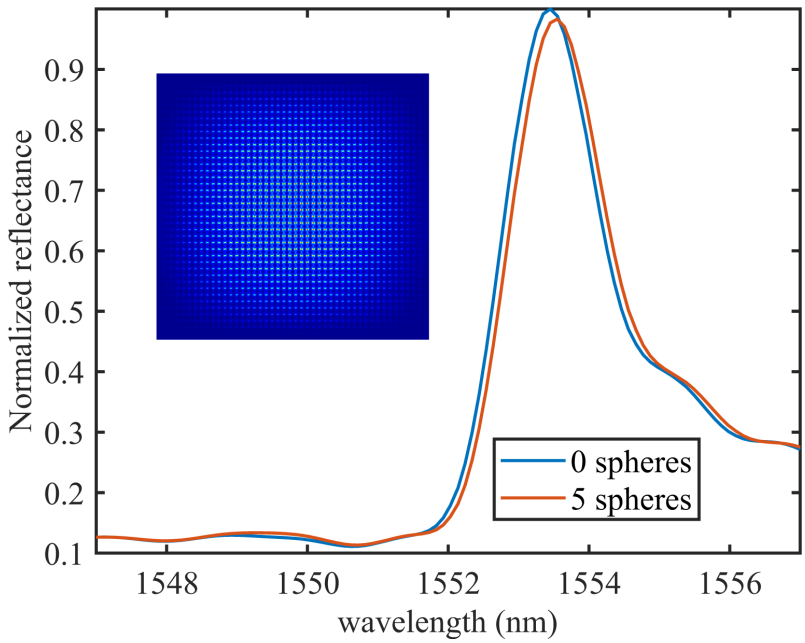

Figure 2.8: Normalized reflection spectrums before and after five silicon spheres are trapped at the center region of a 20μm by 20μm "1 cut" array. PML boundary condition is applied, and the incident light is set as a Gaussian beam with the beam waist radius of 10 μm. Inset: Electric field enhancement distribution for the whole array without particles.

($\sim$ 140), negligible heating effect, and multiple hot spots make such a system a great candidate for trapping-assisted sensing applications. We have also shown that purposefully truncating a small part of the tips of both resonators in each unit cell to give rise to a doubly-truncated system results in an enhanced optical gradient trapping force. We attribute such enhancement to the higher electric field gradient induced in the asymmetric gap of the system. Our results show that the doubly-truncated ("2 cuts") system is more suitable for particle trapping applications in comparison to the complete elliptical nanoantenna system. In addition, we have demonstrated the positive interplay between trapped particles and the cavity in the symmetry-broken system where only one resonator in each unit cell is truncated, in contrast to the trapping-induced suppression of the quasi-BIC modes in the original intact system. This mechanism applies to particles with lower refractive indexes and smaller sizes as well. Future work will focus on experiments to demonstrate these effects. We envision that these results will pave the way for applying quasi-BIC systems into particle trapping-assisted sensing applications and open a new door to harness the particle-cavity interplay to enhance the optical trapping process.

2.5 Apendix

Simulations: The numerical simulations of reflectance spectrums and field distributions presented in the manuscript are performed by commercially available software (Lumerical FDTD Solutions 2019b) using a finite-difference time-domain solver. Periodic boundary conditions are used in the x and y directions while PML boundary conditions are used in the z direction. A maximum mesh step of 10 nm is set for resonators and a maximum mesh step of 3 nm is set for trapped spheres. A mesh accuracy of "5" is set for the simulation region. The dimensions, material properties, and background media are specified in the main text.

The numerical simulations of optical forces are performed by another commercially available software (COMSOL Multiphysics 5.5) using the frequency domain solver in the Wave Optics Module. Periodic boundary conditions are used in the x and y directions while PML boundary conditions are used in the z direction. Normal-incident and x-polarized (perpendicular to the mirror plane of the unit cell) plane wave are defined at the incident port. All forces are calculated by Maxwell Stress Tensor (MST) method and are all normalized to an input power of 1 mW. Material properties are averaged from the Palik database in Lumerical and are set as follows. $n_{\mathrm{Si}} = 3.477, n_{\mathrm{Si22}} = 1.41, n_{\mathrm{PS}} = 1.59$, and $n_{\mathrm{water}} = 1.31 + 0.00013\mathrm{i}$ where i is the imaginary number denoting the loss component. A maximum mesh step of 15 nm is set for resonators and a maximum mesh step of 5 nm is set for trapped spheres. Maximum mesh steps for water and glass substrate are set as 1550 nm/6/1.31 and 1550 nm/6/1.41, respectively. The geometrical parameters are the same as those in Lumerical simulations and are specified in the main text. It should be noted that the resonance wavelength in COMSOL simulations all deviate slightly ($\sim$ 1.5 nm) from that of the same structure in Lumerical FDTD simulations. Therefore, we compare the reflection spectrums and force spectrums separately in the main text to avoid confusion.

Q-factor extraction: We use a Fano model to extract the Q factor from the reflection spectrum following the method reported in previous works [196, 197]. The simulated reflection spectrum is fitted to a Fano line shape by the "CFTool" toolbox in MATLAB. The curve fitting equation is given by $R = \left| a_1 + \mathrm{i}a_2 + \frac{b}{\omega - \omega_0 + \mathrm{i}\gamma} \right|^2$ where a_1, a_2 and b are constant real numbers; ω_0 is estimated by the central resonant frequency and needs to be slightly modified during the fitting process; γ denotes the overall damping rate of the resonance. The frequency terms ω and ω_0 are pre-normalized to $(0,1)$ so that all the unknown parameters will be within (0, 1). The Q factor is then calculated by $Q = (\omega_0/2\gamma)$. In this manuscript, the R-square values of all curve fittings are larger than 99%.

CHAPTER 3

Transport and optical trapping of a single nanoparticle using cascaded BPCNs

PhC cavities have been widely studied due to their ability to generate high Q factor resonances. Prior PhC nanotweezers suffer from a limited mode volume that limits the gradient force as well as low particle capture rates. In this chapter, my collaborators and I propose a nanotweezer system based on BPCNs discussed in Chapter 1. These BPCNs achieve extreme mode confinement and an electromagnetic field enhancement factor of 138 times, while support a high quality factor of 15,000 in water. Furthermore, by harnessing the localized heating of the water layer near the bowtie cavity region combined with an applied alternating current electric field, our system provides long-range transport of particles with average velocities of 30 μm/s towards the bowtie cavities on demand. Once transported to a given bowtie region, synergistic interactions of optical gradient and attractive negative thermophoretic forces stably trap a 10 nm quantum dot in a potential well with a depth of 10 k_BT using a milliwatt (mW) input power. Thus, this system effectively addresses the long-standing challenge of limited capture rate in PhC nanotweezers for the first time. Moreover, this chapter presents the concept of multiplexed long-range transport for hand-off of a single emitter from one cavity to the next by simply switching the wavelength of the input light. This novel multiplexed integrated particle trapping platform is expected to open new opportunities in directed assembly of quantum emitters for quantum photonics and ultrasensitive sensors for single particle spectroscopy.

3.1 Design and numerical investigation

3.1.1 Introduction

Yang, Sen, at al. "Multiplexed long-range electrohydrodynamic transport and nano-optical trapping with cascaded bowtie photonic crystal nanobeams." Physical Review Letters 130, no. 8 (2023): 083802.

On-chip nanophotonic devices have been extensively studied in the past years based on their capability to concentrate and manipulate light [198–201]. Among them, nanoscale optofluidic chips incorporating plasmonic and photonic crystal cavities have recently emerged as a powerful platform for chemical and biological sensing [202], nanomanipulation [203] and optical nano-assembly [76, 204]. Owning to the nanoscale feature of the cavities, the directed transport of nanoparticles and biomolecules to the region of highest electromagnetic field enhancement is critical to device performance. Though plasmonic nanocavities can support localized electromagnetic hotspots, they suffer from intrinsic material loss that gives rise to low quality factor (Q factor) resonances with broad spectral linewidths. This makes realizing multi-resonant plasmonic cavities for wavelength switchable trapping and long-range particle transport extremely challenging. Dielectric

photonic crystal (PhC) cavities, on the other hand confine light by means of a defect in an otherwise periodic arrangement of high index dielectric photonic structures [205, 206] leading to low-loss, narrow linewidth resonances that can be leveraged for wavelength switchable trapping applications. To date, the deterministic transport of particles for interaction with the enhanced field near resonant PhC cavities has been met with challenges. Prior reported attempts to achieve transport of particles to PhC cavities rely on pressure-driven flow [207, 208]. Unfortunately, this has limited particle capture rate because only the particles in the fluid boundary layer near the cavity can interact with the electromagnetic hotspots. Additionally, such pressure driven flow does not provide the mechanism for actively transporting particles from one nano-cavity to the next.

In this letter, we investigate the physics of light-induced near-field trapping, attractive negative thermophoresis and long-range electrohydrodynamic transport of nanoparticles in bowtie PhC cavities for directional delivery of particles and trapping at the cavity region by switching the input wavelength. We note that the earlier work theoretically demonstrating the single nanoparticle trapping capabilities of such PhC structure [209] only considered the optical trapping alone, while other thermal-induced effects such as the wavelength-actuated electrothermal flow was not included. An important distinction between this work and our earlier work with plasmonic tweezers [210] is that the bowtie PhC is effectively lossless so that the electrothermal flow is induced by the enhanced absorption of the water medium layer by the localized and enhanced electric field of the bowtie PhC. In plasmonic tweezers, the plasmonic material is the lossy media. Accordingly, the use of the bowtie PhCs enables both low-loss nanophotonic tweezers and rapid particle transport on-demand. Furthermore, this work describes the actuation of electrothermal flow by means of switching the wavelength of light coupled to the cascaded PhC cavities for the first time. This is only possible in high-Q PhC cavities because of the high-Q and the ability to couple light in-plane. Such multi-wavelength actuation of electrothermal flow is not possible in plasmonic structures which are characterized with large linewidths.

3.1.2 Architecture of the system

As shown in Figure 1, a PhC nanobeam with a bowtie defect at the center is placed beside a bus waveguide to enable evanescent coupling from the side. For multiplexed long-range nanoparticle transport and trapping across cavities, we design the system to contain ($n = 3$) engineered bowtie PhC nanobeams (BPCNs) cascaded along the bus waveguide, each having a specific resonance wavelength. Light is coupled into the device through the bus waveguide and then extremely localized in the bowtie defect. The figure illustrates that a fundamental TE mode with the wavelength of λ_1 is propagating in the bus waveguide and coupled to the middle BPCN (Λ_1), inducing the cavity resonance, and switching the cavity to the "ON" state. With a bus waveguide width of 480 nm and coupling gap of 150 nm, the loaded Q of the side-coupled BPCN is

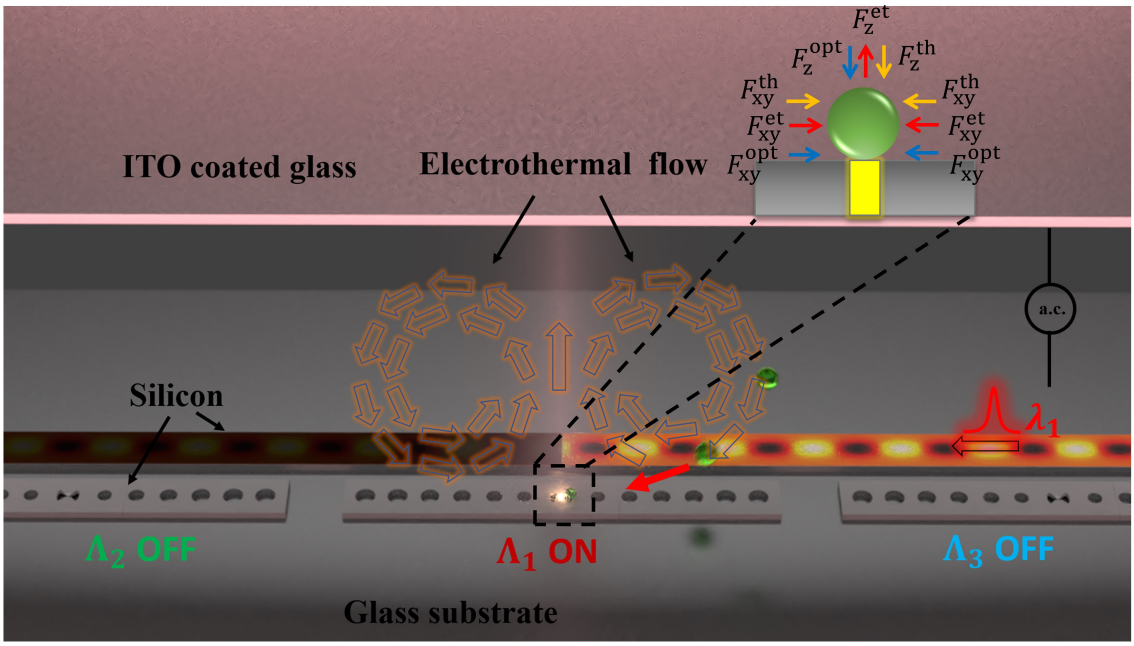

Figure 3.1: Schematic of the PhC-based multiplexed long-range electrohydrodynamic transport and trapping system. The inset shows the forces experienced by a particle trapped at the bowtie. Here "opt", "et" and "th" denote "optical force", "electrothermal force" and "thermophoretic force", respectively.

1.5×10^4 and the coupling efficiency [211] is 62% in a water environment. The peak electric field amplitude is 138 times higher in the bowtie compared to that of the light input into the bus waveguide, resulting in an electromagnetic field intensity enhancement of $\sim$ 19000. The electric field profile of the side-coupled BPCN is shown in Figure 3.2(a), where the extreme light localization at the center of the bowtie can be easily observed. To obtain different resonance wavelengths for the other two BPCNs, we slightly adjust the period of the PhC holes by -4 nm and +4 nm, respectively. Figure 3.2(b) shows the transmission spectra presenting the multi-resonant property of our system.

3.1.3 Optical characterization

Next, we characterize the optical trapping performance of the optimized BPCN system. An enhanced optical gradient trapping force requires a spatially confined electromagnetic field, which is provided by the bowtie gap. The time averaged optical force exerted on a nanoscale object is calculated by integrating the Maxwell's stress tensor (MST) [212] over an arbitrary surface enclosing the nanoscale object, which is given by

$$\langle \mathbf{F} \rangle = \oint_S \langle \overleftrightarrow{\mathbf{T}} \rangle \cdot d\mathbf{S}, \tag{3.1}$$

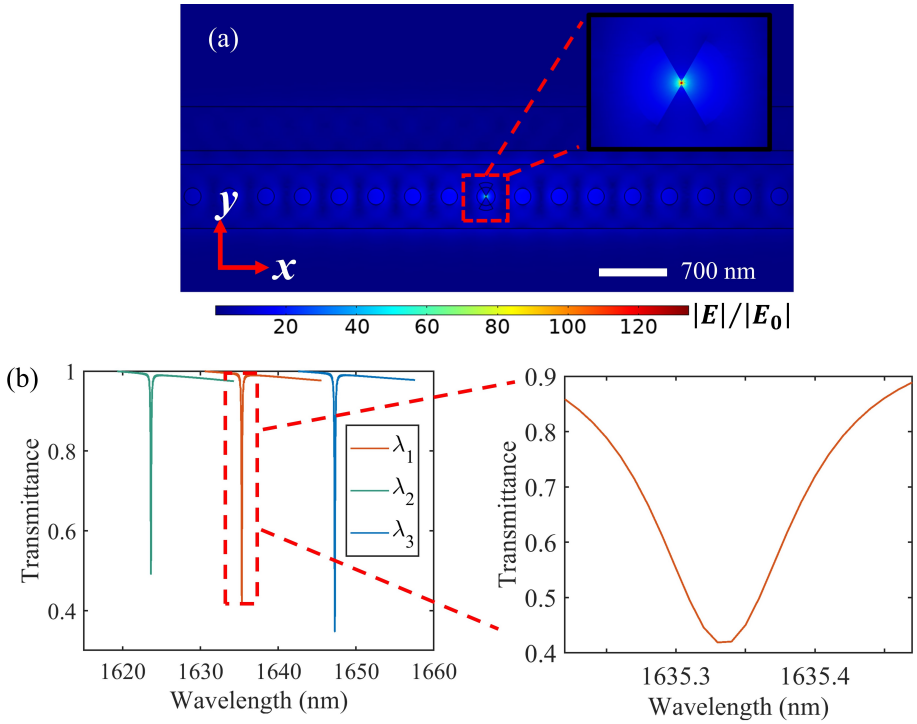

Figure 3.2: (a) Electric field enhancement distribution of the BPCN cavity on resonance in the absence of the particle. The field enhancement is calculated by normalization to the amplitude of the electric field of the input fundamental TE mode in the bus waveguide. Inset: Zoom-in view of the bowtie region. (b) Transmission spectra for the three BPCNs, demonstrating the multi-resonant property of the system. The resonant wavelengths are $\lambda_1 = 1635.33\text{nm}, \lambda_2 = 1623.65\text{nm}, \lambda_3 = 1647.28\text{nm}$.

where $\langle \overleftrightarrow{\mathbf{T}} \rangle$ is the time averaged Maxwell's stress tensor given by:

$$\langle \overleftrightarrow{\mathbf{T}} \rangle = \frac{1}{2}\,\mathrm{Re}\left[\varepsilon \mathbf{E}\mathbf{E}^* + \mu \mathbf{H}\mathbf{H}^* - \frac{1}{2}\left(\varepsilon|\mathbf{E}|^2 + \mu|\mathbf{H}|^2\right) I\right] \tag{3.2}$$

Here $\mathbf{E}\mathbf{E}^*$ and $\mathbf{H}\mathbf{H}^*$ are the outer products of the fields; I is the identity matrix; and ε and μ are the permittivity and the permeability of the medium surrounding the object, respectively. The effective transverse trapping potential resulting from the optical force is given by [213]

$$U(\mathbf{r}_0) = \int_{\infty}^{r_0} \mathbf{F}(\mathbf{r}) d\mathbf{r}. \tag{3.3}$$

Figure 3.3(a) illustrates the force spectra of a 10 nm diameter (D = 10 nm) PbSe quantum dot (refractive index n = 4.73 + 0.24i [214]) positioned 21 nm above the center of the bowtie surface, showing a strong pulling force along the z direction (0.44 pN/2.5mW). This trapping force is at least an order of magnitude higher than those achieved using Mie-resonant dielectric nanoantenna [215] and dielectric nanoantenna supporting anapole states [216]. Figure 3.3(b) to 3.3(d) show the trapping potentials as well as the corresponding trapping

forces when moving the quantum dot along the x, y and z directions, respectively. The depth of the trapping potential well is around 2 $k_{\mathrm{B}}T$/2.5mW for the x and y directions and 10 $k_{\mathrm{B}}T$/2.5mW for the z direction. Here k_{B} is the Boltzmann constant. This provides sufficient potential depth to stably confine the nanoparticle near the bowtie region.

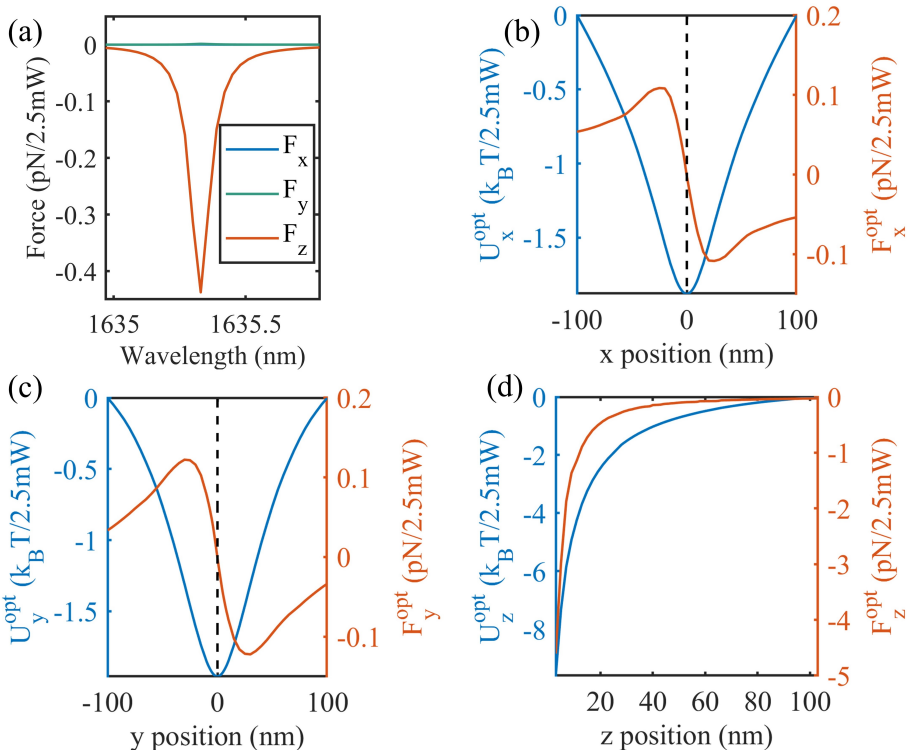

Figure 3.3: Optical trapping characterization for a 10 nm PbSe quantum dot placed 21 nm above the bowtie surface. (a) Trapping force spectra for the quantum dot. (b) – (d) Trapping potential as well as trapping forces when moving the quantum dot along the x, y and z directions, respectively. The vertical dashed lines in (b) and (c) denote the center of the bowtie.

Next, we explore the impact of the particle size and the vertical distance between the particle and the bowtie on the optical forces. We consider three different particle diameters (D = 5, 10, and 20 nm) for the quantum dot positioned at different distances (3, 9, 15, and 21 nm) from the bowtie surface. We choose these parameters for a comparison with a previously reported plasmonic nanoaperture [213]. Figure 3.4(a) shows the depth of the optical trapping potential well along the y direction (U_y^{opt}) with respect to F_y^{opt} and Figure 3.4(b) shows the maximum absolute value of the pulling force F_z^{opt} as a function of the distance z measured from the quantum dot bottom to the bowtie surface (shown in the inset), respectively. Given the stable trapping requirement of 10 $k_{\mathrm{B}}T$ for the trapping potential well, Figure 3.4(a) indicates that the minimum power required for stable trapping of the three particles considered along the y direction is around 17 mW, 3 mW and 0.7 mW, respectively, when z is 3 nm, which is less than a half of the power required by a plasmonic nanoaperture [213] taking into account the refractive index differences. Figure 3.4(b) shows that

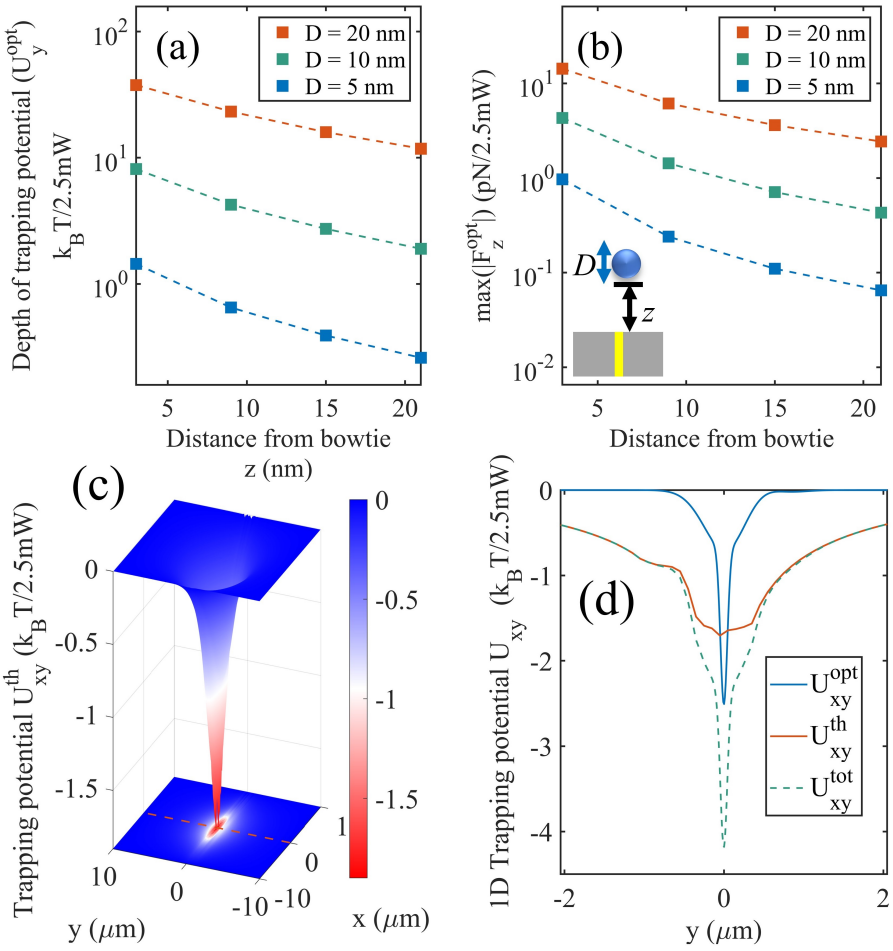

Figure 3.4: (a) Depth of the trapping potential well along the y direction (U_y^{opt}) due to F_y^{opt} and (b) the maximum absolute value of the pulling force F_z^{opt} at different distances z from the bowtie surface (shown in the inset of (b)). z is varied as 3, 9, 15, and 21 nm. Both y axes are in log scale. (c) Transverse thermophoretic trapping potential for a 10 nm quantum dot at z = 21 nm. (d) Transverse trapping potential for the optical trapping and thermophoretic trapping potentials along the y direction (red dash line in (c), z = 21 nm).

the maximum pulling force along the z direction is 0.97 pN/2.5mW, 4.31 pN/2.5mW and 14.30 pN/2.5mW for the three particles considered at the same distance (z = 3 nm). This pulling force drops exponentially as the particle moves away from the bowtie.

Optical power dissipated in the water layer near the bowtie establishes a thermal gradient. To calculate the temperature field distribution, the computed electric field distribution is used to determine the heat source density, which gives the heat dissipated per unit volume and is expressed as [217, 218]

$$q(\mathbf{r}) = \frac{1}{2}\,\mathrm{Re}\left[\mathbf{J}_d^*(\mathbf{r})\cdot\mathbf{E}(\mathbf{r})\right] = \frac{\omega}{2}\,\mathrm{Im}(\varepsilon)|\mathbf{E}(\mathbf{r})|^2, \tag{3.4}$$

where $\mathbf{J}_d = i\omega\mathbf{D}$ with $\mathbf{D} = \varepsilon\mathbf{E}$ is the displacement current density and ε is the permittivity of the specific

material. Since water is the only lossy material in this system, the power density dissipated into water serves as the source term in the heat diffusion equation for computation of the temperature around the BPCN as well as in the surrounding fluid and substrate. The temperature field in the system is determined by solving the steady-state heat equation given by

$$\nabla \cdot [-\kappa \nabla T(\mathbf{r}) + \rho c_p T(\mathbf{r}) \mathbf{u}(\mathbf{r})] = q(\mathbf{r}). \tag{3.5}$$

The first term on the left is the heat conduction term, while the second term is the convection term, which depends on the velocity of the fluid. $T(\mathbf{r})$ and $\mathbf{u}(\mathbf{r})$ are spatial temperature and fluid velocity field, respectively, and the material properties κ, ρ and c_p are thermal conductivity, density and specific heat capacity, respectively.

3.1.4 Effects of thermophoresis

Thermophoresis phenomenon [219, 220] is the motion of particles or molecules in the presence of thermal gradients and provides an attractive trapping force under negative thermophoresis [38, 221, 222]. To compare with the optical trapping, Figure 3.4(c) illustrates the simulated transverse thermophoretic trapping potential (U_{xy}^{th}) for 10 nm particle at $z = 21$ nm. The thermophoretic trapping potential has the same order of magnitude as the optical trapping potential shown in Figure 3, whereas the thermophoretic trapping potential well is much broader than the optical one. For emphasis, the transverse optical trapping and thermophoretic trapping potentials along the y axis are shown in Figure 3.4(d). The asymmetry of the thermophoretic trapping potential curve results from the bus waveguide which affects the heat diffusion. The superposition of the optical trapping and the thermophoretic trapping achieves a long range and 1.7 times deeper trapping potential well. In our system, the force that prevents particles from getting too close or stuck to the surface of the BPCN comes from the interaction between charged surfaces (surface of the particle and the BPCN) in liquid media, described by the DLVO theory [223].

3.1.5 Effects of electrothermal effects

Next, we demonstrate the long-range and rapid transport of individual nanoparticles to the vicinity of the bowtie for optical trapping by generating wavelength-dependent electrohydrodynamic microfluidic vortices based on the electrothermal flow effect in a microfluidic channel. The thermal gradient induced in the water layer near the bowtie results in a gradient in the permittivity and electrical conductivity of the water medium

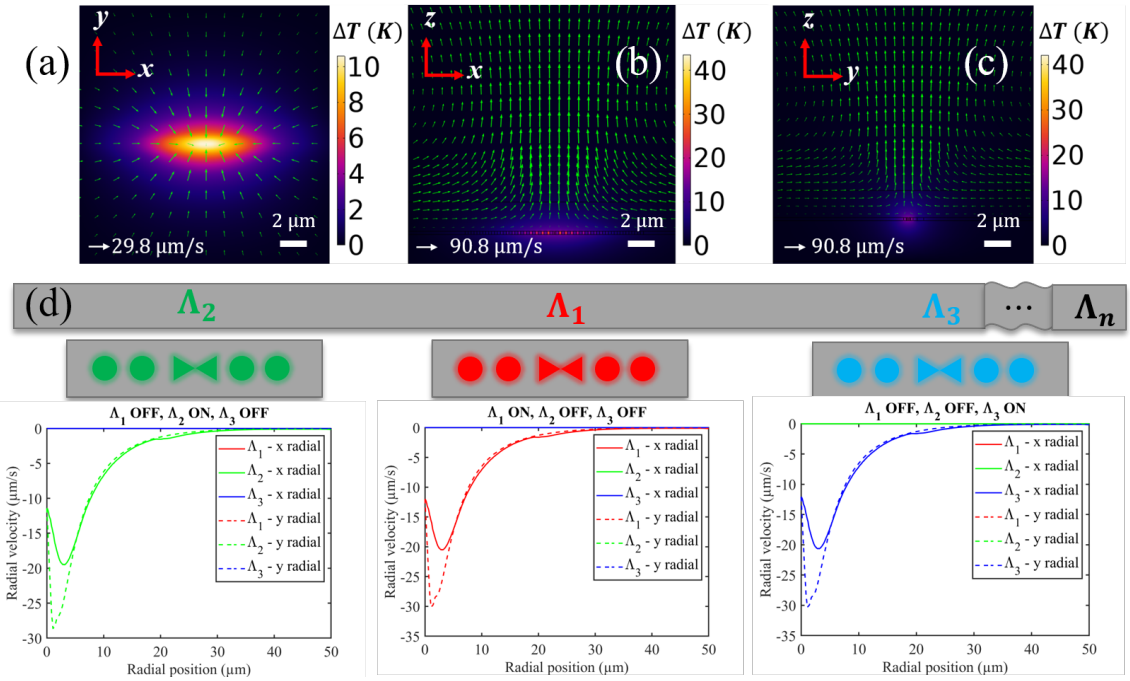

Figure 3.5: (a) Temperature field distribution of the *xy* plane 300 nm above the bowtie surface. The radial velocity vector plot of the electrothermal flow induced around the resonant BPCN is superimposed on the temperature profile. Arrow length represents the magnitude of the flow velocity. (b) Temperature field distribution of the *xz* plane and (c) the *yz* plane. (d) Illustration of three cascaded BPCNs placed beside a bus waveguide. The right three panels show corresponding radial velocity profiles of the induced electrothermal flow along *x* and *y* directions (300 nm above the bowtie surface) around the three BPCNs in different states. The electrothermal flow shows a long-range characteristic ($\sim 50\mu$m). (a) to (c) corresponds to the Λ_1 panel.

near the bowtie. An applied a.c. electric field acts on these gradients to create a volumetric body force in the fluid due to the electrothermal effect [84, 224].

By leveraging the configuration of the cascaded BPCNs, the body force of the electrothermal flow in our system is not only space dependent, but also *wavelength dependent*. That means the spatial distribution of the local temperature gradient can additionally be controlled by the wavelength of the input light, as shown in Figure 3.5(d). Following a perturbative expansion [84], the wavelength dependent time-averaged electrothermal body force per unit volume at a.c. frequency ω can be expressed as:

$$\langle F_{\mathrm{ET}} \rangle \hat{z} = \frac{1}{2}\varepsilon E_z^2 \left[\frac{\sigma^2 \varepsilon(\alpha - \gamma)}{\sigma^2 + \omega^2 \varepsilon^2} - \frac{1}{2}\alpha \right] \frac{\partial T(z,\lambda)}{\partial z} \hat{z}, \tag{3.6}$$

$$\langle F_{\mathrm{ET}} \rangle \hat{r} = -\frac{1}{4}\varepsilon \alpha E_z^2 \frac{\partial T(r,\lambda)}{\partial r} \hat{r}, \tag{3.7}$$

where $\lambda = \lambda_1, \lambda_2, \lambda_3 \ldots \lambda_n$ and n is the number of the cascaded BPCNs; ε, $\tau = \varepsilon/\sigma$, σ and ω are the fluid permittivity, charge relaxation time, electrical conductivity, and applied a.c. frequency, respectively; α and

γ are expressed as $\alpha = (1/\varepsilon)(\partial\varepsilon/\partial T)$, $\gamma = (1/\sigma)(\partial\sigma/\partial T)$ and are given as $-0.004\ \mathrm{K}^{-1}$ and $0.02\ \mathrm{K}^{-1}$, respectively [225]. Eq. 3.6 and Eq. 3.7 describe the axial and radial components of the electrothermal body force.

The velocity field distribution of the fluidic flow when a given BPCN is excited is determined from the solution of the incompressible Navier–Stokes equations given by

$$\rho_0(\mathbf{u}(\mathbf{r})\cdot\nabla)\mathbf{u}(\mathbf{r}) + \nabla p(\mathbf{r}) - \eta\nabla^2\mathbf{u}(\mathbf{r}) = \mathbf{F}, \tag{3.8}$$

$$\nabla\cdot\mathbf{u} = 0. \tag{3.9}$$

The forcing term $\mathbf{F}$ in Eq. 8 describes the body force per unit volume acting on the fluid element, which is given by Eq. 3.6 and Eq. 3.7. We note that the contribution from the buoyancy-driven convection is negligible in this system.

Figure 3.5(a) shows the temperature field distribution in the *xy* plane 300 nm above the bowtie surface. A temperature rise of 10.6 K is observed and the superimposed radial velocity vector plot of the flow shows that the induced electrothermal flow is directed radially inwards towards the thermal hotspot generated by water around the bowtie and serves as a powerful means to deliver suspended particles to the bowtie region. The maximum radial flow velocity is about 29.8 μm/s, which is directed to the bowtie and hence much more efficient than traditional particle delivery methods such as pressure-driven flow and slow Brownian motion. Furthermore, this flow velocity is at least 20 times greater than the 1 μm/s thermoplasmonic convection flow velocity achievable with an array of optimized plasmonic bowtie nanoantenna [73]. Figure 3.5(b) and (c) show the temperature profile in the *xz* and the *yz* plane. The maximum temperature rise is 43.6 K under only 2.5 mW input power due to the high field enhancement. The superimposed velocity vectors verify the induced electrothermal vortex flow shown in Figure 3.1. We note here that the maximum Stokes drag force along the z direction exerted on the particles (10 nm quantum dot for example) from the electrothermal flow is estimated to be far below the order of magnitude of the optical gradient force shown in Figure 3(a) (e.g., 0.0076 pN drag force for the 10 nm quantum dot). Therefore, the electrothermal flow mainly assists in transporting the particles to the vicinity of the BPCN.

Figure 3.5(d) demonstrates the concept of multiplexed nanoparticle transport and nano-optical trapping with the cascaded BPCNs shown in Figure 3.1. When the input wavelength is tuned to λ_1, only the middle BPCN (Λ_1) with a resonance wavelength of λ_1 is excited while the other two are off resonance and not excited. Therefore, the electrothermal flow is only induced around Λ_1 (see the radial velocity plot in the middle panel). By integrating over the radial velocity curve when Λ_2 is on, we estimate that it takes about 8 seconds

for the flow to transport a nanoparticle 25 μm from the vicinity of Λ_1 to Λ_2. The high Q characteristic of the bowtie PhC permits to integrate multiple BPCNs along the low-loss bus waveguide to provide the means to achieve long range particle hand-off from tens of microns to millimeter scale distances by simply switching the wavelength of the input light. We note that the electrothermal flow along the y direction shows a larger magnitude of velocity in comparison to the electrothermal flow along the x direction. This is attributed to the asymmetric spatial distribution of the in-plane thermal hotspots. It is evident that there is a higher temperature gradient along the y direction and hence a stronger electrothermal flow velocity in comparison to that along the x direction. The slightly different radial velocity values presented in the three panels are attributed to the different electric field enhancements of the three BPCNs.

3.1.6 Conclusion

We have proposed and systematically studied a cascaded bowtie photonic crystal nanobeam system that can achieve multiplexed long-range electrohydrodynamic transport and optical trapping of nanoscale particles. Compared with traditional 1D photonic crystal nanobeams, our bowtie photonic crystal cavity can more strongly confine and enhance the electromagnetic field while maintaining a high quality factor. The extremely localized field provides a strong field gradient that is ideal for trapping sub-20 nm particles. Furthermore, the localized water absorption near the cavities serves as heat sources to generate negative thermophoresis that can assist in the optical trapping process. Finally, we harness the localized water absorption to induce on-demand electrothermal flow that can efficiently transport nanoparticles to the vicinity of the localized field of the bowtie photonic crystal cavity region for enhanced optical trapping. Our proposed multiplexed platform could enable millimeter scale transport and hand-off of particles across cavities in miniaturized optofluidic chips by simply switching the wavelength. We envision that our system will be a promising platform in many fields of biology and quantum information, such as in single molecule characterization and assembly of single photon sources.

3.1.7 Appendix

3.1.7.1 Optimal design of bowtie photonic crystal

Our prior work has experimentally demonstrated that bowtie photonic crystal nanobeams can support extreme light localization into a deep sub-wavelength region, i.e., to the bowtie [2, 206]. In this work, we present the design of silicon-on-insulator bowtie photonic crystal (PhC) nanobeams optimized for a water immersion environment for nanoparticle trapping applications. In particular, we designed a side-coupled 1D bowtie PhC

nanobeam with high quality factor (Q), low mode volume, and large electric field enhancement in the bowtie where optical trapping will take place. In this section, we demonstrate the detailed optimization process for the bowtie PhC nanobeam. The following numerical simulations are carried out in Lumerical FDTD Solutions (Ansys Lumerical 2021 R2.1).

We chose a mixed unit cell design [226] comprising circular air holes for the mirror and taper regions of the nanobeam and a single bowtie unit cell in the center of the cavity, as shown in Figure 3.6. The height of the nanobeam and the bus waveguide is 220 nm. This design minimizes the fabrication complexity but maintains the advantages of the low mode volume of the bowtie and the high Q of the PhC nanobeam. Following the mix and match design approach [226], we began with a high Q, air mode PhC nanobeam design with all circular unit cells; our initial design follows from that of Kim et al. [227], with a period of 560 nm, air holes with radii tapering quadratically from 200 nm for the mirror unit cells to 174 nm for the central cavity unit cell. Ten mirror unit cells and twenty-two taper unit cells were included on each side of the central bowtie. A $Q \sim 1.5 \times 10^4$ in a water environment was calculated using the built-in Q analysis monitor in Lumerical FDTD Solutions, employing a mesh quality of 3 for the auto non-uniform meshing option. We next replaced the central cavity circular unit cell with a bowtie-shaped unit cell of the same radius and unit cell width. Due to the difference in fill factor and mode profile supported in the bowtie unit cell and surrounding circular unit cells, scattering losses reduced the Q of the bowtie PhC nanobeam cavity by more than 30% (see Table 3.1). We note that a mesh of 15 nm was added around the smallest features of the bowtie for this simulation to ensure sufficient resolution of the bowtie feature. To recover a higher Q, we carried out a gradient optimization based on the Barzilai-Borwein method [228] to adjust the period and radii of the unit cells, using Q as the figure of merit. Gradient optimization was selected as the design optimization approach due to its computational efficiency and ease of achieving a design space of mixed unit cell PhCs that is well-behaved [226]. After optimization, the air mode bowtie PhC nanobeam cavity achieved a $Q \sim 2.4 \times 10^4$ in water; the optimized design has a period of 400 nm, air holes with radii quadratically tapering from 115 nm for the mirror unit cells to 90 nm for the taper unit cell adjacent to the bowtie, and a bowtie radius of 100 nm. The width of the nanobeam is 700 nm.

Finally, a bus waveguide was added to facilitate evanescent wave side-coupling of light into the bowtie cavity. We note that side-coupled PhCs are more appropriate than in-line coupled PhCs for optical trapping applications because, in the case of in-line PhC nanobeams, light must couple through the mirror sections of the nanobeam, which often results in low transmission intensity at the resonance wavelength and does not facilitate multiplexed operation. In order to maximize the optical intensity at the bowtie cavity region, a state-space overlap approach was utilized to efficiently couple light from the bus waveguide into the bowtie PhC cavity [211]. The bus waveguide width was adjusted such that the wavevector of light in the bus waveguide

matched the wavevector of light in the 1D bowtie PhC nanobeam (without the bus waveguide present) at the resonance wavelength. Then, three-dimensional full-field simulations were carried out to determine the loaded Q of the side-coupled 1D bowtie PhC nanobeam as a function of the coupling gap between the bus waveguide and the nanobeam. PML boundary conditions are applied in x, y, and z directions, and the source is set as a mode source with Fundamental TE Mode selected. With a bus waveguide width of 480 nm and a coupling gap of 150 nm, the loaded Q of the side-coupled 1D bowtie PhC nanobeam is 1.5×10^4 in a water environment. The peak electric field amplitude is 138 times higher in the bowtie compared to that of the light input into the bus waveguide, resulting in an electromagnetic field intensity enhancement of ~ 19000.

Table 3.1 compares the Q and mode volume of the 1D PhC at the various stages of the design process. Using Eq. 3.10 (see Ref. [211]), we estimate a coupling efficiency of 62%, where Q_0 is the intrinsic quality factor of the 1D bowtie PhC nanobeam cavity and Q_L is the loaded quality factor of the side-coupled 1D bowtie PhC nanobeam cavity.

$$\text{Coupling efficiency} = \frac{2\left(\frac{Q_0}{Q_L}-1\right)+\left(\frac{Q_0}{Q_L}-1\right)^2}{\left(\frac{Q_0}{Q_L}\right)^2} \tag{3.10}$$

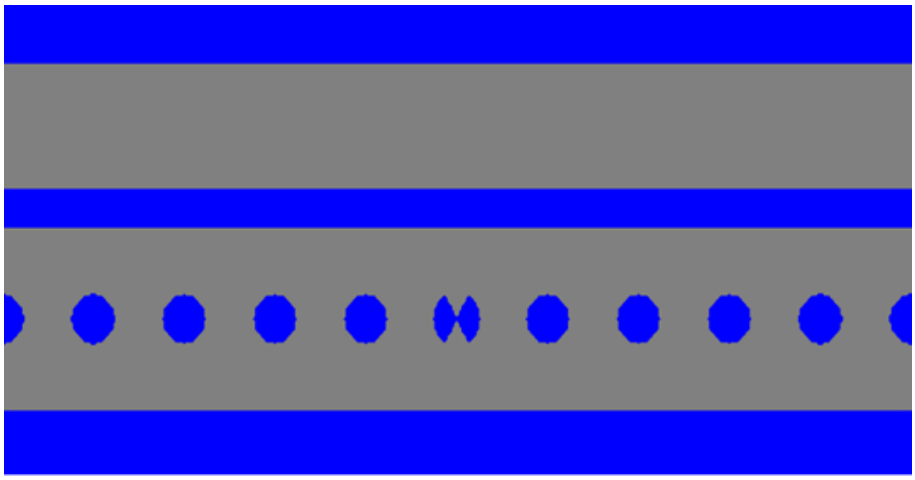

Figure 3.6: Dielectric profile of the side-coupled 1D bowtie PhC nanobeam cavity (gray = silicon, blue = water). The height of the nanobeam and the bus waveguide is 220 nm.

3.1.7.2 Additional discussions on optical forces

3.1.7.2.1 Point-dipole approximation vs. MST

As has been demonstrated, the optical gradient force is proportional to the particle volume [229–231]

$$\mathbf{F}^{\text{opt}}_{\text{grad}}(\mathbf{r}) = \pi\varepsilon_e a^3 \frac{\varepsilon_p - \varepsilon_e}{\varepsilon_p + 2\varepsilon_e} \nabla|\mathbf{E}(\mathbf{r})|^2 \tag{3.11}$$

	PhC nanobeam without bowtie	PhC nanobeam with bowtie	Optimized PhCnanobeam with bowtie	Optimized PhC nanobeam with bowtie and side-coupler
Quality factor	1.5×10^4	1.03×10^4	2.44×10^4	1.5×10^4
Mode volume $(\lambda/n)^3$	0.8	7.1×10^{-3}	6.6×10^{-3}	6.7×10^{-3}

Table 3.1: Quality factor and mode volume metrics at various stages of the design process for the side-coupled 1D bowtie PhC nanobeam cavity. Note that the quality factor for the side-coupled bowtie PhC nanobeam is the loaded quality factor; all other quality factors are intrinsic.

where ε_p and ε_e are the permitivity of the particle and the environment, respectively; a is the diamater of the particle. This expression arises from the point-dipole approximation when the particle size is much smaller than the wavelength (particle radius $a \ll \lambda$, i.e., Rayleigh particles). Optical gradient forces calculated from the point-dipole approximation method were obtained by inserting Eq. 3.11 into COMSOL before performing the optical full-field simulations. Figure 3.7(a) shows the comparison between the MST method and the point-dipole approximation method. Close agreement between the two approaches remains even for the 20 nm particle (the largest particle) at z = 3 nm (the lowest position in z direction considered in this work), indicating that the perturbation from trapped particles is trivial in this system and the optical gradient force is much larger than the optical scattering force. This can be verified by the negligible resonance shift (0.01 nm, equivalent to the wavelength sweep step, while $\sim$ 0.1 nm for the cavity linewidth) before and after trapping the 20 nm quantum dot at z = 3 nm, shown in Figure 3.7(b). The reason for the negligible perturbation is attributed to the modeled small gap size and the low penetration of the electric field from the bowtie, which is tightly confined in the cavity. As a further investigation, here we also simulate the trapping of a 5 nm quantum dot in a 10 nm bowtie gap. The transmission spectrum is shown in Figure 3.7(e) before and after the quantum dot is trapped. The resonance shift caused by trapping the quantum dot is almost negligible (0.01 nm red-shift, equivalent to the wavelength sweep step). This is because the quantum dot is very small (5 nm) compared to the bowtie gap (10 nm wide, 220 nm high).

3.1.7.2.2 Negligible optical scattering force

Based on the point-dipole approximation method, the optical scattering force on a Rayleigh particle is expressed as [229, 231]

$$\mathbf{F}_{\text{scat}}^{\text{opt}}(\mathbf{r}) = \frac{128\pi^5 a^6}{3\lambda^4 c}\left(\frac{\varepsilon_{\text{p}} - \varepsilon_{\text{e}}}{\varepsilon_{\text{p}} + 2\varepsilon_{\text{e}}}\right)^2 \mathbf{S}(\mathbf{r}), \tag{3.12}$$

where ε_p and ε_e are the permittivity of the particle and the environment, respectively; a is the radius of the particle; $\mathbf{S}(\mathbf{r})$ is the time-averaged Poynting vector defined as $\frac{1}{2}\text{Re}[E \times H^*]$. By inserting Eq. 3.12 into

COMSOL before performing the optical full-field simulations, the optical scattering forces were computed. As an example, the maximum absolute value of the z component of the optical scattering force $\left(\max\left(\left|F_z^{\text{scat}}\right|\right)\right.$) on a 20 nm diameter PbSe quantum dot is $6.27\times10^{-5}, 5.36\times10^{-5}, 4.86\times10^{-5}$, and 4.60×10^{-5}fN at $3, 9, 15$, and 21 nm from the PhC surface, respectively. The calculation results show that the scattering force is eight orders of magnitude smaller than the optical gradient forces, which can be neglected when considering the optical trapping.

3.1.7.2.3 Skin depth of the photonic crystal cavity

We have stated that the penetration of the electric field from the bowtie PhC cavity is short-range. Figures 3.7(c) and 3.7(d) verify that the skin depth of the electric field (defined as the electric field enhancement drops to $1/e$ of the peak value) is only 8 nm, validating the tight confinement of the electric field in the cavity.

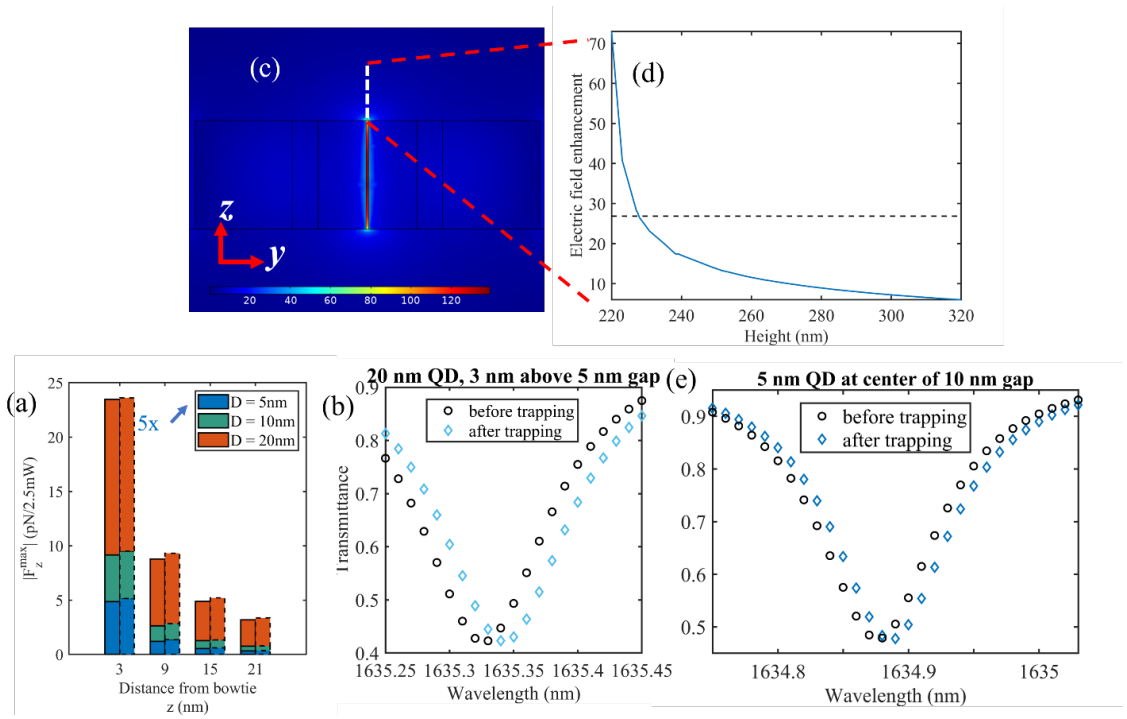

Figure 3.7: (a) The maximum absolute value of the pulling force F_z calculated for cases in Figure 4 (b) of the main text using the comprehensive MST method (solid line) and the point-dipole approximation method (dash line). Values for 5 nm particle (blue) are magnified by a factor of 5 . (b) Transmittance spectra before (black circle) and after (blue diamond) trapping the 20 nm quantum dot at $z = 3$ nm. (c) Electric field enhancement distribution of the yz plane when the bowtie PhC nanobeam is on resonance. (d) Electric field enhancement distribution along the white dash line in (c). The black dash line denotes $1/$ e of the peak electric field enhancement value. (e) Transmittance spectra before (black circle) and after (blue diamond) trapping a 5 nm quantum dot in a 10 nm gap. The quantum is located at the center of the gap. This comparison is intended to study the effect when the particle goes into the gap.

3.1.7.3 Negative thermophoretic trapping characterization

3.1.7.3.1 Expression of the Thermophoretic Force

Thermophoresis phenomenon is the motion of particles or molecules in the presence of thermal gradients. It is important to recognize that the presence of the hotspots due to water absorption can also result in a thermophoretic force on the nanoscale objects. The thermophoretic force is expressed as [232, 233]

$$\mathbf{F}^{\mathrm{th}} = -k_{\mathrm{B}} S_{\mathrm{T}} T \nabla T, \tag{3.13}$$

where T is the temperature, and S_T is the Soret coefficient with $S_T = D_T/D_0$. Here D_0 is the Brownian diffusion coefficient and D_T is the thermophoretic mobility. S_{T} is expressed as [234]

$$S_{\mathrm{T}} = -\frac{2\pi R\varepsilon}{k_{\mathrm{B}}T^2}\frac{2\kappa_l}{2\kappa_l+\kappa_p}\left(1+\frac{\partial \ln \varepsilon}{\partial \ln T}\right)\zeta^2, \tag{3.14}$$

for small particles. Here, η is the solvent viscosity and R is the radius of the particle; ε is the solvent permittivity, which is considered to be the permittivity of water at the applied a.c. frequency; ζ is the zeta potential of the particle; κ_l and κ_p are thermal conductivities of the solvent and the particle, respectively. In bulk water, the differential permittivity change with temperature is $\frac{\partial \ln \varepsilon}{\partial \ln T} = -1.4$ at room temperature. According to previous reports [39, 235], the Soret coefficient S_T needs to be modified for particles near a solid-state substrate due to the induced hydrodynamic boundary effect. The enhancement factor is

$$\beta = \frac{1-\frac{1}{2}\frac{1}{(1+\hat{h})^3}}{1-\frac{9}{8}\frac{1}{1+\hat{h}}+\frac{1}{2}\frac{1}{(1+\hat{h})^3}} \quad (\hat{h}>1), \tag{3.15}$$

where $\hat{h} = h/R$ and h is the particle-surface distance. Here, by considering a 10 nm particle at $z = 21$ nm, the enhancement factor $\beta = 1.3$.

It is important to note that inside an electric double layer (EDL), the value of $\frac{\partial \ln \varepsilon}{\partial \ln T}$ can reach +2.4 by adding ionic surfactants to the solution [222, 236] which may be harnessed to induce a negative thermophoresis behavior. In our tweezer system, the negative thermophoretic force can be leveraged to assist pulling particles to the vicinity of the bowtie for optical trapping.

3.1.7.3.2 Thermophoretic force simulations

The thermophoretic forces were solved by inserting Eq. 3.13 - 3.15 into the Multiphysics model. Values of relative parameters were set as follows. Dynamic viscosity of water: 8.9×10^{-4} Pa$\cdot$s; thermal conductivity of the PbSe quantum dot [235] : 1.1 W$/$(m$\cdot$K); Zeta potential of the PbSe quantum dot [237]: -44mV. The

temperature gradient was obtained from the Heat Transfer in Solids study.

3.1.7.3.3 Range of the thermophoretic force

The thermophoretic force has a shallower and wider trapping potential well and thus has a longer range in comparison to the optical trapping force. This long-range characteristic results from the heat diffusion process that induces the temperature gradient. The distribution of the negative thermophoretic force 300 nm above the PhC surface is shown in Figure 3.8(a). The arrows show that the negative thermophoretic force is pointing towards the bowtie even at micrometer scale, much longer than the range of the optical trapping forces. Figure 3.8(b) shows the thermophoretic trapping potential along z axis. The magnitude of the potential U_z^{th} decreases to half of the maxima at 420 nm above the bowtie while the optical trapping potential U_z^{opt} drops to half of the peak value only less than 10 nm away from the bowtie. Figure 3.8(c) illustrates the depth of the transverse thermophoretic trapping potential well $\left(U_{xy}^{\text{th}}\right)$ at different heights from the bowtie. The depth of the transverse potential well decreases even more slowly and reaches half of the maxima at 900 nm above the PhC surface.

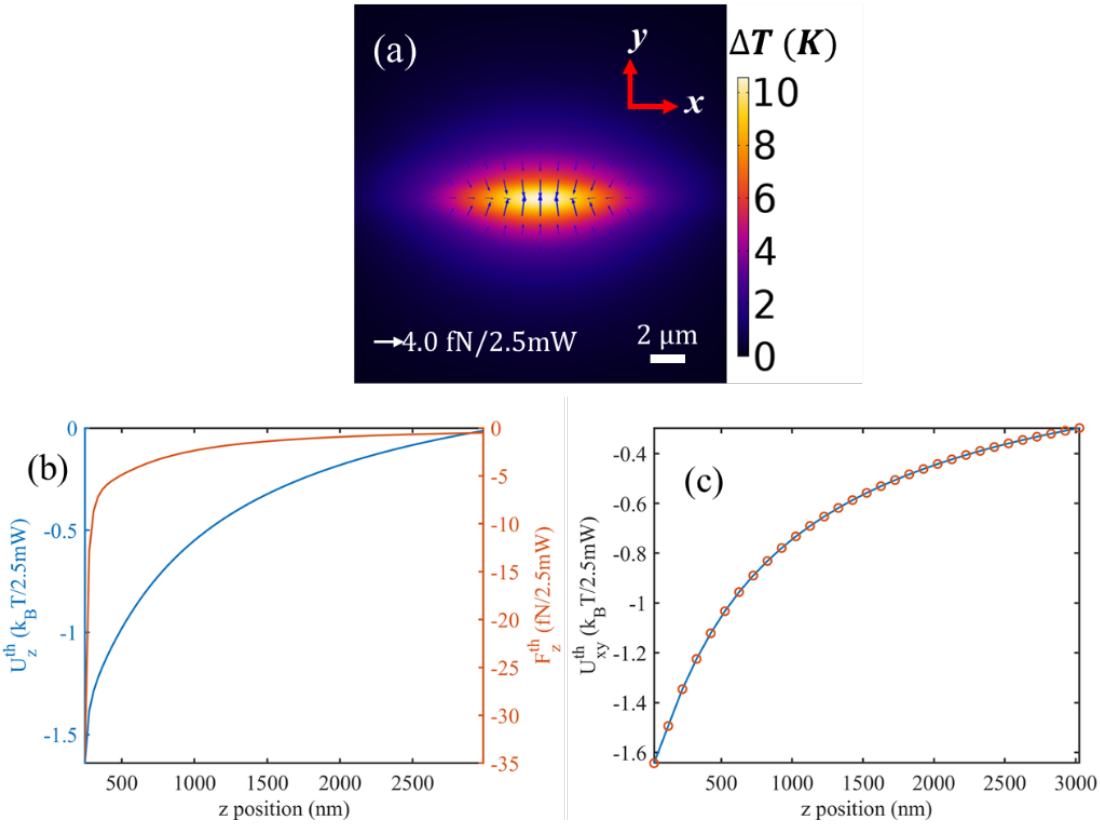

Figure 3.8: (a) Negative thermophoretic force distribution superimposed on the temperature field distribution of the xy plane 300 nm above the bowtie. (b) Thermophoretic trapping potential as well as trapping force when moving the quantum dot along the z axis. (c) Depth of the transverse thermophoretic trapping potential well for the quantum dot at different heights. The diameter of the quantum dot is 10 nm.

3.1.7.4 DLVO theory

The force that prevents particle from getting too close or stuck to the surface of the bowtie photonic crystal (BPC) comes from the interaction between charged surfaces (surface of the particle and the BPC) in liquid media. The theory describes this mechanism is the DLVO theory, named after Derjaguin, Landau, Verwey and Overbeek. Following the methods described in Ref. [223], the interaction potential comprises an attractive van der Waals contribution V_{ydW} and repulsive electrostatic contribution, $\mathrm{V_{ED}}$, due to electric double layer forces:

$$V(d,c_0) = V_{\mathrm{ED}}(d,c_0) + V_{\mathrm{vdW}}(d), \tag{3.16}$$

where d denotes the distance of the surfaces and c_0 the electrolyte concentration in the liquid. The electrostatic potential between a spherical particle and a plane surface is [238]:

$$V_{\mathrm{E}}(d,c_0) \approx 64\pi\varepsilon R \left(\frac{k_{\mathrm{B}}T}{e}\right)^2 \tanh^2\left(\frac{e\zeta}{4k_{\mathrm{B}}T}\right) \mathrm{e}^{-d/\lambda_{\mathrm{D}}}, \tag{3.17}$$

where $\varepsilon = 80\varepsilon_0$ is the dielectric constant of water, e the elementary charge, ζ the zeta potential and $\lambda_D = \sqrt{\varepsilon k_{\mathrm{B}}T/(2N_{\mathrm{A}}e^2c_0)}$ the Debye length with the Avogadro constant NA for ion valence = 1. Note that the concentration c_0 enters Eq. 3.17 via the Debye length λ_D. The van der Waals potential between a spherical particle and a plane surface is [239]

$$V_{\mathrm{VdW}}(d) = -\frac{A_{\mathrm{H}}}{6}\left(\frac{R}{d} + \frac{R}{2R+d} + \ln\left(\frac{d}{2R+d}\right)\right), \tag{3.18}$$

where A_H is the Hamaker constant.

The parameters we use for calculating the DLVO curve are particle radius $R = 10$ nm, zeta potential of substrate surface [240] $\zeta = -30\mathrm{mV}, \mathrm{c_0} = 5\mathrm{mM}$ (below the critical micelle concentration of the surfactant sodium dodecylsulfate (SDS) [28]), Hamaker constant of $A_{\mathrm{H}} = 6.2 \cdot 10^{-20}$ J [241]. The ion valence of SDS is considered to be 1 [242]. The total potential for the quantum dot particle as a function of the distance d to the BPC surface is shown in Figure 3.9, overlapping with the optical gradient force. It can be found that the attractive optical gradient force is always larger than the repulsive force generated from the DLVO potential when d is larger than 3 nm, guaranteeing a trapping behavior along the z direction besides the negative thermophoretic force.

In experiments, we will functionalize the structure surface with charged polymer colloids. The trapped particles under equilibrium would experience a balance of van der Waal's force and electrostatic repulsion. Those forces will prevent a particle from getting too close or stuck to (a few nanometers depending on how we tune the solution parameters such as concentrations, ion species, etc.) the surface. It is for this reason that

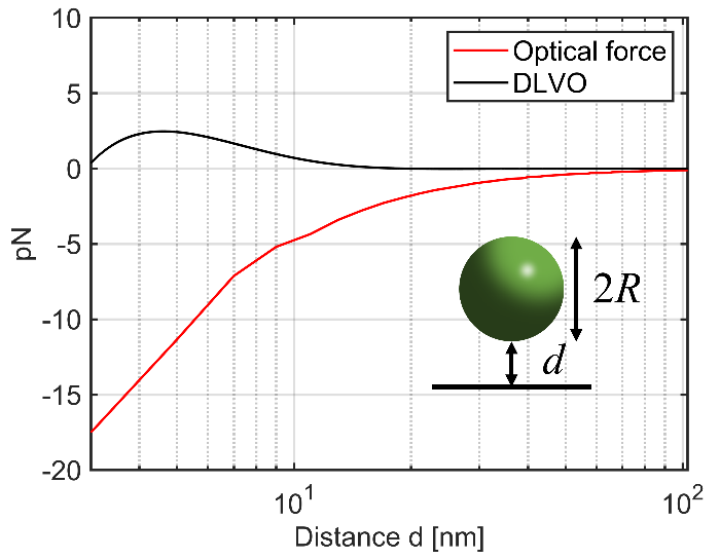

Figure 3.9: Comparison of the force generated from the DLVO potential and the optical gradient force for a 20 nm quantum dot.

we considered the particle to be at least 3 nm above the surface in the main text to count for the background DLVO force. The relative equilibrium position of the DLVO force (i.e., the secondary minimum in the DLVO part of the potential [223]) can be tuned by tuning the surface properties of the structure.

3.1.8 Experiment

In order to validate the functions of our proposed BPCN nanotweezer system, we fabricated the sample and built a measurement setup from scratch. Figure 3.10(c) shows the measured spectra of a set of three cascaded BPCNs exposed in air enviroment. From the images gathered by the near infread camera in 3.10(a) and (b), we can clearly judge the mode profiles of the excited resonances at the center of each BPCN.

As shown in Figure 3.11, the experimental configuration includes a tunable fiber laser with a tuning range of 1500 – 1630 nm. Its signal is amplified via an Erbium-Doped Fiber Amplifier (EDFA) and then polarized by a paddle polarizer. The output from the tapered fiber is coulpled to the end face of a bus waveguide. This tapered fiber is affixed to a translation stage to ease the coupling process. The optofluidic chip is placed on a XYZ translation stage below a home-built upright fluorescent microscope. The emission from the fluorophore-labeled polystyrene beads enters a Charge Coupled Device (CCD) camera after reflected by a beam splitter for imaging.The near infrared signal enters a Short-wave Infrared imaging (SWIR) camera after passing through the same beam splitter for imaging, which assists the fiber-to-waveguide coupling process. For better imaging the chip, all the fluorescent filters are designed as pluggable.

The uncertainties in fabrication leaded to many bowtie gaps unopened. Due to the low loss of water ($\kappa =$

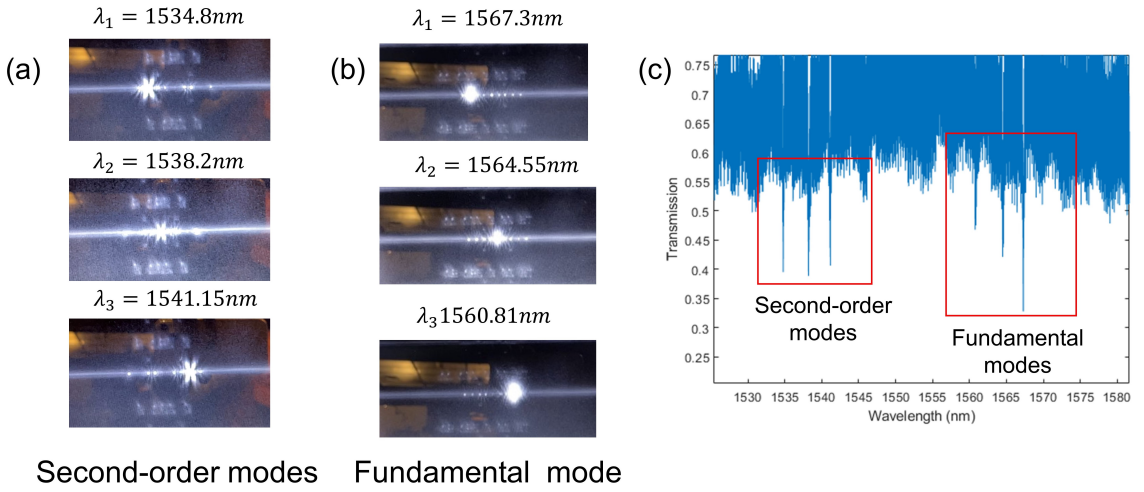

Figure 3.10: (a) Photos of profiles for the second-order modes of the three cascaded BPCNs, respectively. (b) Photos of profiles for the first-order modes of the three cascaded BPCNs, respectively. (c) Measured spectra when coupling light into the bus waveguide. Copyright © 2023 Yanrong Zhang

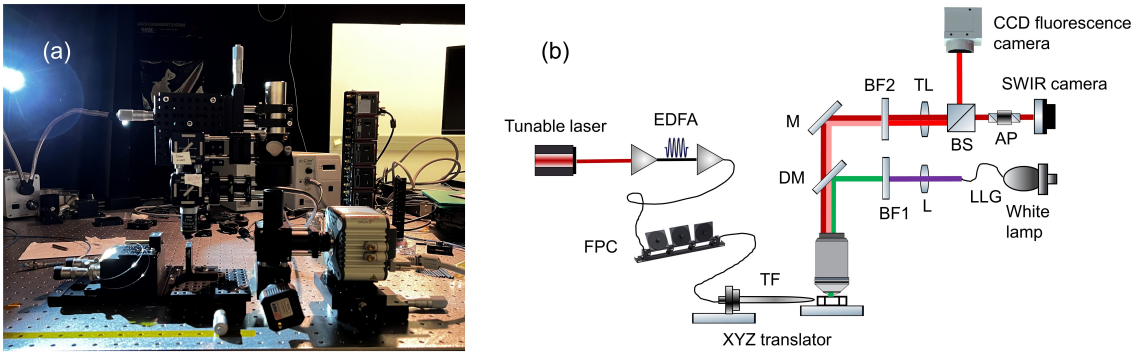

Figure 3.11: (a)Photo of the experiment set up. (b) EDFA, Erbium-doped fiber amplifier used to amplify the power of the input laser; FPC, paddle fiber polarization controller;TF, tapered fiber; L, convex lenses; TL; 200 mm tube lens; M, reflective mirror; DM, dichroic mirror; BS, beam spliter; AP, adjustable pinhole; LLG, liquid light guide; BF1 and BF2, bandpass filters used to filter light used for excitation of the fluorescent particles and light transmitted for imaging on the camera, respectively. Filtered fluorescent illumination is passed through the objective lens (10x or 40x) and focused on the sample.

0.00013), we need to choose BPCNs with opened bowtie gaps so that the interaction between the surrounded water media and the confined and enhanced light field is strong enough. The scanning electron microscope (SEM) image in Figure 3.12(a) presents a typical BPCN we used for experiments. In order to introduce the ET flow, we need to cover the BPCN samples with a conduction layer. One solution is to deposite a thin graphene layer, which will not affect the resonances of the cavities. As an initial demonstration, we chose to only include the negative thermophoresis effect, or thermoelectric effects, to transport particles within a range of $\sim 20\ \mu$m and optically trap a single particle at the bowtie gap.

As depicted in Figure 3.12(b), we did observe a tendency for particles to gravitate towards the gap in

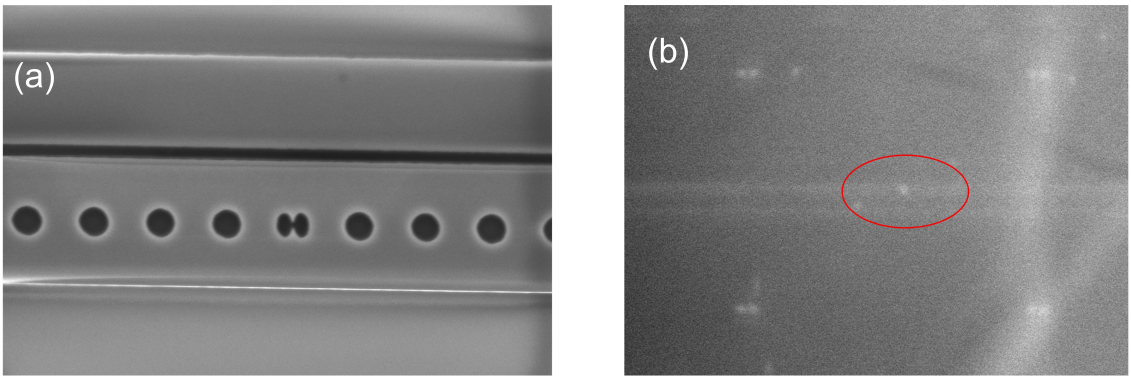

Figure 3.12: (a) Representative SEM image of a BPCN with the bowtie gap opened. Copyright © 2023 Yanrong Zhang (b) Particles were observed to prefer to move around the bowtie gap on resonance, while the gravitation was not sufficient.

the bowtie. However, the thermophoretic force wasn't as strong as anticipated, and we were also unable to observe the optical trapping of a single nanoparticle. After running experiments that involved increasing the input laser power to the tens of milliwatt (mW) range, we attributed these discrepancies to a couple of potential causes: (1) The repeated usage of the samples, had led to significant degradation to the samples, particularly the tips of those bowtie gaps; (2) Given that our current setup does not permit the evaluation or measurement of the power channeled into the bus waveguide and subsequently into the BPCN, it's possible that the actual light power confined in the bowtie cavity is insufficient. We will persist in our investigations and efforts to resolve these issues.

CHAPTER 4

Optofluidic transport and assembly of nanoparticles using an all-dielectric quasi-BIC metasurface

Manipulating fluids by light at the nanoscale has been a long-sought-after goal for lab-on-a-chip applications. Plasmonic heating has been demonstrated to control microfluidic dynamics due to the enhanced and confined light absorption from the intrinsic losses of metals. Dielectrics, the counterpart of metals, has been used to avoid undesired thermal effects due to its negligible light absorption. In this chapter, I report an innovative optofluidic system that leverages a quasi-BIC-driven all-dielectric metasurface to achieve nanoscale control of temperature and fluid motion. The experiments show that suspended particles down to 200 nanometers can be rapidly aggregated to the center of the illuminated metasurface with a velocity of tens of micrometers per second, and up to millimeter-scale particle transport is demonstrated. The strong electromagnetic field enhancement of the quasi-BIC resonance increases the flow velocity up to three times compared with the off-resonant situation. Experimentally investigations are made to study the dynamics of particle aggregation with respect to laser wavelength and power. A physical model is presented and simulated to elucidate the phenomena and surfactants are added to the nanoparticle colloid to validate the model. Studies in this chapter demonstrate the application of the recently emerged all-dielectric thermonanophotonics in dealing with functional liquids and opens new frontiers in harnessing non-plasmonic nanophotonics to manipulate microfluidic dynamics. Moreover, the synergistic effects of optofluidics and high-Q all-dielectric nanostructures hold enormous potential in high-sensitivity biosensing applications.

4.1 Introduction

Yang, Sen, at al. "Optofluidic transport and particle trapping using an all-dielectric quasi-BICmetasurface", under reviewed in Light: Science & Applications (2023)

Controlling the long-range transport of fluids has been a fundamental requirement in microfluidic systems, from standard flow cell assays to lab-on-a-chip devices. Traditionally, pressure-driven control techniques and syringe pumps have been widely used in microfluidics [243]. The evident scale mismatch between the microfluidic system and the bulky control system has inspired significant efforts to develop integrated micrometer scale control techniques [244]. Among them, one promising approach to achieve integrated control of particle and fluid motion is to use light to control the flow of fluids, particularly at the micrometer scale, i.e., optofluidics [245]. The buoyancy-driven toroidal convection generated by heating the water with a laser beam can help transport and concentrate particles, but the flexibility to control the convection flow is limited [246, 247]. One solution to achieve fluid manipulation is to use localized thermal gradients induced

by light illumination3.

Metal nanostructures, when illuminated by light at their plasmonic resonance, can tightly confine the energy to sub-wavelength scales in the vicinity of the nanostructures. The enhanced light absorption from the intrinsic (Ohmic) losses of metals has been considered as side effects such as limited quality factor (Q) [248], and reduced trapping stability in plasmonic nanotweezers due to undesired thermal heating effects [249]. Recently, however, scientists have realized that this enhanced light absorption can efficiently turn metal nanostructures into nanosources of heat, inspiring the study of thermoplasmonics [75, 75, 76]. This finding has found numerous applications in nanotechnology, namely, for photothermal cancer therapy [77], targeted drug delivery [78], solar-powered steam generation [79], as well as nanoscale control of temperature distribution [250] and thereby for optofluidics. Single [80] and arrays [73, 81, 82] of metal nanostructures have been studied to control the convection-driven dynamics. However, the surface of metal nanostructures may have an unnecessarily high temperature which can be harmful to particles touching the surface [251].

All-dielectric nanostructures, on the other hand, have been rapidly developing for the past decade mainly because they are relieved of parasitic Ohmic losses inherent by plasmonic nanostructures [252]. Many works have leveraged its low light absorption and thereby negligible Joule heating to avoid undesired fluid motion and/or positive (repulsive) thermophoresis which can deteriorate the optical trapping stability in plasmonic nanotweezers [74], such as by leveraging silicon dimers [187] and anapole-assisted nanoantennas [216, 253, 254]. Very recently, however, an emerging new field of all-dielectric thermonanophotonics focuses on controlling subwavelength optical heating by precisely tuning optical losses in dielectrics [255]. In ref [255], it was identified that temperature-gradient-driven microfluidic flows may also be controlled by dielectric nanoparticles. In this work, for the first time, we experimentally demonstrate the synergistic effects of optofluidic transport and particle aggregation using an all-dielectric metasurface enabled by quasi-bound states in the continuum (quasi-BIC) resonance.

The concept of BIC, first proposed in quantum mechanics by von Neumann and Eugene Wigner in 1929 [53] has rapidly emerged as a powerful approach for realizing high Q and strong field enhancement in dielectric metasurfaces [256]. The dielectric quasi-BIC metasurfaces are highly promising as they provides high-Q resonances comparable to photonic crystals [257], and strong field enhancements comparable to or even higher than those reported in plasmonic nanostructures. A variety of applications has been demonstrated in this field including lasing [185, 258], biosensing [9, 10, 259, 260], and nonlinear harmonic generation [261]. Among these designs, the intrinsic loss of materials has been identified as a critical issue for the quasi-BIC mode [177, 262]. We reported that the loss of the surrounding environment (refractive index of water at 1.55 μm, n = 1.31 + 0.00013i) can strongly affect the quasi-BIC resonance [241]. The absorptance from water in the proximity of the metasurface composed of elliptical silicon resonators can be as high as 45%, even

though the loss from the resonators made by silicon is negligible. As shown by our recent work in which the water absorption in a single photonic crystal cavity served as a heat source for electrothermal effects [263], in this work, we instead discuss how to leverage the heat dissipation due to water absorption in a quasi-BIC system to engineer the microfluidic flow (see Figure 4.1). Approaching the resonance, the total heat generation comprises of the global absorption by the bulk water in the microfluidic chamber as well as the heat dissipation from the water layer close to the resonators which serves as the local heat source. We show that this localized heating effect due to resonances strongly increases the flow velocity up to about three times in comparison to that of the off-resonant condition. The flow velocity can be precisely controlled by simply tuning the wavelength (within ±7 nm range) and/or power of the input laser. Particles can be rapidly transported (with velocities of 10 to 102 micrometer-per-second) from distances of up to millimeter-scale and aggregated at the center of the laser spot by the flow. The transported particles are then confined close to the metasurface by positive thermophoresis. Fluorophore-labeled tracer polystyrene (PS) beads with a size down to 200 nm are examined and we expect the same effects can be achieved for particles below 100 nm. Finally, we showcase different particle aggregation distributions when adding a cationic surfactant (cetyltrimethylammonium chloride) to the nanoparticle colloid by tuning the metasurface to on or off resonances. This verifies the temperature field distribution is modified by the quasi-BIC resonance. As such, our work opens a new field for controlling thermal-induced microfluidic dynamics at the nanoscale by non-plasmonic nanostructures.

4.2 Working principle and experimental set-up

Our system comprises an all-dielectric quasi-BIC metasurface sitting on the substrate of a microfluidic chamber illuminated with a collimated and linearly polarized laser beam, as shown in Figure 4.1(b). The laser spot follows Gaussian distribution, and the diameter is around 300 μm after it is shrunken through a beam expander by 5-times. The laser power is amplified by an Erbium-doped fiber amplifier (EDFA) such that an output of hundreds of milliwatts can be obtained. Relatively strong water absorption falls within the working range of the EDFA. The metasurface is composed of elliptical silicon nanoantennas arranged in a zigzag array on a glass substrate (see Figure 4.1(a)). When the input wavelength is away from the quasi-BIC resonance (λ_{BIC}), the laser beam is transmitted after passing through the 160 μm height of water (i.e., chamber height). The laser heating induces buoyancy-driven natural convection, which transports particles to the center of the illuminated substrate. Particles are confined close to the substrate in the axial direction (i.e., normal to the substrate) by the positive thermophoresis [264], as depicted in Figure 4.1(a). When the input wavelength is approaching λ_{BIC}, the quasi-BIC resonance is excited. Highly localized field enhancement (see Figure 4.3(b)) in the tip-to-tip gaps induces strong light absorption in the adjoining water medium. These hotspots then serve as local heat sources inducing strong temperature gradients for manipulating microfluidic dynam-

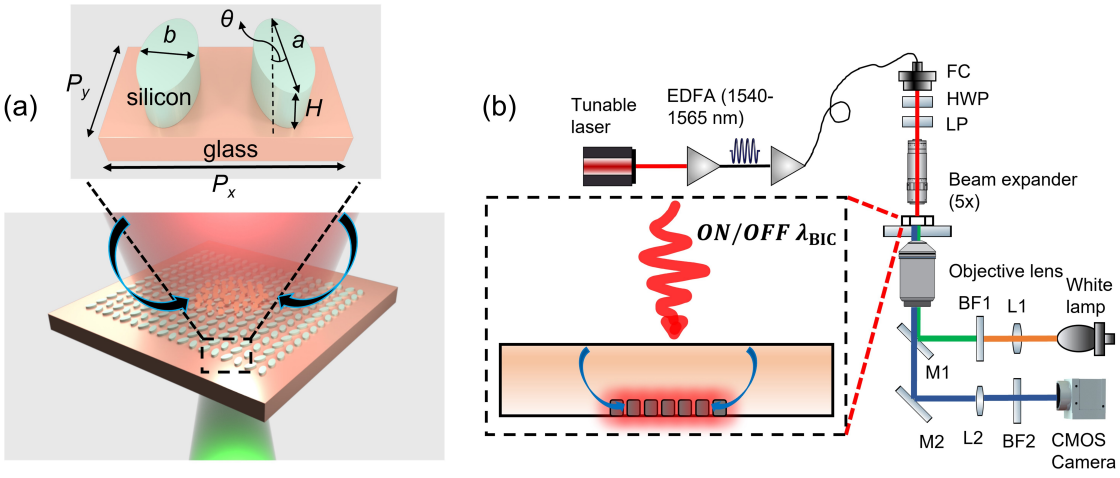

Figure 4.1: Working principle and experimental facility. (a) Schematic of the system. When the metasurface is off-resonance, the laser heating of the bulk water induces buoyancy-driven flow, transporting and aggregating particles to the center of the illuminated region. When the quasi-BIC is excited, additional heat sources come from the heat dissipation of the water layer close to the resonators. The thermal-induced flow velocity is increased up to three times. The flow is represented by the two lobes near the nanoantennas. Inset: a unit cell of the metasurface. The geometrical parameters: periods, $P_x = 950$ nm, $P_y = 778$ nm; $a = 532$ nm, $b = 192$ nm, $H = 190$ nm, $\theta = 10^\circ$. (b) Experimental set-up used for excitation of the quasi-BIC metasurface and imaging of the motion of suspended tracer particles. L1 and L2, focusing lenses; M1 and M2, mirrors; BF1 and BF2, bandpass filters used to filter light used for excitation of the fluorescent particles and light transmitted for imaging on the camera, respectively. Filtered fluorescent illumination is passed through the objective lens (10x or 40x) and focused on the sample. EDFA, Erbium-doped fiber amplifier used to amplify the power of the input laser; FC, fiber collimator; HWP, half wave-plate used to rotate the polarization direction of the laser beam; LP, linear polarizer. The metasurfaces and fluorescent tracer particles are visualized on a complementary metal-oxide-semiconductor camera by collecting signals through the same objective lens.

ics at the nanoscale. Besides the overall increased temperature which induces a faster buoyancy-driven flow, these local hot spots also induce strong thermo-osmotic flow [265, 266] due to the large lateral temperature gradient. Therefore, particles can be aggregated much more rapidly.

4.3 Particle aggregation

The representative aggregation of particles when illuminating the metasurface is shown in Figure 4.2(a). We used 500 nm fluorophore-labeled PS beads as tracer particles to visualize the microfluidic flow. The experimental videos are processed using an open-source particle tracking analysis package called *Trackpy* [267]. Representative particle trajectories are presented in Figure 4.2(b). It can be found that particles are rapidly transported towards the laser spot center and aggregated close to the substrate. The empty region at the center of the trajectory map represents a stagnation zone, i.e., the aggregated particle cluster. Since the aggregated particle cluster only takes 0.13% of the area of the whole metasurface and the refractive index contrast between PS and water is low, we note that the impact of the particles to the quasi-BIC resonance

was neglected. The experimentally measured, angularly averaged radial velocities obtained from the particle tracking analysis are shown in Figure 4.2(c) and 4.2(d). As shown in Figure 4.2(c), the fluid radial velocity when the collimated laser beam is illuminated on the metasurface increases rapidly as the input wavelength approaches the resonance (1544.3 nm). The results show a maximum flow radial velocity of 45 μm/s at 1545.3 nm, two times larger than that at 1551.3 nm. This indicates that the flow velocity can be precisely controlled over a wide range by simply tuning the wavelength within a $\pm$7 nm bandwith due to the high Q attribute of the quasi-BIC resonance. This is not achievable in plasmonic arrays. For example, in ref [73], the wavelength distance for a 2-times difference of the maximum velocity is almost 100 nm, which is two orders of magnitude larger compared to our case. Therefore, the transport and aggregation of particles can be manipulated quite flexibly and benefits from the local thermal gradients caused by the quasi-BIC metasurface.

As shown in Figure 4.2(c) and 4.2(d), the radial flow velocity close to the metasurface initially increases from a radial distance of more than 550 μm (limited by the field of view) until it reaches its maximum at a radial distance of 180 μm from the particle cluster. Inward from this position, the radial velocity decreases towards the center of the laser spot. Thus, we expect particles within at least a range of 550 micrometer-scale radius can be rapidly captured and transported to the center of the illuminated region. The scaling of the flow velocity with laser power is shown in Figure 4.2(d). The flow velocity rises when the input power is increased. The particle tracking analysis is not applicable when the input power is larger than 500 mW as the particles move too fast to be accurately located.

To understand the physics of the observed thermal-induced microfluidic dynamics in this system, we numerically solved the flow field by a commercially available finite element method software package (COMSOL Multiphysics). We consider that two mechanisms contribute to the thermal-induced flows in this system: the buoyancy-driven convection and thermo-osmotic flow [265, 266]. The velocity field distribution is determined from the solution of the incompressible Navier–Stokes equation given by

$$\rho_0(\mathbf{u}(\mathbf{r})\cdot\nabla)\mathbf{u}(\mathbf{r}) + \nabla p(\mathbf{r}) - \eta\nabla^2\mathbf{u}(\mathbf{r}) = \mathbf{F} \tag{4.1}$$

, where $\nabla\cdot\mathbf{u} = 0, \rho_0, p(\mathbf{r})$ and η are fluid density, pressure, and dynamic viscosity, respectively; and $\mathbf{F}$ is the force per unit volume acting on the fluid element. For the buoyancy-driven convection, we employ the Boussinesq approximation given by [73, 80]

$$F_{\text{buoy}} = g\rho_0\beta(T)\left[T(r) - T_0\right] \tag{4.2}$$

,where g and $\beta(T)$ are the gravitational constant, and thermal expansion coefficient of water, respectively. For

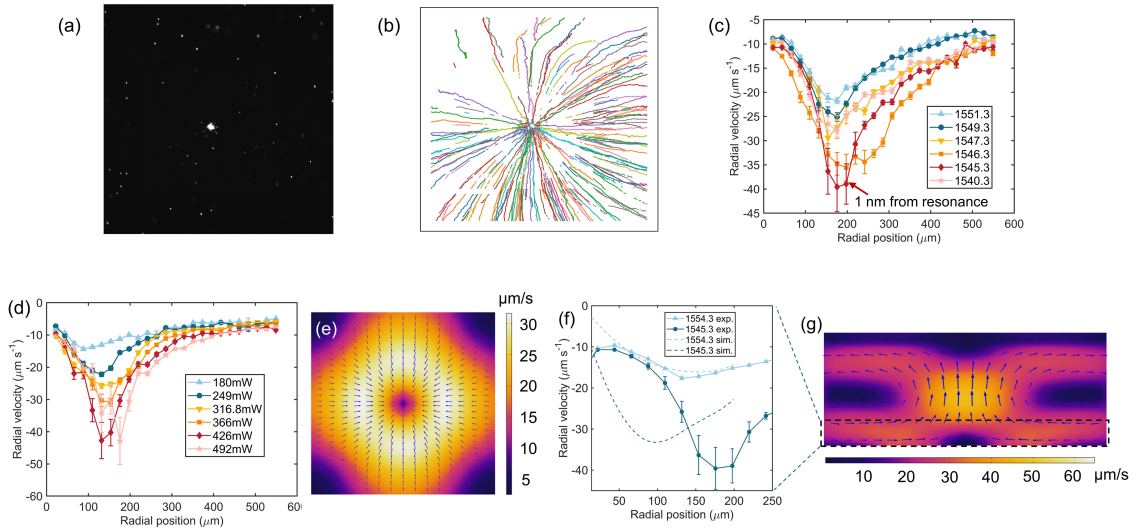

Figure 4.2: Experiment and simulation results for particle transport. All data are obtained under a 10x objective lens. The field of view is 900 μm. (a) Representative particle aggregation when a collimated laser beam is illuminated on the metasurface. (b) Representative particle trajectory map extracted from sequential 600 frames of a recorded video. The frame rate is 10 frames per second. The empty region at the center indicates that particle movement is trivial in this area, corresponding to the aggregated particle cluster. The result shows that the flow is directed radially inwards towards the center of the laser spot and serves as a powerful means to concentrate suspended particles to the vicinity of the metasurface. It's noted that some particle trajectories are interruptted at the edge of the metasurface region. This is due to the low transmittance of silicon in the visible range, which dims the fluorescence of these tracer particles, making them hard to be tracked. (c) Scaling of experimentally measured radial flow velocity with laser wavelength. The negative sign represents the inward direction. The error bar shows the standard error of the mean. The laser power fluctuates around 420 mW. The position where velocity reaches a maximum is slightly farther away from the center for wavelengths closer to the resonance. We attribute this to the stronger positive (repulsive) thermophoresis in the lateral direction due to the stronger heating effect. (d) Scaling of experimentally measured radial flow velocity with laser power. The same repulsive phenomenon is observed for higher laser power. e Simulated flow velocity distributions in the near-resonant condition of the *xy*-plane (5 μm above the substrate) and (g) of the *xz*-plane. Color map shows the velocity magnitude and superimposed arrows show the direction of the flow vectors. Radial velocities in the black dash box region (shown in (g)) are averaged to obtain the dash lines in (f). (f) Simulated (dash lines) and measured (solid lines) radial flow velocity for near-resonance (1545.3 nm) and off-resonance (1554.3 nm). The maximum velocities for 1545.3 nm and 1554.3 nm are 45 μm/s and 17 μm/s, respectively.

the thermo-osmotic flow, we apply a slip velocity to the thin fluid layer close to the surface of the substrate given by [265, 266]

$$v_{\parallel} = \chi \frac{\nabla_{\parallel} T}{T} \tag{4.3}$$

,where χ is the thermo-osmotic coefficient dependent on the properties of the liquid-solid interface (ζ potential, Hamaker constant, etc.) and $\nabla_{\parallel} T$ is the temperature gradient parallel to the surface. The related temperature field distributions and simulations will be discussed in the next section (see Figure 4.3).

The simulated velocity distributions in the *xy*-plane near the substrate and in the *xz*-plane are shown in

Figure 4.2(e) and 4.2(g), respectively. The flow close to the substrate brings particles inwards towards the center of the illuminated area and drags particles away from the surface in the axial direction (z direction). Due to the large depth of field of the 10x objective lens, the measured radial velocities are averaged from particles that appear within 30 μm from the surface . Simulation results implementing the similar averaging are compared with experimental results in Figure 4.2(f). The measured maximum flow velocity at 1545.3 nm reaches around three times of that at 1554.3 nm (11 nm away from resonance). For the off-resonant condition, the simulation agrees well with the measurement. For the near-resonant condition, the trend of the simulation remains consistent with the measurement despite the underestimation. We attribute this difference mainly to the underestimation of the thermo-osmosis contribution. Our simulations show that the thermo-osmotic flow is weak in the off-resonant condition as the lateral temperature gradient is low for the large Gaussian-distributed laser spot and it is insensitive to the changes of the thermo-osmotic coefficient χ. However, when the quasi-BIC mode is excited, the thermo-osmotic flow becomes an important contributor to the total transport flow velocity and significantly increases it. This is due to the strong $\nabla_{\parallel} T$ provided by the hotspots near the nanoantennas. As shown in Figure 4.3(b), the electric field distribution in each the tip-to-tip gap is not uniform and thus should induce a stronger $\nabla_{\parallel} T$ and consequently a stronger thermo-osmotic flow. However, in our simulations, we use a pillar with uniform heat distribution to represent such a non-trivial heat distribution for computational simplicity. This assumption likely underestimates the local temperature gradients and thus leads to a lower flow velocity. Furthermore, our estimation for the zeta potential, ζ, of the water-substrate interface may also play a part.

4.4 Particle dynamics

Up to now, we have demonstrated the boosted particle transport and aggregation assisted by the quasi-BIC metasurface. To elucidate the particle dynamics, the following section focuses on the dynamics of particles [268, 269] when on and off resonances. We start from the optical characterization of the metasurface. The simulated and measured spectra of the metasurface are shown in Figure 4.3(a), respectively. For an infinite array, no light is transmitted and the absorption of water (red dash line in Figure 4.3(a)) accounts for the 10% drop in the reflected power. In our experiments, each metasurface is a 500 μm by 500 μm square array, large enough compared with the laser spot diameter. The finite array size and the fabrication uncertainties (see Figure 4.3(c) for the scanning electron microscopy image) suppress the performance of the resonance mode and increase the background noise during measurement. Therefore, a higher transmittance (from 0% to 46.1%) and a reduced Q (from 500 to 250) are observed in the measured spectra. We expect this reduced Q impairs the heating effect while our experiments show that it is still strong enough to modify the whole temperature field distribution. The large near-field electric field enhancement close to the surface of the

nanoantennas contributes to the strong heating effects, as shown in Figure 4.3(b). It is worth noting that the BIC mode we employ is a symmetry-protected mode and is sensitive to the incident angle and the array size [185]. This is the key reason we choose to use a collimated laser beam instead of a focused laser beam by an objective lens.

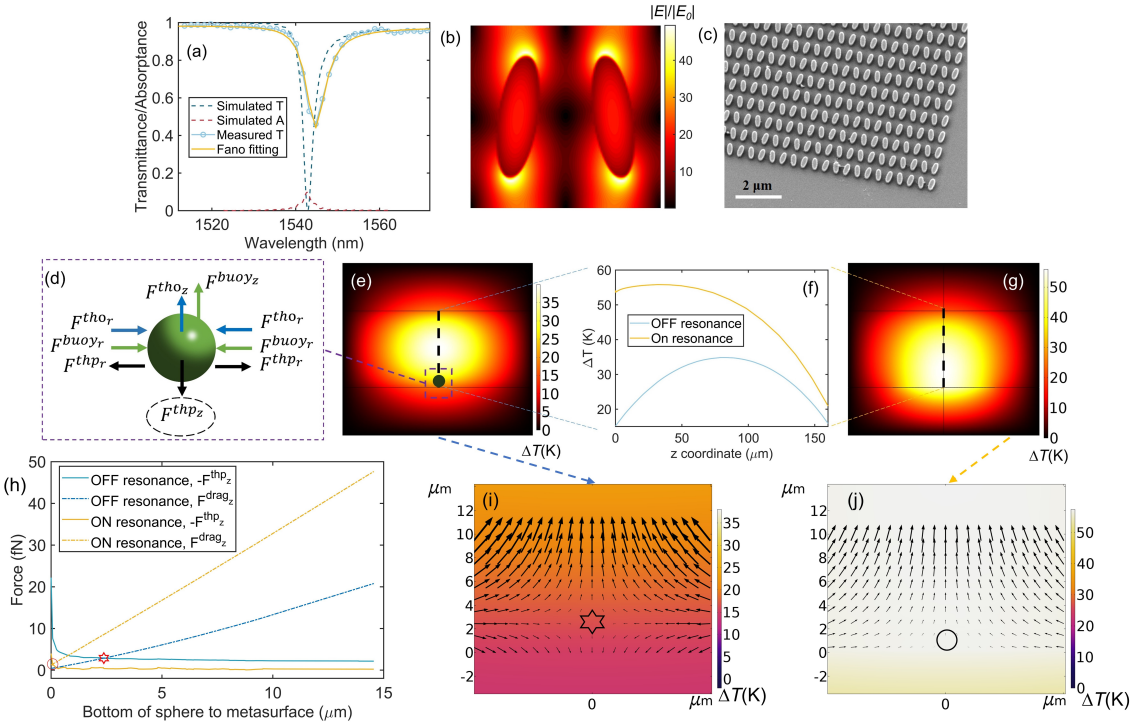

Figure 4.3: Optical characterization and thermal simulation. (a) Simulated and measured spectra of the metasurface. The resonance positions are 1548.9 nm and 1544.8 nm for the simulation and measurement, respectively. The sample shows a larger transmittance (46.1%) and a larger linewidth (6.3 nm) compared to the simulations (0% and 3.0 nm, respectively) attributed to the finite size and fabrication imperfections. The well-overlapped Fano fitting curve (yellow solid line) with the measured transmittance spectrum validates a typical quasi-BIC resonance. (b) Electric field enhancement distribution within one unit cell. The maximum electric field enhancement factor is 49.4, i.e., 2440 times for the intensity enhancement, supporting strongly enhanced water absorption. (c) Representative scanning electron microscopy image of the fabricated metasurface. The array size is 500 μm. (d) Depiction of the major forces acting on the trapped particles suspended in deionized water for the off-resonant condition. tho, thermo-osmosis; buoy, buoyancy; thp, thermophoresis. (e) Simulated temperature field distribution of the xz plane for off-resonant conditions and (g) for on-resonant conditions. Black dash lines mark the lines from which the spatial temperature rise curves in f are extracted. (f) Temperature rise in z direction for off-resonant and on-resonant conditions. $z = 0$ is the surface of the glass substrate. (h) Forces exerted on a 500 nm PS bead. F^{drag_z} corresponds to the Stokes drag force resulting from the fluid flow, which is composed of F^{buoy_z} and F^{tho_z}. The direction of the thermophoretic force is reversed as $-F^{thp_z}$ for a better comparison. A correction factor is used for the thermophoresis due to the hydrodynamic boundary effects [38, 39]. The star and circle symbols represent the balance point for off and on-resonant conditions, respectively. (i) Zoom-in temperature field distribution of the xz plane, superimposed with vectors of the total force exerted on a 500 nm PS bead for off-resonant conditions and (j) on-resonant conditions. The star symbol in (i) and the circle symbol in (j) denote the same symbols in (h).

To understand the modulation of the heat distribution by the quasi-BIC resonance, we numerically solved

the temperature field by COMSOL Multiphysics. The temperature field in the system is determined by solving the steady-state heat equation given by

$$\nabla \cdot \left[-\kappa \nabla T(\mathbf{r}) + \rho c_{\mathrm{p}} T(\mathbf{r}) \mathbf{u}(\mathbf{r})\right] = q(\mathbf{r}) \tag{4.4}$$

The first term on the left corresponds to heat conduction, while the second term corresponds to heat convection depending on the velocity of the flow. $T(\mathbf{r})$ and $\mathbf{u}(\mathbf{r})$ are the spatial temperature and fluid velocity field, respectively; κ, ρ and c_p are the thermal conductivity, density, and heat capacity of the materials, respectively; and $q(\mathbf{r})$ is the heat source density giving by the heat dissipated per unit volume. In our system, $q(\mathbf{r})$ is comprised of two parts. The first part comes from the light absorbed by the bulk water modeled by [81]

$$q(r) = P_0 \frac{\alpha_{\mathrm{c}}}{2\pi\sigma^2} \mathrm{e}^{-\left(\frac{r^2}{2\sigma^2}\right)} \mathrm{e}^{-\alpha_{\mathrm{c}} z} \tag{4.5}$$

$$\alpha_{\mathrm{c}} = \frac{4\pi\bar{\kappa}}{\lambda} \tag{4.6}$$

where P_0 is incident laser power, λ is laser wavelength, α_c is the attenuation coefficient of water, $\bar{\kappa}$ is the imaginary component of the refractive index of water. σ is defined by $w_0 = 2\sigma$ which is the waist radius of the Gaussian beam. The second part comes from the light absorbed by the water near the nanoantennas when the quasi-BIC resonance is excited. For computational simplicity, we approximate the heat dissipation obtained from electromagnetic calculations as uniform at each hotspot while taking into account the spatial Gaussian distribution of the incident laser beam.

To better compare the heat distributions when on and off resonances, we simulate the temperature fields for the two cases, as shown in Figure 4.3(e) and 4.3(g), respectively. The temperature drops from the middle of the chamber down to the substrate. Therefore, particles experience a positive thermophoretic force [264] which pushes particles towards the substrate and acts as the main mechanism to confine particles in the axial direction. Since the thermophoretic force [220] is proportional to $S_T \nabla T$ where S_T is the Soret coefficient, the confinement stability depends on the temperature gradient in the axial direction. Although the highest temperature rise increases from 38 K to 56 K, the location of the highest temperature rise changes from the chamber center in the off-resonant condition to the vicinity of the substrate under the on-resonant condition due to the strong heating effects from the resonators, as depicted in Figure 4.3(f). Therefore, the temperature gradient in the axial direction is decreased significantly in the on-resonant condition, leading to decrease of the downward thermophoretic force.

Based on the aforementioned temperature field analysis, we describe the particle dynamics as follows. The key forces acting on the trapped particles suspended in deionized water are depicted in Figure 4.3(d).

The positive thermophoretic force $-F^{thp}$ pushes particles from the middle down towards the substrate in the axial direction. The drag force $-F^{buoy}$ from the buoyancy-driven convection bring particles towards the center in the lateral direction and take particles away from the substrate in the axial direction. The thermo-osmotic flow is generated due to the lateral temperature gradient close to surface. The related drag force $-F^{tho}$ moves particles in the same direction as the buoyancy-driven convection. In the lateral direction, particles can be confined at the center by these centripetal flows [270]. In the axial direction, these two upward drag forces balance with the downward positive thermophoresis at around 2.4 μm above the substrate, as marked by the star symbol in Figure 4.3(h) and 4.3(i). When a particle is transported to within 2.4 μm from the substrate, it can be further pushed down and confined close to the substrate as the total force points down. However, under on-resonant conditions, the thermo-osmotic flow becomes much stronger due to the increased lateral temperature gradient while the axial thermophoretic force F^{thp_z} becomes weak attributed to the decreased axial temperature gradient. Such a situation leads to a shift of the balance position to only around 70 nm above the substrate, as shown by the circle symbol in Figure 4.3(h) and 4.3(j). This observation indicates that it's hard to confine a particle unless the particle is very close to the substrate, as the total force points up above 70 nm. Thus, we expect a much lower stability for particle aggregation when on resonance. In addition, when the quasi-BIC mode is excited, the short-range optical gradient force derived from the highly enhanced electric field may be another mechanism to pull particles to the hotspots. However, we note that in this work, the thermal forces and increased Brownian motion dominate the dynamics of the particles at on-resonant conditions due to the strong heating effects. Thus, during on-resonant condition, the particle aggregation disappears as depicted in Figure 4.4(c).

Next, we experimentally investigate the dynamics of particles in our system. We compare the evolution of particle aggregation with illumination time when the input wavelength is near-resonant (1545.3 nm) and off-resonant (1551.3 nm), as shown in Figure 4.4(a) and 4.4(b). It can be found that particles are concentrated in a faster manner for near-resonant illumination. More specifically, the time to concentrate particles to reach a similar number of aggregated particles in the near-resonant condition is only two-thirds of that for the off-resonant condition. This agrees with the aforementioned flow velocity measurements. Moreover, the particle cluster is packed more tightly in the near-resonant condition as shown in the last frame of Figure 4.4(a) and 4.4(b). We attribute this to the stronger thermal-induced flow directed towards the center due to stronger heating effects, which exerts larger drag forces on the particles. Notably, approaching the resonance condition does not necessarily improve particle aggregation. The particle cluster at different input wavelengths is shown in Figure 4.4(c). The cluster is packed more tightly from 1553.3 nm to 1546.3 nm as we are approaching the resonance represented by the effective particle distribution region marked by the red circles. However, the concentrated particles start to be lost when the input wavelength is closer to resonance

(1545.3 nm) in which the number of particles is decreased, while the cluster packing is even more tightly packed. For the on-resonant condition (1544.3 nm), the particles can not be aggregated anymore. We note that the slightly different resonance position from the spectra measurement (Figure 4.3(a)) comes from the sample loading process as this symmetry-BIC mode is sensitive to the incident angle33. Three nanometers away from resonance (1541.3 nm), the particle cluster appears again. This observation clearly prove our aforementioned analysis of the particle dynamics. The mechanism for these phenomena is two-fold. First, at resonance (or very close to resonance), the temperature gradient in the axial direction near the metasurface is no longer strong enough to stably confine particles to the substrate by the positive thermophoresis, as seen in Figure 4.3(e)-(g). Second, the thermal-induced fluid flow from both the buoyancy-driven convection and thermo-osmosis is stronger, resulting in stronger drag forces in the axial direction to take particles away from the substrate, as seen in Figure 4.3(h)-(j). We anticipate this can be improved by suppressing the quasi-BIC mode properly to reduce the heating effects from the high electric field enhancement, for example, a larger tilt angle θ for our case.

Finally, to further validate our analysis, we added a cationic surfactant, (cetyltrimethylammonium chloride, CTAC) to the nanoparticle colloid to experimentally investigate the temperature distribution when on and off resonances. CTAC has been widely used for reversing the sign of the effective Soret coefficient, i.e., attracting particles towards hot regions [73]. CTAC molecules adsorbed on the PS particle surface can form a positively charged molecular double layer. Simultaneously, CTAC molecules self-assemble into micelles when above the critical micelle concentration (0.13 – 0.16 mM). As reported in ref [73], when the CTAC concentration is below $\sim$2 mM, a thermoelectric field is generated to attract particles towards the hot region. When the CTAC concentration is above 2 mM, the depletion of the CTAC micelles plays a key role in attracting particles due to the generation of the depletion-attraction force (DAF). In brief, DAF is an osmotic pressure exerted on particles to attract them towards hot regions due to the concentration gradient of micelles generated from the migration of micelles from hot to cold regions [271]. In our case, we consider the latter mechanism as the CTAC concentration in our experiments is 5 mM.

Figure 4.5 shows different particle distributions for on and off-resonance cases, respectively. This verifies our aforementioned discussions that the temperature field distribution is modified by the quasi-BIC resonance of the nanoantennas. For the off-resonant condition, particles are hard to be aggregated on the substrate at low laser power (Figure 4.5(a)) as they are attracted towards the hot center at the center of the chamber (see Figure 4.3(e)) by the DAF. At high power (Figure 4.5(c)), however, particles are aggregated again as the positive thermophoresis overcomes the DAF to push the particles down. On the other hand, for the on-resonant condition, since the hot center is close to the substrate, particles are aggregated at low power (Figure 4.5(b)) but show a ring-like localization at high power (Figure 4.5(d)). This transition from accumulation to

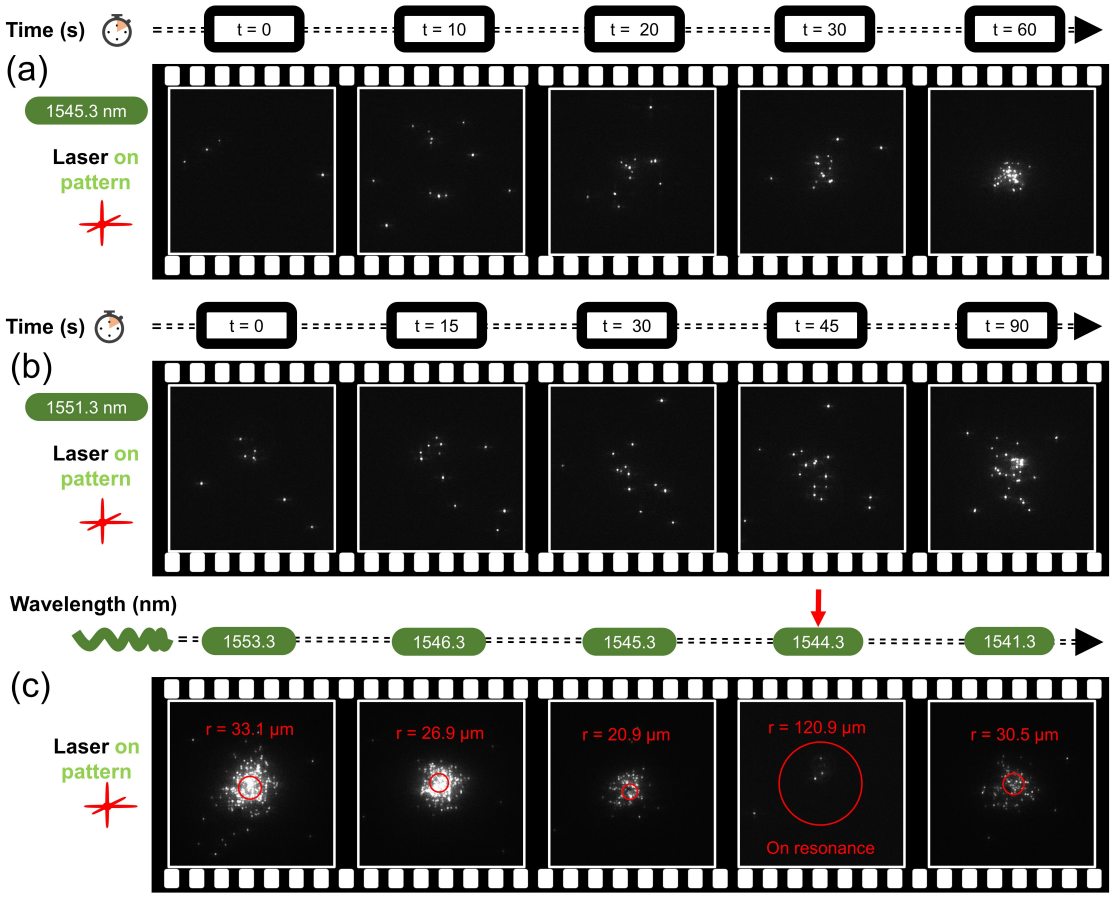

Figure 4.4: Experiment results for particle aggregation. All data are obtained under a 40x objective lens. The laser power fluctuates around 270 mW. (a) Evolution of particle aggregation with illumination time when the input wavelength is near-resonance (1545.3 nm) and (b) off-resonance (1551.3 nm). Particles are aggregated more rapidly and packed more tightly in the near-resonant condition. (c) Evolution of particle aggregation with illumination wavelength. The cluster is packed more tightly when approaching resonance, while the trap starts to lose particles when very close to resonance. No particles can be aggregated on resonance. Particles are aggregated again when away from resonance.

ring-like distribution is due to the interplay between the thermophoresis and DAF and has been reported by several research groups where the hot spot was located at the top wall of the chamber and the concentration of the added polymers was varied [271, 272]. In these works, the chamber height was usually less than 10 μm to suppress thermal convection. In a very recent work, David Simon et al. reported that the transition can also happen between low and high laser power [273]. We emphasize that the positive thermophoretic force in this experiment is strong enough to repel particles in the lateral direction to generate the ring-like distribution when the quasi-BIC mode is excited and the temperature is higher. This enhanced positive thermophoresis is attributed to the following reason. The magnitude and even the sign of the ζ potential of the particles can be significantly modified by the adsorbed surfactant molecules55. In our experiments, the ζ potential

of the 500 nm PS beads is modified from -40 mV suspended in deionized water to +88 mV with the CTAC concentration of 5 mM. If we neglect the permittivity and salinity gradients, the thermophoretic mobility [222, 266] of the particle is proportional to ζ^2. In this case, the natural thermophoretic force repelling particles from the hot center increases up to around five times. We expect this ring-like distribution can be beneficial for concentrating particles at cool regions as well as separating different particles [272].

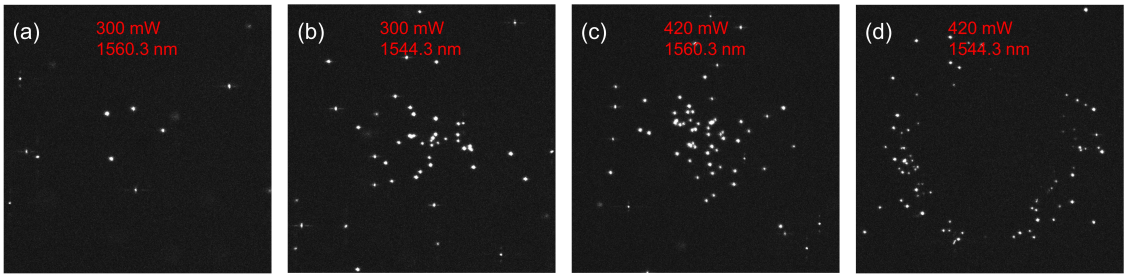

Figure 4.5: Experiment results for CTAC solution. CTAC concentration is 5 mM. All data are obtained under a 10x objective lens. (a) Particles are hard to accumulate at low power (300 mW) and (c) aggregated at high power (420 mW) for the off-resonant condition (1560.3 nm). (b) Particles are aggregated at low power (300 mW) and (d) localized as a ring at high power (420 mW) for the on-resonant condition (1544.3 nm). The aggregation is not as tight as that of previous experiments in deionized water mainly due to the stronger thermophoresis repelling particles from the center.

4.5 Discussions

Besides manipulating microfluidic dynamics, we expect the system we have proposed combining optofluidics and high-Q all-dielectric nanostructures can offer significant potential for biosensing applications. Compared with dielectrics, the nonradiative absorption resulting from the Ohmic losses of metals naturally limits the Q of the resonance, which is crucial for ultrasensitive sensing [274] and lasing applications [275]. Hatice Altug et al. have demonstrated several works employing all-dielectric quasi-BIC metasurfaces as label-free nanophotonic biosensors [9, 10, 259, 260], which have presented promising sensing performances. However, in these systems, the analytes are immobilized on the sensor surface through either dropping droplets, spin coating, or pressure-driven flow. We expect that the ability of our system to concentrate particles suspended in the liquid can further push down the detection limit of such quasi-BIC-based biosensors and in situ refractometric detection is also possible. What's more, due to the strong near-field enhancement, quasi-BIC metasurfaces have been demonstrated to boost surface-enhanced Raman and fluorescence spectroscopy [276, 277]. Benefiting from the more broadly spectral operation range of resonant dielectric nanostructures [274], this system can well separate the operation wavelengths between the optofluidic transport and the high-sensitivity particle detection. Therefore, this system may provide a high signal-to-noise ratio detection as well as quenching-free fluorescence spectroscopy which is a fundamental limit in plasmonics [278].

In summary, we have introduced and demonstrated the nanoscale control of temperature and fluid motion in an all-dielectric system. Owning to the high Q and strong electromagnetic field enhancement of the quasi-BIC mode, we present precise control of the fluid velocity up to three times by simply tuning laser wavelength within several nanometers. We also show long-range (millimeter-scale) and rapid (tens of micrometers per second) particle transport and aggregation. The undesired reduction of aggregation stability at resonance is observed and attributed to the modified temperature field which is altered by the strong heating effects from resonant quasi-BIC nanoantenna elements. This can be improved by slightly suppressing the quasi-BIC mode, for example by illumination with the wavelength slightly away from the resonance or increasing the tilt angle of the nanoantennas in our case. By implementing a physical model, we numerically show how the quasi-BIC resonance altered the temperature field and fluidic dynamics at the nanoscale. Moreover, after adding a cationic surfactant, CTAC, to the nanoparticle colloid, the totally different particle aggregation distributions for on and off-resonant conditions further validate our analysis. The ring-like particle aggregation that arises on resonance also provides potential applications for trapping and separating particles in low-temperature regions.

In addition, we propose that this system can become a powerful tool in colloid science and life science. Although we show aggregation of polystyrene beads down to 200 nm, we expect the same effect can have generality in particle size, shape, and composition, for example for sub-100nm nanoparticles. This can offer many opportunities in biology and medicine such as for the concentration and detection of extracellular vesicles and viruses. What's more, as we have discussed, the combination of optofluidics and high-Q all-dielectric nanostructures can have great potential in boosting the sensitivity of biosensors benefitting from synergistic effects of effective particle aggregation and strong electromagnetic field enhancement in the near field.

4.6 Appendix

Metasurface fabrication: All samples were fabricated on square glass wafers (the glass is from Präzisions Glas & Optik GmbH, with a thickness of 0.7 mm) with a side length of 1.5 cm. Amorphous silicon (a-Si) films with a thickness of 190 nm (measured by visible-NIR ellipsometry) were deposited onto the glass wafers by plasma-enhanced chemical vapor deposition (Trion Orion), followed by the spin coating of a double layer of polymethyl methacrylate (PMMA) resist of different molecular weights (495K A2 and 950K A4) and resistive physical vapor deposition (Angstrom Amod) of a 10 nm chromium conduction layer. The 500 μm by 500 μm patterns were transferred to the resist by 30 keV electron beam lithography (Raith eLiNE), after which the sample was dipped first in the chromium etchant to remove the conduction layer and then in the MIBK/IPA 1:3 for development. A chromium hard mask (10 nm thickness) was vertically deposited via electron-beam

physical vapor deposition (Angstrom Amod) followed by the wet-chemical lift-off in NMP 1165 remover on the 80°C hot plate overnight. Finally, patterns were subsequently transferred into the underlying a-Si layer by fluorine-based dry plasma etching (Oxford PlasmaPro 100 Cobra) with the chromium hard mask residue removed by the chromium etchant.

Surface treatment: To prevent the fluorophore-labeled polystyrene beads (Sigma-Aldrich, negatively charged in the deionized water) from getting too close to the sample surface due to electrostatic interactions and then stuck by the Vander Waals force in the deionized water, we treated the sample surface to make it negatively charged. The sample was first dipped in the 3 mM polystyrene sulfonate (PSS, Sigma-Aldrich) polymer colloid for 10 minutes followed by a rinse with deionized water. Then the sample was dipped in the 1 M potassium chloride (KCL) solution for 10 minutes followed by a rinse with deionized water.

Chip encapsulation: The treated sample was carefully covered by a thin glass coverslip separated by a double-layer adhesive film with an average thickness of 160 μm that sealed the microfluidic chamber. Polystyrene bead colloids with different concentrations were injected into the chamber by syringes.

Optical simulations: The numerical simulations of the spectra and field distributions were performed by commercially available software (Ansys Lumerical FDTD 2021 R2) using a finite-difference time-domain (FDTD) solver. *Periodic* boundary conditions were used in the x and y directions, while *PML* boundary conditions were used in the z direction. The *Anti-Symmetric* boundary conditions were applied in the x direction to save memory and simulation time. A *maximum mesh step* of 10 nm was set for the resonator region while a *mesh accuracy* of "5" was set for the rest. The simulation time was set to 10^5 fs and the *auto shutoff min* was set to 10^-6 to ensure a good convergence of the resonance. The material properties were taken from the Palik dataset included in the software.

Multiphysics Simulations: The temperature and flow field distributions were calculated by the commercially available software COMSOL Multiphysics 5.6.

The dimension of the whole simulation region was set as 200 μm $\times$ 200 μm $\times$ 360 μm. To mimic the encapsulated chip, the materials from top to bottom were glass, water, and glass, with thicknesses of 100 μm, 160 μm, and 100 μm, respectively. A four-fold symmetry (i.e., only a quarter of the whole region was simulated) was applied to reduce the memory requirement and save the simulation time. In other words, the whole area we calculated for was 400 μm $\times$ 400 μm. Two stationary steps solved *Heat Transfer in Solids and Fluids* and *Laminar Flow* studies sequentially.

The *Heat Transfer in Solids and Fluids* study solved the temperature field distribution. The Temperature (293.15 K) boundary condition was set for all the outer boundaries. The thermal conductivity of water and glass was set as 0.598 and 1.38 $\mathrm{W}/(\mathrm{m}\cdot\mathrm{K})$, respectively. The heat capacity of water and glass was set as 4200 and 840 $\mathrm{J}/\mathrm{kg}\cdot\mathrm{K}$, respectively. As we have discussed in the main text, the heat sources are composed of

two components: absorption from the water bulk (global) and the water layer close to the resonators (local). Therefore, we defined the two types of heat sources separately. The Soret coefficient of a 500 nm PS bead56 was set as 1.0 K^{-1}.

The *Laminar Flow* study solved the electrothermal flow induced by the temperature gradient and only the water region was included. The upper boundary was set as *Wall* with no slip while the surrounding boundaries were set as *Open Boundary*. As discussed by Martin Fränzl et al [266], to account for the thermo-osmotic slip flow the lower boundary was defined as a wall with a slip velocity. The *Thermal slip coefficient* σ_T was set as 0.02 assuming a surface zeta potential of -100 mV [279]. The expression of *Volume Force* was expressed below which represents the buoyancy-driven convection force:

$$\mathbf{F} = \mathrm{g}\rho_0\beta(T)\left[T(\mathbf{r}) - T_0\right]\hat{Z} \tag{4.7}$$

where $T_0 = 293.15$ K, $g, \beta(T)$ are the gravitational constant, and thermal expansion coefficient of water, respectively.

CHAPTER 5

Quasi-BIC metasurfaces at mid-infrared: Principles and applications

Metasurfaces governed by BICs are actively investigated for achieving high-quality factors and strong electromagnetic field enhancements. Traditional approaches reported for tuning the performance of quasi-BIC metasurfaces include tuning the resonator size, period, and structure symmetry. In Sention 1 of this chapter, my collaborators and I propose and experimentally demonstrate an alternative approach through engineering slots within a zigzag array of elliptical silicon resonators. Through analytical theory, three-dimensional electromagnetic modeling, and infrared spectroscopy, systematical investigations are made on the spectral responses and field distributions of the slotted metasurface in the mid-IR. The results show that by introducing slots, the electric field intensity enhancement near the apex and the quality factor of the quasi-BIC resonance are increased by a factor of 2.1 and 3.3, respectively, in comparison to the metasurface without slots. Furthermore, the slotted metasurface also provides extra regions of electromagnetic enhancement and confinement, which holds enormous potential in particle trapping, sensing, and emission enhancement. Then, inspired by the novel slots effects in these elliptical resonators, my collaborators and I propose and experimentally demonstrate the Single-peak narrow-band thermal emission of light based on a plasmonic quasi-BIC metasurface in Sention 2 of this chapter. The critical coupling condition is carefully engineered between the intrinsic material loss and the radiative loss of the quasi-BIC mode, resulting in an ultra-narrowband emission peak with a Q factor of approximately 42 and emissivity of 0.56 for a 500 μm pattern under 300°C. This level of performance is not achievable in traditional metallic designs. By introducing slots, we have been able to achieve an even higher Q of approximately 53, with the peak emissivity remaining high at 0.4. This design allows for a designable single-frequency peak ranging from 3 μm to 13 μm while having a relatively simple fabrication process.

5.1 Engineering an all-dielectric quasi-BIC metasurface by slots

5.1.1 Introduction

Yang, Sen, et al. "Engineering Electromagnetic Field Distribution and Resonance Quality Factor Using Slotted Quasi-BIC Metasurfaces." Nano Letters 22, no. 20 (2022): 8060-8067.

Creation of strong electromagnetic field enhancements is essential in nanophotonics and optical devices used for many applications such as biosensing, lasing and quantum information [280]. Plasmonic nanostructures harness the collective oscillation of conduction electrons sustained in metallic nanostructures to generate highly enhanced and tightly confined electromagnetic hotspots in the vicinity of the metallic nanos-

tructures. However, the non-radiative absorption resulting from the intrinsic (ohmic) loss of metals naturally limits the quality factor (Q) of the resonance [281, 282], which is crucial for ultrasensitive sensing and lasing applications [202, 275]. Some efforts have been made towards leveraging Fano resonances induced through interference between plasmonic resonances [283] and the collective diffractive modes in a nanoantenna array [284], though the typical Q is still relatively low [285] ($Q < 100$). We note that some recent works [286, 287] based on surface lattice resonances in plasmonic nanoparticle arrays reported high Qs, with a record-high of 2340 [288], although the energy dissipation is still not avoidable, which inevitably leads to photothermal heating of the plasmonic elements [217]. In parallel, to circumvent the issue of intrinsic loss in plasmonic nanostructures, high-index dielectric materials with low absorption have recently been studied as a promising alternative for light manipulation at the subwavelength scale [289–291].

Recently, the concept of bound states in the continuum (BIC) has emerged as a powerful approach for realizing high Qs and high field enhancements in all-dielectric metasurfaces. BICs are wave solutions embedded in a radiative continuum but are completely decoupled from the radiating waves. The concept of BIC was first proposed in quantum mechanics by von Neumann and Eugene Wigner in 1929 [53] and was then expanded to other fields of wave mechanics, such as optics and acoustics [4]. BIC in optics refers to a kind of non-radiating state of light and has been demonstrated in many structures, such as photonic crystals [54, 292] and optical waveguides [55]. An ideal BIC has no outcoupling, making the true BIC modes inaccessible. If the outgoing radiation is minimized while not totally vanishing, a sharp peak can be observed in the spectrum with a finite Q. Such a case is called a quasi-BIC. Recently, all-dielectric metasurfaces are being investigated as a versatile tool to realize quasi-BIC in finite structures. Such low-loss platforms are highly promising for high-Q resonances comparable to photonic crystals (10^2-10^7) [257] and in some systems, the resulting strong field enhancements are comparable to or even higher than those reported in plasmonic nanostructures, providing opportunities for a variety of applications including lasing [185, 258, 293], biosensing [9, 10, 259], low power nano-optical trapping of particles [76, 241], and nonlinear harmonic generation [180–182, 261].

Currently, the mainstream method [8] of tuning the resonance of a quasi-BIC metasurface is to engineer the structure symmetry of individual resonators [6] or via parameter tuning such as modifying the dimensions of the metasurface elements to excite supercavity modes [294, 295]. In this work, we propose and experimentally demonstrate a new mechanism to improve the quasi-BIC resonance of an all-dielectric metasurface by introducing slots into elliptical silicon resonators arranged in a zigzag array [9]. The "normal" slot effect stems from the continuity of the normal component of the electric displacement field at high index-contrast interfaces. It has been widely leveraged to expose and enhance electromagnetic fields confined in high index materials [296–298]. In our work, besides this well-known slot effect, we demonstrate that introducing slots can also effectively increase the local electromagnetic fields close to the apexes of the constituent elliptical

resonators as well as the Q of the existing quasi-BIC resonance. In addition to these, the slots also provide extra field enhancement and confinement regions due to the "normal" slot effect. Instead of introducing slots to break the symmetry and transition a true BIC to a quasi-BIC mode [299, 300], we here engineer a quasi-BIC system, and the slots are symmetrically introduced to retain the symmetry. Our slotted design therefore opens the door for designing quasi-BIC governed metasurfaces and are especially suitable for applications where high Q and multiple hotspots (i.e., electromagnetic field confined and enhanced regions) are desirable, such as lasing, nonlinear optics, optical trapping and photonic metasensors [301].

5.1.2 Working principle and experimental set-up

The system we have studied is a symmetry-protected quasi-BIC-governed all-dielectric metasurface comprised of elliptical silicon resonators arranged in a zigzag array. First, we symmetrically introduce 1, 2, and 3 slots into each silicon resonator (see Figure 5.1 and 5.2), respectively, and simulate their optical responses including reflectance spectra and electric field distributions. We prove that the Q and the maximum electric field intensity enhancement increase with introducing slots, up to 3.3 times and 2.1 times, respectively, when adding three slots in each resonator. Both Fourier-transform infrared (FTIR) spectroscopy and laser-based spectroscopy are carried out to cross-validate the simulated spectral responses. Next, we implement the optical nanoantenna theory to qualitatively understand the influence of slots on the spectral response. We further investigate the effects of slot geometry for the 1 slot case, which can be predicted by the optical nanoantenna theory. Moreover, our presented methodology is also readily extendable to other dipole-based resonant systems. We also note that this work is different from our prior work in Ref. [241], where a theoretical description of the self-induced back-action optical trapping in a quasi-BIC system was performed.

Our all-dielectric metasurface comprises slotted silicon elliptical resonators with a tilt angle arranged in a zigzag array on a magnesium fluoride (MgF_2) substrate, as shown in Figure 5.1(a). Since one of the applications we propose is biosensing, we design our metasurface to support a resonance at 6 μm free-space wavelength near the frequencies of the amide I and II vibrational bands for proteins. Three slots are introduced into each resonator, with one located at the center and the other two at the upper and the lower portions of the resonator, as shown in Figure 1c. To be consistent, we refer to this slotted system as the "3 slots" design, and similarly, we have "0 slots", "1 slot", and "2 slots" designs (see Figure 5.2 for details). To understand the generation of the quasi-BIC mode, we consider the two inverted electric dipoles (black arrows in the dash box of Figure 1b) excited in the two resonators of a unit-cell by an x-polarized plane wave. We decompose each electric dipole into two components p_x and p_y. Although p_y is dominant in each resonator, their directions are inverted in the two resonators, which results in them cancelling each other out and thus, are decoupled from the radiative continuum. When the tilt angle is small, the overall radiative loss is suppressed significantly,

and only the p_x component is found in the reflected light field. Hence, a narrow reflectance peak, as well as a high field enhancement can be obtained.

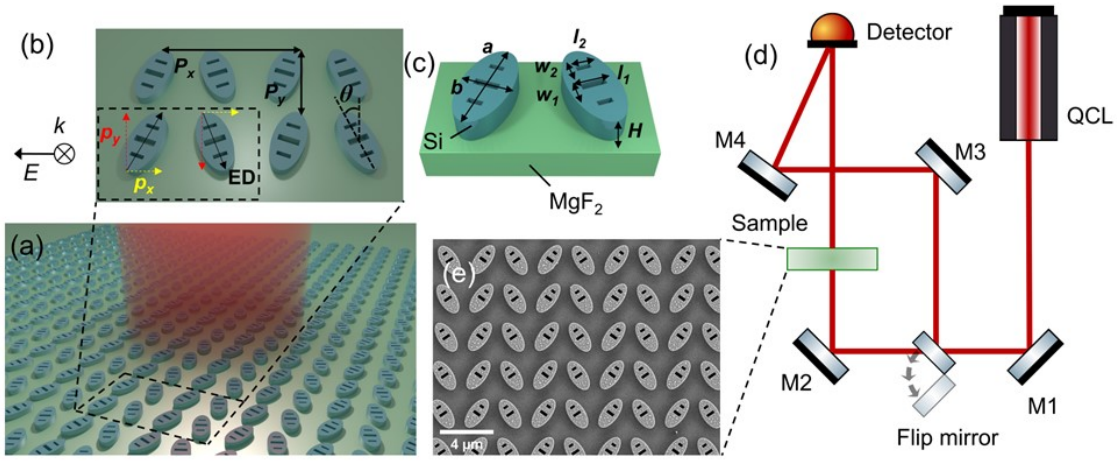

Figure 5.1: Design and measurements of the all-dielectric metasurface. Schematic illustration of (a) the metasurface illuminated with a collimated light beam and (b) a zoom-in view of four unit-cells of the metasurface. The metasurface comprises rectangular lattices (periods, $P_x = 4247$ nm, $P_y = 2448$ nm) of dimers formed by two slotted elliptical resonators with a tilt angle of $\theta = \pm 20^\circ$. The region in the black dash box depicts the electric dipoles (ED) induced in the resonators. The incident light is x-polarized plane wave. The yellow and red dash arrows represent the two components p_x and p_y, respectively. (c) Schematic of a unit cell showing silicon elliptical resonators sitting on the magnesium fluoride (MgF_2) substrate. The geometrical parameters: $a = 2124$ nm, $b = 1040$ nm, $w_1 = 600$ nm, $w_2 = 365$ nm, $l_1 = 180$ nm, $l_2 = 130$ nm, $H = 700$ nm. The slot centers are aligned with the long axis of the ellipse to maintain the structure symmetry. (d) Experimental set-up used for transmission laser-based spectroscopy. M1-M4, mirrors; QCL, quantum cascade laser. (e) Representative SEM image of the "2 slots" sample. The roughness of the surface results from the deposited chromium thin film which works as a charge dissipation layer for better imaging quality.

5.1.3 Optical characterization

The first noticeable improvement of adding slots is the increased Q. Compared to the "0 slots" design, a dramatic increase in Q by as much as a factor of two appears when at least one slot is added into the original resonator. The Q continues to increase for the "2 slots" and "3 slots" cases, as depicted in Table 5.1. In those simulations, we used a tilt angle (θ) of $\pm 20^\circ$ so that they could be directly benchmarked with Ref. [9]. We find that the simulated Q of the "0 slots" design is comparable to the reported value (~ 200), while our slotted design exhibits significantly improved Qs.

In addition to the spectral properties, the field enhancement of quasi-BIC modes is also substantially improved by introducing slots. While the highest field enhancement of all designs is located close to the resonator apex due to the collective resonance [9, 58, 302], the field enhancement values are different: the field enhancement at the apex increases with respect to the number of introduced slots, as shown in Figure 5.2(b)-(e). We attribute this to the fact that the Q increases with additional slots, and thus the increased local

density of states leads to the higher local electric fields46. Besides the field confinement at the apex, the slot effect confines and enhances the electric field in the slots due to the high relative permittivity of silicon. The electric field vectors in slots are oriented along the long axis of the ellipse, denoting the resonances as electric dipoles. To better understand the mechanism of the quasi-BIC mode, we performed the multipole decomposition analysis of the "1 slot" design following referenced procedures [296, 303–306]. The multipole decomposition shows that only the electric dipole component has contributions before and after adding the slot (Figure 5.2(f)), validating that the nature of the modes is maintained. The increased field enhancement of the slotted design is also manifested in the larger electric dipole component.

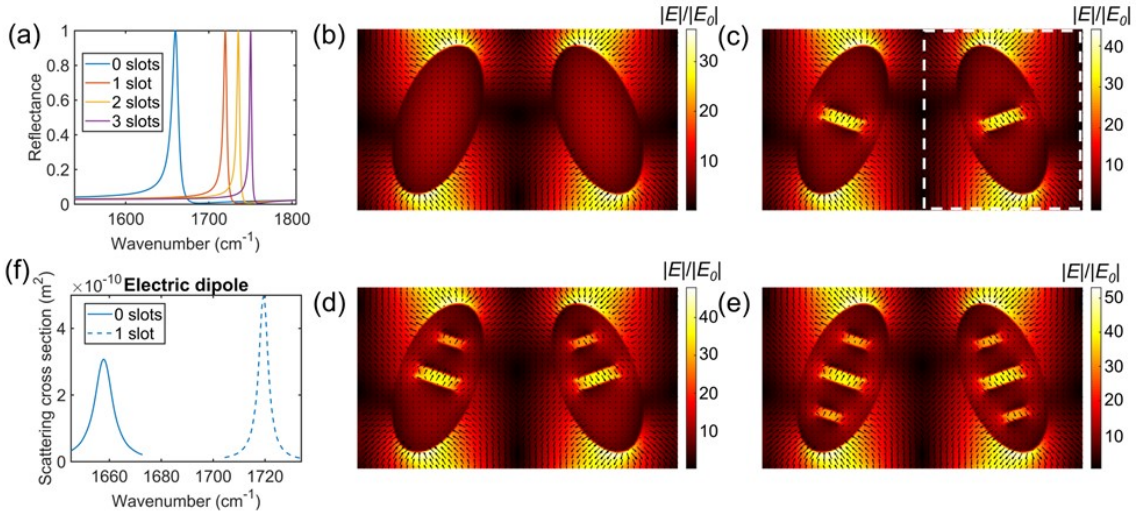

Figure 5.2: Optical characterization of the all-dielectric metasurface by numerical simulations. (a) Reflectance spectra of "0 slots", "1 slot", "2 slots", and "3 slots" designs. (b) - (e) Electric field enhancement distributions of *xy* plane at $z = 350$ nm for "0 slots" to "3 slots" designs, respectively. The electric field vector plot is superimposed on the field profile. Arrow length represents the magnitude of the electric field. (f) Multipole decomposition analysis shows the dominant electric dipole component. The nature of the mode preserves for the slotted designs. The multipole decomposition is applied to the region enclosed by the white dashed rectangle in (c). The solid line corresponds to the "0 slots" design while the dashed line is for the "1 slot" design.

Quantitatively, we compare the field enhancements of different slotted designs by extracting $|E|/|E_0|$ at the apex and the slot center. It can be found that by simply adding three slots, the maximum electric field enhancement at the apex is increased up to 53.1, i.e., 2820 times for the intensity enhancement, which is 2.1 times of the intensity enhancement of the original "0 slots" design, as shown in Table 5.1. Thus, introducing slots provides a simple way to enhance the local field and Q, which is vital importance for lasing. Furthermore, the added slots provide extra "hot spots" for strong interaction between fields and particles or molecules as these slots all have a significant field enhancement. In contrast, the only effective regions of the "0 slots" resonator original design are at the apexes, with the central part of the resonator having almost no accessible field enhancement. The electric field in the middle slot of the "3 slots" design is even comparable

to that at the ellipse apex of the "0 slots" design. Therefore, these extra "hot spots" offer significant potential for applications such as optical trapping, biosensing, and emission enhancement. For example, considering an application of sensing protein molecules51, the inner walls of the three slots increase the total surface area where protein molecules can bind within a high field localization region. To quantify this improvement, we define the average surface enhancement δ as the integral of the electric field intensity enhancement over the total accessible surface area normalized by the area of one unit-cell. δ is expressed as:

$$\delta = \frac{1}{P_x P_y} \iint_A (|E|/|E_0|)^2 \, da, \tag{5.1}$$

where A is the surface area of an ellipse plus that of the inner walls of the slots for slotted designs. The "3 slots" design increases δ by a factor of 2.25 compared with the original "0 slots" design, as shown in Table 5.1. This increased average surface enhancement is promising for applications requiring spatial overlap between the local field and the target. As an example, we illustrate how it facilitates biomaterial sensing application, e.g., monolayer protein detection. Following the discussions by Aurelian John-Herpin et al. [40], we simulated an ideal situation where the (slotted) metasurface is coated by a conformal protein monolayer. Detailed discussions are shown in Figure 5.5.

	0 slots	1 slot	2 slots	3 slots
Q	185	367	463	613
max[$\|E\|/\|E_0\|$] at apex	36.5	44.0	48.0	53.1
[$\|E\|/\|E_0\|$] at slot center	NA	34.2	28.6, 35.8	32.8, 39.2, 32.8
Average surface enhancement δ	139.8	296.9	364.6	453.9

Table 5.1: Resonance response comparison for "0 slots" to "3 slots".

5.1.4 Experimental measurements

To validate our design principle, we fabricated large-scale (0.5 mm by 0.5 mm array) patterns and performed spectroscopy measurements with a representative SEM shown in Figure 5.1(e). To be compatible with our spectral resolution, we tune the geometry parameters with a tilt angle of $\theta = \pm 35^\circ$ for "0 slots" to "2 slots" designs, with the simulated transmittance spectra shown in Figure 5.3(e). We first measured the samples with FTIR (Figure 5.3(a)), and the experimental results confirm that spectra of the slotted designs have a narrower linewidth and shift to a larger wavenumber compared with the "0 slots" structure. However, the broadband light source (a glowbar lamp) used in FTIR caused unavoidable beam divergence: the spectral responses acquired are an integration of responses at different incident angles. As reported in Ref. [259], the resonant response of this zigzag quasi-BIC metasurface is highly sensitive to the incident angle. Therefore, the beam divergence broadens and damps the resonance, and the slotted designs are more sensitive to it, damping the

resonances more severely. Although the FTIR results do not provide quantitative linewidth information, they still qualitatively validate our numerical simulations that adding slots would increase the Q and shift the resonance to larger wavenumbers (Figure 5.3(e)).

To obtain the spectral response of samples without the influence of such large beam divergence, we performed transmission laser-based spectroscopy with a tunable quantum cascade laser (QCL). The experimental set-up is shown in Figure 5.1(d). The beam divergence of the QCL is only 2 mrad, which can be safely neglected, allowing us to determine the lineshape of the quasi-BIC resonances more precisely. Indeed, we find that the full width at half maximum (FWHM) of all samples measured with the QCL is smaller than the values observed via FTIR measurements. Note that the trend of the QCL measurements remains consistent with the FTIR measurements, and the slotted designs exhibit higher Qs than the "0 slots" designs. More specifically, the Q of the "0 slots" structure is determined to be 84 with an FWHM of 18 cm$^-$1 (Figure 5.3(b)), which agrees well with our numerical simulation (Q of 93 and FWHM of 16 cm$^-$1). The Q of the "1 slot" sample is increased from 84 to 197 (Figure 5.3(c)). Furthermore, the Q of the "2 slots" design is even higher (373 ± 80), and the linewidth (4.2 ± 0.9 cm^{-1}) is approaching our instrumental limits ($\sim$ 1 cm$^-$1), as shown in Figure 5.3(d). The extracted resonance properties are tabulated in Table 5.2. We assume the relatively large difference between the QCL measurement and the numerical simulation for the "2 slots" sample come from the sample loading process and/or fabrication imperfections. Therefore, the laser spectroscopy measurements as well as the FTIR measurements validate that the slotted designs manifest narrower linewidths and shift the resonances to larger wavenumbers. Moreover, we anticipate comparable field enhancements in the actual samples considering the good agreements between simulations and experiments.

Number of slots	Resonance frequency (cm^{-1})		Resonance FWHM (cm^{-1})		Q		max[$\|E\|/\|E_0\|$] at apex
	Sim.	Exp.	Sim.	Exp.	Sim.	Exp.	Sim.
0	1488	1511 (0.3)	16	18 (1.2)	93.3	84 (5.6)	19.5
1	1513	1535 (0.2)	9	7.8 (0.9)	170	197 (23)	24.1
2	1519	1567 (0.3)	7	4.2 (0.9)	219	373 (80)	27.9

Table 5.2: Comparison between measurements and simulations. The standard deviation of the resonance frequency and FWHM are extracted from Lorentz fitting, which is included in the parenthesis, and the corresponding errors of the Q are calculated by the error propagation equation.

5.1.5 Optical nanoantenna model

To understand and predict the spectral response of the slotted design, we implement an effective impedance model by regarding each silicon resonator as a nanoantenna based on the optical nanoantenna theory [307–

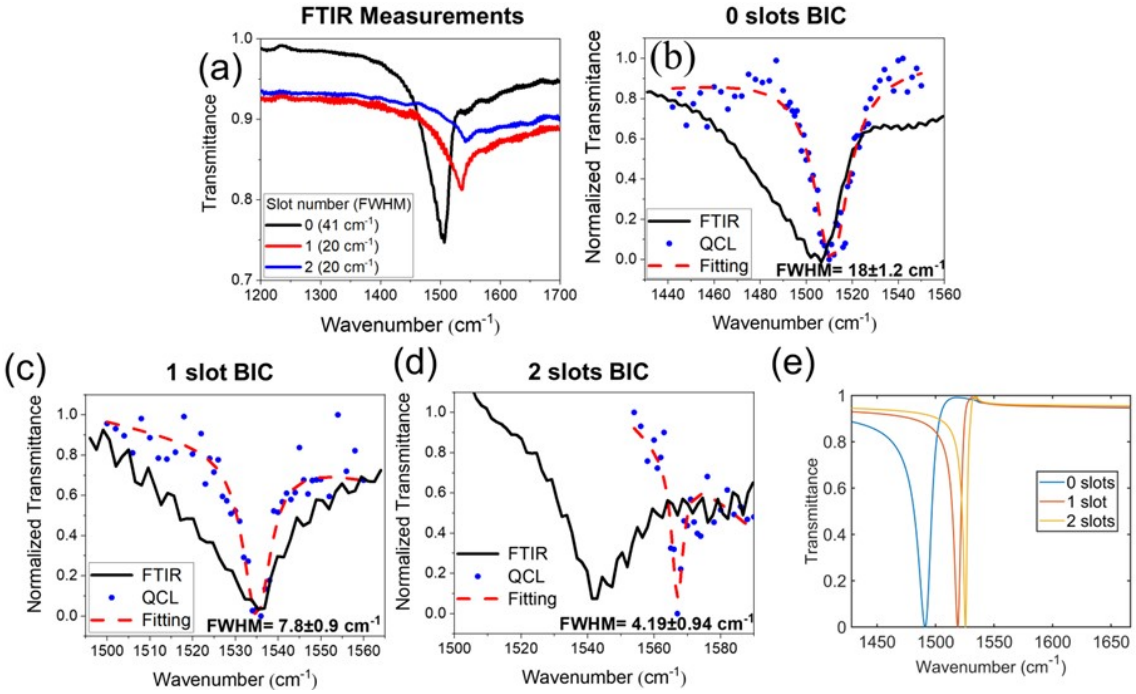

Figure 5.3: Spectroscopy measurements on fabricated samples. (a) FTIR transmission measurements for "0 slots" to "2 slots" samples. The measured transmission is defined as Power $_{\text{metasurface}}$ / Power $_{\text{MgF}_2\ \text{substrate}}$. (b-d) Normalized transmission of "0 slots" to "2 slots" samples measured with the homebuilt laser spectroscopy, respectively. The FTIR measurements in the frequency range of interest extracted from (a) are normalized and plotted in corresponding figures as a comparison. The curve fittings are all performed with Lorentz fitting by commercially available software Origin 2021b. (e) Simulated spectra for "0 slots" to "2 slots" designs.

313]. For simplicity, we assume that the dominant contribution of the near-field electric polarization comes from the electric dipole moment. The resonator only has radiative loss and is positioned in a homogenous background (i.e., air in this work). When only considering the radiative loss, generally a single dipolar nanoantenna can be approximated with a series RLC circuit, associated with the intrinsic impedance of the system expressed as [9]:

$$Z_{\text{int}} = R_{\text{int}} - jX_{\text{int}} = R_{\text{int}} - j\omega L_{\text{int}} - \frac{1}{j\omega C_{\text{int}}}, \tag{5.2}$$

where j is the imaginary unit R_int is the intrinsic resistance and is contributed to by the radiative loss. According to Ref. [307], a dipolar nanoantenna with one loaded gap at the center can act as the series combination of the intrinsic impedance and the load impedance when excited by an external plane wave with the electric field parallel to the nanodipole axis. For positive values of the real part of permittivities for dielectric materials, the optical impedance is capacitive. Since the silicon resonator is approximated as a dipole antenna with the direction of the main dipole moment along the long axis of the ellipse, it's reasonable to regard the original "0 slots" resonator as a nanoantenna with a gap loaded with silicon ($\varepsilon_r = 10.30$), as shown in Figure 5.4(a).

The load nanocapacitance is expressed as [308, 311]:

$$C^{0}_{\text{slot 1}} = \varepsilon_0 \varepsilon_r H b / w, \tag{5.3}$$

When introducing a slot (i.e., the "1 slot" resonator), part of the gap is unloaded (i.e., filled with air) and then the gap can be equivalent to a parallel connection of three capacitors, also seen in Figure 5.4(a). The equivalent circuit model for the "1 slot" design is sketched in Figure 4b and the load nanocapacitance is now given by:

$$C_{\text{slot 1}} = C_{\text{Si}} + C_{\text{air}} + C_{\text{Si}} = \frac{\varepsilon_0 H}{w} \left[\varepsilon_r b - (\varepsilon_r - 1)\, l \right], \tag{5.4}$$

When $l = 0$ (i.e., the air slot is not introduced), $C_{\text{slot 1}} = C^{0}_{\text{slot 1}}$. The resonance peak is achieved when the optical frequency ω equals to ω_0, where ω_0 is the open-circuit resonance frequency expressed as [309]:

$$\omega_0 = \frac{1}{X_{\text{int}} C_{\text{slot 1}}} \tag{5.5}$$

When the slot length l is not $0, C_{\text{slot 1}}$ is always smaller than the nanocapacitance of the " 0 slots" design $C^{0}_{\text{slot 1}}$. The resonance frequency ω_0 thus increases, indicating the reflectance peak shifts to a larger wavenumber. For this series RLC circuit, the Q is defined as $Q = R^{-1}_{\text{int}} \sqrt{L_{\text{int}} / C_{\text{system}}} \propto \sqrt{1/C_{\text{system}}}$. Here, C_{system} is the series connection of C_{int} and $C_{\text{slot 1}}$ expressed as:

$$C_{\text{system}} = \left(1/C_{\text{int}} + 1/C_{\text{slot 1}} \right)^{-1} \tag{5.6}$$

With a decreased $C_{\text{slot 1}}$ by introducing an air slot, the Q increases, explaining the narrower linewidth of the reflectance spectrum of the "1 slot" design. For multi-slot designs (i.e., "2 slots" and "3 slots"), the equivalent circuit model for the load is a series connection of capacitors (see Figure 5.4(c)) with part of the load material changing from silicon to air by introducing air slots, leading to the decrease of the load nanocapacitance C_{slot}. Therefore, the reflectance peaks shift to larger wavenumbers, and the Qs are higher when we introduce more slots, as observed in Figure 5.2(a).

Next, we investigate the impacts of the slot size on both spectra and local field responses by exemplifying the "1 slot" design with the effective impedance model. The continuous evolution of the spectra and the electric field enhancement at the center of the slot are shown in Figure 5.4. When increasing the slot length l with a fixed width w, the reflectance peak shifts to a larger wavenumber while the Q slightly increases as well, as shown in Figure 5.4(d). When we increase the slot width w with a fixed length l, the reflectance peak shifts to a larger wavenumber while the Q still slightly increases, as shown in Figure 5.4(f). Both behaviors are well

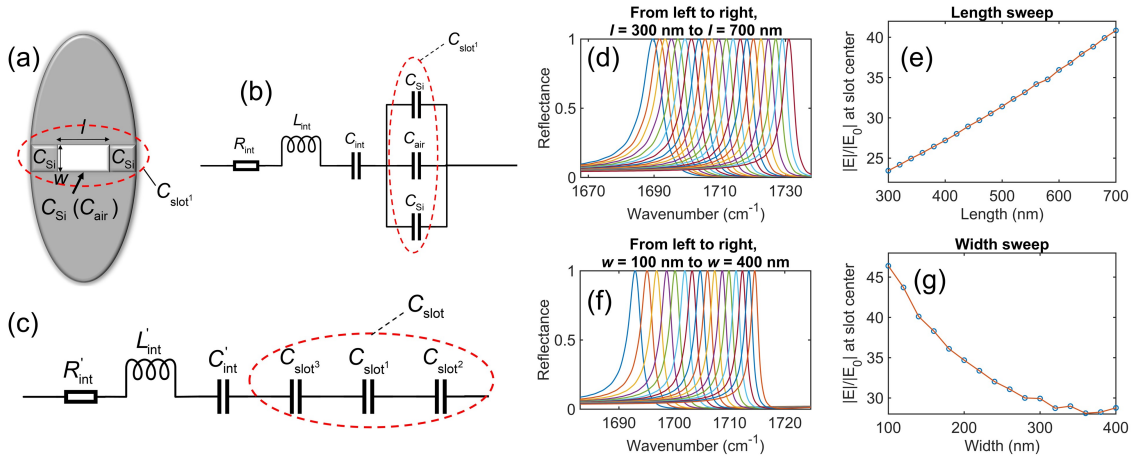

Figure 5.4: Equivalent circuit models and size-dependent resonant responses of the "1 slot" design. (a) Load nanocapacitance before and after introducing a slot to the resonator. Here w and l are the width and length of the air slot, respectively. (b) Equivalent circuit model for the "1 slot" design. (c) Equivalent circuit model for multi-slots design. Here letters R, L, and C stand for resistance, inductance, and capacitance, respectively and "int" means intrinsic. (d) Spectra with different slot lengths l and the fixed width w = 180 nm. The solid lines correspond to l = 300 nm to l = 700 nm from left to right. (e) Field enhancement at the center of the slot with respect to different slot lengths in (d). (f) Spectra with different slot width w and the fixed length l = 600 nm. The solid lines correspond to w = 100 nm to w = 400 nm from left to right. (g) Field enhancement at the center of the slot with respect to different slot widths in (f).

predicted by the effective impedance model. According to Eq. 5.4, a wider gap w and/or a longer length l would decrease $C_{\text{slot}}{}^{1}$, leading to a higher resonance frequency and a larger Q. Notably, length and width play different roles in the field enhancement at the slot, as shown in Figure 5.4(e) and (g). A longer slot induces a higher Q, thus having a higher field enhancement; while a wider slot has a lower field enhancement at the center of the slot, mainly attributed to the continuity of the normal component of the electric displacement field. We note that the electric field at the apex of the resonator arises when the Q increases, i.e., when w or l increases.

5.1.6 Numerical demonstration for sensing applications

Previously, we have numerically and experimentally demonstrated the improved Q, field enhancement, and average surface enhancement of our slotted designs. We here illustrate how those advantages facilitate bio-material sensing, e.g., monolayer protein detection. For this purpose, we simulate the (slotted) metasurfaces coated by a conformal protein monolayer (5 nm thick) following the methods Ref. [40]. To spectrally overlap with the absorption peak of the protein monolayer, resonances of all designs are shifted to near 1660 $\text{cm}^{-}1$, where the Lorentzian resonance of protein permittivity locates (Figure 5.5(a)) [37]. The reflectance spectra before and after coating the protein monolayer on the "0 slots" to "3 slots" designs ($\theta = 20^{\circ}$) are shown in Figure 5.5(b)-(e). It's clear that the reflectance peak drops as more slots are added, indicating stronger

absorption from the protein monolayer and thus improved detection sensitivity. To compare the absorption intensity more directly, we shifted all the reflectance spectra after coating the protein monolayer to the same position, and it can be found that the slotted designs enable appreciably enhanced absorption, as shown in Figure S6f. To quantify the detection sensitivity, we define a figure of merit (FoM) as:

$$\mathrm{FoM} = \frac{\Delta R}{R_0} \times \frac{\Delta \lambda}{\lambda_0 / Q} \times 100, \tag{5.7}$$

where R_0, λ_0, and Q are the peak reflectance, resonance wavelength, and quality factor before coating the protein monolayer, respectively; ΔR and $\Delta \lambda$ are the peak reflectance differences and resonance wavelength shifts before and after coating the protein monolayer, respectively. The FoMs for "0 slots" to "3 slots" structures are calculated as 7.63, 25.13, 33.86, and 45.51, respectively. The 6-fold difference of the FoM between the "3 slots" design and the original "0 slots" design shows a pronounced improvement.

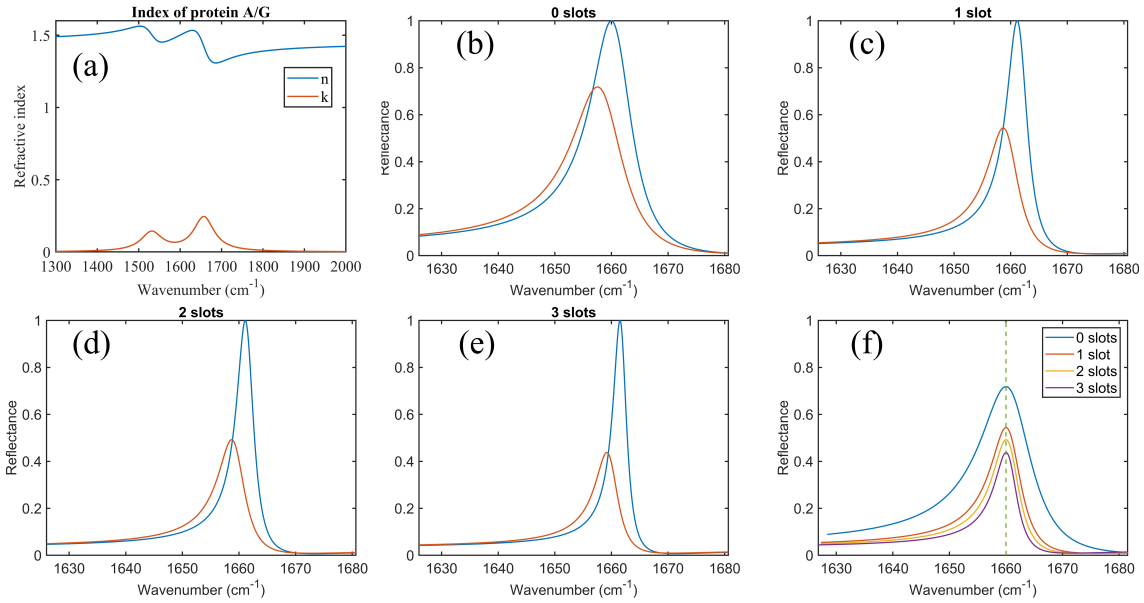

Figure 5.5: Sensitivity of detecting the protein monolayer. (a) Modeled refractive index of the protein monolayer [40]. (b) to (e) Reflectance spectrum before (blue solid lines) and after (red solid lines) coating the 5 nm conformal protein monolayer for "0 slots" to "3 slots" designs, respectively. (f) Reflectance spectra of the "0 slots to "3 slots" designs coated by the protein monolayer are shifted to the same wavenumber position for comparison.

5.1.7 Conclusion

In summary, we have proposed and experimentally demonstrated a new mechanism for tuning the resonant response of a quasi-BIC-governed all-dielectric metasurface composed of elliptical silicon resonators arranged in a zigzag array by symmetrically introducing slots into each resonator. We show that by introducing slots,

the quality factor and electric field intensity can be enhanced by as much as 3.3 times and 2.1 times compared with the original structure without slots, while the quasi-BIC mode is still preserved. Moreover, the enhanced and spatially confined field in the slots provides extra electromagnetic "hot spots" for field-target interaction. By implementing an effective impedance model based on the optical nanoantenna theory, we analytically explain the spectral responses of the slotted metasurface. We envision that these results may find many applications in low-threshold lasing, sensing, biomolecular trapping, nonlinear optics, and engineering spontaneous emission. Our presented design methodology is also readily extendable to other dipole-based single and periodic nanostructures.

5.2 Engineering thermal emission using a plasmonic quasi-BIC metasurface

5.2.1 Introduction

The development of inexpensive and efficient infrared light sources is highly desirable for a variety of applications, including free-space communications, infrared beacons, barcodes, and monitoring environmental pollutants and toxins through molecular sensing metrologies like non-dispersive infrared (NDIR) sensing. Thermal emitters typically have a broad spectrum determined by Planck's law. Consequently, wavelength-selective thermal emitters with a narrow bandwidth and high peak emissivity are of particular interest due to the lack of cost-effective light sources in the mid- to long-wave infrared range. The principle of thermal emission control is based on Kirchhoff's law of thermal radiation, which states that the emissivity of an object equals its absorptivity for a given frequency, direction, and polarization. By creating an optical resonance and engineering the absorptivity at a specific frequency, a well-performing thermal emitter can be achieved. Metallic nanostructures have been extensively studied in this regard; however, their strong free carrier absorption results in undesired emissions over a wide wavelength range, and the emission peaks are broadened ($Q < 10$). Surface-phonon polariton resonances in polar materials are also promising candidates but have intrinsic limitations such as the inability to tune the emission wavelength over a wide range. Thermal metasurfaces offer another promising avenue, as experimentally demonstrated in [126], with the ability to emit arbitrarily polarized and unidirectional light. However, the optical properties of dielectric materials used in these metasurfaces are dependent on temperature.

5.2.2 Design of the thermal emitter

The high-Q property of quasi-BIC metasurfaces suggests a solution to the narrowband and high-efficiency thermal emitter. The reason can be understood as follows [125]. For an absorber (i.e., an emitter), the total Q-factor Q_{tot} is determined by the radiative Q-factor Q_r and non-radiative Q-factor Q_n with the relationship $Q_{\text{tot}} = \left(Q_r^{-1} + Q_n^{-1}\right)^{-1}$. High-Q efficient absorption requires (1) simultaneously high Q_r and Q_n and (2)

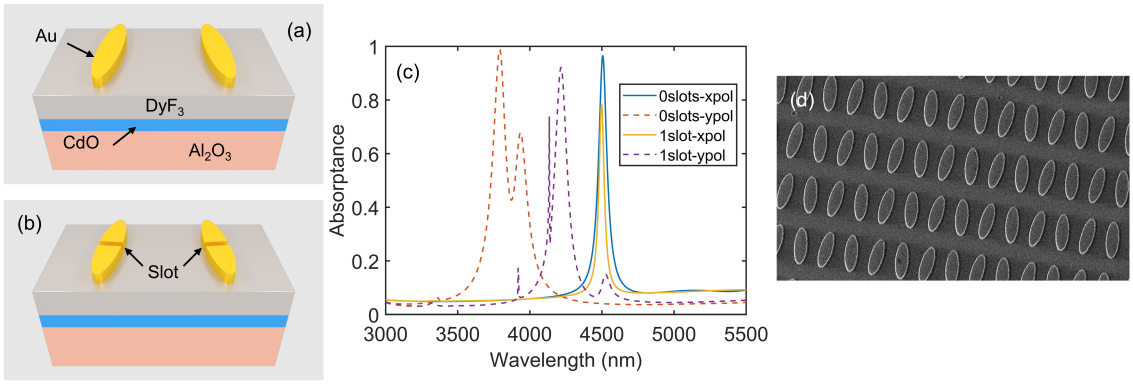

Figure 5.6: Design of the plasmonic quasi-BIC metasurface. (a) Schematic diagram of the "0 slots" metasurface. (b) Schematic diagram of the "1 slot" metasurface. (c) Simulated absorptance spectra of the "0 slots" and "1 slot" metasurfaces illuminated by x and y polarized light. The thickness of the DyF_3 and the CdO layer is 650 nm and 400 nm, respectively. The geometrical parameters for the "0 slots" metasurface are $P_x = 2100$ nm, $P_y = 2100$ nm, $a = 1400$ nm, $b = 420$ nm, $H = 200$ nm, $\theta = 6^\circ$. The geometrical parameters for the "1 slot" metasurface are $P_x = 2508$ nm, $P_y = 2508$ nm, $a = 2006$ nm, $b = 401$ nm, $H = 200$ nm, $\theta = 5^\circ$. (d) Representative SEM image for the "0 slots" metasurface.

critical coupling for the resonance, that is, $Q_r = Q_n$. In the design paradigm, efforts should be exerted not only to increase Q_r and minimize its degradation in the fabrication process but also to achieve a high Q_n and precisely engineer Q_n to reach the critical coupling condition since either overdamping $(Q_n < Q_r)$ or underdamping $(Q_n > Q_r)$ can decrease the absorptance dramatically.

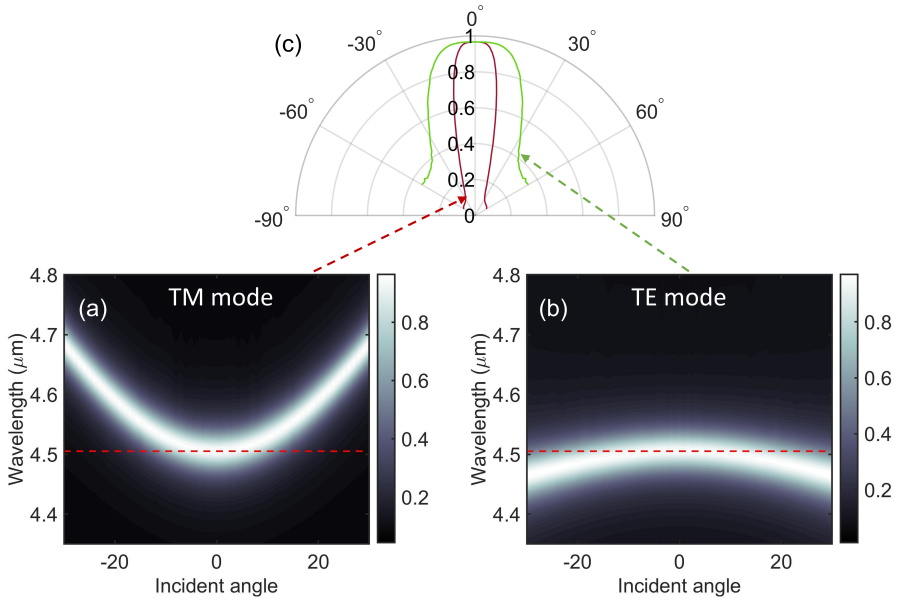

Figure 5.7: Characterization of the emission directivity for the "0 slots" metasurface. (a) Absorption spectra of the TM mode for a range of incidence angles. (b) Absorption spectra of the TE mode for a range of incidence angles. (c) Polar plot of the emissivity (absorptance) at the band-edge mode (white dash lines in (a) and (b)) for TM and TE modes.

Inspired by the perfect absorber reported by J. Wang et al. [111], here we introduce a novel approach to create a narrowband thermal emitter with a single peak using a mirror-coupled plasmonic quasi-BIC metasurface. The metasurface is composed of elliptical gold resonators arranged in a zigzag array, positioned on a DyF_3 dielectric spacer, followed by a CdO reflector and a sapphire substrate, as shown in Figure 5.6(a). Figure 5.6(d) shows the scanning electron microscope (SEM) image of the We have specifically selected these materials to ensure that the optical responses of the emitter remain stable under different temperatures. Moreover, as inspired by the effects of introducing slots mentioned in the previous section, we symmetrically introduce a slot to each of the gold elliptical resonators for further increasing the Q factor, i.e., the "1 slot" case shown in Figure 5.6(b). Similar to the modes in the previous section, the circulating current flows in the tilted gold elliptical resonators of each unit cell show a characteristic anti-parallel behavior. However, we note that due to the existence of the CdO reflector layer which serves as a mirror, anti-parallel circulating currents are induced in the mirror layer and paired with its image in the gold elliptical resonators. In this case, in-plane magnetic dipole moments are induced by these anti-parallel circulating current pairs. They also present a characteristic anti-parallel behavior.

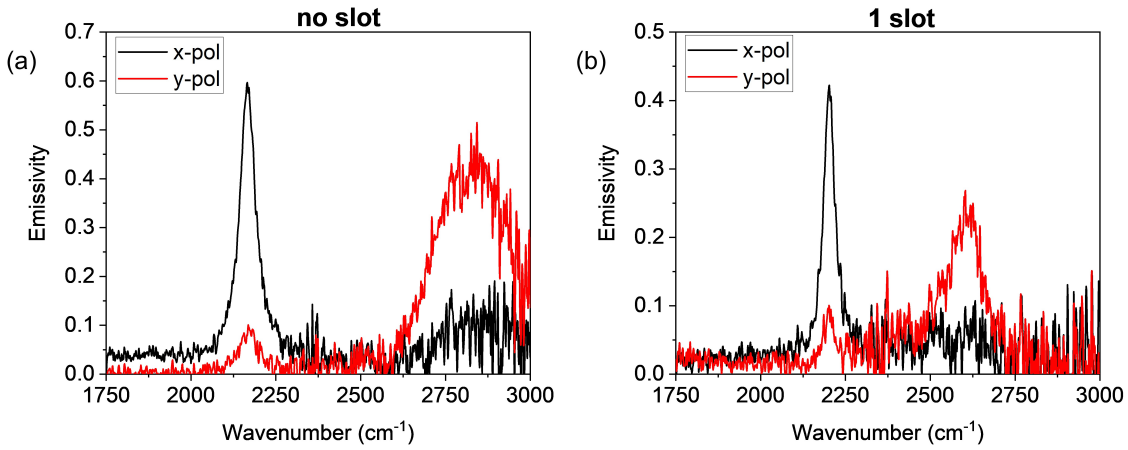

Figure 5.8: Figure 3. Optical response of the "0 slots" and "1 slot" metasurfaces. (a) Emissivity spectra of "0 slots" metasurface for x and y polarizations. (b) Emissivity spectra of "1 slot" metasurface for x and y polarizations. Measurements were conducted under 300 °C with the metasurface size fixed at 500 μm by 500 μm. Copyright © 2023 Mingze He

As shown by the in Figure 5.6(c), our proposed system is designed to support a resonance at around 2222 cm^{-1}, which overlaps with the absorption peak of N_2O, since one of our intended applications is NDIR sensing. Such a strong absorption peak comes from approaching the aforementioned critical coupling condition where the non-radiative Q factor from the intrinsic metal absorption equals the external (radiative) Q factor. It is worth noting that the radiative loss includes contributions from both the gap size associated with the spacer layer and the tilt angle of the gold elliptical resonators. By engineering the critical coupling

between the intrinsic material loss and the radiative loss of the quasi-BIC mode, we numerically obtain an ultra-narrowband absorptance peak with a Q of approximately 61 and near-unity absorptance of 96.5%. This level of performance is not achievable in traditional metallic designs. By introducing slots, the radiative Q factor is increased, leading to the deviation of the critical coupling condition. By adjusting geometry, we have been able to achieve an even higher Q of approximately 98, with the peak absorptance remaining high at 78.4%. Compared to other strategies, such as Tamm plasmon polariton thermal emitters [139], phonon polariton resonances [113], and photonic crystals [116], our design offers a well-balanced performance and fabrication complexity. It allows for a designable single-frequency peak ranging from 3 μm to 13 μm while having a relatively simple fabrication process. We also engineer the polarization responses of the plasmonic quasi-BIC metasurface. As seen in Figure 5.6(c), the spectra of the y polarization are shifted far away from the main peak from the x polarization. In this case, the emitted y polarized light is readily utilized as a calibration signal for dual-band gas detectors rather than degrading the sensitivity of the signal from the x polarized light.

Next, we numerically characterize the directivity of the thermal emission by model the absorptance of the "0 slots" metasurface under different incident angles. We note that the metasurface resonance can be stimulated when the incident light offers a nonzero electric field component along the x-axis. Consequently, we can sweep the angle of light incidence in two distinct planes (yz and xz) of the unit cell while ensuring effective metasurface performance. From this point forward, these two methods of exciting the system will then be referred to as "modes." In particular, the first mode (TE) pertains to light with a k vector in the yz plane and light polarization along the x-axis. The second mode (TM) relates to the k vector and polarization in the xz plane. We plot and compare the band structure of the TM mode and the TE mode, as shown in Figure 5.7(a) and (b). It's clear that the TE mode shows a flatter band than the TM mode. Therefore, the TM mode presents a directional emission with a narrower angular dispersion.

5.2.3 Experimental demonstration

To validate our design, we fabricated the "0 slots" and "1 slot" metasurface and measured their spectra responses. Figure 5.8 shows the emissivity of a 500 μm by 500 μm metasurface under 300°C for the "0 slots" and "1 slot" cases, respectively. The "0 slots" metasurface presents a Q factor of 42 and an emissivity of 56%. For the "1 slot" metasurface, the Q factor is increased to 53 while the emissivity is reduced to 40% due to the deviation from the critical coupling condition. The spectrum of the y polarization for the "0 slots" case shows a broad linewidth. This is due to the strong angular spread effects. While the y polarization for the "1 slot" case has a narrower linewidth and can be applied to calibrate the system drift of a dual-band gas detector.

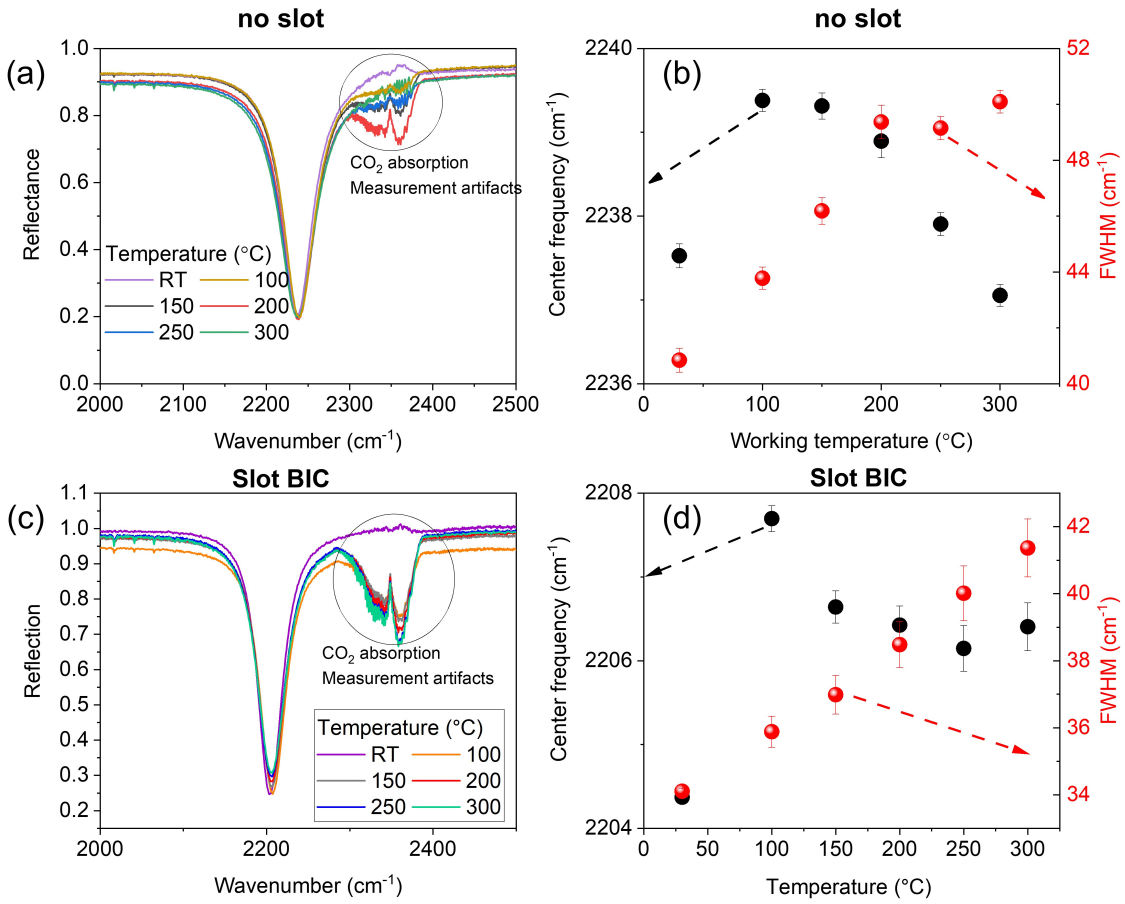

Figure 5.9: Optical responses of the "0 slots" metasurfaces with respect to temperature. (a) Reflectance spectra of "0 slots" metasurface under different temperatures. (b) Center frequency and full width at half maximum (FWHM) of the resonance peak under different temperatures for "0 slots" metasurface. (c) Reflectance spectra of "1 slot" metasurface under different temperatures. (d) Center frequency and full width at half maximum (FWHM) of the resonance peak under different temperatures "1 slot" metasurface. Copyright © 2023 Mingze He

Unlike all-dielectric designs, metallic nanostructures are less susceptible to temperature-dependent resonance variation as their permittivity is dominated by the imaginary part at mid-IR. To verify this benefit of our design, we characterize the optical response of both "0 slots" and "1 slot" cases when varying the operation temperature by measuring their reflection spectra. As shown in Figure 5.9, both 0 slots" and "1 slot" cases show a negligible peak drift, i.e., the center frequency shifts within 2 cm^{-1} in the temperature range of 25°C to 300°C. However, the linewidth of both cases is increased at high temperatures. This is due to increased carrier density in the doped CdO layer, leading to additional material losses.

Moreover, we investigate the influence of the slot width on the performance of the "1 slot" thermal emitter. As can be seen in Figure 5.10, when increasing the width of the slot, the absorption peak shifts to a larger wavenumber, the absorptance decreases due to the deviation from the critical coupling condition, while the

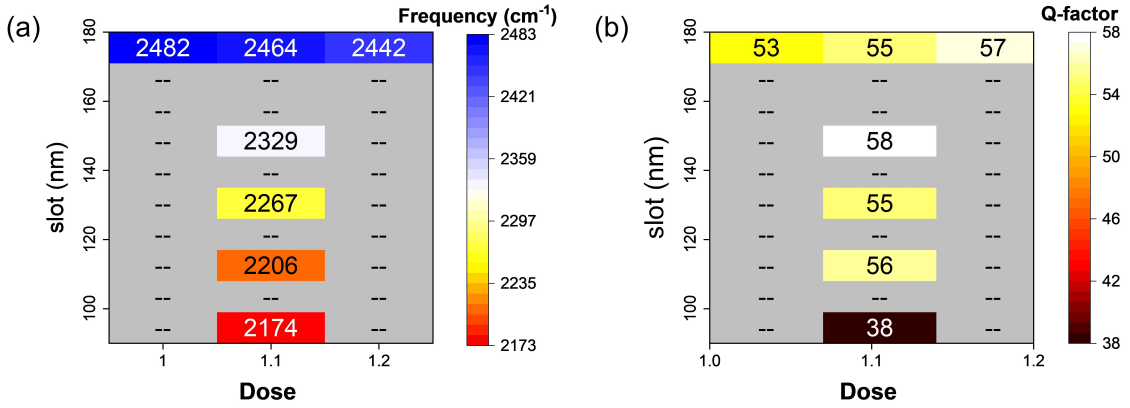

Figure 5.10: Impact of the slot width for "1 slot" metasurface. (a) Resonance wavelength shift with respect to the slot width. (b) Q factor with respect to the slot width. All measurements are conducted under 300°C for 200 μm by 200 μm metasurfaces. Copyright © 2023 Mingze He

Q factor also increases, meaning that the radiative Q factor is increased.

CHAPTER 6

Conclusion

In this dissertation, two novel platforms have been thoroughly studied that achieve high Q, strong field enhancement, and exposed hotspots simultaneously. New physical concepts and mechanisms that were previously unattainable have been demonbstrated. Applications of these platforms in optical trapping, optofluidics, and thermal emission control are presented.

The first platform involves metasurfaces governed by quasi-bound states in the continuum (BIC). Quasi-BIC metasurfaces have recently emerged as a powerful approach to offer high Qs and strong field enhancements, leading to several applications presented in this dissertation that investigate their enormous potential. In Chapter 2, a dielectric quasi-BIC metasurface composed of elliptical silicon resonators is used to demonstrate massive optical trapping of nanoparticles with low-intensity illumination. By cutting the tips of ellipses to break mirror symmetry, a new mechanism of inducing self-induced back-action is proposed. In Chapter 4, when illumination power is increased and the chamber height is large, heating effects dominate nanoparticle movements, inducing positive thermophoresis and fluid convection to rapidly transport and aggregate nanoparticles within millimeter scale to the center of the laser spot. This demonstration opens new frontiers in harnessing non-plasmonic nanophotonics for manipulating microfluidic dynamics. Moreover, the synergistic effects of optofluidics and high-Q all-dielectric metasurfaces hold enormous potential in high-sensitivity biosensing applications. The same elliptical resonators are also investigated at mid-IR wavelengths. In Chapter 5, by introducing slots, enhanced Qs and field enhancements are observed, with benefits for detecting coated proteins shown. Finally, plasmonic resonances can also take advantage of the quasi-BIC mode. A plasmonic metasurface, comprising gold elliptical resonators, is introduced as a thermal emitter, numerically achieving a Q of approximately 100 with almost near unity emissivity. By incorporating slots, the Q can be further enhanced. This was unattainable in earlier metal emitter designs, where the Q was limited to below 10.

The second platform is the bowtie photonic crystal nanobeam (BPCN), which supports extreme electric field localization in a deep-subwavelength region. BPCNs can achieve high Qs (10,000 - 100,000) and mode volumes comparable to plasmonic elements, making them ideal candidates for nanoparticle trapping. In Chapter 3, a BPCN nanotweezer system overcomes the limitations of previous PhC-based trapping techniques, which relied on pressure-driven flow or Brownian motion for deterministic transport of nanoparticles. These methods could only trap particles near the cavity and were very slow. The BPCN nanotweezer system, operating in water media at 1550 nm, utilizes strong electric field confinement and enhancement to absorb

light coupled into the defect and induce localized heating effects, which, in conjunction with negative thermophoresis and/or an applied AC electric field, initiates rapid microscale fluid motion and particle transport at velocities of tens of micrometers per second. This microscale fluidic transport enables on-demand long-range rapid delivery of single nano-objects to the bowtie hotspot, where they can be trapped and ”locked” in place.

CHAPTER 7

Publications and conference presentations

7.1 Publication list

1. **Yang, S.** and Ndukaife, J.C. "Optofluidic transport and particle trapping using an all-dielectric quasi-BICmetasurface", accepted by *Light: Science & Applications* (2023).

2. **Yang, S.**†, Allen, J.A.†, Hong, C., Arnold, K.P., Weiss, S.M. and Ndukaife, J.C. "Multiplexed long-rangeelectrohydrodynamic transport and nano-optical trapping with cascaded bowtie photonic crystalcavities". *Physical Review Letters* (2023), 130(8), pp.083802.

3. **Yang, S.**†, He, M.†, Hong, C., Caldwell, J.D. and Ndukaife, J.C. "Engineering Electromagnetic FieldDistribution and Resonance Quality Factor Using Slotted Quasi-BIC Metasurfaces". *Nano Letters* (2022),22(20), pp.8060-8067.

4. **Yang, S.**, Hong, C., Jiang, Y. and Ndukaife, J.C. "Nanoparticle trapping in a quasi-BIC system". *ACS Photonics* (2021), 8(7), pp.1961-1971.

5. Hong, C.†, **Yang, S.**† and Ndukaife, J.C. "Optofluidic control using plasmonic TiN bowtie nanoantenna". *Optical Materials Express* (2019), 9(3), pp.953-964.

6. Hong, C., **Yang, S.** and Ndukaife, J.C. "Stand-off trapping and manipulation of sub-10 nm objects and biomolecules using opto-thermo-electrohydrodynamic tweezers". *Nature Nanotechnology* (2020), 15(11), pp.908-913.

7. Hong, C., **Yang, S.**, Kravchenko, I.I. and Ndukaife, J.C. "Electrothermoplasmonic Trapping and DynamicManipulation of Single Colloidal Nanodiamond". *Nano Letters* (2021), 21(12), pp.4921-4927.

8. Hong, C., **Yang, S.**, and Ndukaife, J.C. "Exosomes trapping, manipulation and size-based separationusing opto-thermo-electrohydrodynamic tweezers", *Nanoscale Advances* (2023), doi: 10.1039/D3NA00101F.

9. Hong, C., **Yang, S.** and Ndukaife, J.C. "Nanomanipulation with Designer Thermoplasmonic Metasurface". *Nanoplasmonics* (Book chapter), IntechOpen (2020).

7.2 Conference presentation list

1. Talk: "Single-peak narrowband thermal emission of light based on plasmonic metasurfaces driven by quasi-BIC". *The 10th International Conference on Surface Plasmon Photonics (SPP10)*, Houston (2023).

2. Talk: “Multiplexed long-range electrohydrodynamic transport and nano-optical trapping with cascaded bowtie photonic crystal nanobeams”. *SPIE Optics + Photonics*, San Diego (2022).

3. Poster: “Optofluidic transport and particle trapping using all-dielectric quasi-BIC metasurfaces”. *Gordon Research Conference: Plasmonics and Nanophotonics*, Newry (2022).

4. Poster: “Nanoparticle trapping using quasi-BIC modes”. *Frontiers in Optics (FiO+LS)*, Online (2021).

5. Poster: “Nanoparticle trapping in a symmetry-breaking system”. *CLEO: Science and Innovations*, Online (2021)

References

[1] Qifeng Qiao, Ji Xia, Chengkuo Lee, and Guangya Zhou. Applications of photonic crystal nanobeam cavities for sensing. *Micromachines*, 9(11):541, 2018.

[2] Shuren Hu and Sharon M. Weiss. Design of photonic crystal cavities for extreme light concentration. *ACS Photonics*, 3:1647–1653, 2016.

[3] Shuren Hu, Marwan Khater, Rafael Salas-Montiel, Ernst Kratschmer, Sebastian Engelmann, William M.J. Green, and Sharon M. Weiss. Experimental realization of deep-subwavelength confinement in dielectric optical resonators. *Science Advances*, 4, 2018.

[4] Chia Wei Hsu, Bo Zhen, A. Douglas Stone, John D. Joannopoulos, and Marin Soljacic. Bound states in the continuum. *Nature Reviews Materials*, 1, 2016.

[5] John D. Joannopoulos, Steven G. Johnson, Joshua N. Winn, and Robert D. Meade. *Photonic Crystals: Molding the Flow of Light (Second Edition)*. Princeton University Press, 2 edition, 2008.

[6] Kirill Koshelev, Sergey Lepeshov, Mingkai Liu, Andrey Bogdanov, and Yuri Kivshar. Asymmetric metasurfaces with high- q resonances governed by bound states in the continuum. *Physical Review Letters*, 121:193903, 2018.

[7] Ershad Mohammadi, Ahad Tavakoli, Parisa Dehkhoda, Yasaman Jahani, Kosmas L Tsakmakidis, Andreas Tittl, and Hatice Altug. Accessible superchiral near-fields driven by tailored electric and magnetic resonances in all-dielectric nanostructures. *Acs Photonics*, 6(8):1939–1946, 2019.

[8] Kirill Koshelev, Andrey Bogdanov, and Yuri Kivshar. Meta-optics and bound states in the continuum. *Science Bulletin*, 64:836–842, 2019.

[9] Duk-Yong Choi, Yuri S. Kivshar, Dragomir N. Neshev, Mingkai Liu, Hatice Altug, Andreas Tittl, Filiz Yesilkoy, and Aleksandrs Leitis. Imaging-based molecular barcoding with pixelated dielectric metasurfaces. *Science*, 360:1105–1109, 2018.

[10] Filiz Yesilkoy, Eduardo R. Arvelo, Yasaman Jahani, Mingkai Liu, Andreas Tittl, Volkan Cevher, Yuri Kivshar, and Hatice Altug. Ultrasensitive hyperspectral imaging and biodetection enabled by dielectric metasurfaces, 6 2019.

[11] Kirill Koshelev, Sergey Kruk, Elizaveta Melik-Gaykazyan, Jae-Hyuck Choi, Andrey Bogdanov, Hong-Gyu Park, and Yuri Kivshar. Subwavelength dielectric resonators for nonlinear nanophotonics. *Science*, 367(6475):288–292, 2020.

[12] Kirill Koshelev, Sergey Kruk, Elizaveta Melik-Gaykazyan, Jae-Hyuck Choi, Andrey Bogdanov, Hong-Gyu Park, and Yuri Kivshar. Subwavelength dielectric resonators for nonlinear nanophotonics. *Science*, 367(6475):288–292, 2020.

[13] Kai Wang, Ethan Schonbrun, Paul Steinvurzel, and Kenneth B Crozier. Trapping and rotating nanoparticles using a plasmonic nano-tweezer with an integrated heat sink. *Nature communications*, 2(1):469, 2011.

[14] Brian J. Roxworthy, Kaspar D. Ko, Anil Kumar, Kin Hung Fung, Edmond K.C. Chow, Gang Logan Liu, Nicholas X. Fang, and Kimani C. Toussaint. Application of plasmonic bowtie nanoantenna arrays for optical trapping, stacking, and sorting. *Nano Letters*, 12:796–801, 2012.

[15] Weihua Zhang, Lina Huang, Christian Santschi, and Olivier J.F. Martin. Trapping and sensing 10 nm metal nanoparticles using plasmonic dipole antennas. *Nano Letters*, 10:1006–1011, 2010.

[16] J. Berthelot, S. S. Aćimović, M. L. Juan, M. P. Kreuzer, J. Renger, and R. Quidant. Three-dimensional manipulation with scanning near-field optical nanotweezers. *Nature Nanotechnology*, 9:295–299, 2014.

[17] Yuanjie Pang and Reuven Gordon. Optical trapping of a single protein. *Nano Letters*, 12:402–406, 2012.

[18] Daehan Yoo, Kargal L. Gurunatha, Han Kyu Choi, Daniel A. Mohr, Christopher T. Ertsgaard, Reuven Gordon, and Sang Hyun Oh. Low-power optical trapping of nanoparticles and proteins with resonant coaxial nanoaperture using 10 nm gap. *Nano Letters*, 18:3637–3642, 2018.

[19] Dong Kim, Jaesool Shim, Han-Sheng Chuang, and Kyung Chun Kim. Effect of array and shape of insulating posts on proteins focusing by direct current dielectrophoresis. *Journal of Mechanical Science and Technology*, 28:2629–2636, 2014.

[20] Ronald Pethig, Ying Huang, Xiao-Bo Wang, and Julian PH Burt. Positive and negative dielectrophoretic collection of colloidal particles using interdigitated castellated microelectrodes. *Journal of Physics D: Applied Physics*, 25(5):881, 1992.

[21] Joel Voldman, Martha L Gray, Mehmet Toner, and Martin A Schmidt. A microfabrication-based dynamic array cytometer. *Analytical chemistry*, 74(16):3984–3990, 2002.

[22] Yoon-Kyoung Cho, Suhyeon Kim, Kyusang Lee, Chinsung Park, Jeong-Gun Lee, and Christopher Ko. Bacteria concentration using a membrane type insulator-based dielectrophoresis in a plastic chip. *Electrophoresis*, 30(18):3153–3159, 2009.

[23] Meltem Elitas, Rodrigo Martinez-Duarte, Neeraj Dhar, John D McKinney, and Philippe Renaud. Dielectrophoresis-based purification of antibiotic-treated bacterial subpopulations. *Lab on a Chip*, 14(11):1850–1857, 2014.

[24] Pei Yu Chiou, Aaron T Ohta, and Ming C Wu. Massively parallel manipulation of single cells and microparticles using optical images. *Nature*, 436(7049):370–372, 2005.

[25] Hywel Morgan, Nicolas G Green, et al. Ac electrokinetics: colloids and nanoparticles. Technical report, Research Studies Press, 2003.

[26] Todd M Squires and Martin Z Bazant. Induced-charge electro-osmosis. *Journal of Fluid Mechanics*, 509:217–252, 2004.

[27] MR Bown and CD Meinhart. Ac electroosmotic flow in a dna concentrator. *Microfluidics and Nanofluidics*, 2:513–523, 2006.

[28] Meng Lian, Nazmul Islam, and Jie Wu. Particle line assembly/patterning by microfluidic ac electroosmosis. In *Journal of Physics: Conference Series*, volume 34, page 589. IOP Publishing, 2006.

[29] Pei-Yu Chiou, Aaron T Ohta, Arash Jamshidi, Hsin-Yi Hsu, and Ming C Wu. Light-actuated ac electroosmosis for nanoparticle manipulation. *Journal of Microelectromechanical Systems*, 17(3):525–531, 2008.

[30] Arash Jamshidi, Steven L Neale, Kyoungsik Yu, Peter J Pauzauskie, Peter James Schuck, Justin K Valley, Hsan-Yin Hsu, Aaron T Ohta, and Ming C Wu. Nanopen: dynamic, low-power, and light-actuated patterning of nanoparticles. *Nano letters*, 9(8):2921–2925, 2009.

[31] Meng Lian, Nazmul Islam, and Jie Wu. Ac electrothermal manipulation of conductive fluids and particles for lab-chip applications. *Iet Nanobiotechnology*, 1(3):36–43, 2007.

[32] Antonio González, Antonio Ramos, Hywel Morgan, Nicolas G Green, and Antonio Castellanos. Electrothermal flows generated by alternating and rotating electric fields in microsystems. *Journal of Fluid Mechanics*, 564:415–433, 2006.

[33] Justus C. Ndukaife, Alexander V. Kildishev, Agbai George Agwu Nnanna, Vladimir M. Shalaev, Steven T. Wereley, and Alexandra Boltasseva. Long-range and rapid transport of individual nano-objects by a hybrid electrothermoplasmonic nanotweezer. *Nature Nanotechnology*, 11:53–59, 2016.

[34] Jose Garcia-Guirado, Raúl A. Rica, Jaime Ortega, Judith Medina, Vanesa Sanz, Emilio Ruiz-Reina, and Romain Quidant. Overcoming diffusion-limited biosensing by electrothermoplasmonics. *ACS Photonics*, 5:3673–3679, 2018.

[35] H. T. Miyazaki, T. Kasaya, M. Iwanaga, B. Choi, Y. Sugimoto, and K. Sakoda. Dual-band infrared metasurface thermal emitter for co2 sensing. *Applied Physics Letters*, 105, 9 2014.

[36] Haixu Leng, Brian Szychowski, Marie Christine Daniel, and Matthew Pelton. Strong coupling and induced transparency at room temperature with single quantum dots and gap plasmons. *Nature Communications*, 9, 2018.

[37] Daniel Rodrigo, Odeta Limaj, Davide Janner, Dordaneh Etezadi, F. Javier García De Abajo, Valerio Pruneri, and Hatice Altug. Mid-infrared plasmonic biosensing with graphene. *Science*, 349:165–168, 2015.

[38] Linhan Lin, Xiaolei Peng, Xiaoling Wei, Zhangming Mao, Chong Xie, and Yuebing Zheng. Thermophoretic tweezers for low-power and versatile manipulation of biological cells. *ACS Nano*, 11:3147–3154, 3 2017.

[39] Alois Würger. Hydrodynamic boundary effects on thermophoresis of confined colloids. *Physical Review Letters*, 116:1–5, 2016.

[40] Aurelian John-Herpin, Andreas Tittl, and Hatice Altug. Quantifying the limits of detection of surface-enhanced infrared spectroscopy with grating order-coupled nanogap antennas. *ACS Photonics*, 5:4117–4124, 10 2018.

[41] Steven G Johnson, Shanhui Fan, Pierre R Villeneuve, John D Joannopoulos, and LA Kolodziejski. Guided modes in photonic crystal slabs. *Physical Review B*, 60(8):5751, 1999.

[42] Shanhui Fan and John D Joannopoulos. Analysis of guided resonances in photonic crystal slabs. *Physical Review B*, 65(23):235112, 2002.

[43] Shigeki Takahashi, Katsuyoshi Suzuki, Makoto Okano, Masahiro Imada, Takeshi Nakamori, Yuji Ota, Kenji Ishizaki, and Susumu Noda. Direct creation of three-dimensional photonic crystals by a top-down approach. *Nature materials*, 8(9):721–725, 2009.

[44] JS Foresi, Pierre R Villeneuve, J Ferrera, ER Thoen, G Steinmeyer, S Fan, JD Joannopoulos, LC Kimerling, Henry I Smith, and EP Ippen. Photonic-bandgap microcavities in optical waveguides. *nature*, 390(6656):143–145, 1997.

[45] Ph Lalanne, Solène Mias, and Jean-Paul Hugonin. Two physical mechanisms for boosting the quality factor to cavity volume ratio of photonic crystal microcavities. *Optics Express*, 12(3):458–467, 2004.

[46] Philippe Lalanne and Jean Paul Hugonin. Bloch-wave engineering for high-q, small-v microcavities. *IEEE Journal of Quantum Electronics*, 39(11):1430–1438, 2003.

[47] Philippe Velha, E Picard, T Charvolin, E Hadji, Jean-Claude Rodier, Philippe Lalanne, and David Peyrade. Ultra-high q/v fabry-perot microcavity on soi substrate. *Optics express*, 15(24):16090–16096, 2007.

[48] Masaya Notomi, E Kuramochi, and H Taniyama. Ultrahigh-q nanocavity with 1d photonic gap. *Optics Express*, 16(15):11095–11102, 2008.

[49] Qimin Quan, Parag B Deotare, and Marko Loncar. Photonic crystal nanobeam cavity strongly coupled to the feeding waveguide. *Applied Physics Letters*, 96(20):203102, 2010.

[50] Qimin Quan and Marko Loncar. Deterministic design of wavelength scale, ultra-high q photonic crystal nanobeam cavities. *Optics express*, 19(19):18529–18542, 2011.

[51] Sami I Halimi, Zhongyuan Fu, Francis O Afzal, Joshua A Allen, Shuren Hu, and Sharon M Weiss. Controlling the mode profile of photonic crystal nanobeam cavities with mix-and-match unit cells. *JOSA B*, 37(11):3401–3406, 2020.

[52] Daquan Yang, Huiping Tian, and Yuefeng Ji. High-q and high-sensitivity width-modulated photonic crystal single nanobeam air-mode cavity for refractive index sensing. *Applied optics*, 54(1):1–5, 2015.

[53] J. Wigner E. von Neumann. Über merkwürdige diskrete eigenwerte. *Phys. Z.*, 30:465–467 (in German), 1929.

[54] Jeongwon Lee, Bo Zhen, Song Liang Chua, Wenjun Qiu, John D. Joannopoulos, Marin Soljačić, and Ofer Shapira. Observation and differentiation of unique high-q optical resonances near zero wave vector in macroscopic photonic crystal slabs. *Physical Review Letters*, 109:1–5, 2012.

[55] Yonatan Plotnik, Or Peleg, Felix Dreisow, Matthias Heinrich, Stefan Nolte, Alexander Szameit, and Mordechai Segev. Experimental observation of optical bound states in the continuum. *Physical Review Letters*, 107:28–31, 2011.

[56] Shaimaa I Azzam, Vladimir M Shalaev, Alexandra Boltasseva, and Alexander V Kildishev. Formation of bound states in the continuum in hybrid plasmonic-photonic systems. *Physical review letters*, 121(25):253901, 2018.

[57] DC Marinica, AG Borisov, and SV Shabanov. Bound states in the continuum in photonics. *Physical review letters*, 100(18):183902, 2008.

[58] Mingkai Liu and Duk-Yong Choi. Extreme huygens' metasurfaces based on quasi-bound states in the continuum. *Nano letters*, 18(12):8062–8069, 2018.

[59] Mingkai Liu, David A Powell, Rui Guo, Ilya V Shadrivov, and Yuri S Kivshar. Polarization-induced chirality in metamaterials via optomechanical interaction. *Advanced Optical Materials*, 5(16):1600760, 2017.

[60] Christopher N. Lafratta. Optical tweezers for medical diagnostics. *Analytical and Bioanalytical Chemistry*, 405:5671–5677, 2013.

[61] Dhawal Choudhary, Alessandro Mossa, Milind Jadhav, and Ciro Cecconi. Bio-molecular applications of recent developments in optical tweezers. *Biomolecules*, 9:1–19, 2019.

[62] Shun Fa Wang, Tetsuhiro Kudo, Ken Ichi Yuyama, Teruki Sugiyama, and Hiroshi Masuhara. Optically evolved assembly formation in laser trapping of polystyrene nanoparticles at solution surface. *Langmuir*, 32:12488–12496, 2016.

[63] Tetsuhiro Kudo, Shun Fa Wang, Ken Ichi Yuyama, and Hiroshi Masuhara. Optical trapping-formed colloidal assembly with horns extended to the outside of a focus through light propagation. *Nano Letters*, 16:3058–3062, 2016.

[64] A. Ashkin, J. M. Dziedzic, J. E. Bjorkholm, and Steven Chu. Observation of a single-beam gradient force optical trap for dielectric particles. *Optics Letters*, 11:288–290, 1986.

[65] A. Ashkin, J. M. Dziedzic, and T. Yamane. Optical trapping and manipulation of single cells using infrared laser beams. *Nature*, 330:769–711, 1987.

[66] A. Ashkin and J. M. Dziedzic. Optical trapping and manipulation of viruses and bacteria. *Science*, 235:1517–1520, 1987.

[67] The Royal Swedish Academy of Sciences. Scientific background on the nobel prize in physics 2018: Groundbreaking inventions in laser physics. *Scientific Background on the Nobel Prize in Physics 2018: Groundbreaking inventions in Laser physics*, 50005:1–16, 2018.

[68] Mathieu L. Juan, Maurizio Righini, and Romain Quidant. Plasmon nano-optical tweezers. *Nature Photonics*, 5:349–356, 2011.

[69] Yuanjie Pang and Reuven Gordon. Optical trapping of 12 nm dielectric spheres using double-nanoholes in a gold film. *Nano Letters*, 11:3763–3767, 2011.

[70] Quanbo Jiang, Benoit Rogez, Jean-Benoît Claude, Guillaume Baffou, and Jérôme Wenger. Temperature measurement in plasmonic nanoapertures used for optical trapping. *ACS photonics*, 6(7):1763–1773, 2019.

[71] Steven Jones, Ahmed A Al Balushi, and Reuven Gordon. Raman spectroscopy of single nanoparticles in a double-nanohole optical tweezer system. *Journal of Optics*, 17(10):102001, 2015.

[72] OL Kantidze, AK Velichko, AV Luzhin, and SV Razin. Heat stress-induced dna damage. *Acta Naturae ( )*, 8(2 (29)):75–78, 2016.

[73] Brian J. Roxworthy, Abdul M. Bhuiya, Surya P. Vanka, and Kimani C. Toussaint. Understanding and controlling plasmon-induced convection. *Nature Communications 2014 5:1*, 5:1–8, 1 2014.

[74] Kenneth B. Crozier. Quo vadis, plasmonic optical tweezers? *Light: Science Applications 2019 8:1*, 8:1–6, 4 2019.

[75] Guillaume Baffou, Frank Cichos, and Romain Quidant. Applications and challenges of thermoplasmonics, 9 2020.

[76] Chuchuan Hong, Sen Yang, Ivan I. Kravchenko, and Justus C. Ndukaife. Electrothermoplasmonic trapping and dynamic manipulation of single colloidal nanodiamond. *Nano Letters*, 21:4921–4927, 2021.

[77] Ardeshir R. Rastinehad, Harry Anastos, Ethan Wajswol, Jared S. Winoker, John P. Sfakianos, Sai K. Doppalapudi, Michael R. Carrick, Cynthia J. Knauer, Bachir Taouli, Sara C. Lewis, Ashutosh K. Tewari, Jon A. Schwartz, Steven E. Canfield, Arvin K. George, Jennifer L. West, and Naomi J. Halas. Gold nanoshell-localized photothermal ablation of prostate tumors in a clinical pilot device study. *Proceedings of the National Academy of Sciences of the United States of America*, 116:18590–18596, 9 2019.

[78] Brian P. Timko, Tal Dvir, and Daniel S. Kohane. Remotely triggerable drug delivery systems. *Advanced Materials*, 22:4925–4943, 11 2010.

[79] Oara Neumann, Alexander S. Urban, Jared Day, Surbhi Lal, Peter Nordlander, and Naomi J. Halas. Solar vapor generation enabled by nanoparticles. *ACS Nano*, 7:42–49, 1 2013.

[80] Jon S. Donner, Guillaume Baffou, David McCloskey, and Romain Quidant. Plasmon-assisted optofluidics. volume 5, pages 5457–5462. American Chemical Society, 7 2011.

[81] Guillaume Baffou, Pascal Berto, Esteban Bermúdez Ureña, Romain Quidant, Serge Monneret, Julien Polleux, and Hervé Rigneault. Photoinduced heating of nanoparticle arrays. *ACS Nano*, 7:6478–6488, 8 2013.

[82] B. Ciraulo, J. Garcia-Guirado, I. de Miguel, J. Ortega Arroyo, and R. Quidant. Long-range optofluidic control with plasmon heating. *Nature Communications*, 12, 12 2021.

[83] Herbert A Pohl. The motion and precipitation of suspensoids in divergent electric fields. *Journal of applied Physics*, 22(7):869–871, 1951.

[84] A. Ramos, H. Morgan, N. G. Green, and A. Castellanos. Ac electrokinetics: a review of forces in microelectrode structures. *Journal of Physics D: Applied Physics*, 31:2338, 9 1998.

[85] Antonio Castellanos, Antonio Ramos, Antonio Gonzalez, Nicolas G Green, and Hywel Morgan. Electrohydrodynamics and dielectrophoresis in microsystems: scaling laws. *Journal of Physics D: Applied Physics*, 36(20):2584, 2003.

[86] Hywel Morgan, Nicolas Green, and Antonio Ramos. Nano-scale ac electrokinetics and electrohydrodynamics. *Journal of Physics D: Applied Physics*, 50(1):1–3, 2016.

[87] Eva-Maria Laux, Xenia Knigge, Frank F Bier, Christian Wenger, and Ralph Hölzel. Aligned immobilization of proteins using ac electric fields. *Small*, 12(11):1514–1520, 2016.

[88] John C Berg. *An introduction to interfaces & colloids: the bridge to nanoscience*. World Scientific, 2010.

[89] Herbert A Pohl and Ira Hawk. Separation of living and dead cells by dielectrophoresis. *Science*, 152(3722):647–649, 1966.

[90] Charles L Asbury, Alan H Diercks, and Ger Van Den Engh. Trapping of dna by dielectrophoresis. *Electrophoresis*, 23(16):2658–2666, 2002.

[91] Hywel Morgan and Nicolas G Green. Dielectrophoretic manipulation of rod-shaped viral particles. *Journal of Electrostatics*, 42(3):279–293, 1997.

[92] Nicolas G Green and Hywel Morgan. Dielectrophoretic separation of nano-particles. *Journal of Physics D: Applied Physics*, 30(11):L41, 1997.

[93] Rodrigo Martinez-Duarte. Microfabrication technologies in dielectrophoresis applications—a review. *Electrophoresis*, 33(21):3110–3132, 2012.

[94] Arthur Ashkin. Acceleration and trapping of particles by radiation pressure. *Physical review letters*, 24(4):156, 1970.

[95] Hans-Jürgen Butt and Michael Kappl. *Surface and interfacial forces*. John Wiley & Sons, 2018.

[96] AD2195547 Kaiser. On the internal structure of bacteriophage lambda. *The Journal of general physiology*, 49(6):171–178, 1966.

[97] NA Stakhin. Electrostriction in dielectrics and metals. *Russian physics journal*, 41(11):1107–1111, 1998.

[98] J. C. Ndukaife, V. M. Shalaev, and A. Boltasseva. Plasmonics–turning loss into gain. *Science*, 351:334–335, 2016.

[99] Vincent Studer, Anne Pépin, Yong Chen, and Armand Ajdari. An integrated ac electrokinetic pump in a microfluidic loop for fast and tunable flow control. *Analyst*, 129(10):944–949, 2004.

[100] Takuya Inoue, Menaka De Zoysa, Takashi Asano, and Susumu Noda. Realization of narrowband thermal emission with optical nanostructures. *Optica*, 2:27, 1 2015.

[101] Koray Aydin, Vivian E. Ferry, Ryan M. Briggs, and Harry A. Atwater. Broadband polarization-independent resonant light absorption using ultrathin plasmonic super absorbers. *Nature Communications*, 2, 2011.

[102] Andrej Lenert, David M. Bierman, Youngsuk Nam, Walker R. Chan, Ivan Celanović, Marin Soljačić, and Evelyn N. Wang. A nanophotonic solar thermophotovoltaic device. *Nature Nanotechnology*, 9:126–130, 2014.

[103] Walker R. Chan, Peter Bermel, Robert C.N. Pilawa-Podgurski, Christopher H. Marton, Klavs F. Jensen, Jay J. Senkevich, John D. Joannopoulos, Marin Soljačić, and Ivan Celanovic. Toward high-energy-density, high-efficiency, and moderate-temperature chip-scale thermophotovoltaics. *Proceedings of the National Academy of Sciences of the United States of America*, 110:5309–5314, 4 2013.

[104] Masahiro Suemitsu, Takashi Asano, Takuya Inoue, and Susumu Noda. High-efficiency thermophotovoltaic system that employs an emitter based on a silicon rod-type photonic crystal. *ACS Photonics*, 7:80–87, 1 2020.

[105] Hitoshi Sai and Hiroo Yugami. Thermophotovoltaic generation with selective radiators based on tungsten surface gratings. *Applied Physics Letters*, 85:3399, 10 2004.

[106] Marin Soljačić, Ivan Celanovic, Yi Xiang Yeng, John D. Joannopoulos, Veronika Rinnerbauer, Jay J. Senkevich, and Walker R. Chan. High-temperature stability and selective thermal emission of polycrystalline tantalum photonic crystals. *Optics Express, Vol. 21, Issue 9, pp. 11482-11491*, 21:11482–11491, 5 2013.

[107] Xianliang Liu, Talmage Tyler, Tatiana Starr, Anthony F. Starr, Nan Marie Jokerst, and Willie J. Padilla. Taming the blackbody with infrared metamaterials as selective thermal emitters. *Physical Review Letters*, 107, 7 2011.

[108] Xianliang Liu, Tatiana Starr, Anthony F. Starr, and Willie J. Padilla. Infrared spatial and frequency selective metamaterial with near-unity absorbance. *Physical Review Letters*, 104, 5 2010.

[109] N. I. Landy, S. Sajuyigbe, J. J. Mock, D. R. Smith, and W. J. Padilla. Perfect metamaterial absorber. *Physical Review Letters*, 100, 5 2008.

[110] Che Qu, Shaojie Ma, Jiaming Hao, Meng Qiu, Xin Li, Shiyi Xiao, Ziqi Miao, Ning Dai, Qiong He, Shulin Sun, and Lei Zhou. Tailor the functionalities of metasurfaces based on a complete phase diagram. *Physical Review Letters*, 115, 12 2015.

[111] Juan Wang, Thomas Weber, Andreas Aigner, Stefan A Maier, and Andreas Tittl. Mirror-coupled plasmonic bound states in the continuum for tunable perfect absorption. *arXiv*.

[112] J.J. Greffet, R. Carminati, K. Joulain, J.P. Mulet, S. Mainguy, and Y. Chen. Coherent emission of light by thermal sources. *Nature*, 2002.

[113] Guanyu Lu, Christopher R. Gubbin, J. Ryan Nolen, Thomas Folland, Marko J. Tadjer, Simone de Liberato, and Joshua D. Caldwell. Engineering the spectral and spatial dispersion of thermal emission via polariton-phonon strong coupling. *Nano Letters*, 21:1831–1838, 2 2021.

[114] W. Streyer, S. Law, A. Rosenberg, C. Roberts, V. A. Podolskiy, A. J. Hoffman, and D. Wasserman. Engineering absorption and blackbody radiation in the far-infrared with surface phonon polaritons on gallium phosphide. *Applied Physics Letters*, 104:131105, 4 2014.

[115] Austin Howes, Joshua R. Nolen, Joshua D. Caldwell, and Jason Valentine. Near-unity and narrowband thermal emissivity in balanced dielectric metasurfaces. *Advanced Optical Materials*, 8, 2 2020.

[116] Menaka De Zoysa, Takashi Asano, Keita Mochizuki, Ardavan Oskooi, Takuya Inoue, and Susumu Noda. Conversion of broadband to narrowband thermal emission through energy recycling. *Nature Photonics*, 6:535–539, 8 2012.

[117] Takuya Inoue, Takashi Asano, Menaka De Zoysa, Ardavan Oskooi, and Susumu Noda. Design of single-mode narrow-bandwidth thermal emitters for enhanced infrared light sources. *Journal of the Optical Society of America B*, 2012.

[118] Takuya Inoue, Menaka De Zoysa, Takashi Asano, and Susumu Noda. Filter-free nondispersive infrared sensing using narrow-bandwidth mid-infrared thermal emitters. *Applied Physics Express*, 7, 1 2014.

[119] Takuya Inoue, Menaka De Zoysa, Takashi Asano, and Susumu Noda. Single-peak narrow-bandwidth mid-infrared thermal emitters based on quantum wells and photonic crystals. *Applied Physics Letters*, 102, 5 2013.

[120] Masahiro Imada, Susumu Noda, Alongkarn Chutinan, Takashi Tokuda, Michio Murata, and Goro Sasaki. Coherent two-dimensional lasing action in surface-emitting laser with triangular-lattice photonic crystal structure. *Applied physics letters*, 75(3):316–318, 1999.

[121] Binbin Weng, Jiangang Ma, Lai Wei, Lin Li, Jijun Qiu, Jian Xu, and Zhisheng Shi. Room temperature mid-infrared surface-emitting photonic crystal laser on silicon. *Applied Physics Letters*, 99(22):221110, 2011.

[122] Binbin Weng, Jiangang Ma, Lai Wei, Jian Xu, Gang Bi, and Zhisheng Shi. Mid-infrared surface-emitting photonic crystal microcavity light emitter on silicon. *Applied Physics Letters*, 97(23):231103, 2010.

[123] AB Ikyo, IP Marko, K Hild, AR Adams, S Arafin, M-C Amann, and SJ Sweeney. Temperature stable mid-infrared gainassb/gasb vertical cavity surface emitting lasers (vcsels). *Scientific Reports*, 6(1):19595, 2016.

[124] Christopher A Curwen, John L Reno, and Benjamin S Williams. Broadband continuous single-mode tuning of a short-cavity quantum-cascade vecsel. *Nature Photonics*, 13(12):855–859, 2019.

[125] Jianbo Yu, Binze Ma, Rui Qin, Pintu Ghosh, Min Qiu, and Qiang Li. High-q absorption in all-dielectric photonics assisted by metamirrors. *ACS Photonics*, 9(10):3391–3397, 2022.

[126] J Ryan Nolen, Adam C Overvig, Michele Cotrufo, and Andrea Alù. Arbitrarily polarized and unidirectional emission from thermal metasurfaces. *arXiv*.

[127] Prasad P. Iyer, Ryan A. DeCrescent, Yahya Mohtashami, Guillaume Lheureux, Nikita A. Butakov, Abdullah Alhassan, Claude Weisbuch, Shuji Nakamura, Steven P. DenBaars, and Jon A. Schuller. Unidirectional luminescence from ingan/gan quantum-well metasurfaces. *Nature Photonics*, 14:543–548, 9 2020.

[128]

[129] J. D. Hoyland and D. Sands. Temperature dependent refractive index of amorphous silicon determined by time-resolved reflectivity during low fluence excimer laser heating. *Journal of Applied Physics*, 99, 2006.

[130] Chi Yin Yang, Jhen Hong Yang, Zih Ying Yang, Zhong Xing Zhou, Mao Guo Sun, Viktoriia E. Babicheva, and Kuo Ping Chen. Nonradiating silicon nanoantenna metasurfaces as narrowband absorbers. *ACS Photonics*, 5:2596–2601, 7 2018.

[131] Honghao Yu, Qing Xiong, Hong Wang, Ye Zhang, Yi Wang, Jianjun Lai, and Changhong Chen. Near-infrared free carrier absorption enhancement of heavily doped silicon in all-dielectric metasurface. *Applied Physics Letters*, 117:134101, 9 2020.

[132] Lorelle N. Pye, Ayman F. Abouraddy, Walker D. Larson, Soroush Shabahang, Lane Martin, and Massimo L. Villinger. Octave-spanning coherent perfect absorption in a thin silicon film. *Optics Letters, Vol. 42, Issue 1, pp. 151-154*, 42:151–154, 1 2017.

[133] Jingyi Tian, Hao Luo, Qiang Li, Xuelu Pei, Kaikai Du, and Min Qiu. Near-infrared super-absorbing all-dielectric metasurface based on single-layer germanium nanostructures. *Laser Photonics Reviews*, 12:1800076, 9 2018.

[134] Jianbo Yu, Binze Ma, Ao Ouyang, Pintu Ghosh, Hao Luo, Arnab Pattanayak, Sandeep Kaur, Min Qiu, Pavel Belov, and Qiang Li. Dielectric super-absorbing metasurfaces via pt symmetry breaking. *Optica*, 8:1290, 10 2021.

[135] M. Kaliteevski, I. Iorsh, S. Brand, R. A. Abram, J. M. Chamberlain, A. V. Kavokin, and I. A. Shelykh. Tamm plasmon-polaritons: Possible electromagnetic states at the interface of a metal and a dielectric bragg mirror. *Physical Review B - Condensed Matter and Materials Physics*, 76:165415, 10 2007.

[136] Atsushi Sakurai, Kyohei Yada, Tetsushi Simomura, Shenghong Ju, Makoto Kashiwagi, Hideyuki Okada, Tadaaki Nagao, Koji Tsuda, and Junichiro Shiomi. Ultranarrow-band wavelength-selective thermal emission with aperiodic multilayered metamaterials designed by bayesian optimization. *ACS Central Science*, 5:319–326, 2 2019.

[137] Zhiyu Wang, J. Kenji Clark, Ya Lun Ho, Sebastian Volz, Hirofumi Daiguji, Jean Jacques Delaunay, and Jean Jacques Delaunay. Ultranarrow and wavelength-tunable thermal emission in a hybrid metal-optical tamm state structure. *ACS Photonics*, 7:1569–1576, 6 2020.

[138] Zhiyu Wang, J. Kenji Clark, Ya Lun Ho, Bertrand Vilquin, Hirofumi Daiguji, and Jean Jacques Delaunay. Narrowband thermal emission realized through the coupling of cavity and tamm plasmon resonances. *ACS Photonics*, 5:2446–2452, 6 2018.

[139] Mingze He, J. Ryan Nolen, Josh Nordlander, Angela Cleri, Nathaniel S. McIlwaine, Yucheng Tang, Guanyu Lu, Thomas G. Folland, Bennett A. Landman, Jon Paul Maria, and Joshua D. Caldwell. Deterministic inverse design of tamm plasmon thermal emitters with multi-resonant control. *Nature Materials*, 20:1663–1669, 12 2021.

[140] D. Costantini, A. Lefebvre, A. L. Coutrot, I. Moldovan-Doyen, J. P. Hugonin, S. Boutami, F. Marquier, H. Benisty, and J. J. Greffet. Plasmonic metasurface for directional and frequency-selective thermal emission. *Physical Review Applied*, 4, 7 2015.

[141] Sungho Kang, Zhenyun Qian, Vageeswar Rajaram, Sila Deniz Calisgan, Andrea Alù, and Matteo Rinaldi. Ultra-narrowband metamaterial absorbers for high spectral resolution infrared spectroscopy. *Advanced Optical Materials*, 7, 1 2019.

[142] Takuya Inoue, Menaka De Zoysa, Takashi Asano, and Susumu Noda. Realization of dynamic thermal emission control. *Nature Materials*, 13:928–931, 10 2014.

[143] Takuya Inoue, Menaka De Zoysa, Takashi Asano, and Susumu Noda. High-q mid-infrared thermal emitters operating with high power-utilization efficiency. *Optics Express*, 24:15101, 6 2016.

[144] Nir Dahan, Avi Niv, Gabriel Biener, Yuri Gorodetski, Vladimir Kleiner, and Erez Hasman. Extraordinary coherent thermal emission from sic due to coupled resonant cavities. *Journal of Heat Transfer*, 130:1–5, 11 2008.

[145] Tao Wang, Peining Li, Dmitry N. Chigrin, Alexander J. Giles, Francisco J. Bezares, Orest J. Glembocki, Joshua D. Caldwell, and Thomas Taubner. Phonon-polaritonic bowtie nanoantennas: Controlling infrared thermal radiation at the nanoscale. *ACS Photonics*, 4:1753–1760, 7 2017.

[146] Lu Cai, Qiang Li, Jianbo Yu, Hao Luo, Kaikai Du, and Min Qiu. Simultaneous single-peak and narrowband thermal emission enabled by hybrid metal-polar dielectric structures. *Applied Physics Letters*, 115, 8 2019.

[147] Roberto Fenollosa, Fernando Ramiro-Manzano, Moisés Garín, and Ramón Alcubilla. Thermal emission of silicon at near-infrared frequencies mediated by mie resonances. *ACS Photonics*, 6:3174–3179, 12 2019.

[148] Tun Cao, Xinyu Zhang, Weiling Dong, Li Lu, Xilin Zhou, Xin Zhuang, Junhong Deng, Xing Cheng, Guixin Li, and Robert E. Simpson. Tuneable thermal emission using chalcogenide metasurface. *Advanced Optical Materials*, 6, 8 2018.

[149] Mikhail A. Kats, Romain Blanchard, Shuyan Zhang, Patrice Genevet, Changhyun Ko, Shriram Ramanathan, and Federico Capasso. Vanadium dioxide as a natural disordered metamaterial: Perfect thermal emission and large broadband negative differential thermal emittance. *Physical Review X*, 3:041004, 10 2014.

[150] Kaikai Du, Qiang Li, Yanbiao Lyu, Jichao Ding, Yue Lu, Zhiyuan Cheng, and Min Qiu. Control over emissivity of zero-static-power thermal emitters based on phase-changing material gst. *Light: Science Applications 2017 6:1*, 6:e16194–e16194, 7 2016.

[151] Bojan Milic, Johan O.L. Andreasson, Daniel W. Hogan, and Steven M. Block. Intraflagellar transport velocity is governed by the number of active kif17 and kif3ab motors and their motility properties under load. *Proceedings of the National Academy of Sciences of the United States of America*, 114:E6830–E6838, 2017.

[152] Giro Cecconi, Elizabeth A. Shank, Carlos Bustamante, and Susan Marqusee. Biochemistry: Direct observation of the three-state folding of a single protein molecule. *Science*, 309:2057–2060, 2005.

[153] Teresa Naranjo, Kateryna M. Lemishko, Sara de Lorenzo, Álvaro Somoza, Felix Ritort, Emilio M. Pérez, and Borja Ibarra. Dynamics of individual molecular shuttles under mechanical force. *Nature Communications*, 9:1–7, 2018.

[154] Chuchuan Hong, Sen Yang, and Justus C. Ndukaife. Stand-off trapping and manipulation of sub-10 nm objects and biomolecules using opto-thermo-electrohydrodynamic tweezers. *Nature Nanotechnology*, page 41565, 2020.

[155] Justus C. Ndukaife, Yi Xuan, Agbai George Agwu Nnanna, Alexander V. Kildishev, Vladimir M. Shalaev, Steven T. Wereley, and Alexandra Boltasseva. High-resolution large-ensemble nanoparticle trapping with multifunctional thermoplasmonic nanohole metasurface. *ACS Nano*, 12:5376–5384, 2018.

[156] Mathieu L. Juan, Reuven Gordon, Yuanjie Pang, Fatima Eftekhari, and Romain Quidant. Self-induced back-action optical trapping of dielectric nanoparticles. *Nature Physics*, 5:915–919, 2009.

[157] Amr A.E. Saleh and Jennifer A. Dionne. Toward efficient optical trapping of sub-10-nm particles with coaxial plasmonic apertures. *Nano Letters*, 12:5581–5586, 2012.

[158] Abhay Kotnala and Reuven Gordon. Quantification of high-efficiency trapping of nanoparticles in a double nanohole optical tweezer. *Nano Letters*, 14:853–856, 2014.

[159] Zhe Xu, Wuzhou Song, and Kenneth B. Crozier. Direct particle tracking observation and brownian dynamics simulations of a single nanoparticle optically trapped by a plasmonic nanoaperture. *ACS Photonics*, 5:2850–2859, 2018.

[160] Kai Wang and Kenneth B. Crozier. Plasmonic trapping with a gold nanopillar. *ChemPhysChem*, 13:2639–2648, 8 2012.

[161] Chuchuan Hong, Sen Yang, and Justus C. Ndukaife. Optofluidic control using plasmonic tin bowtie nanoantenna. *Optical Materials Express*, 9:953, 2019.

[162] V. Garcés-Chávez, R. Quidant, P. J. Reece, G. Badenes, L. Torner, and K. Dholakia. Extended organization of colloidal microparticles by surface plasmon polariton excitation. *Physical Review B - Condensed Matter and Materials Physics*, 73:1–5, 2006.

[163] Yoshito Tanaka and Keiji Sasaki. Optical trapping through the localized surface-plasmon resonance of engineered gold nanoblock pairs. *Optics Express*, 19:17462, 2011.

[164] Yoshito Tanaka and Keiji Sasaki. Efficient optical trapping using small arrays of plasmonic nanoblock pairs. *Applied Physics Letters*, 100:21102, 1 2012.

[165] Domna G. Kotsifaki, Viet Giang Truong, and Síle Nic Chormaic. Dynamic multiple nanoparticle trapping using metamaterial plasmonic tweezers. *Applied Physics Letters*, 118, 2021.

[166] Xue Han, Viet Giang Truong, and Sile Nic Chormaic. Sequential trapping of single nanoparticles using a gold plasmonic nanohole array. *Photonics Research*, 6, 2018.

[167] Nanfang Yu, Patrice Genevet, Mikhail A. Kats, Francesco Aieta, Jean Philippe Tetienne, Federico Capasso, and Zeno Gaburro. Light propagation with phase discontinuities: Generalized laws of reflection and refraction. *Science*, 334:333–337, 2011.

[168] Seyedeh Mahsa Kamali, Ehsan Arbabi, Amir Arbabi, and Andrei Faraon. A review of dielectric optical metasurfaces for wavefront control. *Nanophotonics*, 7:1041–1068, 6 2018.

[169] Nanfang Yu and Federico Capasso. Flat optics with designer metasurfaces. *Nature Materials*, 13:139–150, 2 2014.

[170] Amir Arbabi, Yu Horie, Mahmood Bagheri, and Andrei Faraon. Dielectric metasurfaces for complete control of phase and polarization with subwavelength spatial resolution and high transmission. *Nature Nanotechnology*, 10:937–943, 11 2015.

[171] Yuanmu Yang, Wenyi Wang, Parikshit Moitra, Ivan I. Kravchenko, Dayrl P. Briggs, and Jason Valentine. Dielectric meta-reflectarray for broadband linear polarization conversion and optical vortex generation. *Nano Letters*, 14:1394–1399, 2014.

[172] Sen Yang, Chuang Li, Tongming Liu, Haixia Da, Rui Feng, Donghua Tang, Fangkui Sun, and Weiqiang Ding. Simple and polarization-independent dammann grating based on all-dielectric nanorod array. *Journal of Optics (United Kingdom)*, 19, 2017.

[173] Tongming Liu, Sen Yang, Donghua Tang, Haixia Da, Rui Feng, Tongtong Zhu, Fangkui Sun, and Weiqiang Ding. Polarization conversion based on an all-dielectric metasurface for optical fiber applications. *Journal of Physics D: Applied Physics*, 50, 2017.

[174] Elham Nazemosadat, Mikael Mazur, Sergey Kruk, Ivan Kravchenko, Joel Carpenter, Jochen Schröder, Peter A. Andrekson, Magnus Karlsson, and Yuri Kivshar. Dielectric broadband metasurfaces for fiber mode-multiplexed communications. *Advanced Optical Materials*, 7:1–7, 2019.

[175] Wei Ting Chen, Alexander Y. Zhu, Vyshakh Sanjeev, Mohammadreza Khorasaninejad, Zhujun Shi, Eric Lee, and Federico Capasso. A broadband achromatic metalens for focusing and imaging in the visible. *Nature Nanotechnology 2017 13:3*, 13:220–226, 1 2018.

[176] Mohammadreza Khorasaninejad, Wei Ting Chen, Robert C. Devlin, Jaewon Oh, Alexander Y. Zhu, and Federico Capasso. Metalenses at visible wavelengths: Diffraction-limited focusing and subwavelength resolution imaging. *Science*, 352:1190–1194, 6 2016.

[177] Jae Woong Yoon, Seok Ho Song, and Robert Magnusson. Critical field enhancement of asymptotic optical bound states in the continuum. *Scientific Reports*, 5:1–8, 2015.

[178] Zarina F. Sadrieva, Ivan S. Sinev, Kirill L. Koshelev, Anton Samusev, Ivan V. Iorsh, Osamu Takayama, Radu Malureanu, Andrey A. Bogdanov, and Andrei V. Lavrinenko. Transition from optical bound states in the continuum to leaky resonances: Role of substrate and roughness. *ACS Photonics*, 4:723–727, 2017.

[179] Abdoulaye Ndao, Liyi Hsu, Wei Cai, Jeongho Ha, Junhee Park, Rushin Contractor, Yuhwa Lo, and Boubacar Kanté. Differentiating and quantifying exosome secretion from a single cell using quasi-bound states in the continuum. *Nanophotonics*, 2020.

[180] Kirill Koshelev, Sergey Kruk, Elizaveta Melik-Gaykazyan, Jae Hyuck Choi, Andrey Bogdanov, Hong Gyu Park, and Yuri Kivshar. Subwavelength dielectric resonators for nonlinear nanophotonics. *Science*, 367:288–292, 2020.

[181] Luca Carletti, Kirill Koshelev, Costantino De Angelis, and Yuri Kivshar. Giant nonlinear response at the nanoscale driven by bound states in the continuum. *Physical Review Letters*, 121:33903, 2018.

[182] Kirill Koshelev, Yutao Tang, Kingfai Li, Duk Yong Choi, Guixin Li, and Yuri Kivshar. Nonlinear metasurfaces governed by bound states in the continuum. *ACS Photonics*, 6:1639–1644, 2019.

[183] Kirill Koshelev, Yasaman Jahani, Andreas Tittl, Hatice Altug, and Yuri Kivshar. Enhanced circular dichroism and chiral sensing with bound states in the continuum. *2019 Conference on Lasers and Electro-Optics, CLEO 2019 - Proceedings*, pages 4–5, 2019.

[184] Xuefan Yin, Jicheng Jin, Marin Soljačić, Chao Peng, and Bo Zhen. Observation of topologically enabled unidirectional guided resonances. *Nature*, 580:467–471, 2020.

[185] Ashok Kodigala, Thomas Lepetit, Qing Gu, Babak Bahari, Yeshaiahu Fainman, and Boubacar Kanté. Lasing action from photonic bound states in continuum. *Nature*, 541:196–199, 2017.

[186] Jeongwon Lee, Bo Zhen, Song Liang Chua, Wenjun Qiu, John D. Joannopoulos, Marin Soljačić, and Ofer Shapira. Observation and differentiation of unique high-q optical resonances near zero wave vector in macroscopic photonic crystal slabs. *Physical Review Letters*, 109:1–5, 2012.

[187] Zhe Xu, Wuzhou Song, and Kenneth B. Crozier. Optical trapping of nanoparticles using all-silicon nanoantennas. *ACS Photonics*, 5:4993–5001, 2018.

[188] Eun Soo Kwak, Tiberiu Dan Onuta, Dragos Amarie, Radislav Potyrailo, Barry Stein, Stephen C. Jacobson, W. L. Schaich, and Bogdan Dragnea. Optical trapping with integrated near-field apertures. *Journal of Physical Chemistry B*, 108:13607–13612, 2004.

[189] Chang Chen, Mathieu L. Juan, Yi Li, Guido Maes, Gustaaf Borghs, Pol Van Dorpe, and Romain Quidant. Enhanced optical trapping and arrangement of nano-objects in a plasmonic nanocavity. *Nano Letters*, 12:125–132, 2012.

[190] Pau Mestres, Johann Berthelot, Srdjan S. Acimovic, and Romain Quidant. Unraveling the optomechanical nature of plasmonic trapping. *Light: Science and Applications*, 5:1–6, 2016.

[191] Tongtong Zhu, Yongyin Cao, Lin Wang, Zhongquan Nie, Tun Cao, Fangkui Sun, Zehui Jiang, Manuel Nieto-Vesperinas, Yongmin Liu, Cheng Wei Qiu, and Weiqiang Ding. Self-induced backaction optical pulling force. *Physical Review Letters*, 120:1–6, 2018.

[192] Nicolas Descharmes, Ulagalandha Perumal Dharanipathy, Zhaolu Diao, Mario Tonin, and Romuald Houdré. Observation of backaction and self-induced trapping in a planar hollow photonic crystal cavity. *Physical Review Letters*, 110:1–4, 2013.

[193] Lukas Neumeier, Romain Quidant, and Darrick E. Chang. Self-induced back-action optical trapping in nanophotonic systems. *New Journal of Physics*, 17:123008, 2015.

[194] P. Grahn, A. Shevchenko, and M. Kaivola. Electromagnetic multipole theory for optical nanomaterials. *New Journal of Physics*, 14, 2012.

[195] Markus Aspelmeyer, Tobias J. Kippenberg, and Florian Marquardt. Cavity optomechanics. *Reviews of Modern Physics*, 86:1391–1452, 2014.

[196] Chihhui Wu, Nihal Arju, Glen Kelp, Jonathan A. Fan, Jason Dominguez, Edward Gonzales, Emanuel Tutuc, Igal Brener, and Gennady Shvets. Spectrally selective chiral silicon metasurfaces based on infrared fano resonances. *Nature Communications*, 5:1–9, 2014.

[197] Yuanmu Yang, Ivan I. Kravchenko, Dayrl P. Briggs, and Jason Valentine. All-dielectric metasurface analogue of electromagnetically induced transparency. *Nature Communications*, 5:1–7, 12 2014.

[198] Qing Hu, Di Hu Xu, Yu Zhou, Ru Wen Peng, Ren Hao Fan, Nicholas X. Fang, Qian Jin Wang, Xian Rong Huang, and Mu Wang. Position-sensitive spectral splitting with a plasmonic nanowire on silicon chip. *Scientific Reports*, 3, 10 2013.

[199] Jon A. Schuller, Edward S. Barnard, Wenshan Cai, Young Chul Jun, Justin S. White, and Mark L. Brongersma. Plasmonics for extreme light concentration and manipulation. *Nature Materials*, 9:193–204, 2010.

[200] Yingying Zhu, Hao Jing, Ru Wen Peng, Cheng Yao Li, Jie He, Bo Xiong, and Mu Wang. Realizing anderson localization of surface plasmon polaritons and enhancing their interactions with excitons in 2d disordered nanostructures. *Applied Physics Letters*, 116:201106, 5 2020.

[201] Xiang Xiong, Siwen Wei, Wenjie Tang, Ruwen Peng, Ruwen Peng, Mu Wang, Mu Wang, and Mu Wang. Realizing transmissive and reflective focusing with an on-chip metalens. *Optics Letters, Vol. 47, Issue 15, pp. 3696-3699*, 47:3696–3699, 8 2022.

[202] Hatice Altug, Sang Hyun Oh, Stefan A. Maier, and Jiří Homola. Advances and applications of nanophotonic biosensors. *Nature Nanotechnology 2022 17:1*, 17:5–16, 1 2022.

[203] J. Berthelot, S. S. Aćimović, M. L. Juan, M. P. Kreuzer, J. Renger, and R. Quidant. Three-dimensional manipulation with scanning near-field optical nanotweezers. *Nature Nanotechnology 2014 9:4*, 9:295–299, 3 2014.

[204] Michael Geiselmann, Renaud Marty, Jan Renger, F. Javier García De Abajo, and Romain Quidant. Deterministic optical-near-field-assisted positioning of nitrogen-vacancy centers. *Nano Letters*, 14:1520–1525, 3 2014.

[205] John D. Joannopoulos, Steven G. Johnson, Joshua N. Winn, and Robert D. Meade. *Photonic crystals: Molding the flow of light (Second Edition)*. Princeton University Press, 10 2011.

[206] Shuren Hu, Marwan Khater, Rafael Salas-Montiel, Ernst Kratschmer, Sebastian Engelmann, William M.J. Green, and Sharon M. Weiss. Experimental realization of deep-subwavelength confinement in dielectric optical resonators. *Science Advances*, 4, 2018.

[207] Yih Fan Chen, Xavier Serey, Rupa Sarkar, Peng Chen, and David Erickson. Controlled photonic manipulation of proteins and other nanomaterials. *Nano Letters*, 12:1633–1637, 2012.

[208] Xavier Serey, Sudeep Mandal, Yih Fan Chen, and David Erickson. Dna transport and delivery in thermal gradients near optofluidic resonators. *Physical Review Letters*, 108:1–5, 2012.

[209] Yan Gao and Yaocheng Shi. Design of a single nanoparticle trapping device based on bow-tie-shaped photonic crystal nanobeam cavities. *IEEE Photonics Journal*, 11, 6 2019.

[210] Justus C. Ndukaife, Alexander V. Kildishev, Agbai George Agwu Nnanna, Vladimir M. Shalaev, Steven T. Wereley, and Alexandra Boltasseva. Long-range and rapid transport of individual nano-objects by a hybrid electrothermoplasmonic nanotweezer. *Nature Nanotechnology*, 11:53–59, 2016.

[211] Francis O. Afzal, Sami I. Halimi, and Sharon M. Weiss. Efficient side-coupling to photonic crystal nanobeam cavities via state-space overlap. *Journal of the Optical Society of America B*, 36:585, 2019.

[212] Martin Ploschner. Optical forces near a nanoantenna. *Journal of Nanophotonics*, 4:041570, 2010.

[213] Amr A.E. Saleh and Jennifer A. Dionne. Toward efficient optical trapping of sub-10-nm particles with coaxial plasmonic apertures. *Nano Letters*, 12:5581–5586, 11 2012.

[214] Zeger Hens and Iwan Moreels. Light absorption by colloidal semiconductor quantum dots. *Journal of Materials Chemistry*, 22:10406–10415, 5 2012.

[215] Zhe Xu, Wuzhou Song, and Kenneth B. Crozier. Optical trapping of nanoparticles using all-silicon nanoantennas. *ACS Photonics*, 5:4993–5001, 2018.

[216] J. J. Hernández-Sarria, Osvaldo N. Oliveira, and J. R. Mejía-Salazar. Toward lossless infrared optical trapping of small nanoparticles using nonradiative anapole modes. *Physical Review Letters*, 127:186803, 10 2021.

[217] Guillaume Baffou and Romain Quidant. Thermo-plasmonics: using metallic nanostructures as nano-sources of heat. *Laser Photonics Reviews*, 7:171–187, 3 2013.

[218] Guillaume Baffou, Christian Girard, and Romain Quidant. Mapping heat origin in plasmonic structures. *Physical Review Letters*, 104, 4 2010.

[219] Roberto Piazza. 'thermal forces': colloids in temperature gradients. *Journal of Physics: Condensed Matter*, 16:S4195, 9 2004.

[220] R. Piazza and A. Parola. Thermophoresis in colloidal suspensions. *Journal of Physics Condensed Matter*, 20, 4 2008.

[221] Yuval Lamhot, Assaf Barak, Or Peleg, and Mordechai Segev. Self-trapping of optical beams through thermophoresis. *Physical Review Letters*, 105:1–4, 2010.

[222] Linhan Lin, Xiaolei Peng, Zhangming Mao, Xiaoling Wei, Chong Xie, and Yuebing Zheng. Interfacial-entropy-driven thermophoretic tweezers. *Lab on a Chip*, 17:3061–3070, 9 2017.

[223] Martin Fränzl and Frank Cichos. Hydrodynamic manipulation of nano-objects by optically induced thermo-osmotic flows. *Nature Communications*, 13, 12 2022.

[224] James R. Melcher and Millard S. Firebaugh. Traveling-wave bulk electroconvection induced across a temperature gradient. *The Physics of Fluids*, 10:1178, 12 1967.

[225] David R Lide. *CRC handbook of chemistry and physics*, volume 85. CRC press, 2003.

[226] Sami I. Halimi, Zhongyuan Fu, Francis O. Afzal, Joshua A. Allen, Shuren Hu, and Sharon M. Weiss. Controlling the mode profile of photonic crystal nanobeam cavities with mix-and-match unit cells. *Journal of the Optical Society of America B*, 37:3401, 2020.

[227] Sejeong Kim, Hwi-Min Kim, and Yong-Hee Lee. Single nanobeam optical sensor with a high q-factor and high sensitivity. *Optics Letters*, 40(22):5351–5354, 2015.

[228] Jonathan Barzilai and Jonathan M Borwein. Two-point step size gradient methods. *IMA journal of numerical analysis*, 8(1):141–148, 1988.

[229] Kai Wang and Kenneth B. Crozier. Plasmonic trapping with a gold nanopillar. *ChemPhysChem*, 13:2639–2648, 2012.

[230] Tongtong Zhu, Yongyin Cao, Lin Wang, Zhongquan Nie, Tun Cao, Fangkui Sun, Zehui Jiang, Manuel Nieto-Vesperinas, Yongmin Liu, Cheng-Wei Qiu, et al. Self-induced backaction optical pulling force. *Physical Review Letters*, 120(12):123901, 2018.

[231] Keir C. Neuman and Steven M. Block. Optical trapping. *Review of Scientific Instruments*, 75:2787, 9 2004.

[232] Roberto Piazza and Alberto Parola. Thermophoresis in colloidal suspensions. *Journal of Physics: Condensed Matter*, 20(15):153102, 2008.

[233] Jerome Burelbach, Mykolas Zupkauskas, Robin Lamboll, Yang Lan, and Erika Eiser. Colloidal motion under the action of a thermophoretic force. *The Journal of Chemical Physics*, 147(9):094906, 2017.

[234] Shawn A Putnam, David G Cahill, and Gerard CL Wong. Temperature dependence of thermodiffusion in aqueous suspensions of charged nanoparticles. *Langmuir*, 23(18):9221–9228, 2007.

[235] Linhan Lin, Xiaolei Peng, Xiaoling Wei, Zhangming Mao, Chong Xie, and Yuebing Zheng. Thermophoretic tweezers for low-power and versatile manipulation of biological cells. *ACS nano*, 11(3):3147–3154, 2017.

[236] B. V. Derjaguin, N. V. Churaev, and V. M. Muller. *Surface Forces*. Springer US, 1987.

[237] Linhan Lin, Mingsong Wang, Xiaolei Peng, Emanuel N. Lissek, Zhangming Mao, Leonardo Scarabelli, Emily Adkins, Sahin Coskun, Husnu Emrah Unalan, Brian A. Korgel, Luis M. Liz-Marzán, Ernst Ludwig Florin, and Yuebing Zheng. Opto-thermoelectric nanotweezers. *Nature Photonics*, 12:195–201, 3 2018.

[238] Quanbo Jiang, Benoît Rogez, Jean-Benoît Claude, Guillaume Baffou, and Jérôme Wenger. Quantifying the role of the surfactant and the thermophoretic force in plasmonic nano-optical trapping. *Nano Letters*, 20(12):8811–8817, 2020.

[239] Dajiang Yang, Chenguang Lu, Huiming Yin, and Irving P Herman. Thermoelectric performance of pbse quantum dot films. *Nanoscale*, 5(16):7290–7296, 2013.

[240] G Shiva Shanker, Abhishek Swarnkar, Arindom Chatterjee, S Chakraborty, Manabjyoti Phukan, Naziya Parveen, Kanishka Biswas, and Angshuman Nag. Electronic grade and flexible semiconductor film employing oriented attachment of colloidal ligand-free pbs and pbse nanocrystals at room temperature. *Nanoscale*, 7(20):9204–9214, 2015.

[241] Sen Yang, Chuchuan Hong, Yuxi Jiang, and Justus C. Ndukaife. Nanoparticle trapping in a quasi-bic system. *ACS Photonics*, 8:1961–1971, 2021.

[242] Jacob N Israelachvili. *Intermolecular and surface forces*. Academic press, 2011.

[243] Brian D. Iverson and Suresh V. Garimella. Recent advances in microscale pumping technologies: A review and evaluation. *Microfluidics and Nanofluidics*, 5:145–174, 8 2008.

[244] Todd M. Squires and Stephen R. Quake. Microfluidics: Fluid physics at the nanoliter scale. *Reviews of Modern Physics*, 77:977–1026, 7 2005.

[245] Jiajie Chen, Jacky Fong Chuen Loo, Dongping Wang, Yu Zhang, Siu Kai Kong, and Ho Pui Ho. Thermal optofluidics: Principles and applications, 1 2020.

[246] Chao Liu, Junxiang Zhao, Fei Tian, Lili Cai, Wei Zhang, Qiang Feng, Jianqiao Chang, Fangning Wan, Yunjie Yang, Bo Dai, et al. Low-cost thermophoretic profiling of extracellular-vesicle surface proteins for the early detection and classification of cancers. *Nature biomedical engineering*, 3(3):183–193, 2019.

[247] E. Flores-Flores, S. A. Torres-Hurtado, R. Páez, U. Ruiz, G. Beltrán-Pérez, S. L. Neale, J. C. Ramirez-San-Juan, and R. Ramos-García. Trapping and manipulation of microparticles using laser-induced convection currents and photophoresis. *Biomedical Optics Express*, 6:4079, 10 2015.

[248] Jacob B Khurgin and Alexandra Boltasseva. Reflecting upon the losses in plasmonics and metamaterials. *MRS bulletin*, 37(8):768–779, 2012.

[249] Yuquan Zhang, Changjun Min, Xiujie Dou, Xianyou Wang, Hendrik Paul Urbach, Michael G Somekh, and Xiaocong Yuan. Plasmonic tweezers: for nanoscale optical trapping and beyond. *Light: Science & Applications*, 10(1):59, 2021.

[250] Guillaume Baffou and Romain Quidant. Thermo-plasmonics: Using metallic nanostructures as nanosources of heat, 3 2013.

[251] Miao Li, Theobald Lohmüller, and Jochen Feldmann. Optical injection of gold nanoparticles into living cells. *Nano Letters*, 15:770–775, 1 2015.

[252] Arseniy I. Kuznetsov, Andrey E. Miroshnichenko, Mark L. Brongersma, Yuri S. Kivshar, and Boris Luk'yanchuk. Optically resonant dielectric nanostructures. *Science*, 354, 11 2016.

[253] Donato Conteduca, Giuseppe Brunetti, Giampaolo Pitruzzello, Francesco Tragni, Kishan Dholakia, Thomas F Krauss, and Caterina Ciminelli. Exploring the limit of multiplexed near-field optical trapping. *Acs Photonics*, 8(7):2060–2066, 2021.

[254] Ikjun Hong, Chuchuan Hong, Guodong Zhu, Theodore Anyika, and Justus C. Ndukaife. Anapole-assisted near-field optical trapping. *https://doi.org/10.1117/12.2632549*, PC12198:PC121981E, 10 2022.

[255] George P. Zograf, Mihail I. Petrov, Sergey V. Makarov, and Yuri S. Kivshar. All-dielectric thermonanophotonics. *Advances in Optics and Photonics*, 13:643, 9 2021.

[256] Shereena Joseph, Saurabh Pandey, Swagato Sarkar, and Joby Joseph. Bound states in the continuum in resonant nanostructures: An overview of engineered materials for tailored applications. *Nanophotonics*, 10:4175–4207, 12 2021.

[257] Zihao Chen, Xuefan Yin, Jicheng Jin, Zhao Zheng, Zixuan Zhang, Feifan Wang, Li He, Bo Zhen, and Chao Peng. Observation of miniaturized bound states in the continuum with ultra-high quality factors. *Science Bulletin*, 67(4):359–366, 2022.

[258] Can Huang, Chen Zhang, Shumin Xiao, Yuhan Wang, Yubin Fan, Yilin Liu, Nan Zhang, Geyang Qu, Hongjun Ji, Jiecai Han, et al. Ultrafast control of vortex microlasers. *Science*, 367(6481):1018–1021, 2020.

[259] Aleksandrs Leitis, Andreas Tittl, Mingkai Liu, Bang Hyun Lee, Man Bock Gu, Yuri S Kivshar, and Hatice Altug. Angle-multiplexed all-dielectric metasurfaces for broadband molecular fingerprint retrieval. *Science advances*, 5(5):eaaw2871, 2019.

[260] Yasaman Jahani, Eduardo R Arvelo, Filiz Yesilkoy, Kirill Koshelev, Chiara Cianciaruso, Michele De Palma, Yuri Kivshar, and Hatice Altug. Imaging-based spectrometer-less optofluidic biosensors based on dielectric metasurfaces for detecting extracellular vesicles. *Nature Communications*, 12(1):3246, 2021.

[261] Zhuojun Liu, Yi Xu, Ye Lin, Jin Xiang, Tianhua Feng, Qitao Cao, Juntao Li, Sheng Lan, and Jin Liu. High-q quasibound states in the continuum for nonlinear metasurfaces. *Physical review letters*, 123(25):253901, 2019.

[262] Daria V Bochek, Nikolay S Solodovchenko, Denis A Yavsin, Alexander B Pevtsov, Kirill B Samusev, and Mikhail F Limonov. Bound states in the continuum versus material losses: Ge2sb2te5 as an example. *Physical Review B*, 105(16):165425, 2022.

[263] Sen Yang, Joshua A Allen, Chuchuan Hong, Kellen P Arnold, Sharon M Weiss, and Justus C Ndukaife. Multiplexed long-range electrohydrodynamic transport and nano-optical trapping with cascaded bowtie photonic crystal nanobeams. *Physical Review Letters*, 130(8):083802, 2023.

[264] Dieter Braun and Albert Libchaber. Trapping of dna by thermophoretic depletion and convection. *Physical Review Letters*, 89, 2002.

[265]

[266] Martin Fränzl and Frank Cichos. Hydrodynamic manipulation of nano-objects by optically induced thermo-osmotic flows. *Nature Communications*, 13, 12 2022.

[267] John C. Crocker and David G. Grier. Methods of digital video microscopy for colloidal studies. *Journal of Colloid and Interface Science*, 179:298–310, 4 1996.

[268] Y. Z. Shi, S. Xiong, Y. Zhang, L. K. Chin, Y. Y. Chen, J. B. Zhang, T. H. Zhang, W. Ser, A. Larson, L. S. Hoi, J. H. Wu, T. N. Chen, Z. C. Yang, Y. L. Hao, B. Liedberg, P. H. Yap, D. P. Tsai, C. W. Qiu, and A. Q. Liu. Sculpting nanoparticle dynamics for single-bacteria-level screening and direct binding-efficiency measurement. *Nature Communications*, 9, 12 2018.

[269] Yuzhi Shi, Sha Xiong, Lip Ket Chin, Jingbo Zhang, Wee Ser, Jiuhui Wu, Tianning Chen, Zhenchuan Yang, Yilong Hao, Bo Liedberg, Peng Huat Yap, Din Ping Tsai, Cheng-Wei Qiu, and Ai Qun Liu. Nanometer-precision linear sorting with synchronized optofluidic dual barriers. *Science Advances*, 2018.

[270] Iliya D. Stoev, Benjamin Seelbinder, Elena Erben, Nicola Maghelli, and Moritz Kreysing. Highly sensitive force measurements in an optically generated, harmonic hydrodynamic trap. *eLight*, 1, 12 2021.

[271] Hong Ren Jiang, Hirofumi Wada, Natsuhiko Yoshinaga, and Masaki Sano. Manipulation of colloids by a nonequilibrium depletion force in a temperature gradient. *Physical Review Letters*, 102, 5 2009.

[272]

[273] David Simon, Tobias Thalheim, and Frank Cichos. Optical manipulation of single dna molecules by depletion interactions. In *Optical Trapping and Optical Micromanipulation XIX*, page PC121981C. SPIE, 2022.

[274] Hatice Altug, Sang-Hyun Oh, Stefan A Maier, and Jiří Homola. Advances and applications of nanophotonic biosensors. *Nature nanotechnology*, 17(1):5–16, 2022.

[275] TK Hakala, HT Rekola, AI Väkeväinen, J-P Martikainen, Marek Nečada, AJ Moilanen, and P Törmä. Lasing in dark and bright modes of a finite-sized plasmonic lattice. *Nature communications*, 8(1):13687, 2017.

[276] Silvia Romano, Maria Mangini, Erika Penzo, Stefano Cabrini, Anna Chiara De Luca, Ivo Rendina, Vito Mocella, and Gianluigi Zito. Ultrasensitive surface refractive index imaging based on quasi-bound states in the continuum. *ACS nano*, 14(11):15417–15427, 2020.

[277] Silvia Romano, Gianluigi Zito, Stefano Managò, Giuseppe Calafiore, Erika Penzo, Stefano Cabrini, Anna Chiara De Luca, and Vito Mocella. Surface-enhanced raman and fluorescence spectroscopy with an all-dielectric metasurface. *The Journal of Physical Chemistry C*, 122(34):19738–19745, 2018.

[278] Qiang Su, Cheng Jiang, Deming Gou, and Yi Long. Surface plasmon-assisted fluorescence enhancing and quenching: From theory to application. *ACS Applied Bio Materials*, 4(6):4684–4705, 2021.

[279] D. Bastos and F. J. De las Nieves. *On the zeta-potential of sulfonated polystyrene model colloids*, volume 93. Springer-Verlag GmbH Company KG, 1993.

[280] Lukas Novotny and Bert Hecht. Principles of nano-optics. *Principles of Nano-Optics*, 9781107005464:1–564, 1 2009.

[281] Jacob B. Khurgin and Alexandra Boltasseva. Reflecting upon the losses in plasmonics and metamaterials. *MRS Bulletin*, 37:768–779, 8 2012.

[282] Jacob B. Khurgin and Greg Sun. Scaling of losses with size and wavelength in nanoplasmonics and metamaterials. *Applied Physics Letters*, 99, 11 2011.

[283] Chihhui Wu, Alexander B. Khanikaev, Ronen Adato, Nihal Arju, Ahmet Ali Yanik, Hatice Altug, and Gennady Shvets. Fano-resonant asymmetric metamaterials for ultrasensitive spectroscopy and identification of molecular monolayers. *Nature Materials 2011 11:1*, 11:69–75, 11 2011.

[284] Ronen Adato, Ahmet A. Yanik, Jason J. Amsden, David L. Kaplan, Fiorenzo G. Omenetto, Mi K. Hong, Shyamsunder Erramilli, and Hatice Altug. Ultra-sensitive vibrational spectroscopy of protein monolayers with plasmonic nanoantenna arrays. *Proceedings of the National Academy of Sciences of the United States of America*, 106:19227–19232, 11 2009.

[285] Boris Luk'Yanchuk, Nikolay I. Zheludev, Stefan A. Maier, Naomi J. Halas, Peter Nordlander, Harald Giessen, and Chong Tow Chong. The fano resonance in plasmonic nanostructures and metamaterials. *Nature Materials*, 9:707–715, 2010.

[286] Shikai Deng, Ran Li, Jeong-Eun Park, Jun Guan, Priscilla Choo, Jingtian Hu, Paul JM Smeets, and Teri W Odom. Ultranarrow plasmon resonances from annealed nanoparticle lattices. *Proceedings of the National Academy of Sciences*, 117(38):23380–23384, 2020.

[287] Quynh Le-Van, Erwin Zoethout, Erik-Jan Geluk, Mohammad Ramezani, Matthijs Berghuis, and Jaime Gómez Rivas. Enhanced quality factors of surface lattice resonances in plasmonic arrays of nanoparticles. *Advanced Optical Materials*, 7(6):1801451, 2019.

[288] M. Saad Bin-Alam, Orad Reshef, Yaryna Mamchur, M. Zahirul Alam, Graham Carlow, Jeremy Upham, Brian T. Sullivan, Jean Michel Ménard, Mikko J. Huttunen, Robert W. Boyd, and Ksenia Dolgaleva. Ultra-high-q resonances in plasmonic metasurfaces. *Nature Communications*, 12, 12 2021.

[289] Saman Jahani and Zubin Jacob. All-dielectric metamaterials. *Nature Nanotechnology 2016 11:1*, 11:23–36, 1 2016.

[290] Kirill Koshelev and Yuri Kivshar. Dielectric resonant metaphotonics, 1 2021.

[291] Yuanmu Yang, Ivan I. Kravchenko, Dayrl P. Briggs, and Jason Valentine. All-dielectric metasurface analogue of electromagnetically induced transparency. *Nature Communications 2014 5:1*, 5:1–7, 12 2014.

[292] Chia Wei Hsu, Bo Zhen, Jeongwon Lee, Song-Liang Chua, Steven G Johnson, John D Joannopoulos, and Marin Soljačić. Observation of trapped light within the radiation continuum. *Nature*, 499(7457):188–191, 2013.

[293] Min-Soo Hwang, Hoo-Cheol Lee, Kyoung-Ho Kim, Kwang-Yong Jeong, Soon-Hong Kwon, Kirill Koshelev, Yuri Kivshar, and Hong-Gyu Park. Ultralow-threshold laser using super-bound states in the continuum. *Nature Communications*, 12(1):4135, 2021.

[294] Song Han, Longqing Cong, Yogesh Kumar Srivastava, Bo Qiang, Mikhail V Rybin, Abhishek Kumar, Ravikumar Jain, Wen Xiang Lim, Venu Gopal Achanta, Shriganesh S Prabhu, et al. All-dielectric active terahertz photonics driven by bound states in the continuum. *Advanced Materials*, 31(37):1901921, 2019.

[295] Andrey A. Bogdanov, Kirill L. Koshelev, Polina V. Kapitanova, Mikhail V. Rybin, Sergey A. Gladyshev, Zarina F. Sadrieva, Kirill B. Samusev, Yuri S. Kivshar, and Mikhail F. Limonov. Bound states in the continuum and fano resonances in the strong mode coupling regime. *https://doi.org/10.1117/1.AP.1.1.016001*, 1:016001, 1 2019.

[296] Yuanqing Yang, Vladimir A. Zenin, and Sergey I. Bozhevolnyi. Anapole-assisted strong field enhancement in individual all-dielectric nanostructures. *ACS Photonics*, 5:1960–1966, 5 2018.

[297] Allen H.J. Yang, Sean D. Moore, Bradley S. Schmidt, Matthew Klug, Michal Lipson, and David Erickson. Optical manipulation of nanoparticles and biomolecules in sub-wavelength slot waveguides. *Nature 2008 457:7225*, 457:71–75, 1 2009.

[298] Gianni Q Moretti, Emiliano Cortés, Stefan A Maier, Andrea V Bragas, and Gustavo Grinblat. Engineering gallium phosphide nanostructures for efficient nonlinear photonics and enhanced spectroscopies. *Nanophotonics*, 10(17):4261–4271, 2021.

[299] Cizhe Fang, Qiyu Yang, Qingchen Yuan, Linpeng Gu, Xuetao Gan, Yao Shao, Yan Liu, Genquan Han, and Yue Hao. Efficient second-harmonic generation from silicon slotted nanocubes with bound states in the continuum. *Laser & Photonics Reviews*, 16(5):2100498, 2022.

[300] Zhanghua Han, Fei Ding, Yangjian Cai, and Uriel Levy. Significantly enhanced second-harmonic generations with all-dielectric antenna array working in the quasi-bound states in the continuum and excited by linearly polarized plane waves. *Nanophotonics*, 10(3):1189–1196, 2020.

[301] Arash Ahmadivand and Burak Gerislioglu. Photonic and plasmonic metasensors. *Laser & Photonics Reviews*, 16(2):2100328, 2022.

[302] Mingkai Liu, David A Powell, Rui Guo, Ilya V Shadrivov, and Yuri S Kivshar. Polarization-induced chirality in metamaterials via optomechanical interaction. *Advanced Optical Materials*, 5(16):1600760, 2017.

[303] Yuanqing Yang, Andrey E Miroshnichenko, Sarah V Kostinski, Mikhail Odit, Polina Kapitanova, Min Qiu, and Yuri S Kivshar. Multimode directionality in all-dielectric metasurfaces. *Physical Review B*, 95(16):165426, 2017.

[304] Andrey B. Evlyukhin, Tim Fischer, Carsten Reinhardt, and Boris N. Chichkov. Optical theorem and multipole scattering of light by arbitrarily shaped nanoparticles. *Physical Review B*, 94:205434, 11 2016.

[305] P. Grahn, A. Shevchenko, and M. Kaivola. Electromagnetic multipole theory for optical nanomaterials. *New Journal of Physics*, 14:093033, 9 2012.

[306] Andrey B. Evlyukhin, Carsten Reinhardt, and Boris N. Chichkov. Multipole decomposition in discrete dipole approximation. *AIP Conference Proceedings*, 1475:125, 8 2012.

[307] Andrea Alù and Nader Engheta. Wireless at the nanoscale: Optical interconnects using matched nanoantennas. *Physical Review Letters*, 104:213902, 5 2010.

[308] Andrea Alu and Nader Engheta. Tuning the scattering response of optical nanoantennas with nanocircuit loads. *Nature photonics*, 2(5):307–310, 2008.

[309] Andrea Alù, Alessandro Salandrino, and Nader Engheta. Parallel, series, and intermediate interconnections of optical nanocircuit elements. 2. nanocircuit and physical interpretation. *JOSA B*, 24(12):3014–3022, 2007.

[310] Andrea Alu and Nader Engheta. Input impedance, nanocircuit loading, and radiation tuning of optical nanoantennas. *Physical review letters*, 101(4):043901, 2008.

[311] Yang Zhao, Nader Engheta, and Andrea Alù. Effects of shape and loading of optical nanoantennas on their sensitivity and radiation properties. *JOSA B*, 28(5):1266–1274, 2011.

[312] Nader Engheta, Alessandro Salandrino, and Andrea Alu. Circuit elements at optical frequencies: nanoinductors, nanocapacitors, and nanoresistors. *Physical Review Letters*, 95(9):095504, 2005.

[313] Mario Agio and Andrea Alù. *Optical antennas*. Cambridge University Press, 2013.